Theoretical and Experimental Investigations of Non Collinear High Harmonic Generation and Magnetic Helicoidal Dichroism

Mekha Vimal

université
PARIS-SACLAY

Theoretical and Experimental Investigations of Non Collinear High Harmonic Generation and Magnetic Helicoidal Dichroism

Étude théorique et expérimentale de la génération non colinéaire d'harmoniques d'ordre élevé et du dichroïsme hélicoïdal magnétique

Thèse de doctorat de l'université Paris-Saclay

École doctorale n°572, Ondes et matière (EDOM)
Spécialité de doctorat : Physique
Graduate School : Physique. Référent : Faculté des sciences d'Orsay

Thèse préparée dans l'unité de recherche **LIDYL** (Université Paris-Saclay, CEA, CNRS), sous la direction de **Thierry RUCHON**, directeur de recherche, et le co-encadrement de **Pascal SALIÈRES**, directeur de recherche

Thèse soutenue à Paris-Saclay, le 2 juin 2022, par

Mekha VIMAL

Composition du jury

Marc HANNA Directeur de recherche, CNRS, Institut d'Optique, Université Paris-Saclay	Président
Eric CONSTANT Directeur de Recherche, CNRS, Institut Lumière Matière (iLM)	Rapporteur & Examinateur
Christoph HEYL Directeur de Recherche, Helmholtz-Institute Jena and DESY	Rapporteur & Examinateur
Caterina VOZZI Directrice de recherche, Institute for Photonics and Nanotechnologies of the Italian National Research Council (IFN-CNR)	Examinatrice
Franck VIDAL Professeur des Universités, Institut des Nanosciences de Paris, Sorbonne Université	Examinateur
Thierry RUCHON Directeur de recherche, CEA (LIDYL)	Directeur de thèse

THESE DE DOCTORAT
NNT : 2022UPASP052

université PARIS-SACLAY

ÉCOLE DOCTORALE
Ondes et matière
(EDOM)

Titre : Étude théorique et expérimentale de la génération non colinéaire d'harmoniques d'ordre élevé et du dichroïsme hélicoïdal magnétique

Mots clés : Génération d'harmoniques élevées non colinéaires, impulsions attosecondes XUV, spectroscopie photonique, moment angulaire orbital (MAO)

Résumé : La génération d'harmoniques d'ordre élevé (GHOE) est un processus extrêmement non-linéaire au cours duquel une impulsion laser intense interagit avec la matière. Cette interaction a pour conséquence l'émission d'impulsions de lumière ultra-brèves, constituées d'harmoniques du champ laser fondamental. Aujourd'hui, ce phénomène est la pierre angulaire de la science attoseconde, et constitue une source de lumière permettant une grande variété d'applications, telles que l'imagerie, la spectroscopie, ou l'étude de phénomènes physiques ultra-rapides. Dans cette thèse, nous étudions la GHOE pilotée par deux faisceaux fondamentaux non-colinéaires (NCHHG, pour « Non-Collinear High Harmonic Generation », en anglais). Ces travaux, à la fois expérimentaux et théoriques, portent sur une large plage de ratios d'intensité entre les deux faisceaux. On passe ainsi du régime perturbatif, où l'un des deux faisceaux est seulement une perturbation de l'autre, au régime non perturbatif, où les deux faisceaux ont des intensités similaires. A l'aide d'un modèle analytique basé sur la description classique du champ laser, nous avons établi des lois décrivant le comportement de l'intensité de l'émission d'harmoniques dans cette géométrie. Les résultats expérimentaux confirment de manière très précise ces prédictions théoriques. Nous proposons également une interprétation des observations en termes des « canaux photoniques » associés à chaque direction d'émission, et construisons ainsi un lien avec des interprétations existantes limitées au régime perturbatif. Cette description plus générale du processus de NCHHG pourrait se solder par de nouvelles techniques de spectroscopie. De plus, nous avons également mené une étude détaillée des effets d'accord de phase en NCHHG. Le développement de modèles théoriques bidimensionnels nous a permis d'identifier le rôle de l'accord de phase transverse et longitudinal dans l'intensité de l'émission. Ces études numériques et théoriques sont encore une fois confirmées par des données expérimentales. Enfin, nous proposons une application de la NCHHG, où celle-ci constitue une source de lumière dans l'ultraviolet extrême (UVX) portant du moment angulaire orbital (MAO). La réflexion différentielle de faisceaux UVX portant un moment angulaire orbital positif ou négatif par des structures magnétiques constitue un nouveau champ de recherche : le dichroïsme hélicoïdal magnétique. Cette approche est novatrice dans le sens où elle considère les effet magnéto-optiques à travers le prisme du MAO, et non de la polarisation circulaire.

université PARIS-SACLAY

ÉCOLE DOCTORALE
Ondes et matière
(EDOM)

Title : Theoretical and Experimental Investigations of Non Collinear High Harmonic Generation and Magnetic Helicoidal Dichroism

Keywords : Non collinear HHG, XUV attosecond pulses, photon spectroscopy, orbital angular momentum (OAM).

Abstract : High Harmonic Generation (HHG) is an extremely non-linear process involving the interaction of intense laser pulses with matter, resulting in the emission of ultrashort pulses of high order harmonics of the fundamental laser field. Today, it is the basis of attosecond science, used as a source for a variety of applications like imaging, spectroscopy, or investigation of ultrafast processes in gas and condensed matter. In this thesis, we investigate High Harmonic Generation driven by two Non Collinear beams (NCHHG). The work extends theoretically and experimentally over a very large range of intensity ratios of the two beams, from the perturbative to the non perturbative regime. Using a field based analytical model, we could establish the scaling laws of the yields of the harmonic emission in such a geometry. The experimental results are in very good agreement with the theoretical model. These results could also be interpreted in terms of photon channels associated to each beamlet, bridging the gap with previous interpretations restricted to the low perturbation regime. The establishment of this general description of NCHHG opens novel spectroscopic approaches. In addition, we also conduct an extensive study of phase matching effects in NCHHG. By developing a two dimensional theoretical model, we identify the contribution of longitudinal and transverse phase matching effects to the emission yields. The theoretical and numerical studies are complemented by experimental results. Finally, we present an application of NCHHG as a source of XUV attosecond pulses carrying orbital angular momentum. We identified an uneven reflection of XUV light vortices by magnetic structures, which we call magnetic helicoidal dichroism (MHD). It opens a new way of looking at the magneto-optical scattering process in terms of OAM, highly promising for studying complex spin textures.

THEORETICAL AND EXPERIMENTAL INVESTIGATIONS OF NON COLLINEAR HIGH HARMONIC GENERATION AND MAGNETIC HELICOIDAL DICHROISM

Printed in Saclay, 2022

Plateforme ATTOLab
Laboratoire Interactions, Dynamiques et Lasers
Institut Rayonnement Matière Saclay
Direction de la Recherche Fondamentale
Commissariat à l'Énergie Atomique et aux Énergies Alternatives
91191 Gif-sur-Yvette
France

http://iramis.cea.fr/LIDYL/index.php

Abstract

High Harmonic Generation (HHG) is an extremely non-linear process involving the interaction of intense laser pulses with matter, resulting in the emission of ultrashort pulses of high order harmonics of the fundamental laser field. Through this phenomenon, we can generate a broad band of extreme ultraviolet radiation in the form of short pulses with attosecond duration. Today, it is the basis of attosecond science, used as a source for a variety of applications like imaging, spectroscopy, or investigation of ultrafast processes in gas and condensed matter. HHG has the very unique advantage that properties of the fundamental field like angular momentum can be transferred to the harmonics, enabling the generation of tailored XUV attosecond pulses.

In this thesis, we investigate High Harmonic Generation driven by two Non Collinear beams (NCHHG). The work extends theoretically and experimentally over a very large range of intensity ratios of the two beams, from the perturbative to the non perturbative regime. Until now NCHHG has been explained using a very intuitive photon model and the emission yields have been found to follow a perturbative scaling law. Using a field based analytical model, we could go beyond this existing phenomenological prediction and establish the scaling laws of the yields of the harmonic emission in such a geometry from the perturbative, through the intermediate to the non perturbative regime. The experimental results are in very good agreement with the theoretical model. These results could also be interpreted in terms of photon channels associated to each beamlet, bridging the gap with previous interpretations restricted to the low perturbation regime. The establishment of this general description of NCHHG opens novel spectroscopic approaches. In addition, we also conducted an extensive study of phase matching effects in NCHHG. By developing a two dimensional theoretical model that draws on concepts from X-ray diffraction in crystals, we could identify the contribution of longitudinal and transverse phase matching effects to the emission yields. With this model, we are able to retrieve the results of the standard model of phase matching in HHG as well as gain new

insights into the amplitude distribution of the emission yields in NCHHG. The theoretical and numerical studies are complemented by experimental results.

Finally, we present an application of NCHHG as a source of XUV attosecond pulses carrying orbital angular momentum (OAM). We identified an uneven reflection of XUV light vortices by magnetic structures, which we call magnetic helicoidal dichroism (MHD). There is a redistribution of OAM modes of the incident radiation, when reflected from a magnetic sample having non uniform magnetisation. We developed a classical electromagnetic theory to explain this phenomenon which was later validated by experimental investigations. It opens a new way of looking at the magneto-optical scattering process in terms of OAM, highly promising for studying complex spin textures. NCHHG being a source of XUV beams carrying tunable OAM, is a promising tool for such studies.

Synthèse

La génération d'harmoniques d'ordre élevé (GHOE) est un processus extrêmement non-linéaire au cours duquel une impulsion laser intense interagit avec la matière, ce qui a pour effet l'émission d'impulsions de lumière ultra-brèves, constituées d'harmoniques du champ laser fondamental. Ce phénomène permet d'obtenir un rayonnement lumineux dans l'ultraviolet extrême (UVX), avec une large bande spectrale, sous la forme d'impulsions de durée attoseconde. Aujourd'hui, la GHOE est la pierre angulaire de la science attoseconde, et constitue une source de lumière permettant une grande variété d'applications, telles que l'imagerie, la spectroscopie, ou l'étude de phénomènes physiques ultra-rapides. L'une des propriétés uniques de la GHOE est de permettre le transfert de grandeurs portées par le champ fondamental, telles que le moment angulaire, aux harmoniques, permettant ainsi de contrôler les propriétés des des impulsions UVX. Dans cette thèse, nous étudions la GHOE pilotée par deux faisceaux fondamentaux non-colinéaires (NCHHG, pour Non-Collinear High Harmonic Generation , en anglais). Ces travaux, à la fois expérimentaux et théoriques, portent sur une large plage de ratios d'intensité entre les deux faisceaux. On passe ainsi du régime perturbatif, où l'un des deux faisceaux est seulement une perturbation de l'autre, au régime non perturbatif, où les deux faisceaux ont des intensités similaires. Jusqu'à présent, la NCHHG a été interprétée à l'aide d'un modèle intuitif faisant appel au concept de photon, et il était admis que la distribution d'intensité de l'émission harmonique obéit à une loi d'échelle perturbative. A l'aide d'un modèle analytique basé sur la description classique du champ laser, nous avons pu dépasser les limites de ces prédictions phénoménologiques, et décrire correctement l'intensité de l'émission d'harmoniques dans cette géométrie, du régime perturbatif au régime non perturbatif, en passant par des régimes intermédiaires. Les résultats expérimentaux confirment de manière très précise ces prédictions théoriques. Nous proposons également une interprétation des observations en termes des canaux photoniques associés à

chaque direction d'émission, et construisons ainsi un lien avec les interprétations existantes limitées au régime perturbatif. Cette description plus générale du processus de NCHHG pourrait mener à de nouvelles techniques de spectroscopie. De plus, nous avons également mené une étude détaillée des effets d'accord de phase en NCHHG. Le développement de modèles théoriques bidimensionnels, s'inspirant des concepts propres à la diffraction par rayons X, nous a permis d'identifier les rôles des accords de phase transverses et longitudinaux dans l'intensité de l'émission. Ce modèle nous permet de retrouver les résultats connus des descriptions "standards" de l'accord de phase en GHOE, mais également de comprendre plus précisément la distribution de l'intensité harmonique en NCHHG. Ces études numériques et théoriques sont encore une fois confirmées par des données expérimentales. Enfin, nous proposons une application de la NCHHG, où celle-ci constitue une source de lumière UVX portant du moment angulaire orbital (MAO). Nous avons identifié une réflexion différentielle de faisceaux UVX portant un moment angulaire orbital positif ou négatif par des structures magnétiques, ce que nous avons appelé le dichroïsme hélicoïdal magnétique (DHM). Le spectre de MAO de la lumière est modifié lorsque le faisceau se réfléchit sur un matériau ayant une magnétisation non uniforme. Nous avons développé un théorie faisant appel à l'électromagnétisme classique pour expliquer ce phénomène, et l'avons validé expérimentalement. Cette approche est novatrice dans le sens où elle considère les effets magnéto-optiques à travers le prisme du MAO, et non de la polarisation circulaire, et est prometteuse pour l'étude des textures de spin. La NCHHG, en tant que source de faisceaux UVX portant un MAO ajustable, est appelée à devenir un outil précieux pour de telles expériences.

Contents

Part I

Introduction

CHAPTER 1

Introduction

This thesis is mainly dedicated to the study of high harmonic generation (HHG) of extreme XUV radiation using two beams in non collinear geometry, with the intention of developing an in-depth understanding of the far field emission properties in such a case of HHG and prepare dedicated structured sources for an upcoming generation of spectroscopies.

1.1 High Harmonic Generation

The phenomenon of HHG was discovered about 35 years ago, almost simultaneously by [1] and [2]. It is a highly non-linear process that results from the interaction between an intense electric field and a set of atoms or molecules in the gas phase. The emitted spectrum can extend over several tens or hundreds of electronvolts, making it a unique source of ultra short XUV pulses. In a laser field with several optical cycles, the harmonic emission corresponds to a train of attosecond pulses spaced by an optical half-period, perfectly synchronized with the fundamental field [3, 4, 5]. The emission is coherent both spatially and temporally, in the sense that the phase of the XUV field is well defined and varies regularly in space and time, with small divergence, typically a few mrad. At the microscopic level, it is the universal response of atoms and molecules to strong femtosecond laser field that rules HHG [6, 7, 8, 9]. And at the macroscopic level, it is the coherent build up of light emitted from many atoms through phase matching [8, 9, 10]. The unique ability of x rays to capture structure and dynamics at the nanoscale level, and the femtosecond to attosecond time resolution offered by these pulses has spurred the growth of this field and today, HHG is the corner stone of attosecond science.

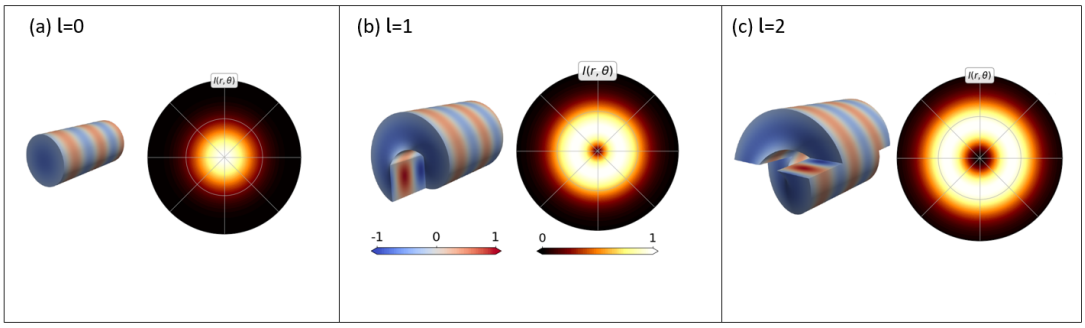

Figure 1.1: 3D representation of the electric field amplitude for Laguerre Gaussian beams with (a) $l = 0$, (b) $l = 1$ and (c) $l = 2$, showing zero, one and two intertwined spirals, respectively, along with the projection of the intensity on a transverse plane.

1.2 Towards structured XUV light and its applications

By now, the attosecond community has a comprehensive understanding of the microscopic and macroscopic effects involved in the physics of high harmonic generation. We already have high conversion efficiency [11, 12] and are pushing to shorter wavelength sources [13] and isolated attosecond pulses [14, 15, 16]. It has important applications in atomic, molecular and condensed-matter physics [17] and is now a table-top commercial technology, a relatively inexpensive source of pulsed XUV radiation, compared to free electron laser facilities.

Since HHG has been established as a concrete, reliable source of XUV radiation for studying light matter interactions, it is time to look into new directions. In this context, it is now possible to create complex, structured and coherent light waves using HHG. Especially, the generation and control of such structured light with tailored spin angular momentum (SAM) [18, 19, 20], first made available, allowed breakthroughs in studying light-matter interaction. For example, many systems, such as magnetic materials or chiral molecules, exhibit circular dichroism, i.e., they interact differently with different helicities of light. Therefore, a circularly polarized HHG source was desired to probe these "chiral" phenomena. And to resolve these phenomena in the ultra fast time scales, circularly polarized ultrafast light pulses are necessary [21]. More recently, light pulses with time varying polarization state has been used as the probe in chiroptical studies. Subcycle-shaped electric fields, whose instantaneous chirality can be controlled within the optical cycle, can be engineered to study subcycle chiroptical processes [22].

However, in recent times, structured light options became richer, with the inclusion of orbital angular momentum (OAM) in the shaping toolbox. The seminal publication of Allen et.al. [23], in 1992, demonstrated the existence of OAM of light and even proposed an experiment to demonstrate the transfer of OAM from light to matter. The key contribution of Allen and coworkers in 1992 was connecting an azimuthally varying, quantized phase, $e^{il\varphi}$, to photonic energy flow. This implied a quantized, optical OAM given as $l\hbar$, where l is the standard integer OAM quantum number, i.e., each

photon in a beam with the phase factor $e^{il\varphi}$ carries an orbital angular momentum of $l\hbar$. Such beams are characterized by the presence of a phase singularity (typically located on the beam axis), which is characterized by a rapidly varying azimuthal phase structure resulting in a point of zero intensity in the transverse plane (see Fig. 1.1). Allen et al. showed that these optical vortex beams were natural solutions of the Helmholtz equation in a cylindrically symmetric coordinate system, suggesting that they could be generated, propagated, and even controlled. A natural basis for such beams are the Laguerre Gaussian beams, essentially a product of Gaussian beams, an amplitude distribution described in terms of Laguerre polynomials, and an azimuthal phase. And since then, such structured light beams carrying OAM has been generated using diffractive optical elements like spiral phase plates, SLMs and so on. The applications have extended from imaging and 3D micromanipulation to classical and quantum communication [24]. However angular momentum control and generation with HHG is still an evolving field.

Today, generating XUV pulses carrying orbital angular momentum (OAM) [25, 26, 27, 28] is a hot topic in the ultrafast community. But, unlike studies involving pulsed, polarized XUV light, studies using pulsed, XUV OAM beams as a probe have been predicted [29, 30, 31], but no experiment has been reported. This makes it an available light source with the potential to form the basis of advanced spectroscopies, with no reported application when we started this work.

Application in light-matter interaction studies

Every interaction between light and matter has the capacity, in principle, to reveal fundamental properties of one or the other component. The coherent nature of XUV sources is a good tool for probing the fundamental mechanisms for photon emission and detection. However, almost all investigations of interaction of light with magnetic materials are based on light carrying spin angular momentum. As it is a local property, this limits the study to structures with homogeneous magnetisation or requires a scanning method or indirect retrieval algorithms. However, non-uniform magnetic structures being privileged information vectors, could be the future of magnetism. Could we access all this information more efficiently? Structured light beams, carrying OAM, could be the key to opening up new dimensions for control of spin dynamics, in matter and the study of non-uniform magnetic structures at ultrashort timescales. This is the main inspiration behind developing the theory on magnetic helicoidal dichroism (MHD), a phenomenon analogous to magnetic circular dichroism (MCD) involving the interaction of light carrying OAM with magnetic materials. Just as SAM is used to probe chiral phenomena, could not OAM be used as a similar probe to study inhomogeneous magnetic materials? With this idea, we set out to develop a universal framework describing the interaction of light carrying OAM with a magnetic structure with generic symmetry [32]. And today, we can also complement our theoretical model with the experimental evidence of magnetic helicoidal dichroism, observed in the interaction of an extreme ultraviolet vortex beam carrying orbital angular momentum with a magnetic vortex [33]. These experiments were performed at the FEL facility, FERMI in Trieste. For such experiments to become a standard in any laboratory, it is first necessary to understand the generation of structured light and even further, to optimize such sources.

1.3 How do we make tailored XUV light?

The most popular technique to shape the driving field is to combine several laser beams to modify the light field. And the best way to gain control is through the geometry of the combining laser beams. Along these lines, HHG with two fields in non collinear geometry (NCHHG) has been drawing increasing attention in both fundamental studies and applications. Some of the more recent work are listed below. Setting a crossing angle between the two beams such that less than one interference fringe appears in the overlapping region, specific dynamics during HHG were observed [34, 35], laser pulse temporal profiles measured [36, 37], individual isolated attosecond pulses synthesized [38], an opto-optical modulator demonstrated [34] and so on. All these applications derive from the interpretation of the angular deflection of the HHG spectrum driven by the second perturbative field. In the case where several fringes are formed by the two beams, each harmonic splits into a series of separate beamlets [39, 40, 41, 42] with possibly different physical properties. Importantly for us, beamlets with varying spin [18, 43] and orbital [44, 45, 46] angular momenta were observed, opening the road to applications [47, 32].

The most obvious experimental advantage of this geometry is that since the emitted harmonic orders are naturally angularly separated from both the driving laser beams and from each other, fragile samples can be placed directly into the EUV beams without filtering out the driving lasers and the high harmonic orders can be separated without the use of a lossy spectrometer, both of which significantly increase the usable HHG flux. Also, it is a test-bed for any two-beams HHG geometry: while the different beamlets corresponding to different processes are merged in collinear arrangements, they may be characterized and studied individually in NCHHG. While NCHHG is proving to be a useful source for such applications, it is important and necessary to study the fundamental physics behind it. It is the objective of this thesis to get a complete understanding of the physics behind NCHHG. What are the far field properties? Is the single atom response the same as in the case of single beam HHG? Above all, what are the ramifications of phase matching effects in this case? Since the focus is to use the emission from NCHHG as a light source, it is important to study the emission yields. Is there a decrease in efficiency? Or an enhancement? Can we control the amplitude distribution of the different beamlets? Is it possible to selectively generate certain diffraction orders while extinguishing others? All these questions are addressed in this thesis.

Having developed the source of XUV OAM beams, the second objective is to introduce a fundamental understanding of the phenomenon of MHD, paving the way towards the control of the magnetic state at the femtosecond timescale.

1.4 Thesis outline

Part I is the introductory chapter explaining the motivations behind this thesis work. In Part II of this thesis, we introduce the existing knowledge on the theoretical basis of the generation of higher order harmonics in the most conventional case, explaining the microscopic and macroscopic aspects of HHG.

In Part III, we delve into the original work done as a part of this thesis to study NCHHG through experiments and analytical modelling. Chapter 4 is dedicated to introduce the state-of-the art to the reader. We will focus on the emission yields in NCHHG and the existing theories on the subject, as it is important to understand what instigated our studies. Chapter 5 is a technical description of the development of the HHG XUV source in ATTOLab, CEA, Saclay. It involves the planning, construction and commissioning of the XUV beamline during the course of this thesis. Next, we move on to the analytical framework developed to study NCHHG in chapter 6. We will find that NCHHG has to be treated differently for the two regimes of the perturbative and the non perturbative case. Chapter 7 and 8 are dedicated to studying these two regimes, including experimental results. Throughout this part, we neglect phase matching effects, which will be addressed later on.

In Part IV, we take up the task of studying phase matching effects in NCHHG. In chapter 9, we introduce the existing literature on phase matching effects in NCHHG, before presenting a discretized version of the 1D model which will form the basis of our study. In chapter 10, we describe the 2D theoretical model that was developed. The highlight of this model is the ability to individually study longitudinal and transverse phase matching contributions. In the last chapter of this part, chapter 11, we present the results of numerical simulations and experiments of an extensive study of phase matching effects in NCHHG. Interestingly, we find new features in the intensity distribution curves through this study.

In part V, we present the new and evolving topic of magnetic helicoidal dichroism. It is presented as two individual chapters through two pioneering publications from our group. The first publication, chapter 13, is the theoretical framework for MHD which forms the basis for the experimental work described in the second publication in chapter 14. This part is an application of NCHHG for which the groundwork was laid in Part III and Part IV.

Part II

High Harmonic Generation in Gases

CHAPTER 2

Theory of High Harmonic Generation

High Harmonic Generation (HHG) is an extremely non-linear process in which an intense infrared laser is coherently upconverted into its higher order harmonics to generate extreme ultraviolet (EUV) or soft x-ray radiation [2, 1, 48, 6]. This associated XUV spectrum is typically composed of odd harmonics of the driving laser. Being a highly non perturbative process, the conversion efficiency"plateau"), before falling abruptly in the "cutoff" region. And interestingly, the properties of the IR can be transferred to the XUV to generate tailored attosecond pulses which find use in numerous applications including high harmonic spectroscopy [49], ultrafast spectroscopy, nanoscale imaging etc.[50, 17, 51]. Moreover, the directional emission of harmonics along the laser axis, which only covers a very small angle, ensures substantially high spectral brightness per pulse.

In this chapter, we introduce the basic theory of HHG, starting with the semi-classical three-step model, before moving on to a brief description of the quantum mechanical model.

2.1 Semiclassical description: Three step model

Soon after the experimental discovery of HHG by two different research groups, in 1987 in Chicago [2] and in 1988 at CEA, Saclay [1], a semi-classical description was put forth in 1993 by [6] and [52]. It should be mentioned that a quantum description of the mechanism called "atomic antenna", giving quite similar insights, was published much before in 1987 by [53].

HHG emission firstly involves an intense laser field and a single atom response to this field. The three step model gives a qualitative understanding of this microscopic response. According to the model, in the vicinity of an intense laser field, an electron leaves the atom via tunnel ionization (Step

I). It then moves along a closed trajectory, being successively accelerated away from the ionic core by the strong laser field (Step II), and then pulled back, before finally recombining with the ion (Step III), emitting its kinetic energy in the form of photons. The three steps are briefly described below.

2.1.1 Step I: Tunnel ionization

Strong field regime and Keldysh parameter

As already stated, HHG is a strong field phenomenon. The strong field regime can be characterised as the case where the electrical field strength of laser radiation applied to an atom or molecule is strong enough to induce significant modifications of its energy landscape [Shchatsinin, 2009]. In this context, the ponderomotive energy is important. It describes the average oscillation energy that is acquired by a free electron in the radiation field of the laser pulse. The ponderomotive energy is given by the following equation

$$U_P = \frac{q^2}{2m_e\varepsilon_0 c\omega^2} I,$$

where q is the electron charge, m_e is the mass of the electron, ε_0 is the dielectric constant in vacuum, c is the speed of light, ω is the angular frequency of the laser radiation, and I is the laser field intensity. The ponderomotive energy depends on the square of the wavelength and is linearly dependent on the intensity. This can be numerically expressed as

$$U_P[\text{eV}] = 9.34 \times 10^{-20} \times (\lambda[\text{nm}])^2 \times I\left[\,\text{W/cm}^2\right].$$

After energy is deposited into the atom through strong laser radiation, relaxation occurs by the release of the excess energy, usually, by ionization. At low intensities, photoionization can occur only if the energy of the absorbed photon ($\hbar\omega$) is larger than the ionization potential (I_p) of the atom; it is a single photon process. At higher intensities, it is possible for the atom to absorb multiple photons of energy $\hbar\omega$ to reach the required I_p. Such a process is called multiphoton ionization (MPI). And, if the electric field strength becomes comparable with the atomic Coulomb potential, then the electron can tunnel through the potential barrier and leave the atom. This is referred to as tunnel ionization. The dependence of the ionization probability on the ionization potential and properties of the laser radiation (intensity I and frequency ω) was theoretically investigated by L. V. Keldysh [54]. It was found that the MPI and the tunnelling ionization are two limiting regimes of nonlinear ionization. The Keldysh parameter, γ, was introduced to define the transition between these two different ionization regimes, where

$$\gamma = \sqrt{\frac{I_p}{2U_P}}. \tag{2.1}$$

In terms of Keldysh parameter, tunnel ionization occurs if γ is very small, less than 1. Using a 800 nm field of intensity $2 * 10^{14} W/cm^2$ to ionize argon gas of $I_p = 15.76\,eV$, $U_p = 12\,eV$ and $\gamma = 0.8$ falls well within the tunnel ionization regime.

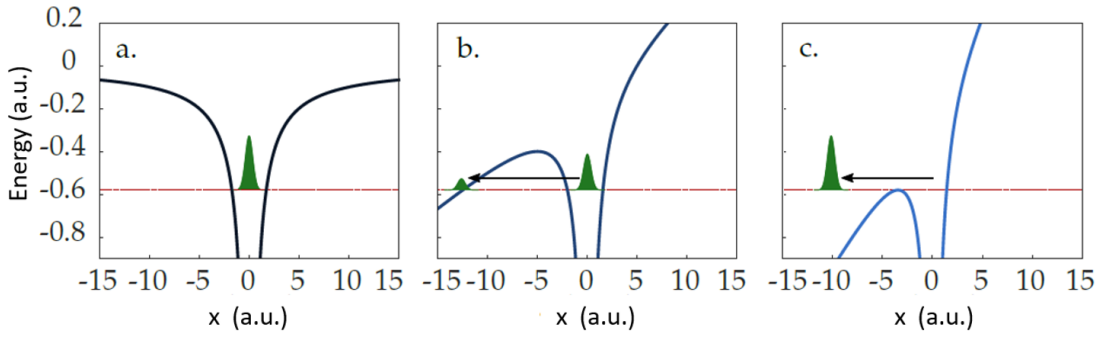

Figure 2.1: Potential experienced by an electron in argon, I_p = 15.76 eV = 0.58 a.u. (represented by the dotted line), in the absence of an electric field (a), in the presence of a field $E_0 = 0.04\ a.u.$ ($I = 5.5 * 10^{13}\ W/cm^2$) (b) and in the presence of a field at the over the barrier intensity of argon $E_0 = E_{\text{OTB}} = 0.084\ a.u.$ ($I = 2.4 * 10^14\ W/cm^2$) (c). Adapted from [55].

Over the barrier ionization

Consider an isolated atom in its ground state. An electron in this state is subjected to the Coulomb potential of the nucleus, $V_0(x) = -\frac{1}{|x|}$, where x is the distance between the electron and the nucleus (Fig. 2.1.(a)). In the presence of an electric field $E(t) = E_0 \cos(\omega t)\hat{x}$, linearly polarized along $\hat{x}$, with an angular frequency ω, the total potential V(x,t) felt by the electron will become:

$$V(x,t) = V_0(x,t) + xE(t) \tag{2.2}$$

In the case of strong field regime ($\gamma < 1$), the potential barrier is lowered enough such that a part of the electron wave packet can tunnel out of the barrier (Fig. 2.1.(b)). And in the case when the laser field is high enough to reach a threshold value, E_{OTBI}, corresponding to an intensity called the over the barrier intensity, I_{OTBI}, the potential barrier is completely suppressed and ionization occurs (Fig. 2.1.(c)). Let us try to obtain this value of I_{OTBI} for a given atom. Taking the derivative of equation 2.2,

$$\frac{\partial V}{\partial x} = \frac{1}{x^2} + E_0 = 0. \tag{2.3}$$

We get the distance $x_m = 1/\sqrt{-E_0}$ at which the potential has the maximum value, $V(x_m) = -2\sqrt{-E_0}$. E_{OTBI} is the value at which the potential barrier is just low enough for the electron to escape, i.e, $V(x_m) = -2\sqrt{-E_{\text{OTBI}}} = -I_p$. Thus the over the barrier intensity will be,

$$I_{\text{OTBI}}\left[W/\text{cm}^2\right] = 4 \times 10^9 I_p^4\ [eV]. \tag{2.4}$$

For HHG, the laser intensity must be lower than this intensity so that the ground state is not completely depleted. From equation 2.4, it is clear that atoms with higher I_p can withstand more laser intensity. Since the laser field is oscillating in time, it is important that the duration during which the barrier is lowered is enough for the electron to escape. This "tunneling time" (τ) can be estimated

from the width of the barrier and the speed of the electron under the barrier, as explained in this lecture [56]. For the width of the barrier, let us look for the locations where $V(x) = -I_p$:

$$\frac{1}{x} + E_0 x = -I_p$$
$$E_0 x^2 + I_p x + 1 = 0$$

The discriminant of this second order polynomial equation reads $\Delta = I_p^2 - 4E_0$, and the difference between the roots is

$$\Delta x = \frac{\sqrt{I_p^2 - 4E_0}}{E_0} = \frac{I_p}{E_0}\sqrt{1 - \frac{E_0}{E_{OTBI}}}.$$

Now, if we approximate the energy of the particle equals to its kinetic energy, then the speed of the particle in the barrier is, $v \simeq \sqrt{2I_p}$. The time that the particle spends through the barrier thus reads

$$\tau = \frac{\Delta x}{v} \simeq \sqrt{\frac{I_p}{2E^2}}.$$

In this case, the Keldysh parameter can be interpreted as

$$\gamma = \frac{\tau}{T}, \tag{2.5}$$

where τ is the time needed for the electron to cross the Coulomb barrier and $T = 2\pi/\omega$, the period of oscillation of the laser field. When $\gamma < 1$, it is possible for the electron to be tunnel ionized.

2.1.2 Step II: Excursion in the continuum

Being in the strong field regime, the laser field is not a perturbation to the strong coulomb potential. We can say that the interaction of the electron with the ionic core is much weaker than its interaction with the driving field. The Coulomb potential is neglected and the electron is treated classically by solving Newton's equation of motion:

$$m\ddot{x} = -eE_0 \cos(\omega t). \tag{2.6}$$

We denote t_i as the moment when the electron wave packet is ionized, and we assume that $x(t_i) = 0$ and $\dot{x}(t_i) = 0$, meaning that we neglect the movement across the barrier and that the electron is born with zero kinetic energy (KE). By integrating equation 2.6, we obtain:

$$\dot{x}(t) = v(t) = -\frac{eE_0}{m\omega}\left[\sin(\omega t) - \sin\left(\omega_{t_i}\right)\right],$$

and the trajectory of the free electron in the laser field as

$$x(t) = \frac{eE_0}{m\omega^2}\left[\cos(\omega t) - \cos(\omega t_i)\right] + \frac{eE_0}{m\omega}\sin(\omega t_i)(t - t_i). \tag{2.7}$$

The first term is oscillatory and the second term is a drift term with a constant velocity. After the laser pulse has passed, the oscillatory motion of the electron vanishes and only the drift motion remains.

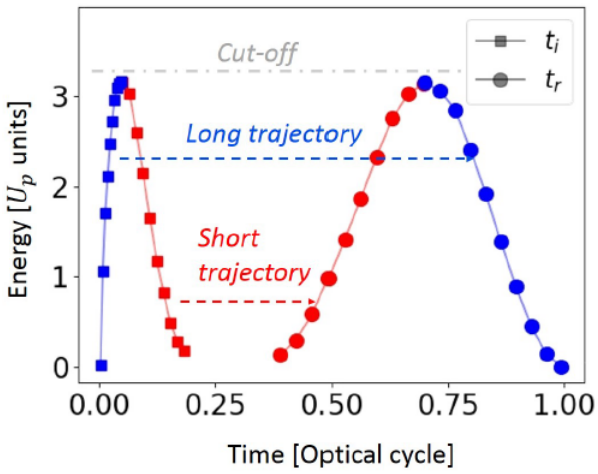

Figure 2.2: Kinetic energy at recollision as a function of the ionization (squares) and recombination times (circles) calculated by the semi-classical model, for a driving pulse with $I = 2.5 * 10^{14} W/cm^2$. Two examples of short (red) and long (blue) trajectories are given. The position of the cut-off is plotted in grey. Taken from [57].

2.1.3 Step III: Radiative recombination

During the oscillatory motion, there is a non zero probability that the electron may return to the ionic core. By solving $x(t_r) = 0$ for $t_r > t_i$, we can find the time, t_r at which the electron returns. From equation 2.7, we obtain the electron trajectories corresponding to different ionization times t_i. Depending on the phase of ionization time ωt_i and the electric field profile, it can return once, several times, or never. Only those electrons with a phase of ionization, $0 < \omega t_i < \pi/2$, revisit the ion. In case of recombination, the electron can give back the kinetic energy (KE) acquired during the excursion in the field as a photon of energy,

$$\hbar\omega = I_p + KE(t_r), \tag{2.8}$$

where

$$KE(t_r) = 2U_p \left[\sin(\omega t_r) - \sin(\omega t_i)\right]^2 \tag{2.9}$$

The maximum value which KE(t_r) can have is $3.17U_p$, giving rise to the famous cut-off law [58] in HHG,

$$\hbar\omega_{\max} = I_p + 3.17U_p. \tag{2.10}$$

The highest harmonic that can be generated in a given gas medium is limited by the laser intensity and its wavelength through $U_p \propto \lambda^2$. The time of birth and the corresponding recombination time (t_r) decides the emitted photon energy. By increasing the intensity, the position of the cut-off can be shifted but we are limited by the saturation intensity (I_{sat}) of the medium. Another way to increase

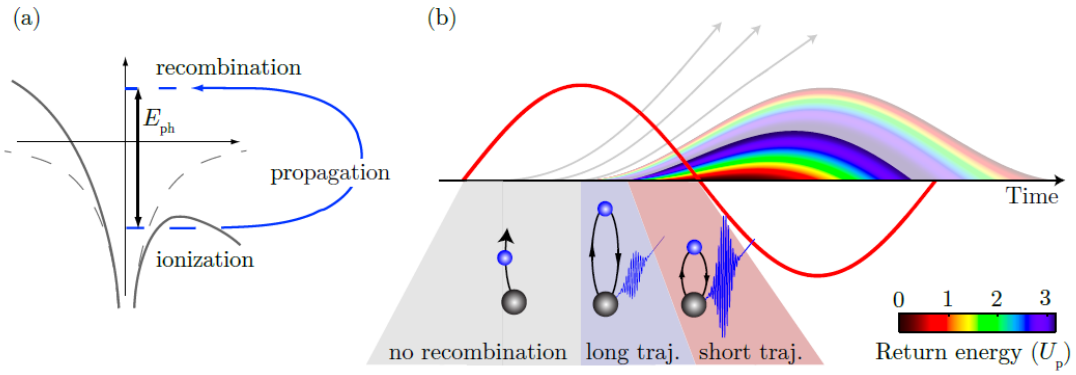

Figure 2.3: Illustration of the three-step process. (a) The distortion of the Coulomb potential leads to tunnel ionization, subsequent acceleration of the electron in the external laser field and possibly recombination leading to the emission of a photon of energy E_{ph}. (b) Classical trajectories, which depend on the time of ionization. The red line indicates the sinusoidal laser field, gray and colored trajectories indicate non returning and returning electrons, respectively. The color scale visualizes the return energy in units of U_p with saturated colors for short trajectories and transparent colors for long trajectories. Taken from [61].

the cut-off for a given gas medium is to increase the wavelength of the driving laser field. However, the generation efficiency decreases with wavelength, roughly as $\lambda^{-(5-8)}$ [59, 60].

Long and short trajectories

It is observed that two trajectories recombining at different times can emit the same energy. These two first trajectories are the so called *short* and *long* trajectories. In Fig. 2.2, we observe two pairs of $(t_i,\ t_r)$ that correspond to short and long trajectory, respectively. The first corresponds to short propagation times in the continuum, which increases with the harmonic order. The second corresponds to the case where the electron is ionized near the maximum of the electric field and has a propagation time which decreases with the harmonic order. The harmonics emitted during these different trajectories have distinct spectral and spatial characteristics, which depend on the so-called dipole phase, the phase accumulated by the electron during its trajectory, which will be addressed in section 2.2.2. Finally, Fig.2.3 is an illustration of the three step model. In (a), the distorted Coulomb potential is shown and the three steps of HHG are indicated. The trajectories that an electron can take in a sinusoidal laser field are displayed in (b), the colors indicating the return energy. Three different branches of electron trajectories can be identified, determined by the time that the electron leaves the atom.

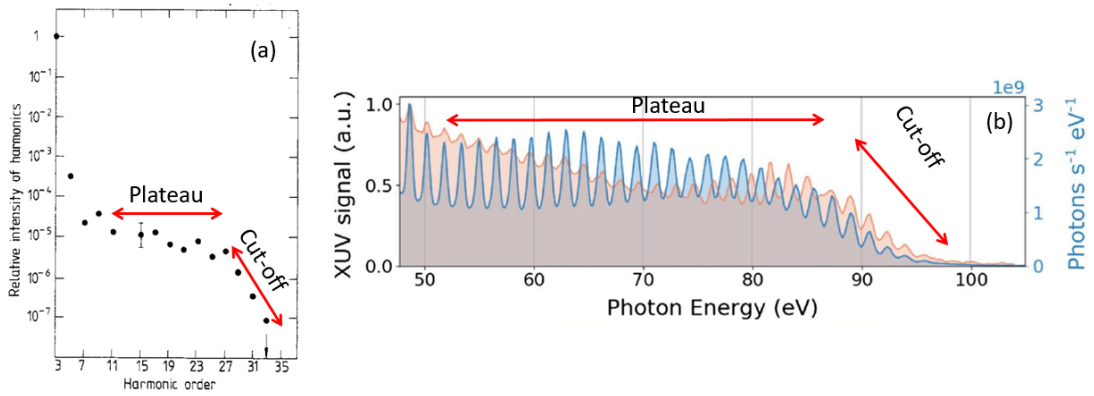

Figure 2.4: Typical experimental high harmonic spectra. (a) One of the very first observation of higher order harmonics by Ferray et al.[1] using 1064nm driving laser and Argon gas. (b) A more recent experiment by Gonzalez et al.[62] generating high photon energies using an OPCPA source at 1.55μm in Argon.

2.1.4 High harmonic spectrum

The three-step process is repeated every half cycle of the fundamental field. The periodicity in time leads to a periodicity in frequency, and odd order harmonics of the laser field frequency are emitted. This harmonic spectrum is a result of the interference of the coherent attosecond pulses emitted at each half cycle. The spectrum shows a characteristic plateau where the harmonics have comparable intensities, which ends at the cut-off energy where the intensity drops (Fig.2.4).

2.2 Quantum Mechanical Description

In the semi classical model, the step of tunnel ionization is treated quantum mechanically, while the dynamics of the free electron in the field are treated in a classical way. It gives a simple picture of the process which allows access to important quantities such as cut-off energy and ionization and recombination times. However, the HHG process is the result of the interference between part of the ionized EWP and its remaining part in the ground state. Thus, in order to study this process in detail, it is necessary to describe it with a quantum mechanical model.

2.2.1 Lewenstein model

In 1994, Maciej Lewenstein proposed a quantum theory of the HHG process [7]. This model, often referred to as the Strong Field Approximation (SFA) or Lewenstein model, is based on an approximate solution of the Time Dependent Schrödinger Equation (TDSE) and recovers the interpretations of the semi classical model.

We consider an atom in the approximation of a single active electron interacting with the laser field $\vec{E}(t)$, linearly polarized along the $\hat{x}$ direction. The electronic dynamics is described by the Schrödinger equation (in atomic units):

$$i\frac{\partial}{\partial t}|\psi(\vec{x},t)\rangle = \left(-\frac{1}{2}\nabla^2 + V_0(\vec{x}) - E_0 x\cos(\omega t)\right)|\psi(\vec{x},t)\rangle.$$

In the Strong Field Approximation (SFA), one makes the following assumptions:

1. The electrons in the continuum states are seen as free electrons that are only affected by the laser field, and the Coulomb potential of the ionic core is ignored.
2. The ground state is not depleted. This implies that the laser intensity is not too high, especially for long driving pulses.
3. Among the bound states, only the ground state contributes to the high-order harmonic radiation. The other bound states are neglected. This approximation is valid only if no resonances perturb the process.

It gives the following expression for the position of the electron at time of recombination t_r,

$$\vec{x}(t_r) = -i\int_0^{t_r} dt_i \int d\vec{p} \quad \underbrace{\vec{d}^*_{\vec{p}+e\overrightarrow{A(t_r)}}}_{recombination} \quad \underbrace{e^{i\frac{S(\vec{p},t_i,t)}{\hbar}}}_{excursion} \underbrace{\vec{E}(t_i)\cdot\vec{d}_{\vec{p}+e\overrightarrow{A(t_i)}}}_{ionization}. \tag{2.11}$$

Equation 2.11 recovers and justifies the semi-classical three-step model. More specifically:

- **ionization**: $\vec{E}(t_i)\,\vec{d}_{\vec{p}+e\vec{A}(t_i)}$ represents the probability amplitude for the laser-induced transition to the continuum state with momentum $\vec{p}$ at time t_i.
- **excursion**: The EWP gains kinetic energy during the laser oscillation and acquires an extra phase:

$$S(\vec{p},t_i,t_r) = -\int_{t_t}^{t_r}\left(I_p + \frac{(\vec{p}+\vec{A}(t))^2}{2}\right)dt.$$

- **recombination**: $\vec{d}^*_{\vec{p}+e\overrightarrow{A(t_r)}}$ indicates that the electronic wave function eventually recombines to the ground state at time t_r and releases the energy in the form of photon emission.

The Fourier transform of the position, that is to say, the induced dipole, gives the radiated spectrum. It reads

$$\tilde{\vec{x}}(\omega) = \int_{-\infty}^{+\infty} dt\,\vec{x}(t)e^{i\omega t}. \tag{2.12}$$

The quantum mechanical electron can tunnel out at any time $t_i < t_r$ and, may recombine with any momentum at a later time: i.e. all paths are possible and can, in principle, contribute to HHG. In the spirit of Feynman's path integral formalism [63], each path that the electron takes can be associated with a quasi-classical action. The most likely paths are those which minimize the action, i.e. the classical ones. Equation 2.11 can be solved with the help of saddle-point approximations [7], yielding complex quantities for t_i and t_r. This is linked to the tunnel nature of the process: the electron should not be able to escape the barrier in a classical world, while in the quantum world, the real part of t_i is interpreted as the time at which the electron exits the barrier [64].

2.2.2 Dipole amplitude and phase

If we consider only the classical quantum paths, equation 2.11 can be rewritten as a sum over all contributing paths. The corresponding spectral amplitude for harmonic order q then reads as:

$$D_q = \sum_j A_j(q,I) \exp\left[\mathrm{i}\Phi_j(q,I)\right],$$

where the sum over j denotes the sum over short and long electron trajectories. Within the high harmonic plateau, the dipole amplitude $A_j(q,I) \propto E^{q_{\mathrm{eff}}}$ is only weakly dependent on the harmonic order. q_{eff} is the effective non linearity constant of HHG (to be discussed in section 8.2.2). However, the dipole phase $\phi_j(q,I)$, changes significantly within the plateau. It also depends strongly on the trajectory considered, as well as on the driving field intensity. It therefore has a large impact on the spectral and spatial properties of the attosecond pulses, both on a subcycle level and over the duration of the driving laser pulse [62, 65]. $\Phi_j(q,I)$ can be written as:

$$\Phi_j(q,I) = q\omega_0 t_{\mathrm{r}} - \frac{1}{\hbar}\int_{t_{\mathrm{i}}}^{t_{\mathrm{r}}} \mathrm{d}t \left[\frac{p^2}{2m} + I_{\mathrm{p}}\right] \tag{2.13}$$

where $p = p(q,I)$ denotes the electron momentum. As in the three-step model, the classical ionization and recombination times (t_i, t_r) are considered here. Strictly speaking, using classical trajectory simulations to calculate $\phi_j(q,I)$ is an approximation, but it can be useful to help with understanding the underlying physical processes as well as for minimizing computation time. The first term in equation 2.13 is a phase term, which depends on the intensity and the harmonic order and which arises from the timing of when the electron recombines. This term is present in the three-step model. The second term describes the phase acquired by the electron upon propagation. The dipole phase can be approximated as:

$$\Phi_j(q,I) \approx \alpha_0 + \alpha_{\mathrm{at}} I,$$

where both α_0 and α_{at} depend on the trajectory, harmonic order and a reference intensity. α_0 is often neglected, but needs to be taken into account when the spectral dependence of $\phi_j(q,I)$ is considered. α_{at} for long trajectories are significantly higher than for short trajectories. Besides, the dipole phase changes slightly for the short trajectory, and significantly for the long trajectory, as the generation intensity is changed.

CHAPTER 3

Macroscopic Effects in HHG

3.1 Phase Matching Effects in HHG

Macroscopic aspects of HHG, often referred to as phase matching effects, commonly denote effects arising from the propagation of the XUV field and the generating laser field along the optical axis through the nonlinear medium. On a macroscopic scale, usable HHG radiation comprises radiation from a bunch of emitters of the same frequency. All of these single-frequency components must add up constructively to accumulate a spatially coherent short-wavelength source. Depending on the location in the medium, the driving laser propagates different lengths to reach the atoms, getting dephased, and so do the elementary XUV fields radiated when propagating to the detector, as there might be:

- different ions/electron densities vs neutral density ratios, hence different optical indices of the driving laser and XUV.
- different intensities, hence giving different "three-step responses" and in particular, different phases of the emission.
- different optical phases of the driver: the medium is usually of a fraction of a mm to a few mm long, not always negligible with respect to the Rayleigh length (z_R) of the beam. The Gouy phase and curvature of the beam may vary in the generating medium.

Phase matching is about finding the conditions in which all elementary electric fields add up coherently, hence reducing the variation of these dephasings with space and time as shown in Fig. 3.1.

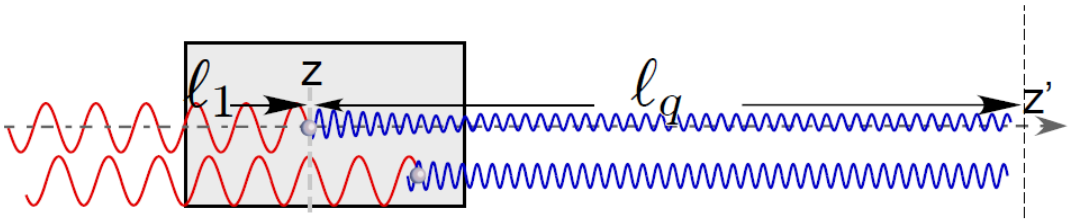

Figure 3.1: Phase matching principle. The incoming beam is in red. The XUV field in blue. For two atoms that may generate XUV light located at two different points, the driving laser propagate different lengths to reach the atoms, getting dephased, and so do the elementary XUV fields radiated when propagating to the detector. Adapted from [56].

Their understanding and optimization is crucial for efficient harmonic generation. As in the case of regular non linear optics, phase matching in HHG is usually illustrated using a k-vector model. In order to ensure phase-matched generation, the wave vector ($\vec{k}_q$) of the generated field has to match the sum of the generating field vectors ($q\vec{k}_1$) making the wave vector mismatch,

$$\Delta\vec{k}_q = q\vec{k}_1 - \vec{k}_q \tag{3.1}$$

And $\Delta\vec{k}_q = 0$ for perfect phase matching. However, this is not an easy task due to the above mentioned factors that build up when traversing a nonlinear interaction medium. This wave vector mismatch can essentially be written as a sum over four components,

$$\Delta\vec{k}_q = \Delta\vec{k}_{\text{Gouy}} + \Delta\vec{k}_{\text{dipole}} + \Delta\vec{k}_{\text{neutral}} + \Delta\vec{k}_{\text{plasma}} \tag{3.2}$$

where $\Delta\vec{k}_{\text{Gouy}}$ denotes the wave vector mismatch due to the Gouy phase, $\Delta\vec{k}_{\text{dipole}}$ is the wave vector mismatch induced by the dipole phase, and $\Delta\vec{k}_{\text{neutral}}$ and $\Delta\vec{k}_{\text{plasma}}$ are caused by dispersion in the partially ionized medium. All four components are described below.

3.1.1 Gouy phase

The Gouy phase φ_{Gouy} is defined as the on-axis phase accumulated by a Gaussian beam in propagation, in excess of the phase accumulated by a plane wave [66]. If the field of the Gaussian beam propagating along z shows a phase dependence that goes as $e^{ikz+\varphi_{\text{Gouy}}}$, the Gouy phase is defined as

$$\varphi_{\text{Gouy}} = \arctan\left(\frac{z}{z_R}\right) \text{ where,} \tag{3.3}$$

$$z_R = \frac{\pi\omega_0^2}{\lambda} \tag{3.4}$$

with ω_0, the beam waist of the laser and z_R, the Rayleigh range. This phase significantly varies within the Rayleigh range, close to the focus of the laser beam where we position the gas jet. The z-dependent geometric phase may be written as

$$-kz + \varphi_{\text{Gouy}} \simeq -\left(k + k_{\text{Gouy}}\right)z, \tag{3.5}$$

with

$$k_{\text{Gouy}} = -\frac{d\varphi_{\text{Gouy}}}{dz} = -\frac{1}{1+\frac{z^2}{z_R^2}} \cdot \frac{1}{z_R}. \simeq -\frac{1}{z_R} \tag{3.6}$$

Considering that the harmonics have a Gaussian spatial distribution and that the total harmonic signal I_q varies as $I_q \propto I_{IR}^{q_{\text{eff}}}$ [65], we will find the beam waist of the harmonic beam to be,

$$\omega_q = \frac{\omega_0}{\sqrt{q_{\text{eff}}}}. \tag{3.7}$$

Thus,

$$z_R = \frac{\pi\omega_0^2}{q_{\text{eff}}\lambda_q} = \frac{q}{q_{\text{eff}}} z_R. \tag{3.8}$$

Finally, we find

$$\Delta\vec{k}_{Gouy} = q k_{Gouy}(\omega_1) - k_{Gouy}(\omega_q) = -\frac{1}{z_R}(q - \frac{q_{\text{eff}}}{q}). \tag{3.9}$$

where q_{eff} is the effective order of nonlinearity of the HHG process.[1] Thus $\Delta\vec{k}_{Gouy}$ is always negative. And it does not depend on any ionization/composition of the medium. It plays a more important role when the Rayleigh length is small, i.e, when the numerical aperture is large, or the beam is tightly focused.

3.1.2 Dipole phase

This contribution comes from the intrinsic, intensity-dependent dipole phase of the q^{th} harmonic order. This dipole phase for a harmonic q, from trajectory, j, is defined by

$$\varphi_j(q, I) = \omega_q t_{\text{r}} - \frac{1}{\hbar}\int_{t_1}^{t_{\text{r}}} \mathrm{d}t \left[\frac{p^2}{2m} + I\right], \tag{3.10}$$

and depends on the intensity within the medium, and so varies with spatial position. As a first approximation, it remains linear with the intensity ($\varphi_j(q, I) = \alpha_{\text{at}} I$) with an α_{at} coefficient that is negative, and whose magnitude is much larger for the long trajectory than for the short. Using this approximation, the wave vector mismatch introduced by the dipole phase can be written as

$$\Delta k_{\text{dipole}} = \alpha\vec{\nabla} I. \tag{3.11}$$

In a free focus geometry, the intensity varies with x and z, leading to dramatic variations of $\Delta\varphi$ within the nonlinear medium, especially for the long trajectory contribution. Thus, Δk_{dipole} has both a radial and longitudinal component. Its sign changes with the position relative to the focus which leads to different behaviors when focusing before or after the gas jet (this will be addressed in detail in section 3.2.1).

[1] $\Delta\vec{k}_{Gouy}$ is usually approximated as $-\frac{1}{z_R}(q-1)$. Since q_{eff} is usually a fraction of q, $\frac{q_{\text{eff}}}{q}$ appear as small corrections to the dominant term proportional to q.

3.1.3 Neutral dispersion

The wave vector of any light wave with wavelength, λ, and angular frequency, ω, depends on the refractive index (n) of the medium as

$$k(\lambda) = n(\lambda)\frac{\omega}{c} \tag{3.12}$$

where c is the speed of light in vacuum. In the gas medium, there will remain some neutral atoms that do not show the same optical indices for XUV harmonic and the fundamental beam leading to a wave vector mismatch. This mismatch is,

$$\begin{aligned}\Delta k_{\text{neutral}} &= n(\lambda_1)\frac{q\omega_1}{c} - n(\lambda_q)\frac{\omega_q}{c} \\ &= \frac{q\omega_1}{c}\left[n(\lambda_1) - n(\lambda_q)\right].\end{aligned} \tag{3.13}$$

Usually this mismatch factor is neglected for HHG in gases, as its contribution is small compared to the other three mismatch components.

3.1.4 Electronic dispersion

The propagation time of the charged particles out of the ionized focal region is much longer (nanoseconds) than the duration of laser pulse (femtoseconds). Therefore the contribution from the dispersion in this plasma should be taken into account. The wave vector mismatch due to dispersion in the plasma can be calculated similar to $\Delta k_{\text{neutral}}$ where n is replaced by n_{plasma}, the value of the refractive index in plasma. The plasma contribution to the wave-vector mismatch,

$$\Delta k_{\text{plasma}} = \frac{q\omega_1}{c}\left[n_{\text{plasma}}(\lambda_1) - n_{\text{plasma}}(\lambda_q)\right] \tag{3.14}$$

The plasma frequency is given by $\omega_p = e\sqrt{\frac{N_e}{\epsilon_0 m_e}}$, where ϵ_0 is the dielectric constant, m_e is the electron mass, e is the charge of the electron, and N_e is the density of the free electrons. The index associated to the electrons reads

$$n_{plasma}(\omega) = \sqrt{1 - \frac{\omega_p^2}{\omega^2}} = \sqrt{1 - \frac{N_e}{N_c(\omega)}}, \tag{3.15}$$

where $N_c = \frac{\epsilon_0 m_e \omega^2}{e^2}$ is the critical plasma density at which the plasma medium completely absorbs all the electromagnetic waves of frequency ω. In common situations, the free-electron density generated is much lower than the critical density ($2*10^{21}$ atoms/ cm^3 at 800nm).[2]. Thus we can make the approximation,

$$n_{plasma}(\omega) \simeq 1 - \frac{\omega_p^2}{2\omega^2}. \tag{3.16}$$

Substituting equation.(3.16) in equation.(3.14), we get

$$\Delta k_{\text{plasma}} = -\frac{\omega_p^2}{2qc\omega_1}(q^2 - 1). \tag{3.17}$$

[2]There exists cases where good phase matching has been achieved above critical density, as in the work of Ellis et al. [43], for example

This makes a negative contribution to the total phase-mismatch for harmonic orders $q > 1$. It should be noted that it has a linear dependence on the electron density through ω_p^2. It thus varies spatially and temporally due to Gaussian intensity profile of the pulse in both domains.

3.1.5 Reabsorption in the medium

When talking about dispersion in the medium in 3.1.3, we considered only the real part of the refractive index of the medium contributing to dephasing. However, the refractive index is complex valued. Even if the contribution to dispersion from the real part is usually not dominant, the corresponding imaginary part of the optical index, responsible for the absorption by the neutral atoms plays a very important role. The imaginary part of the refractive index describes rather directly the attenuation of electromagnetic waves in the medium due to absorption as,

$$I(z) = I_0\, e^{-2k^{\mathrm{im}}.z} \tag{3.18}$$

where $k^{\mathrm{im}} = n^{\mathrm{im}}(\lambda)\frac{\omega}{c}$. And absorption length L_{abs} is defined as the propagation length over which the intensity decreases by 1/e,

$$I_0\, e^{-2k^{\mathrm{im}}.L_{\mathrm{abs}}} = I_0 e^{-1}, \tag{3.19}$$

giving the absorption length of a medium as

$$L_{\mathrm{abs}} = \frac{1}{2k^{\mathrm{im}}} \tag{3.20}$$

Even if the collective phase matching effects are optimized, the maximum efficiency of HHG is affected by the absorption of the harmonics by the gas medium. The pioneering work of E.Constant et.al [10] on this sets a limit on the generation efficiency due to this re-absorption in gas. The output photon flux for on-axis emission of the q^{th} harmonic is given as

$$I_q \propto \rho^2 A_q^2 \frac{4L_{\mathrm{abs}}^2}{1+4\pi^2\left(L_{\mathrm{abs}}^2/L_{\mathrm{coh}}^2\right)}\left[1+\exp\left(-\frac{L_{\mathrm{med}}}{L_{\mathrm{abs}}}\right)-2\cos\left(\frac{\pi L_{\mathrm{med}}}{L_{\mathrm{coh}}}\right)\exp\left(-\frac{L_{\mathrm{med}}}{2L_{\mathrm{abs}}}\right)\right] \tag{3.21}$$

in [10] where ρ is the gas density assumed to be constant and A_q is the amplitude of the atomic response at the harmonic frequency, independent of z. Here, $L_{\mathrm{coh}} = \pi/\Delta k$ is the coherence length ($\Delta k = k_q - q k_1$). L_{coh} represents the length over which the nonlinear polarization and the harmonic field get dephased by π, and L_{abs} is the distance over which the XUV radiation is reabsorbed by the generating medium. $L_{\mathrm{abs}} = 1/(\sigma\rho)$, with σ, the ionization cross section and ρ, the atomic density. It characterizes the critical length at which reabsorption begins to play an important role. If no reabsorption was present, the number of emitted photons would grow quadratically in case of infinite coherence length. When absorption becomes significant the output photon flux saturates. The saturation level depends on the coherence length, and becomes very low if the coherence length becomes equal to the absorption length. Based on equation (3.21), Constant et.al showed that, for a medium of length, L_{med}, two conditions:

$$L_{\mathrm{med}} > 3L_{\mathrm{abs}} \tag{3.22}$$

$$L_{\mathrm{coh}} > 5L_{\mathrm{abs}} \tag{3.23}$$

must be fulfilled for the harmonic photon flux to reach half of its maximum value. We will return in detail to this model in Part IV of this thesis.

3.2 Experimental implications of macroscopic effects

We have already seen that the harmonic generation is limited by three main factors: dephasing between the IR and the XUV, defocusing of the beam due to the free electron dispersion and finally, the reabsorption of the XUV in the medium. The choice over the optimum HHG experimental geometry can be reduced to a discussion over three typical lengths: the medium length, L_{med} , the coherence length, L_{coh} and the absorption length L_{abs}. Generating high-order harmonics that are fully phase-matched implies that $\Delta k_q = 0$ for all x, z and t, a condition which is strictly speaking not possible to achieve. While $\Delta k_{\text{neutral}}$ can be approximated as spatially and temporally constant, all other components vary spatially and temporally, thus making phase matching a spatially localized transient process which depends on a number of parameters, in particular on the gas pressure, the intensity, the nonlinear medium, and the focusing condition. However, the experimental parameters can still be regulated up to an extent to ensure efficient generation of harmonics, in particular the gas pressure and the $f\#$ of the laser beam. The selection of harmonic emission from long or short trajectories can also be easily done in the experiment by the positioning of the gas jet with respect to the laser focus.

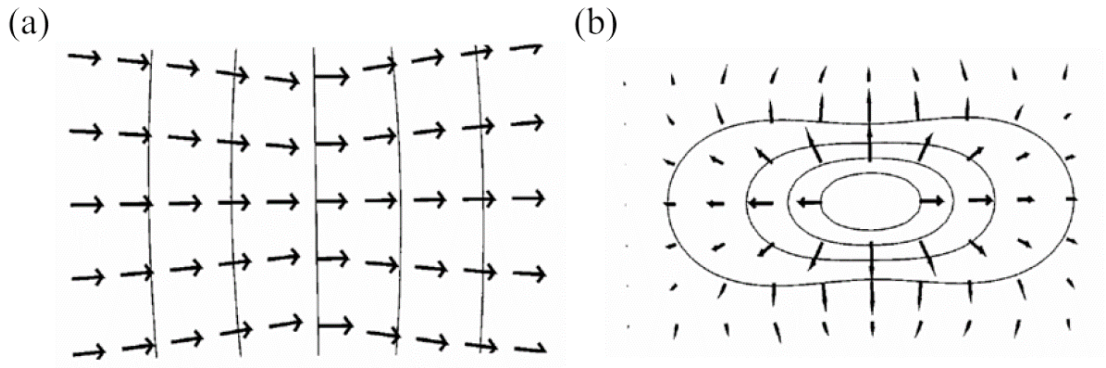

Figure 3.2: (a)Wave vector $\vec{k}_1$ of the fundamental laser beam going through a focus including the effect of the Gouy phase shift. (b) The effective dipole phase wave vector $\vec{K}$ in the focal region. Figure taken from [67].

3.2.1 Phase matching of long and short trajectories

It is well known that for selecting short trajectories, the gas jet should be positioned after the laser focus, while it should be positioned before focus for long trajectories [8]. This is mainly due to the different atomic phases (α_{at}) attributed to the long and short trajectories. The work of Ph. Balcou

et.al [9] proposes a simple interpretation for this based on wave vector conservation. Neglecting dispersive effects, the phase matching conditions is summarized as

$$\vec{k}_q = q\vec{k}_1 + \vec{K}. \tag{3.24}$$

Here, $\vec{k}_q$ is the wave vector of the emitted high harmonics. The wave vector $\vec{k}_1$ is a sum of fundamental wave vector and the $\vec{k}_{Gouy}$. This leads to a phase difference of wavefronts before and after the focus which amounts to exactly π. The effective wave vector $\vec{K}$ is the gradient of the atomic dipole phase. Phase matching conditions can now be established when adding these two vectors (Fig. 3.2) [3]. The laser axis is horizontal at figure center, and the laser pulse is assumed to propagate from left to right. As expected, $\vec{k}_1$ is mostly directed along the z direction, converges towards the focal point for z<0, and diverges for z>0. In contrast, $\vec{K}$ points at a direction opposite to the focal point, yielding a star pattern. As a result of these very different distributions, the way these wave vectors combine differs strongly from point to point near the focus. Fig. 3.3 depicts four different conditions when

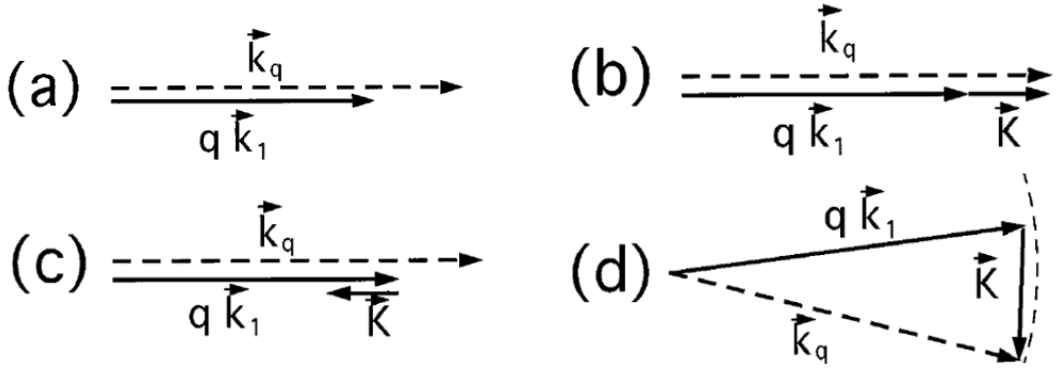

Figure 3.3: Phase matching at different points of the focal region: (a) On axis at focus, (b) on axis after the focus, (c) on axis before the focus and (d) off-axis before the focus. Figure adapted from [9].

overlapping the wave vector $\vec{k}_1$ of the fundamental beam and the effective dipole phase wave vector at different positions of the beam. It is clear that perfect phase matching cannot be fulfilled at focus as the effective wave vector is zero and cannot compensate the mismatch (Fig. 3.3.(a)).

On-axis generation

If the focus is placed before the generating medium, the phase mismatch can be compensated and on axis emission will occur, thus realizing collinear phase matching (Fig. 3.3.(b)). When displacing the focus in the other direction after the generating medium, compensation will not be possible (Fig. 3.3.(c)). Now, let us look at the on-axis case by considering all the wave vector components that

[3] Note that in this specific paragraph, we follow the convention of defining the phasemismatch as $\Delta\vec{k}_q = \vec{k}_q - q\vec{k}_1$ followed in Ph. Balcou et al [9]. We will revert to the definition in equation 3.1 for the rest of the thesis

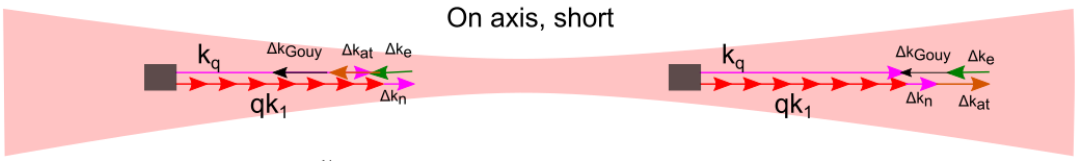

Figure 3.4: Sum of wave vectors to assess good phase matching. We consider two locations, on opposite sides of the focus (a fraction of the Rayleigh range), on axis, and a small atomic phase corresponding to the short trajectory. Note the difference in the definition of $\Delta\vec{k}_q$ compared with Fig. 3.3. Figure adapted from [56].

contribute to phase matching. In Fig. 3.4, we see that when the jet is placed after the focus, the atomic phase associated to short trajectories can help to compensate the Gouy phase. On the contrary, when placing the jet before the focus, it is extremely hard to phase match the harmonics on axis.

Off-axis generation

However, one can find locations for which non collinear phase matching is achieved, provided we consider points off axis and still before the focus (Fig. 3.3.(d)). Moreover, it can be noticed in the example of Fig. 3.3.(d) that the transverse components of $q\vec{k}_1$ and $\vec{k}_q$ are opposite, so that the generated harmonic field may be divergent even though the laser field is convergent. However, these can be phase matched off-axis. Fig. 3.5 shows the wave vector representation of the same considering all

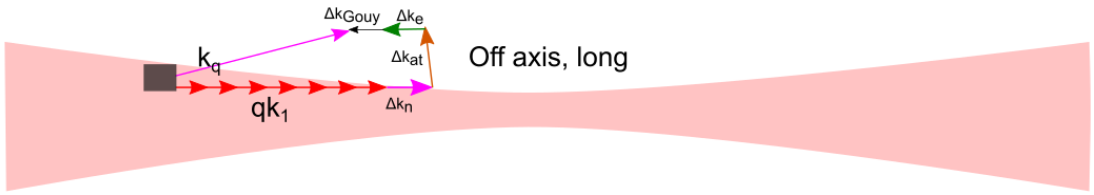

Figure 3.5: Sum of wave vectors to assess good phase matching, considering a large atomic contribution, off axis, corresponding to the long trajectory. Figure adapted from [56].

the phase matching components. Such points will form a large ring around the laser axis, yielding an annular structure to the emitted harmonic field. In the experiment, one can clearly distinguish between these ring shaped harmonics from the long trajectory that is formed around the intense central spot from the short trajectory as shown in Fig. 3.7.

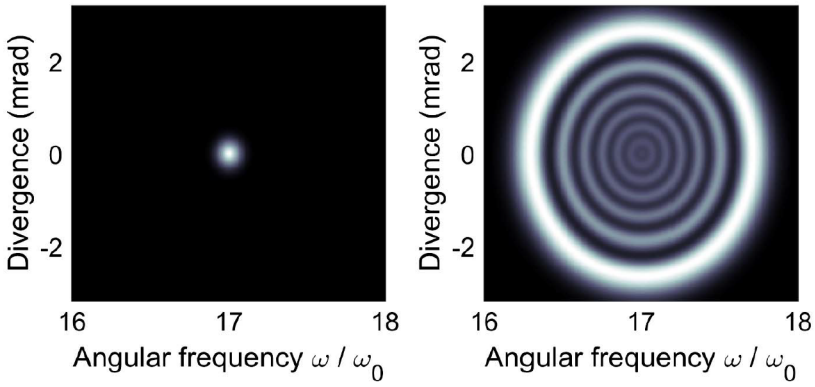

Figure 3.6: Intensity in the spatio-spectral domain in the far field calculated for short trajectories (left, $q\text{eff} = 4, \alpha_{at} = 2$) and long trajectories (right, $q\text{eff} = 4, \alpha_{at} = 20$). Figure taken from [62].

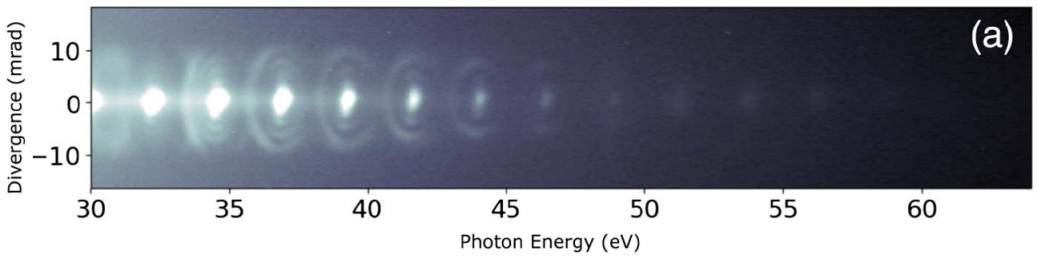

Figure 3.7: Experimental image of intensity in the spatio-spectral domain in the far field [62].

3.2.2 Intensity and gas pressure as optimization parameters

Within the pulse duration, the maximum harmonic emission is obtained as a compromise between phase-matching considerations and atomic response. High atomic response would require high laser intensity but at the same time high intensity generates a high ionization level that damages phase matching. Considering that the dipole response increases non linearly with increasing intensity, and that an increased generation pressure should allow more atoms to contribute, one could assume that the overall generation efficiency increases with increasing intensity and pressure. However, generation at higher intensities does not necessarily result in an increased efficiency, as in this case, phase-matched generation is limited to small volumes and short time intervals. For HHG in gases, the efficiency scales as ρ^2 (see equation 3.21). This is typically the case at low generation pressures where dispersion and reabsorption in the gas is negligible. A quadratic signal growth with pressure during the experiment is thus a clear indication that the phase matching conditions are not changing significantly with gas pressure and the reabsorption is negligible (see chapter 9). For a given set of optimization parameters in the experiment, we can see that the intensity of the harmonic grows between the lowest gas density and up to the chosen optimal pressure, and then decreases as the pressure keeps

increasing. This is because the efficiency of the harmonic generation surpasses the absorption limit at which the intensity exponentially decays with pressure. We also see that this optimum pressure depends on the harmonic order because absorption by the gas is wavelength dependent.

To conclude, phase matching in HHG is a rather complex process. In practice, the optimization of macroscopic generation parameters is most easily done by an iterative tuning of multiple control parameters, particularly pressure, intensity, iris size and gas cell positioning. In this context it is important to note that the investigations on phase matching effects are continuously evolving [68] and these very effects which were once considered to be limiting are now being leveraged to boost the performance of HHG sources through new technologies, like microfluidic glass devices allowing guided geometry, for example [69].

Part III

Non collinear high harmonic generation in the approximation of perfect phase matching

CHAPTER 4

High harmonic generation with two beams: state-of-the-art

4.1 Introduction

Collinear High Harmonic Generation

High Harmonic Generation (HHG) as a source has a growing number of applications requiring ever more demanding control of the beam. Since the generation of harmonics is strongly dependent on the shape of the electric field of the driving laser, altering the driving field is one of the most handy ways to control the properties of the emitted XUV radiation for each specific application. For instance, it has been reported as early as 1993 that the use of $\omega - 2\omega$ mixed field, co propagating and of identical polarization can be used to generate even harmonics [70]. In this article, they demonstrated that the harmonic yield can be enhanced by up to an order of magnitude with the addition of the 2ω field to the fundamental. When the two fields have orthogonal polarization [71, 72], HHG can produce harmonics with various linear polarization and when they are circularly polarized, circularly polarized harmonics are produced [18, 19, 20]. More recently, it was shown that the superposition of two fields of incommensurate frequencies also leads to an enhancement in the yield of the harmonics [73]. The control of the relative phase between the two fields can also be used for trajectory selection between the long and short electron trajectories [74]. Finally, theoretical work suggests that an inhomogenous bichromatic driver permits to increase substantially the cut-off beyond the water window [75], including the possibility of generating and controlling the attosecond pulse train. On the contrary, additional weak counter-propagating light could shut down certain harmonics due to

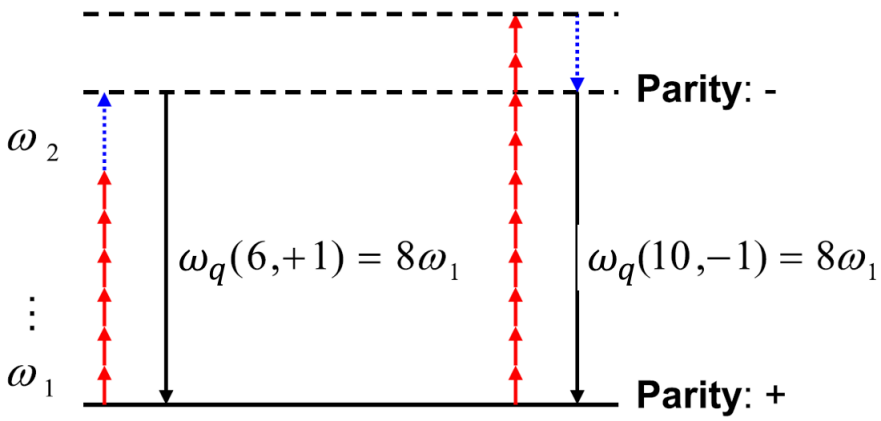

Figure 4.1: Frequency-domain perspective on two-colour ($\omega - 2\omega$) non collinear HHG. (a) Sum and difference frequency emission: $\omega_q = n_1\omega_1 + n_2\omega_2$. Only the net totals $n_1 + n_2$ which have odd values are dipole-allowed transitions. Illustrated is the production of ω_q with $n_2 = \pm 1$, leading to harmonic 8. Adapted from [42].

phase matching effects [76]. But the same could enhance harmonic production by suppressing out of phase emission. Thus, the use of two beams gives great flexibility and control on the XUV light.

Non Collinear High Harmonic Generation

The use of non collinear geometry of laser beams was proposed as early as 1965 to increase the yield of various low order wave mixing processes [77]. The theoretical work of [39, 78] in 1996 proposed the use of crossed laser beams for increasing the HHG yield. And in 2001 was published a theoretical work [40] showing that the use of two almost co-propagating beams crossing at a very small angle leads to improved phase matching. Over the years, it has become an important technique in generating structured light. But the physics behind it still not completely understood. Most often, NCHHG is explained with a photon model or by considering the structure of the driving field, both of which will be introduced below.

4.2 Field based analysis of NCHHG

In the wave model of NCHHG, it is the composite electric field in the interaction region that is analyzed and that plays the leading role. In the case of linearly polarized driving lasers, crossing the two beams at an angle results in intensity interference at the overlap, which produces a field amplitude grating. High harmonics are generated by this amplitude grating, resulting in a high harmonic source that also looks like a grating and therefore produces diffracted high harmonic orders in the far field. The number of contributing harmonic sources (fringes of the interference pattern), depends on

the beam waist and the non collinear angle; increasing with increasing non collinear angle. Later, in chapter 6, we will see that two more phase gratings should be considered in this description.

In the case of circularly polarized counter-rotating driving beams there is no intensity interference pattern at the crossing plane because the polarizations are orthogonal. However, if the amplitudes of the two beams are equal then the combined polarization is locally linear everywhere across the region of overlap. Because the relative phase of the beams varies across the transverse direction, the orientation of the linear polarization also rotates across the transverse direction and forms a rotating polarization grating. Therefore, in the interaction region, atoms emit high harmonic radiation polarized in the direction of the local linear fundamental field, which imprints the rotating polarization grating on the harmonic light [79]. If one considers the horizontally and vertically polarized components individually, the high harmonic source function varies sinusoidally in space for both, with a relative phase shift of $\pi/2$ between them. Consequently, in the far field there are only two diffracted orders (+1,-1), with a relative phase shift of $\pm\pi/2$ between the horizontally and vertically polarized components. This results in the emission of two HHG channels with right and left-circular polarization, which is in agreement with the photon model as we will see in the next section. This locally linear field in the rotating polarization grating is advantageous since the single-atom HHG process is identical to that of traditional single-beam HHG with linear polarization everywhere across the focal spot.

However this field based analysis cannot predict the harmonic emission yields and hence the photon model has been favoured in describing NCHHG.

4.3 Multiphoton model

The very early work of Perry et al. [70] allowed to establish certain conservation rules based on an intuitive multiphoton model. Due to its simplicity, this model was subsequently widely used to describe the results of two-beam harmonic generation. Being very intuitive, it even inspired many experiments to demonstrate new conservation laws [80, 18, 25, 44, 45]. In the photon model, each driving laser is considered as a bath of photons and high harmonic photons are produced by adding up all of the allowed combinations of those driving laser photons, in accordance with certain conservation laws.

4.3.1 Conservation of energy

Like for any nonlinear optical process, the law of conservation of energy during the generation of harmonics with two beams is written as:

$$\omega_q = n_1\omega_1 + n_2\omega_2. \tag{4.1}$$

where ω_1, ω_2 and ω_q are respectively the angular frequencies of the first and second generating field and the q^{th} order harmonic generated. Experimentally, the intensity of the generating field is much larger than the perturbating field. Therefore, the main contributions in the generation of the harmonics come from the multiple absorption of ω_1 photons. Hence, we can consider without loss of

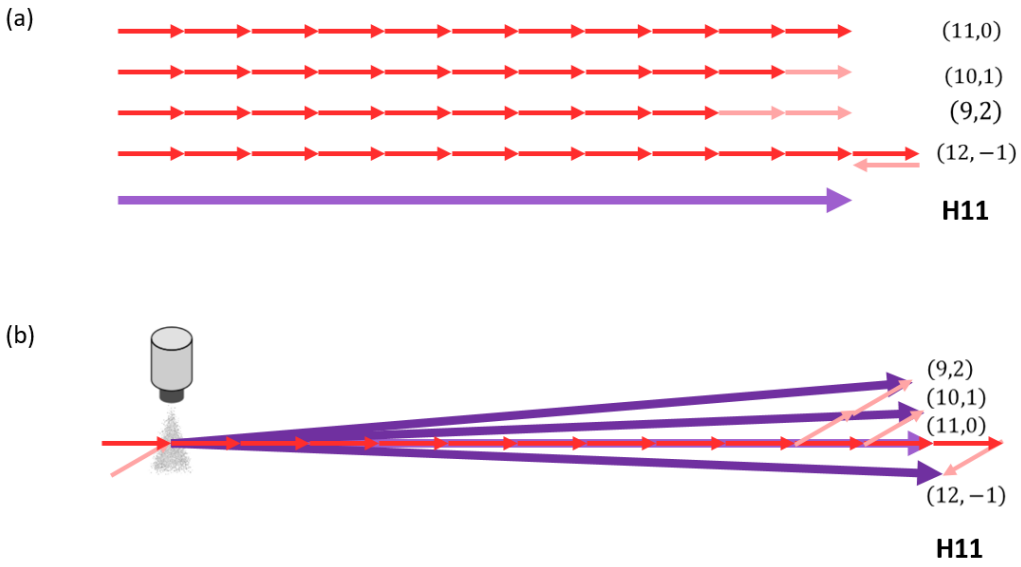

Figure 4.2: Wave-vector domain perspective of photon model for $\omega - \omega$ mixing for generation of harmonic eleven in (a) collinear geometry and (b) non collinear geometry, showing the conservation of linear momentum. The arrows represent the relevant wave vectors. Dark and light red arrows refer respectively to the fundamental field and the weaker second field while violet arrow are associated to the XUV. The non collinear scheme offers the advantage of spatially distinguishing the different photon channels (n_1, n_2).

generality that n_1 is a positive integer and n_2, a positive or negative integer, accounting for the sum or the difference frequencies respectively.

High harmonic radiation comes from the recombination of an electron back to its ground state through an electric dipole transition. This electric dipole transition stipulates that the wave function of the continuum electron and the ion together be in a state of different parity (+ or -) than the original ground state (- or +) [70, 81]. Only the absorption of an odd number of photons changes this parity and thus the sum $n_1 + n_2$ must be always odd. With this approach, it is possible to produce the same frequency ω_q with various (n_1, n_2) combinations. This also explains the generation of even $(2\omega_1)$ harmonic orders of the fundamental beam with the use of two harmonics, ω_1 and $2\omega_1$. For example, $\omega_q = 8\omega_1$ can be obtained from the net sum $(n_1, n_2) = (6, 1)$, or the net difference (10, -1) frequency-mixing pathways (see Fig. 4.1). Thus it is possible to generate the same harmonic through Sum Frequency Generation (SFG) as well as through Difference Frequency Generation (DFG). In general, a n_2 odd (even) number of photons involved from the second field results in the observation of even (odd) harmonic orders [42].

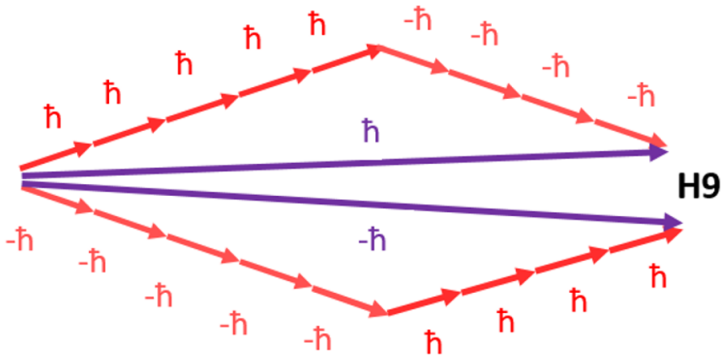

Figure 4.3: Wave-vector domain perspective of photon model for $\omega - \omega$ mixing for generation of harmonic nine in non collinear geometry showing the conservation of spin angular momentum when mixing left circularly polarized (LCP) and right circulary polarized (RCP) beams. Only two possible combinations are possible. The wave vectors of the driving beams and the XUV are respectively represented by red and violet arrows.

4.3.2 Conservation of linear momentum

When the two driving lasers are crossed, each bath of photons has its own associated linear momentum that must be conserved when building a high harmonic photon as,

$$\vec{k}_q = n_1 \vec{k}_1 + n_2 \vec{k}_2, \tag{4.2}$$

where $\vec{k}_1$, $\vec{k}_2$ and $\vec{k}_q$ are the wave vectors of the driving fields and the q^{th} order harmonic. In non-collinear geometry, this conservation of linear momentum means that the number of photons that are absorbed form each driving laser beam will define the direction in which the harmonics are emitted. When the driving lasers are linearly polarized there is no restriction on the relative number of photons that can be absorbed from each beam, which results in the emission of several high harmonic beamlets corresponding to different permutations of driving laser photons. For example, Fig. 4.2 shows various possible combinations (n_1, n_2) producing eleventh harmonic order in a collinear (Fig. 4.2.(a)) and a non collinear (Fig. 4.2.(b)) geometry. While these two cases result in the same photon energy, they are emitted in different directions when the generating fields are non collinear.

4.3.3 Conservation of angular momentum

If the driving lasers are circularly polarized, then spin angular momentum must also be conserved in addition to linear momentum. Projected on the propagation axis, it reads as

$$\sigma_q = n_1 \sigma_1 + n_2 \sigma_2, \tag{4.3}$$

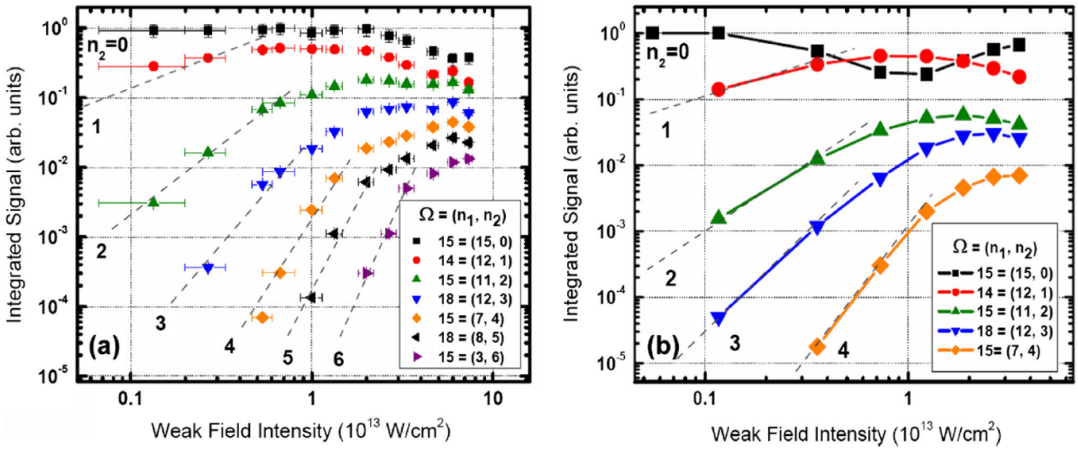

Figure 4.4: Figure 3 of Bertrand et al. [42]. Evolution of the intensity for diffraction orders as a function of the perturbation intensity. (a) Experimental data. (b) Numerical simulations.

where σ_1, σ_2 and σ_q are respectively the projection of the spin of the generating field, perturbating field and the q^{th} order harmonic generated, on their propagation axis. This conservation of spin angular momentum shuts down most of the HHG channels because the only allowed spin angular momentum states for photons are $\sigma = \pm 1$. For purely circularly polarized driving laser beams, there are only photons in a single angular momentum state present in each beam, i.e., the left circularly polarized (LCP) driving laser consists of only $\sigma = +1$ photons and the right circularly polarized (RCP) driving laser is made up of only $\sigma = -1$ photons. Therefore, according to the photon model, it is not possible to generate harmonics with circular polarization with a single beam or with two beams having only photons of the same spin value. For generating circularly polarized harmonics, it is necessary to have two oppositely polarized driving beams as it is possible to conserve spin angular momentum only if the difference in the number of photons absorbed from each beam is ± 1. This constraint results in the emission of only two HHG beamlets for each harmonic order, each of which will have a well defined angular momentum state, where the absorption of an extra photon from the LCP beam results in LCP harmonics and the absorption of an extra photon from the RCP beam results in RCP harmonics as shown in Fig. 4.3. This was experimentally demonstrated using a two-colour field in Argon in Hickstein et al. [18].

In the case of driving beams carrying orbital angular momentum (OAM), typically the case of helically phased light beams, OAM conservation predicts

$$l_q = n_1 l_1 + n_2 l_2, \tag{4.4}$$

where l_q, l_1 and l_2 are the topological charges of the harmonic and the two generating beams respectively, making it possible to generate harmonics with any arbitrary value of OAM [45, 44].

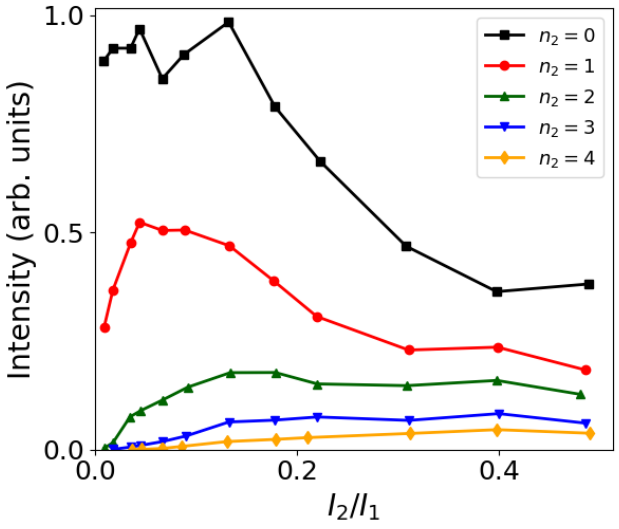

Figure 4.5: The experimental data of Bertrand et al. [42] (extracted from Fig. 4.4.(a)) plotted in linear scale, without giving any offset on the Y-axis. n_2 is the number of photons absorbed from the second field as per the photon model.

4.3.4 Models for the yields of diffraction orders

NCHHG being such a unique source for the generation of harmonics with OAM, circularly polarized harmonics and angularly separated harmonics, it is in our interest to study the far field properties and the emission yields of these diffraction orders to harness the various possibilities of using it as an XUV source. In spite of this broad interest, our understanding of NCHHG, especially of the yields of the beamlets, remains limited to very specific limit cases.

A seminal experimental work was carried out by Bertrand et al. [42], using a fundamental beam and its second harmonic. Relying on their experimental data and their numerical simulations based on the strong field approximation, they concluded that for low intensities of the second field (I_2), the intensity ($I_{[n_1,n_2]}$) of the orders generated follows a perturbative law,

$$I_{[n_1,n_2]} \propto I_2^{n_2},$$

where absorption of n_1 photons from the fundamental field and n_2 photons from the weak field generates diffraction order n_2. This law indicates that the yield of each diffraction order should increase with the intensity of the perturbation. However, a closer look at their data (see Fig. 4.4 and Fig. 4.5), shows that for the highest values of the intensity of the "perturbative" beam, the intensity of the lowest diffraction orders starts to decrease. Although it is far from being negligible (the scale is logarithmic), the authors do not comment on this part of the curve. They compared these experimental results to those of an SFA-based model. They also observed this increase, followed by a decrease in

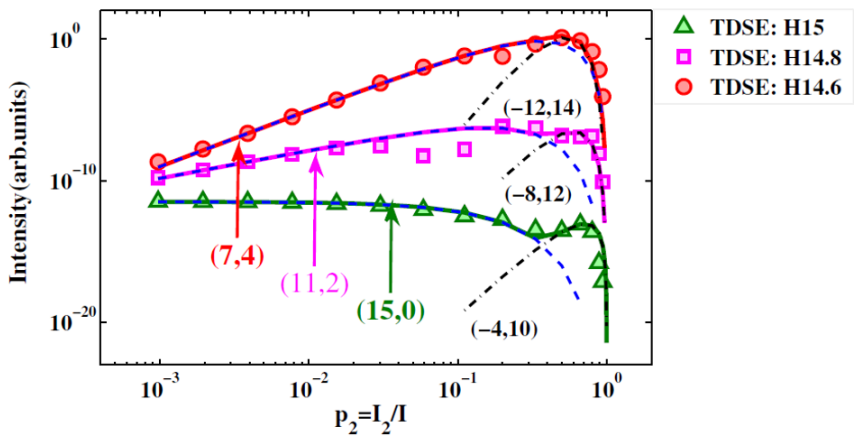

Figure 4.6: Figure 3 of Li et al. [82]. High harmonic yield as a function of p_2. The triangles, squares, and circles represent the results with TDSE simulations. The dashed and the dash-dotted curves show the contributions of different photon channels predicted with the quantum model and the solid curves show the sum of them. For clarity, the curves for H14.8 and H14.6 are shifted vertically.

almost all their theoretical curves. In some cases, for instance the $n_2 = 0$ case in Fig. 4.5, one may also note the appearance of a revival in intensity, which was not commented at this time. We can ask a few questions here. What happens when we go to "perturbation" higher than shown here? Would the curves be generally bell-shaped? Also, in the theoretical plot, diffraction orders 5 and 6 (which results from high perturbation) are omitted and the reason is not commented upon. What is the yield distribution for these higher orders of diffraction?

More recently Li et al. [82] proposed a theoretical model based on TDSE. To identify the different channels, instead of introducing an angle between the two beams, they considered two beams with unmatched angular frequencies (ω and 1.9ω), causing the “diffraction orders” to appear at different spectral frequencies instead of angular locations. This trick greatly reduces the computational cost, as in this case, considering a single atom is sufficient to observe the equivalent of the diffraction orders in the spectral domain. They quantized both the driving laser and the high harmonics and introduced the photon channel that is the sum of all the quantum paths involving the same net number $[n_1,n_2]$ of photons. The intensity distribution ($I_{[n_1,n_2]}$) was found to follow,

$$I_{[n_1,n_2]} \propto p_1^{n_1} p_2^{n_2} \text{ where,} \tag{4.5}$$

$$p_1 = \frac{I_1}{I_1 + I_2} \tag{4.6}$$

$$p_2 = \frac{I_2}{I_1 + I_2} \tag{4.7}$$

I_1 and I_2 being the intensities of the fundamental and the weak/perturbative beam respectively. Although not explicit from the article [82], this expression can be simplified in the case of single-colour

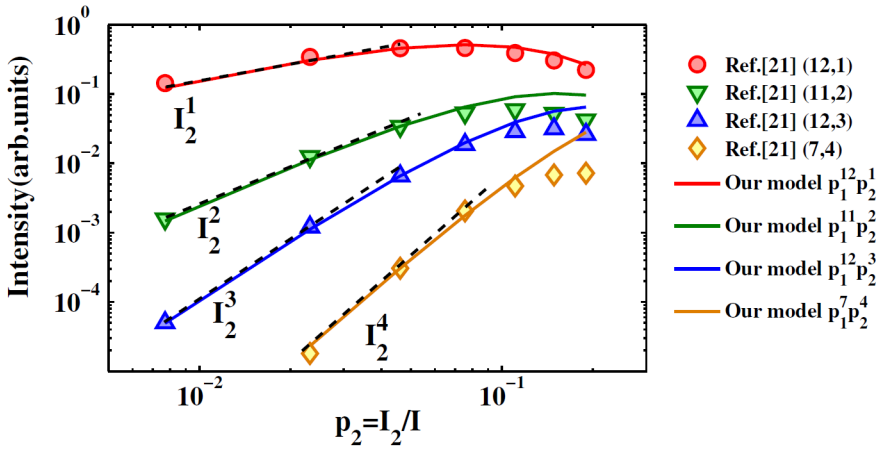

Figure 4.7: Comparison between the HHG yields in the non collinear two-colour field obtained from [42] (markers) and their quantum model (solid curves). Figure 4 of Li et al. [82].

NCHHG as:

$$I_{[n_1,n_2]} \propto p_1^{n_1} p_2^{n_2} = \left(\frac{1}{1+\alpha^2}\right)^{n_1} \left(\frac{\alpha^2}{1+\alpha^2}\right)^{n_2} = \frac{\alpha^{2n_2}}{(1+\alpha^2)^{n_1+n_2}} = \alpha^{2n_2} \sum_{k\geq 0} (-1)^k C_k \alpha^{2k} \tag{4.8}$$

where $\alpha = \sqrt{I_2/I_1}$. Thus,

$$\begin{aligned} I_{[n_1,n_2]} &\propto \alpha^{2p}(1 - a_2'\alpha^2 + a_4'\alpha^4 - a_6'\alpha^6 + ...) \\ &\propto a_{2p}\alpha^{2p} - a_{2p+2}\alpha^{2p+2} + a_{2p+4}\alpha^{2p+4} - a_{2p+6}\alpha^{2p+6} + ... \end{aligned} \tag{4.9}$$

where $p = n_2$ and $q = n_1 + n_2$. We see that the first term in equation 4.9 is indeed the perturbative law established by the team of Bertrand et al.[42]. However, there are additional terms that come into play which are not explored. And more physical questions to be answered. For example, why do only even powers of α survive? And is there a physical significance to the alternance in the sign of the coefficients of the expansion?

In Fig.4.7, the quantum model [solid line] is compared to the experimental data of Bertrand et al.[42] (markers). The quantum model fits particularly well with the experimental values for the diffraction order p=1 for all intensities. However, it deviates for p=2, 3 and 4 for intensity ratio higher than 0.2. The black dashed line is the power scaling law, which is valid only up to $p_2 = 0.04$ corresponding to $\alpha = 0.2$. This is evident from the last data point for $p_2 = 0.2$, correspondingly $\alpha = 0.5$. This is definitely not in the perturbative regime, not within the scope of their quantum model. The power scaling law is clearly not sufficient anymore.

As noted above, for each harmonic, there are multiple (n_1, n_2) channels that are allowed. Each of them corresponding to a different diffraction order. Finally, the sum of these channels give the overall amplitude distribution for each harmonic. In Li et al., the authors have addressed the question of

channel competition between the different diffraction orders to reach the same harmonic order. At higher α, higher diffraction orders (high n_2) are dominant. For instance, in Fig. 4.6, Li et al. [82] show the photon channels [15,0], corresponding to diffraction order, p=0 and [-4,10] corresponding to diffraction order, p=10. But there are many orders of diffraction between 0 and 10 that are omitted. It is puzzling that they do not show the data with non-collinear geometry where all the diffraction orders could be easily identified.

Moreover, for each harmonic and each diffraction order, there are also multiple pathways which may contribute. It is relevant to raise the question whether there is a preferred photon channel to achieve the same diffraction order. Li et al. [82] shortly addressed this question, noting in particular that quantum paths involving stimulated emission steps could be involved. This could significantly alter the intensity distribution of a given diffracted order. Indeed, the authors conclude that it could give rise to a certain phase factor, but provides no additional details.

To complete this discussion on the state-of-the-art, two groups investigated phase matching effects in NCHHG [83, 43, 44, 84] , and predicted dramatic effects such as a change of the dominant channel from SFG to DFG. It was attributed to a geometrical phase-mismatch factor and to the ionization level of the HHG medium. We will dedicate a specific section on this important aspect later in part IV of this thesis.

From this brief state-of-the-art, we thus note that diverse conclusions are drawn depending on the approach.

4.4 Objectives of this part

The objective of this part is to provide a solid and general understanding of NCHHG from the perturbative to the non perturbative regime. In addition, it also aims at introducing the high harmonic spectroscopic approaches used. Based on the analysis of the generating amplitude and phase grating formed by the two beams in the nonlinear medium, we provide a unique picture, reproducing the results over all perturbation levels. It provides a framework compatible with the *field-based* interpretation of NCHHG [39, 41, 36], commonly used with small angles or collinear geometries, while also keeping a *photon-based* translation, compatible with currently favored interpretations of NCHHG with large crossing angles [42, 82]. In the next few chapters we will attempt to answer the following questions:

- What is the behaviour of the emission yields of the different photon channels as a function of the intensity of the perturbating laser pulse?
- Is there a "perturbative range" for each diffraction order of a given harmonic?
- Is there a dominant channel of emission among the different diffraction orders for a given harmonic?
- Is there a dominant photon-pathway [among all combinations leading to the same n_2] for a particular diffraction order?

- What is the contribution from stimulated emission pathways and its effect on the intensity distribution of each diffraction order?

The plan of this part of the thesis is as follows. In chapter 5, we will describe the experimental set-up. In chapter 6, we will introduce the field-based analytical model to obtain the electric field amplitude of the emitted harmonics before separating the process of NCHHG into two separate regimes, *perturbative* and *non perturbative*, which will be treated in two separate chapters, 7 and 8, respectively, where we will present our theoretical and experimental results.

CHAPTER 5

Design and development of the FAB-1-Bis beamline at ATTOLab

5.1 General context

For a long time, XUV and X-ray radiation have been almost exclusively associated with synchrotrons and free electron lasers (FELs) respectively. Both systems are very big, cost-intensive machines. HHG opened up the possibility to access these photon energies by means of compact tabletop systems, and is capable of providing pulses in the microjoule range [11, 12]. Even though achieved photon fluxes are weaker than in synchrotrons (conversion efficiency around 10^{-6}), the emission from HHG is temporally and spatially coherent. Another advantage of HHG is their short pulse duration, allowing highest temporal resolutions, down to the attosecond time scale. This makes HHG the best source for time-resolved experiments in the XUV domain today. All this, combined with the moderate pump energy requirements make HHG a promising approach to developing a compact attosecond XUV source and a number of laboratories offer this possibility today. These considerations were at the origin of the construction of the ATTOLab facility. It is a consortium between nine laboratories situated on the plateau of Saclay, France, dedicated to the interdisciplinary studies of ultra-fast electronic and nuclear dynamics at femtosecond and attosecond timescales in gas, condensed and plasma phases. The experimental site at CEA- L'orme des merisiers, inaugurated officially on February 2017, is specialized in gas phase and solid state studies. Initially, it consisted of two Femtosecond-Attosecond Beamlines (FAB 1 and FAB 10), each including an IR femtosecond laser and a HHG-based attosecond XUV source, respectively at 1 kHz and 10 kHz repetition rates, coupled to experimental end-stations.

A major component of this thesis work was the design of a new beamline, namely FAB-1-Bis. FAB-1-Bis includes a laser source that delivers 1.5 mJ, 25 fs, IR pulses at a repetition rate of 1 kHz. Our aim was to develop a home-built, compact and low-budget HHG beamline for the exclusive study of non-collinear HHG with two beams. The objective was to understand the physics behind it and harness its possibility as a new XUV source for spectroscopic applications, in particular for resolving spin and orbital angular momentum. Of course, while building the beamline, the design possibilities for its future use as an experimental end-station for external users and in-house experiments were considered and implemented as well.

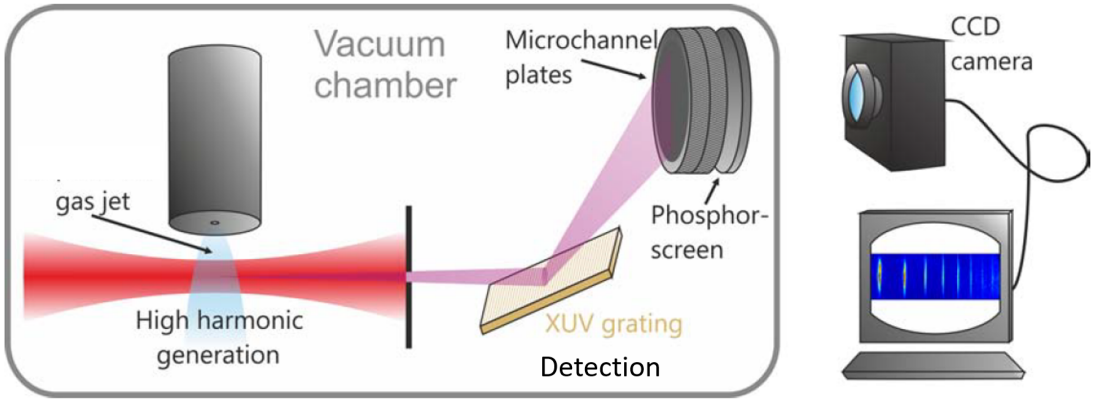

Figure 5.1: Simple experimental setup for spectroscopically resolving a high harmonic spectrum. The generation of harmonics and their detection are done in a vacuum chamber with the imaging system outside the vacuum. Adapted from [67].

5.2 Experimental considerations in high harmonic generation

As already mentioned, the major drawback of HHG is its low conversion efficiency. The low conversion efficiency of HHG is due to the combination of two factors: the weak atomic response to the laser field and the phase mismatches between fundamental and harmonic fields during the macroscopic construction of the field. The global optimization involves the delicate control of multiple parameters that influence the generation process, among which the more important are the fundamental beam energy, input beam waist, pulse duration, the choice of gas, gas pressure and the gas cell position relative to the laser focus. The set-up has to be designed keeping in mind the possibility for the adjustment of these parameters. The optics associated with manipulating and characterizing the harmonic radiation have to be compatible with the XUV spectrum as well. First, we will describe in detail the HHG set-up which is in vacuum and then the interferometric set-up used for non-collinear high harmonic generation. This optical set-up is in air, preceding the HHG set-up.

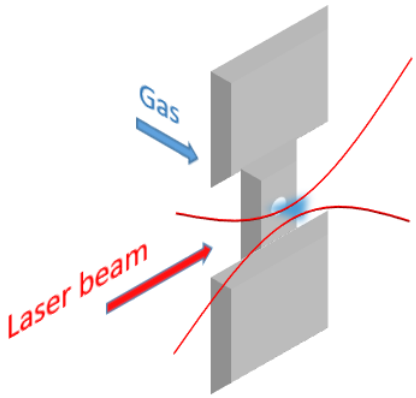

Figure 5.2: Schematic of the gas inlet.

5.3 Design of the tabletop XUV-light source

Fig. 5.1 shows the most basic experimental scheme for high harmonic generation and detection. The primary challenge associated when working with XUV light is that the typical absorption length of this photon-energy spectrum is $\sim 100\mu m$ in air at atmospheric pressure. This makes the use of vacuum chambers necessary. The generation, subsequent propagation and detection of the high harmonics are thus done in vacuum. The driving laser is coupled into a vacuum chamber and focused into a localised gas medium to generate the harmonics. The gas expands into the vacuum chambers and has to be efficiently pumped away to make sure that the created harmonics are not re-absorbed. In FAB-1-Bis beamline, we designed the experimental set-up as a combination of three separate vacuum chambers: 1) the generation chamber, 2) the differential pumping chamber and 3) the detection chamber (or the photon spectrometer), all connected by vacuum tubes. Each chamber has its own turbomolecular pumping system and the detection chamber can be easily isolated from the rest of the experiment by a gated-valve. Two different configurations of the beamline were designed, one in non focusing geometry and the other in focusing geometry. In focusing geometry, an additional vacuum chamber is introduced before the spectrometer, housing a toroidal mirror + silica plate combination (see Fig. 5.4). The silica plate is used to reflect the beam on to the toroidal mirror to provide the required 11.5° angle of incidence while also eliminating some of the fundamental beam due to its low reflectivity for IR. In non focusing mode, this additional chamber is not present.

5.3.1 Generation stage

The generation chamber is a custom-built 6-way-cross made of stainless steel (SS) material. The laser beam enters this chamber through a UV fused silica window with anti-reflective (AR) coating for IR radiation and is focused at a distance of 25 cm from the window, in front of the gas jet. The AR coating

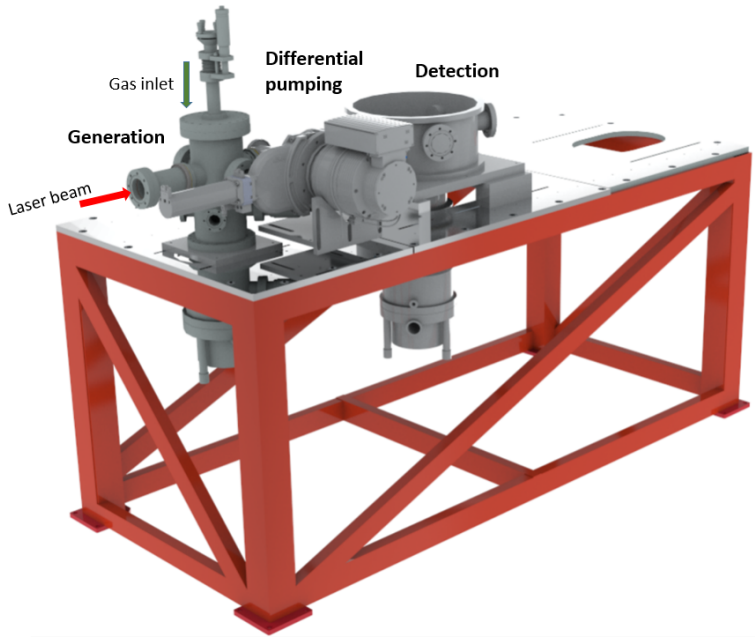

Figure 5.3: Design model of the tabletop HHG source at FAB-1-Bis in non focusing mode.

prevents the back propagation of the focusing, reflected light into the optical system. From the top descends an X-Y-Z manipulator which positions the gas inlet at the center of the chamber. The gas inlet is an aluminium tube with a pre-drilled hole on one side and connected to an external gas bottle on the other side. The gas is diffused into the chamber through the hole, 500 μm in diameter (see Fig. 5.2). Depending on the need (density, molecular cooling. . .), a continuous jet, pulsed jet, or a cell can be easily mounted. The longitudinal extent of the gas jet was approximated to be around 1 mm. However we did not perform any experimental characterisation of the length and the density of the gas medium, along the lines proposed in Comby et al. [85], for example.

The chamber is pumped by a 1300 L/s turbo molecular pump from Adixen, capable of achieving a background pressure of 10^{-6} mbar. During the experiment, with a continuous influx of gas, a residual pressure of around $3\text{x}10^{-3}$ mbar is maintained. We observed that even with a simple, continuous diffusive jet and no gas cell, the phase-matching conditions are favourable for a range of residual pressure from $2\text{x}10^{-3}$ to $8\text{x}10^{-3}$ mbar in the chamber. The focus of the laser beam is placed just before the gas jet to optimise the phase-matching conditions that favour short trajectories (see section 3.2). This is done by the translation of the focusing lens, keeping the position of the gas inlet fixed. We focus our studies on short trajectories and low order harmonics for which our analytical model was developed.

The control of the laser intensity is also important. HHG requires laser intensities in the range of 10^{13} W/cm^2 to 10^{15} W/cm^2 depending on the selected gas. As already noted in Part II, one could in principle reach arbitrarily high photon energies simply by increasing the driving laser intensity.

In practice, however, one observes that above over the barrier intensity, the large fraction of plasma prevents emission of HHG at higher photon energies. This is due to three effects. First, most of the atoms get ionized on the rising edge of the pulse, becoming unavailable targets for subsequent HHG. Second, the plasma induces defocusing of the IR laser pulse, effectively decreasing the laser intensity. And thirdly, the conversion efficiency is low due to the large spectral dispersion in the plasma and the resulting phase mismatch between the laser and the soft x-rays. In our set-up, the driving laser beam is usually apertured down by a variable diameter iris typically between 9 and 15 mm and focused by a 75 cm lens. Control of the beam size allows for re-adjustments of the focusing geometry as well as laser energy and intensity distribution at focus. It also changes the wave front curvature in the neighborhood of the focus, where the gas target is positioned. So the divergence of the HHG will change, changing the ionization rates as well. Thus it allows us to optimize phase-matching. However, quantifying the enhancement factor is not an easy task and there is no set-rule for optimization of signal.

The coherent XUV radiation generated, emerges collinear with the rest of the IR beam and propagates to the differential pumping chamber.

5.3.2 Differential pumping stage

Differential pumping is applied to maintain different stages of a vacuum system at a large difference in pressure. In our case, it is between the detector, which is operating in high vacuum, and the generation chamber with a high gas load. The pressure difference is maintained by connecting the two chambers through a smaller chamber (the so-called differential pumping chamber) and providing individual pumping systems to all three chambers. This connecting chamber must be as small as possible, ideally a long tube of very small diameter (which in our case is a little slit). In this way, each chamber reaches the pressure determined by the performance of their corresponding vacuum pumps, without being influenced by gas flux from each other. This strategy can work because of the very long mean free path of molecules in high vacuum.

The differential pumping chamber in our set-up is a 4-way-cross of stainless steel of length 10.5 cm. The entrance and exit flanges of the chamber have pre-drilled rectangular slits of dimension 3x2 mm and 5x3 mm respectively, calculated in accordance with the divergence of the harmonic beam. This chamber itself is pumped by a smaller, magnetically-levitated turbomolecular pump (1100 l/s, Oerlikon Leybold MAG). Finally, the pressure in the chamber is around $1x10^{-6}$ mbar, thus succesfully isolating the next chamber from the generation chamber.

5.3.3 Detection stage

In the experimental results shown in this thesis, the XUV beams were not focused. Hence, the detection chamber was placed directly after the differential pumping system, omitting the intermediate focusing chamber. It is a custom-built SS chamber about 40.6 cm in diameter and 20 cm high with four CF-flange ports. The IR beam enters the chamber through a CF 40 inlet flange which is guarded by a gate valve. The chamber is pumped by a 1300 l/s Turbo Molecular Pump (TMP) from Alcatel

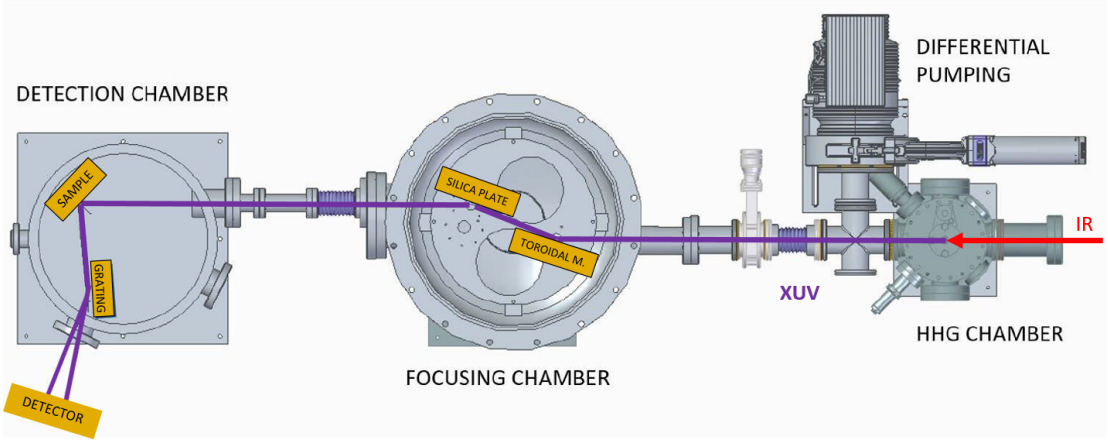

Figure 5.4: Design model showing the possibility of using the beamline as an XUV source for spectroscopic applications. The beam path shown in this figure is for the study of the magneto optical properties of any magnetic sample in reflection geometry, for example, a Transverse Magneto Optical Kerr Effect (T-MOKE) experiment.

and houses the photon spectrometer. During the experiment, the pressure inside the chamber is maintained around 1x10^{-6} mbar, compatible with the use of a microchannel plate detector.

Photon spectrometer

The design of the photon spectrometer is inspired from the thesis of Ruf Hartmut [67]. The XUV beams generated at the focus of the argon gas jet travels a distance of 1 m to reach a B_4C coated, 1" spherical mirror (ROC 600 mm). This mirror reflects 10-30%, up to harmonic order 19 of the 800 nm light onto a near-normal-incidence XUV grating (Spectrogon). It spatially separates the harmonics which fall on the microchannel plate (MCP), along the transverse horizontal direction. The XUV grating is a blazed grating with 700 lines/mm and 20 x 50 x 15 mm in dimension. The blazing angle of the grating is optimized at an angle of incidence of 6° for a wavelength of 100 nm. The grating is placed 10 cm before the focus of the spherical mirror. Near the focus of the spherical mirror we place a slit which can be opened and closed to choose the harmonics of interest. The slit mechanism is essentially two pieces of beam blockers mounted on a translation stage which can span the transverse horizontal plane. One of the pieces is then placed on an additional translation stage, again along the transverse horizontal axis, so that it can be moved towards (or away) from the other piece to close (or open) the slit. This is especially useful when carrying out experiments with Laguerre Gaussian beams which have a large divergence making the beams overlap spatially on the detector. However, for the experiments mentioned in this part, we keep the slits fully open. The MCP is placed around 17 cm after the slits.

For experiments with high perturbation (comparable energy in the second beam), we used an alternate configuration of the spectrometer, shown as the inset in Fig. 5.6. A grazing incidence vari-

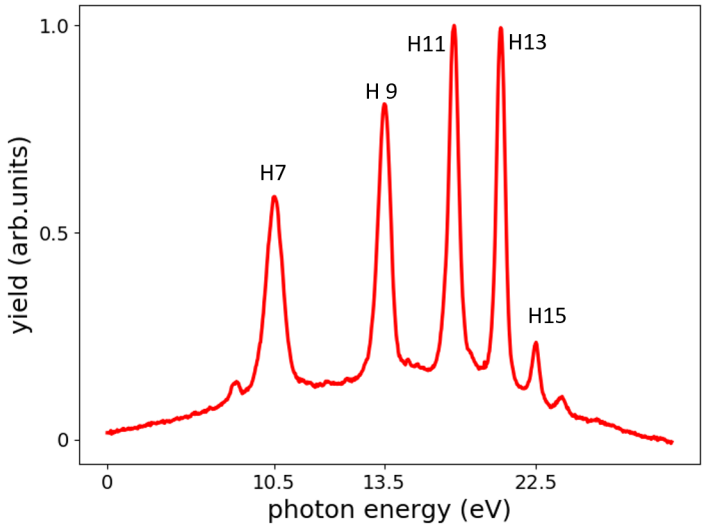

Figure 5.5: Experimentally obtained high order harmonic spectra in argon gas using an infrared beam of 1.55 eV photon energy using the normal incidence grating spectrometer.

able line spacing diffraction grating (Shimadzu, model:30-002 1623622) offering a larger collection angle directly focuses the harmonics on the detector without the spherical mirror. It is an aberration corrected concave gold grating for flat-field spectrographs (Hitachi: Part No. 001-0437*1,2) which resolves the generated harmonics spectrally. The flat field image is achieved by a varied groove spacing. It has 1200 lines/mm at its central region, a radius of curvature of R=5649 mm and a blaze angle of 3.2°. According to the manufacturer instruction, the grating must be used at an angle of incidence of 87° with an object distance of r=237 mm and an imaging distance of r'=235.3 mm for obtaining a flat field image in a wavelength range of 5-20 nm. The detection system consists of a stack of two microchannel plates (MCPs) of 80 mm diameter and a phosphor screen anode. The phosphor screen converts the output charge distribution from the MCP into a visible image. It is then imaged by a CMOS digital camera (Hamamatsu Photonics, model: ORCA Spark C11440-36U) placed at the exit of CF-63 viewport of the chamber. The images give access to the spectral amplitude in one direction and the spatial profile in the other one. This detector is particularly useful when optimizing the HHG process. Fig. 5.5 presents a typical integrated harmonic spectra obtained in argon gas in our experiment.

5.4 Optical set-up

5.4.1 General alignment

The laser system is a Ti:Sapphire femtosecond laser delivering pulses of around 1.5 mJ energy, 25 fs FWHM duration, at a repetition rate of 1 kHz, developed by Amplitude Technologies. This beam

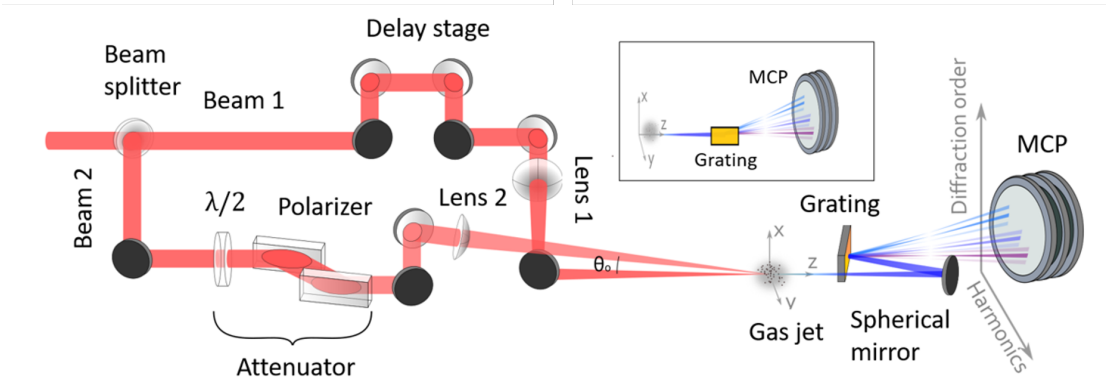

Figure 5.6: Schematic of the optical-set up and the HHG beamline. In the inset is shown the alternate configuration of the spectrometer with the variable line spaced grating at grazing incidence.

with a waist of 15 mm is used in a Mach-Zehnder like interferometric set-up for NCHHG. It is split into two, using an optical beamsplitter, optimised for 50:50 (or 75:25 as required) beamsplitting of s-polarized light at 45° angle of incidence. Both beams are focused in an argon gas jet by two identical lenses of 75 cm focal length. We optimise the HHG yield with combinations of focal lengths in the two arms, use of shorter/longer focal lengths in both arms, different gas inlets etc. The highest signal of diffraction orders was determined with the same focal length, 75 cm for both the beams. A diagnostic camera that can be inserted in the beam path is used to image the focus and check the overlap of the two beams. Fig. 5.6 shows the schematic outline of the optical set-up. The main beam carries enough energy to generate harmonics on its own while the second beam is passed through an adjustable attenuator consisting of a rotatable half-wave plate and two reflective polarizers setting an s-polarization. This enables the adjustment of the second field over a range of energies as per requirement. We define α as $|E_2/E_1|$, the ratio of the peak amplitudes of the two beams at focus. The relative delay between the two beams is controlled by a motorised delay stage in one of the arms of the interferometer allowing us to be sure that the two beams are temporally overlapped at the focus. The delay stage consists of two mirrors forming 90° angle, mounted on a linear translation stage from Newport with a step size of 100 nm and spanning a range of 20 mm.

5.4.2 Intensity calibration

The attenuator system consists of a half wave plate (HWP) and two polarizers. The polarizers are Brewster type plate polarizers optimised for 800 nm wavelength which reflect s-polarized light while transmitting p-polarized light. The principle of operation is based on Malus' Law. In the case of an ideal polarizer and fully polarized light, the intensity (I) of the polarized light that passes through the polarizer is given by,

$$I = I_0 \cos^2(\theta) \tag{5.1}$$

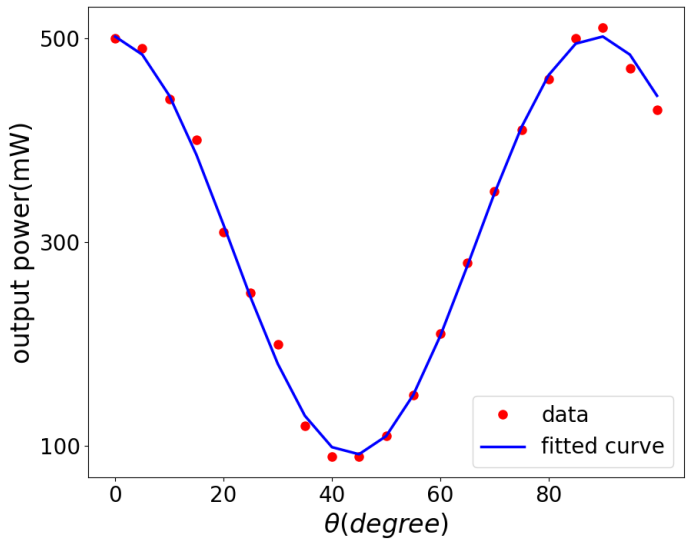

Figure 5.7: Calibrating the attenuator. Markers are the data points obtained for measured output power at different rotation angles of the HWP and the blue solid curve is the fitting of the data.

where I_0 is the input intensity, and θ is the angle between the beam's initial direction of polarization and the axis of the polarizer. The beam is reflected from the first polarizer whose axis is aligned with $\phi = 0°$ rotation of the HWP. The beam is then reflected from the second polarizer whose axis is aligned with the first polarizer. The second polarizer is an additional filter for p-polarized light while also making the light beams going into and out of the attenuator parallel to one another. Intensity at the output of the attenuator would then be

$$I = I_0 \cos^2(2\phi) \tag{5.2}$$

During a typical energy scan, the HWP is rotated from 0° to 45° to obtain the full range of attenuation from minimum to maximum; usually in steps of 1°. To find the power of the beam at the output of the attenuator for each angle of rotation, we need to calibrate the attenuator.

Calibrating the attenuator

The power of the perturbing beam over a set of values for the angle of rotation of polarization was measured after the final iris. For a full rotation of the HWP, the measured data was fitted to the formula $P = P_0 \cos^2 2(\theta + \theta_0) + c$. P is the power out of the attenuator when the angle of the rotation stage is θ. θ_0 is the arbitrary reading offset between the zero of the rotation stage and the zero of the wave plate, the c value accounts for imperfections in the polarizing optics, and P_0 is the power output for $\theta = 0$ of the rotation stage. P_0 and θ_0 are the free parameters of the fit. In the current mounting system of the wave plate, the offset angle θ_0 was found to be 30°. Figure 5.7 shows an example of such a calibration.

The two beams are first apertured down by an iris and then focused by a lens at the gas jet. In this case, the electric field of a Gaussian beam at the focus is given by

$$E_f = \frac{2\pi E_0}{i\lambda f} e^{\frac{ikr_f^2}{2f}} \int_a^b J_0\left(\frac{2\pi r_0 r_f}{\lambda f}\right) r_0 e^{\frac{-r_0^2}{\omega_0^2}} dr_0 \tag{5.3}$$

where,

$$E_0 = \frac{4E_{in}\sqrt{ln2}}{\pi\sqrt{\pi}\omega_0^2\tau}. \tag{5.4}$$

E_{in} is the energy per pulse, τ is the temporal width, b is the diameter of the aperture and r_0 and r_f are the radial coordinates at the iris and at the focus respectively. The average power, measured before the iris, gives the value of $E_{in}(= P_{in}/rep.rate)$ and the electric field at focus can be calculated using the formula in equation 5.3. The above calibration considers a perfect wavefront and a perfect Gaussian spatial profile of the IR beams. This is not the case in reality and it is not a perfect estimation of the electric field at focus. Hence, a precise calculation of the amplitude ratio at the focus is difficult.

5.4.3 Achieving non-collinear geometry

The main beam (#1) and the *"perturbing"* beam (#2) should cross at an adjustable angle at focus in the generating medium. This was done in two configurations, (#a) and (#b) used for the perturbative and the non-perturbative regimes respectively. Figure 5.8(a) and 5.8(b) show the piling up of the wave vectors according to the photon model in both cases. In the first case, the main beam is along the horizontal plane and the second beam makes an angle θ_0 with the horizontal. This is achieved by raising the beam height of one arm of the interferometer and using the last mirror on this arm to give a slight tilt. However, for high levels of perturbation when many orders of diffraction are visible, the B_4C mirror which is 1" in diameter cannot accommodate all the SFG orders that show up. To capture them on the MCP, the optical set-up was aligned such that the main beam pointing upwards and the second beam pointing downwards meet at the focus of the gas jet, each making an angle of approximately $\frac{\theta_0}{2}$ with respect to the horizontal axis.

5.5 Stability of the beamline

Many sources of beam path fluctuations may occur in an experimental lab. Vibrations may arise from the location of the experimental setup in the building and from the vacuum pumping system. ATTOLab was constructed to account for all these interferences. In addition, we took care to setup our beamline with the best possible passive stabilization. The strategy for the passive stabilization was to isolate the optical table supporting all the beam steering of the beamline until the generation chamber. This gives maximum stability to the interferometric set up. In the HHG part of the set up, the root pump providing the primary vacuum is installed in an isolated room so that mechanical and acoustical vibrations are drastically reduced. The vacuum chambers are mounted on a heavy sand filled metal table to decouple the optical setup from the vibrations of the turbo-molecular pumps.

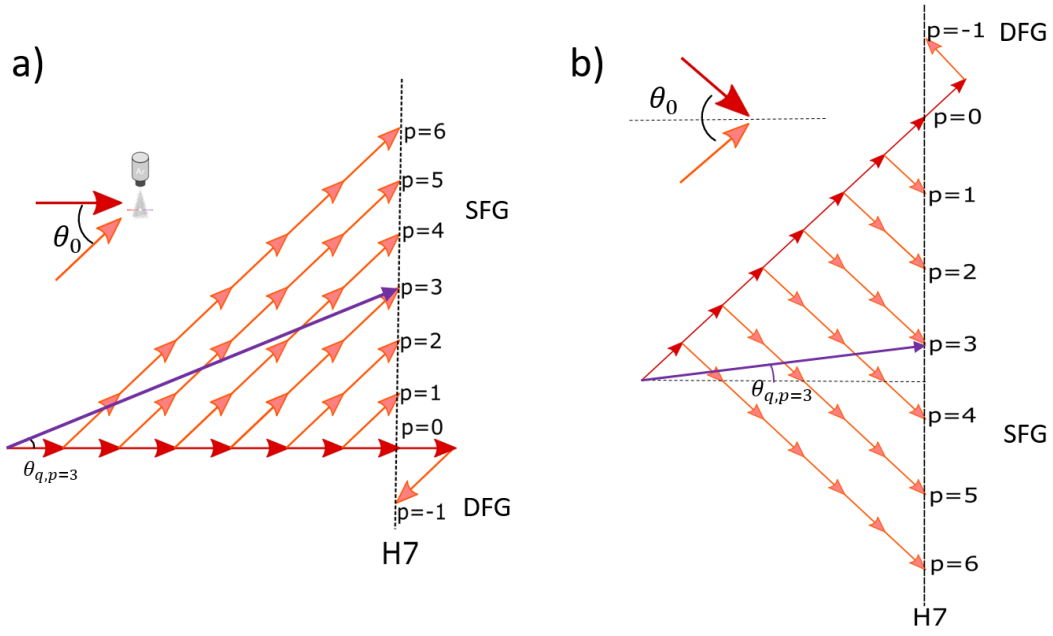

Figure 5.8: Photon model representation of the non-collinear beam mixing, predicting the spatial positions of harmonic 7 according to the law of conservation of linear momentum. The wave vectors of the fundamental (dark red) and perturbation beam (light red) could accumulate in different ways as shown to generate a given diffraction order p. The wave vector for $p = 3$ is shown in violet. (a) and (b) are for two different geometries of intersection.

However, the optical breadboard inside the detection chamber is directly connected to the TMP and is susceptible to some vibrations. Since this stage is further downstream from the recombination stage of the interferometer, it did not hinder our investigation.

The set-up could produce harmonics routinely with minimum optimization procedure, making it a robust source of XUV radiation. Even in the non-collinear, two beam configuration, the diffraction images could be retrieved from day to day with almost zero adjustment. The set-up can be easily adapted to any laser power, spatial mode of the laser, different gas input, pulsed or continuous gas jet, and varied spectroscopic applications. Even though the focus of this thesis is two-beam HHG, it should be noted that the set-up could be used in the conventional one beam HHG mode as well at any time, just by blocking the second arm of the interferometer. Also, we could study NCHHG in many configurations, by changing the polarization, wavelength, spatial profile etc of the beams.

5.6 Calibration of the spectrometer

In order to analyse the results of various experiments, it is necessary to identify the harmonic orders. For this, we can take advantage of the the non-collinear geometry of the interfering beams and the photon model. For calibration, we use the configuration in the Fig. 5.8.(b) to give the required angle

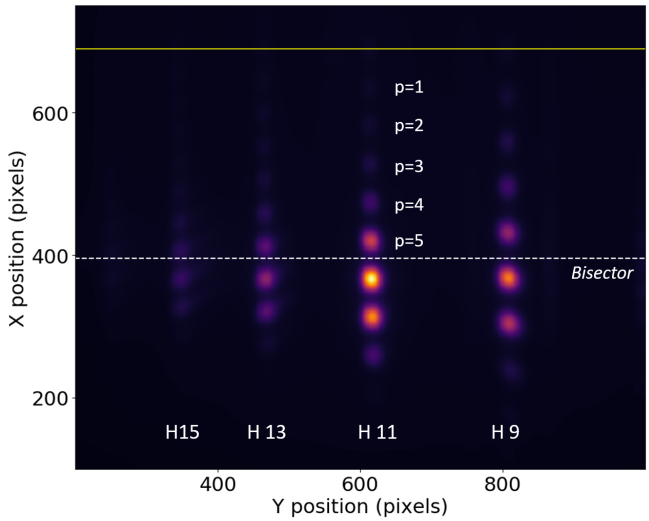

Figure 5.9: Calibrating the spectrometer using the 2p+1 rule. The image shows the far-field pattern on the MCP when two beams are crossed in a non-collinear geometry. The solid yellow line marks the 0^{th} order of diffraction. The dashed, white line is the bisector of the two beams.

between the two beams. In this case, knowing the location of the bisector of the two beams on the image and counting the number of diffraction orders visible until just above the bisector, we can find the harmonic number of any given set of diffraction orders. For example, from Fig. 5.8.(b), we know that there should be diffraction orders up to p=3 for H7 above the bisector in accordance with the law of conservation of linear momentum. The general rule is that if there are "p" diffraction orders above the bisector, the corresponding harmonic order is 2p+1.

Fig. 5.9 is a typical experimental image obtained with the two beams interfering in this configuration. The yellow line on the image marks the position of harmonics generated with just the fundamental beam. This helps us to identify the $p = 0^{th}$ order of diffraction. We see that the SFG orders of diffraction are generated and knowing the bisector (dashed, white line on the image), we can clearly identify the number of orders above it. Using the "2p+1" rule, we can now calibrate the harmonics. In this example, the H11 can be easily calibrated as shown.

CHAPTER 6

A general wave model for non collinear high harmonic generation

In this chapter, we investigate High order Harmonic Generation driven by two Non Collinear beams (NCHHG) theoretically. By introducing the composite field which forms an "active optical grating" in an empirical model based on the Strong-Field Approximation (SFA), we establish the scaling laws of the yields of the multiple beamlets that are generated.

6.1 Analysis of the driving field: three intertwined gratings model

Since HHG is a strong field phenomenon, it is the structure of the total electric field at the generation focus that rules the emission process. In Chappuis et al.[86] was introduced the "active grating model", an analytical frame-work to explain the characteristics of harmonic radiation in the far field. The superposition of the two non collinear beams results in a modulation of the intensity at the focus which induces a spatial modulation of the phase of the dipole. In this field-based model, the two beams create the grating and at the same time generate the harmonics. The *active* grating denomination stems from the fact that the grating is formed by the field, which simultaneously drives the generation of new frequencies, distinguishing it from the transient grating spectroscopic technique [87] where a passive grating is formed by two beams and the harmonic generation is driven by an additional third beam. With the active grating model, it was shown that the resulting electric field at the focus presents a fairly complex structure, but can be approximated to that of a "blaze" grating. The main benefit of this model is that it can analytically predict many observations. Here, we expand it to

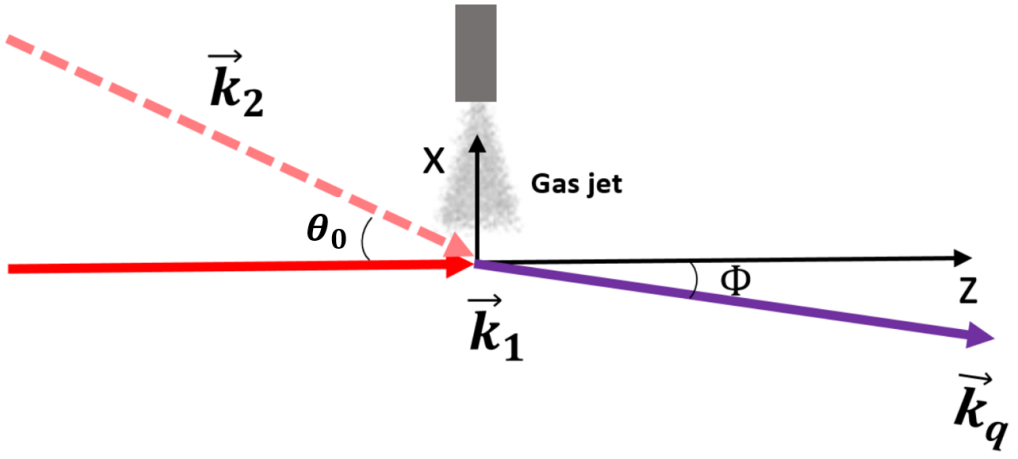

Figure 6.1: NCHHG geometry considered in the analytical modeling. The $\vec{k}_1$ beam is along the horizontal plane and $\vec{k}_2$ comes at an angle θ_0.

allow quantitative predictions of the yield of the beamlets for any intensity ratio of the two beams, as well as for the two-colour case. We will first recall the main results of the active grating model, before proceeding to differentiate the perturbative and non perturbative regimes in the next two chapters.

Let us expand on the active grating model introduced in [86] by introducing a two-colour field instead of a composite $\omega-\omega$ field. Consider two laser beams, propagating in the (xOz) plane (see Fig. 6.1) , linearly polarized along x [1], of infinite transverse extension, with wave vectors $\vec{k}_1$ and $\vec{k}_2$ forming an angle θ_0 and angular frequencies ω_1 and ω_2. We write $\Delta\vec{k} = \vec{k}_2 - \vec{k}_1$ and $\Delta\omega = \omega_2 - \omega_1$. $k_2 = \eta k_1$ and $\Delta k^{\perp}$ is the projection of $\Delta\vec{k}$ along the transverse x direction. The ω_1 beam, with amplitude E_1, is propagating along the z-axis, while the "perturbative" ω_2 beam has an amplitude $E_2 = \alpha E_1$, with $\alpha > 0$ and $\alpha \in \mathbb{R}$. The sum of the electric fields of the two beams without including a temporal or spatial envelope is

$$\begin{aligned} E_s &= \mathscr{R}\left[E_1 e^{i\omega_1 t - i\vec{k}_1\cdot\vec{r}} + \alpha E_1 e^{i\omega_2 t - i\vec{k}_2\cdot\vec{r}}\right] \\ &= E_1 \mathscr{R}\left[e^{i\omega_1 t - i\vec{k}_1\cdot\vec{r}}\left(1 + \alpha e^{i\Delta\omega t - i\Delta\vec{k}\cdot\vec{r}}\right)\right], \end{aligned} \tag{6.1}$$

where $\mathscr{R}$ stands for the real part. To extract the composite wave vector, $\vec{k}_s$, and the composite angular frequency, ω_s, of this composite field, E_s, we write $(1+\alpha e^{i\Delta\omega t - i\Delta\vec{k}\cdot\vec{r}})$ as $f_s(\alpha,\vec{r},t)e^{-i\varphi(\alpha,\Delta\omega t,\Delta\vec{k}\cdot\vec{r})}$, giving an equivalent of the analytical signal:

$$\tilde{E}_s = E_1 f_s(\alpha,\vec{r},t)\cdot e^{i\omega_1 t - i\vec{k}_1\cdot\vec{r} - i\varphi(\alpha,\Delta\omega t,\Delta\vec{k}\cdot\vec{r})}, \tag{6.2}$$

[1] We consider linear polarizations along x and neglect the weak longitudinal fields along z.

with

$$f_s(\alpha,\vec{r},t) = \sqrt{1+\alpha^2+2\alpha\cos\left(\Delta\vec{k}\cdot\vec{r}-\Delta\omega t\right)} \text{ and,} \tag{6.3}$$

$$\varphi(\alpha,\vec{r},t) = \arctan\frac{\alpha\sin\left(\Delta\vec{k}\cdot\vec{r}-\Delta\omega t\right)}{1+\alpha\cos\left(\Delta\vec{k}\cdot\vec{r}-\Delta\omega t\right)}. \tag{6.4}$$

The local wave vector ($\vec{k}_s(\vec{r})$) of the sum of the two fields given by equations 6.2 and 6.4 is

$$\vec{k}_s(\vec{r},t) = \vec{k}_1 + \vec{\nabla}\varphi \tag{6.5}$$

$$= \vec{k}_1 + \frac{\alpha(\alpha+\cos(\Delta\vec{k}\cdot\vec{r}-\Delta\omega t))}{1+\alpha^2+2\alpha\cos(\Delta\vec{k}\cdot\vec{r}-\Delta\omega t)}\Delta\vec{k}. \tag{6.6}$$

f_s^2 is the standard interference pattern for intensity. Thus the interfering beams form an amplitude grating in the medium, symmetric along the x-direction. The planes of equal intensities are defined by the normal to $\Delta\vec{k}$. In particular, in the (xOy) plane, a series of fringes with periodicity,

$$\Lambda_x = \frac{2\pi}{|\Delta k^{\perp}|} \simeq \frac{2\pi}{k_1\eta\sin\theta_0} \tag{6.7}$$

is observed. This amplitude grating decides the locations of generation of harmonics. Only at sufficiently high intensities in the medium HHG can occur and the local wave vector $\vec{k}_s(\vec{r})$ at these locations decides the emission direction.

Along the same lines, we can also introduce the spatially varying local angular frequency as

$$\omega_s(\vec{r},t) = \omega_1 t + \frac{\partial\varphi}{\partial t} = \omega_1 + \frac{\alpha(\alpha+\cos(\Delta\vec{k}\cdot\vec{r}-\Delta\omega t))}{1+\alpha^2+2\alpha\cos(\Delta\vec{k}\cdot\vec{r}-\Delta\omega t)}\Delta\omega. \tag{6.8}$$

Thus the composite field can be approximated by a plane-wave like formula,

$$\tilde{E}_s \simeq E_1 f_s(\alpha,\Delta\omega t,\Delta\vec{k}\cdot\vec{r})\, e^{i\omega_s t - i\varphi_s} \tag{6.9}$$

where,

$$\varphi_s = \vec{k}_s\cdot\vec{r}. \tag{6.10}$$

One colour case: When both fields have the same angular frequency, $\eta = 1$ and $\Delta\omega = 0$. The composite field has an angular frequency $\omega_s = \omega_1$. E_s for such a case is represented in Fig. 6.2 for $\alpha = 0.1$ and $\alpha = 0.7$, together with $\vec{k}_s(\vec{r},t)$. We note, as expected, i) the oscillation of the amplitude of the field along the transverse direction progressively forming a network of high/low magnitudes when increasing α, and ii) the wiggling of $\vec{k}_s(\vec{r},t)$ about a tilted mean value given by the solid green line. With increasing α, the phase goes from a sinusoidal modulation to a more blazed structure.

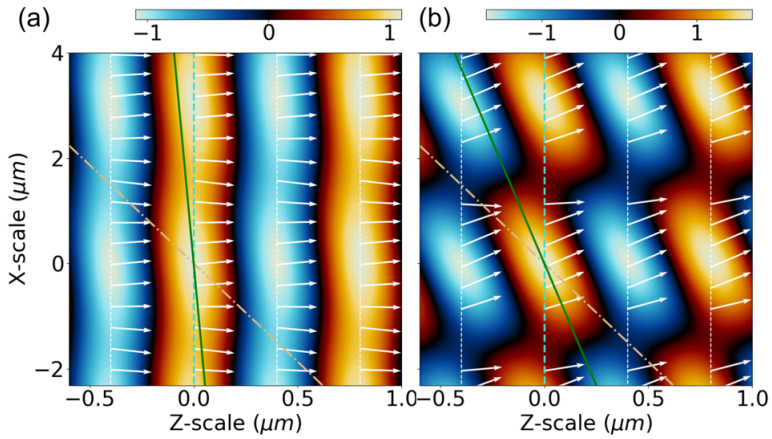

Figure 6.2: (a-b). Colourmaps of the composite electric field resulting from the interference of a beam propagating along z of amplitude 1 (wave front in turquoise dashed line), and a beam propagating at an angle of 15 degrees to the top right corner (wave front in beige dash dotted line). The approximate wavefront of the composite field (normal to $\vec{k}_s$) is in green. In (a) the second field has an amplitude of 0.1, in (b) of 0.7. White arrows: local wave vectors of the composite field. It should be noted that the longitudinal and transverse scales are different, yielding irrelevant angular values.

Two colour case: In the case, where the second field has an angular frequency, $\omega_2 = 2\omega_1$, the analysis carried out with a single colour still holds but two main differences may be identified in the composite electric field (Fig. 6.3): i) the interference pattern is moving in time with a velocity $\Delta\omega/\Delta\vec{k}$, and ii) the wave vector difference is no longer almost perpendicular to the main beam, but rather collinear to it :

$$\Delta\vec{k} \widehat{=} \begin{bmatrix} \Delta k^{\perp} \\ \Delta k^{\parallel} \end{bmatrix} = |\vec{k}_1| \begin{bmatrix} \eta \sin\theta_0 \\ \eta\cos\theta_0 - 1 \end{bmatrix}. \tag{6.11}$$

$\perp$ being the transverse direction (Ox) and $\parallel$ the longitudinal (Oz). The periodicity of the grating is lower, giving rise to more zones of HHG emission as can be seen in Fig. 6.3.

6.2 Intensity profile in the near and far fields

As explained in chapter 2, HHG in gases is attributed to a three-step process during which an outermost electron of the atom is tunnel ionized, accelerated in the continuum, and finally recombined with the ionic core, emitting its excess of energy as an XUV photon [6, 52, 88, 89]. When the atom is subjected to the composite electric field E_s, the electric field of this XUV radiation (near field, superscript nf) emitted with an angular frequency $\omega_q (= q\omega_1 = q_s\omega_s)$ reads

$$E_q^{nf} \propto A_q e^{i(q_s\omega_s t + q_s\varphi_s + \varphi_{at})}, \tag{6.12}$$

where φ_s is the geometrical phase accumulated from the macroscopic response of the medium while the atomic phase φ_{at} comes from the single atom response. It should be noted that what is con-

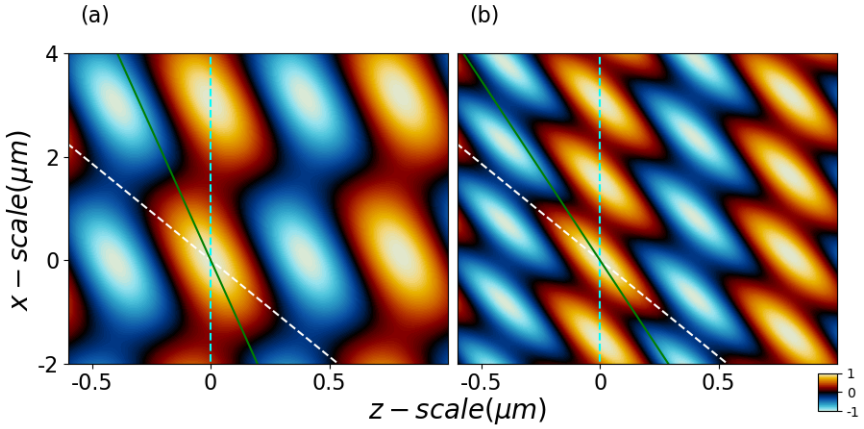

Figure 6.3: Same as Fig. 6.2, but a comparison between the one-colour and the two colour case. (a-b). Colour maps of the composite electric field resulting from the interference of a beam propagating along z (wave front in turquoise dashed line), and a beam propagating at an angle of 15 degrees to the top right corner (wave front in white dashed line). The approximate wavefront of the composite field is in green. The ratio of the amplitudes of the two fields is 0.6. In (a) is shown the single colour case, and in (b) $\omega_2 = 2\omega_1$. It should be noted that the longitudinal and transverse scales are different, yielding irrelevant angular values.

ventionally referred to as harmonic q of the fundamental frequency ω_1 where $\omega_q = q\omega_1$ is now the q_s^{th} harmonic of the composite field of angular frequency ω_s. Although all three steps depend finely on the exact waveform of the driving field in a non linear manner [88, 90], the SFA approach with saddle point approximation predicts the amplitude of the electric field of harmonic q to simply vary as $A_q \propto E_s^{q_{\text{eff}}}$. The atomic phase (see section 2.2.2) is found to vary like $\varphi_{at} = \alpha_{at} I_s$ in the plateau region of the spectrum, with α_{at} describing the strength of the atomic-response-induced phase [65]. Equation 6.12 can be written as

$$E_q^{nf} \propto e^{iq_s\omega_s t} \cdot \underbrace{E_s^{q_{\text{eff}}}(\alpha, \vec{r}, t)} \cdot \underbrace{e^{iq_s\varphi_s(\alpha,\vec{r},t)}} \cdot \underbrace{e^{i\alpha_{at}E_1^2 \cdot f_s^2(\alpha,\vec{r},t)}}. \tag{6.13}$$

Due to the modulation of the amplitude of the field and that of the wavevector (Fig. 6.2), three types of gratings are thus present in the medium, corresponding to the three terms on the right-hand side of this equation, with the same periodicity but contributing different effects. According to the Fresnel propagation theory, the experimentally observed far field profile will be the spatial Fourier transform of this expression. In the following sections, we will discuss each of these terms successively.

6.2.1 Amplitude grating

As already mentioned, f_s^2, which varies like a cosine, forms an amplitude grating, with no up-down asymmetry along the transverse x direction. It firstly modulate the amplitude of HHG. The periodicity of modulation depends on the non collinear angle between the two beams and different regimes can

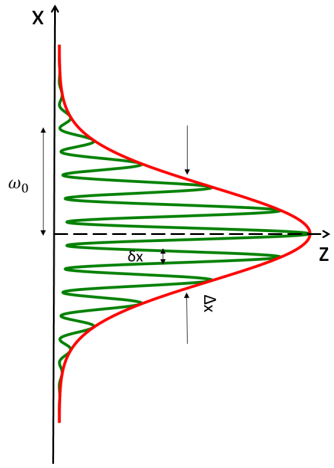

Figure 6.4: Amplitude grating: A simple model of a series of Gaussian generating gates. The green curve models the intensity interference pattern within an overall Gaussian envelope (red).

be characterised based on the number of contributing fringes [83]. Here, we focus on the case where there are many interference fringes. The simplest way to model them would be as a series of identical, spatially offset functions, denoted by G_1, multiplied by an overall spatial envelope that comes from the intensity profile of the Gaussian beam, denoted by G_2. If we model it this way as shown in figure 6.4, the near field is proportional to,

$$\left[G_1\left(\frac{x}{\delta x}\right) \otimes \text{Ш}\left(\frac{x}{a}\right)\right] G_2\left(\frac{x}{\Delta x}\right), \tag{6.14}$$

where δx is a normalization constant, ruling the width of the fringes, and Δx is the width of the envelope. The convolution is a Dirac comb $\sum_n \delta(x - na)$ modelling the repetition of the bright fringes along the x-direction with a period $a = \lambda_1/\eta \sin\theta_0$. The Fourier transform of this periodic function makes a series of diffraction peaks appear in the far field. The intensity profile in the far field thus appears as a series of peaks, equally spaced by 1/a, with an amplitude decreasing along a large envelope of width $\propto 1/\delta x$. G_2 transforms the Dirac peaks into finite peaks, contributing to the width $\propto 1/\Delta x$, of each diffraction order.

6.2.2 Blazed phase grating

The spatial phase in the generating grating is approximated by its first derivative.

$$\varphi_s = \vec{k_s} \cdot \vec{r} = k_s^{\perp} \cdot x, \tag{6.15}$$

where $k_{s_\perp}$ is the component of $\vec{k_s}$ along the transverse (Ox) direction. For high α, where the generation is limited to decreasing volumes of the composite field, $k_s^{\perp} = \frac{\alpha}{1+\alpha}\Delta k^{\perp}$ as a first approximation of

equation 6.6. Thus,

$$\varphi_s = \frac{\alpha}{1+\alpha} \cdot \Delta k^{\perp} \cdot x \tag{6.16}$$
$$= \frac{\alpha}{1+\alpha} \cdot \eta \cdot k_1 \cdot \theta_0 \cdot x \tag{6.17}$$
$$= \frac{\alpha}{1+\alpha} \cdot \eta \cdot \theta_0 \cdot \frac{x}{\lambda} \cdot 2\pi \tag{6.18}$$
$$= \frac{\alpha}{1+\alpha} \cdot 2\pi \cdot \frac{x}{\Lambda} \tag{6.19}$$
$$= \varphi_0 \cdot \frac{x}{\Lambda}. \tag{6.20}$$

The phase is approximately linear with x. We thus have a spatial phase that can be modelled as a *blazed* phase grating, asymmetric with respect to x, which gets superimposed on the amplitude grating pattern discussed above. This is true everywhere along z in the medium, at focus, upstream and downstream: the dominant blaze angle always has the same sign.

Let us try to model the far field diffraction pattern due to such a blazed grating. The classical blazed grating is a reflection grating with a saw-tooth groove profile. It has very high efficiency for a given incident angle (the blaze angle) and a given diffraction order. For a single period Λ, the complex transparency of such a blazed grating can be modelled as

$$t_g(x) = rect(x - \Lambda/2)\, e^{i\varphi_0 \frac{x}{\Lambda}}, \tag{6.21}$$

where Λ is the grating periodicity. And the rectangle function is defined as

$$rect(x) \equiv \begin{cases} 0 & \text{for } |x| > \frac{1}{2} \\ \frac{1}{2} & \text{for } |x| = \frac{1}{2} \\ 1 & \text{for } |x| < \frac{1}{2}. \end{cases} \tag{6.22}$$

Here, the rectangle function plays the role of G_1 above, to yield an overall continuous function. For a blaze repeated in space periodically,

$$t_g(x) = \left[rect(x - \Lambda/2)\, e^{i\varphi_0 \frac{x}{\Lambda}} \right] \otimes \text{Ш}\left(\frac{x - \Lambda/2}{\Lambda} \right) \tag{6.23}$$

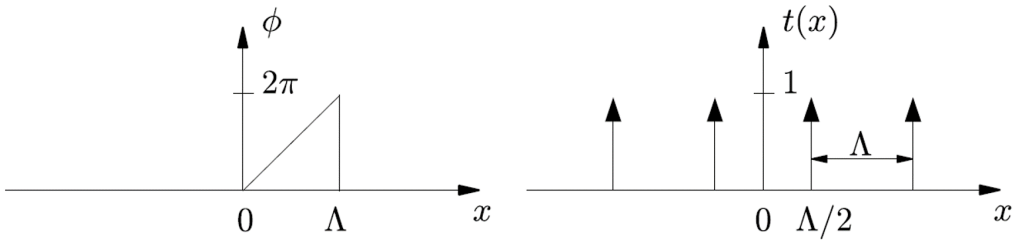

(a) Phase of one period of the grating.

(b) Desired comb function

Figure 6.5: Blazed grating: The complex transparency of the grating can be constructed by the convolution of a triangular phase profile and a comb function.

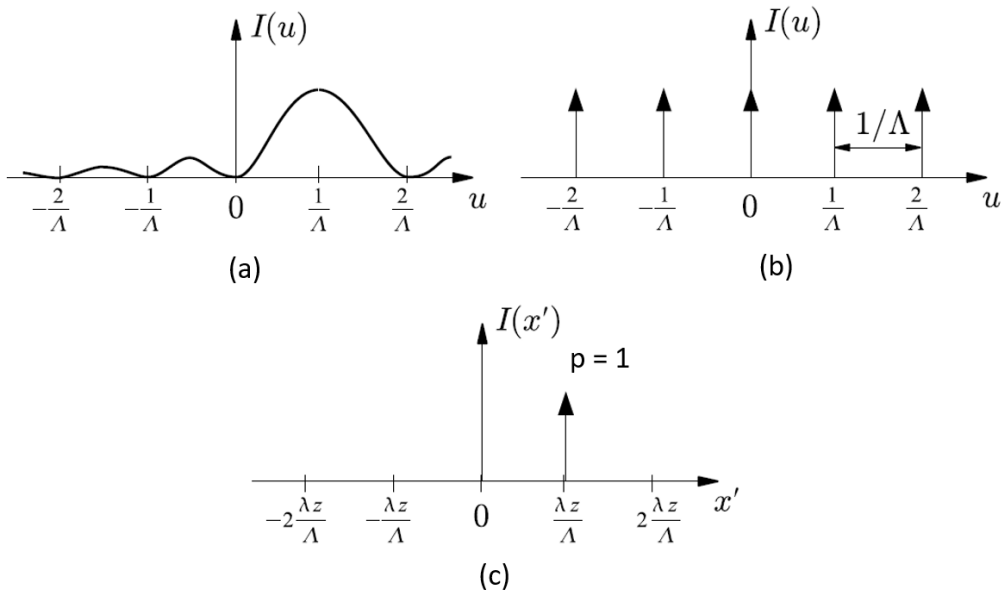

Figure 6.6: (a) the $sinc^2$ and (b) comb functions. (c) shows the Fraunhofer diffraction pattern at an observation plane. Adapted from MIT-OCW lecture.

as shown in Fig. 6.5, for the case $\varphi_0 = 2\pi$. The intensity of the Fraunhoffer diffraction pattern of this blazed grating reads,

$$I(u) = sinc^2(\Lambda\left[u - \varphi_0/\Lambda\right]) \otimes \text{Ш}(\Lambda u), \tag{6.24}$$

where u is the spatial co-ordinate in the Fourier plane. The $sinc^2$ stems from the Fourier transform of the rectangle function. Fig. 6.6.(c) shows the Fraunhofer diffraction pattern replacing with $x^{'} = u\lambda z$, at an observation plane for $\varphi_0 = 2\pi$, with $x^{'}$, z, being the coordinates in the observation plane. Only one order of diffraction survives. But if the phase contrast is reduced from 2π to any value φ_0, many orders of diffraction would become possible. Thus in the observation plane we will have several diffraction orders with a maximum amplitude at $\varphi_0/2\pi$, i.e., the diffraction efficiencies can be tuned by changing the phase modulation. The diffraction efficiency of the diffraction order p, which is defined by the comb function will be

$$I_p \sim sinc^2(p - \frac{\varphi_0}{2\pi}). \tag{6.25}$$

Now, in the case of the active grating model, it is the composite field which forms the blazed phase grating. The periodicity of this grating is $a = \lambda_1/\eta \sin\theta_0$, where λ_1 is the wavelength of the first beam and $\eta = \lambda_1/\lambda_2$. In the observation plane, we obtain a single diffraction order, p=1, for the fundamental frequency as shown in Fig. 6.7.(a). However for the q^{th} harmonic of wavelength λ_1/q, many orders

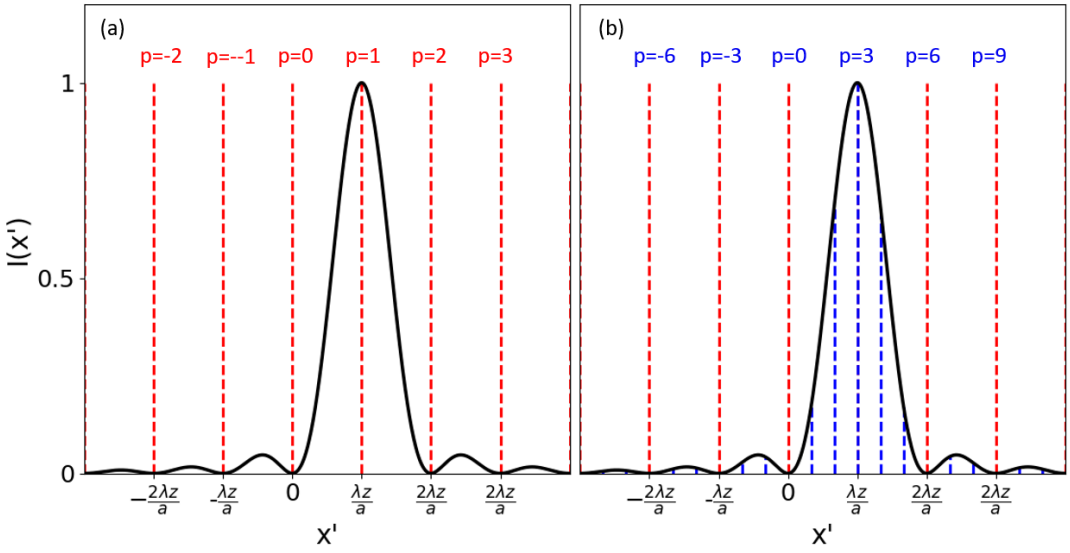

Figure 6.7: Fraunhofer diffraction figures for an infinite dimensional blazed grating for the fundamental wavelength (a) and its third harmonic (b), for $\varphi_0 = 2\pi$. The solid black curve is cardinal sine function giving the diffraction efficiency, the dashed lines are for the Dirac comb with the corresponding diffraction orders (in red for the fundamental and in blue for harmonic 3). Both the x-axes denote the wavelength of the fundamental.

of diffraction are possible even when $\varphi_0 = 2\pi$. This is shown in Fig. 6.7.(b) for $q = 3$ where multiple diffraction orders are possible and $p = 3$ is the dominant order of diffraction.

In practice, the grating has a finite dimension due to the spatial Gaussian envelope of the beam. We must therefore define an "envelope" function which specifies the contours of the grating, and study the effect of this function on the Fraunhoffer diffraction pattern. The complex transmission of the blazed grating will then be multiplied by the function representing this envelope, which will result in a convolution of the diffraction pattern by the Fourier transform of the envelope. The complex transmission is then:

$$t_g(x) = \left[rect(x - \Lambda/2) e^{i\varphi_0 \frac{x}{\Lambda}} \right] \otimes \left[\text{Ш}\left(\frac{x - \Lambda/2}{\Lambda} \right) \cdot G_2\left(\frac{x}{\Delta x} \right) \right]. \tag{6.26}$$

The diffraction orders are no longer Dirac peaks but have a Gaussian form, since the Fourier transform of a Gaussian is a Gaussian. Note that for a given harmonic q, all diffraction orders have the same width $\sim 1/\Delta x$. And the spatial phase is dependent on α. It means that a modulation in α will modulate the number of diffraction orders of the active grating that will be visible, as well as the dominant order of diffraction. This will be clearly seen in the experimental data shown in Fig. 6.10 for different α values, for instance. Fig. 6.8 shows the diffraction orders for harmonic 3 of the fundamental. When $\varphi_0 = 2\pi$ (Fig. 6.8.(a)), the fundamental (in red) only shows p=1 while the harmonic (in blue) shows many diffraction orders with p=3 as the dominant order. But for a reduced phase

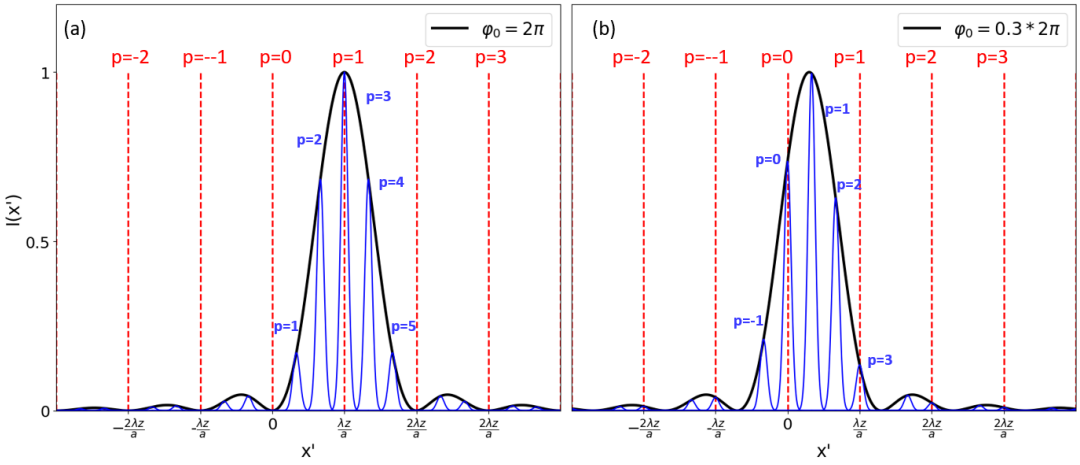

Figure 6.8: Fraunhofer diffraction figures for an finite dimensional blazed grating limited by a Gaussian envelope for different phase contrasts of $\varphi_0 = 2\pi$ (a) and $\varphi_0 = 0.3 * 2\pi$ (b). The solid black curve is $sinc^2$ function giving the diffraction efficiency, the red, dashed lines are for the Dirac comb with the corresponding diffraction orders in red for the fundamental. And in blue are the Gaussian-shaped diffraction peaks observed for harmonic 3. Both the x-axes denote the wavelength of the fundamental.

contrast of $\varphi_0 = 0.3 * 2\pi$ (Fig. 6.8.(b)), the fundamental as well as the harmonic shows more than one order of diffraction and the dominant order is now p=1 for H3.

6.2.3 Atomic phase grating

The final term of equation 6.13 gives the atomic phase dependence. Like the first amplitude grating, it is a symmetric amplitude grating along x due to the intensity dependence of the atomic phase ($\varphi_{at} = \alpha_{at} I$). And since the harmonic dipole phase depends on the driving field intensity, different harmonic sources will emit XUV radiation with different phases.

6.3 Origin of the diffraction orders and the competition between SFG and DFG

We can now predict the direction of the beamlets of harmonic, q. At a given location $\vec{r}$ in the medium, the emission is directed along $\vec{k}_q = q\vec{k}_s$, with $\vec{k}_s(\vec{r})$ given by equation 6.6. It is no longer purely along $\vec{k}_1$ but includes a contribution along $\Delta\vec{k}$, whose amplitude strongly depends on the location in the medium as well as the strength of the perturbation. Depending on the spatial position of the origin of the harmonic, $\vec{k}_s$ could be along the positive or negative direction. Interference of the fields form several zones of emission, along the same direction, leading to the appearance of well defined diffraction peaks. which we refer to as the "diffraction orders" of the active grating. Basically, the periodicity builds up some interference and the emission bunches along discrete angles. This is the basis of the

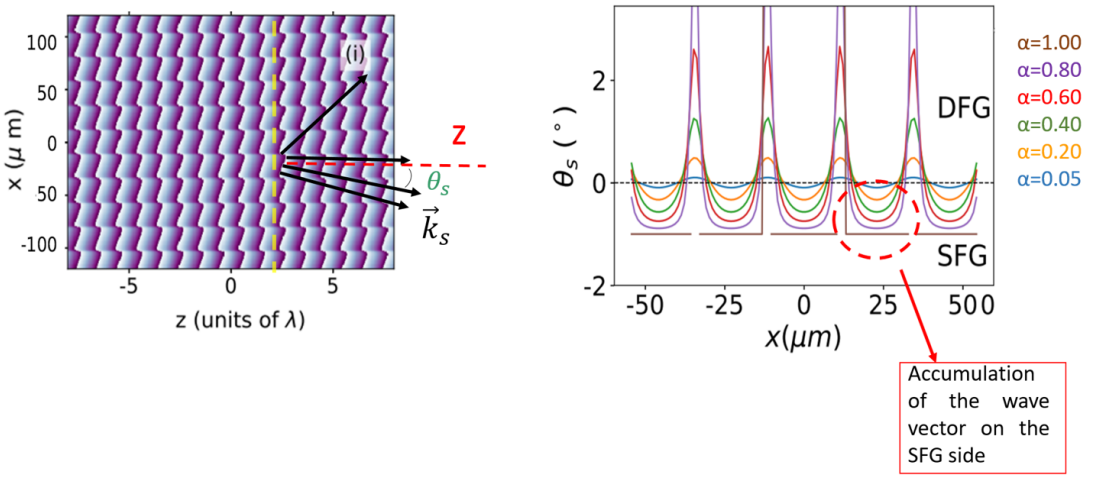

Figure 6.9: The phase map of the composite electric field for α =0.8 (left). Angle of emission of XUV with respect to horizontal, across the transverse direction (x) for different amplitude ratios of the two fields (right). Figure is adapted from [86].

"active grating" model which models the driving field as a symmetric amplitude grating given by f_s and a blazed phase grating by φ_s at any given time.

One of the interesting questions in NCHHG over the years have been the competition between the positive and negative diffraction channels. Can the processes involving sums of frequencies (SFG) dominate those carrying out frequency differences (DFG), or vice versa? The multiphoton model does not allow the consideration of such eventualities. Nevertheless, the literature shows somewhat contradictory findings on this subject: in the case where the two beams are collinear [91], and have non commensurate frequencies, it was observed that for low photon energies (between 15 and 30 eV), SFG dominates with respect to DFG and this tendency is reversed for higher photon energies (greater than 40 eV). More recently, in the context of non collinear geometry, Bertrand et al. [42] also reported that the generation of sum of frequencies is more efficient than the difference, unlike Heyl et al. [83] who observe that DFG is the dominant channel and support this claim by introducing an additional term of phase matching due to the non collinear geometry. Neglecting phase matching effects for now, we can predict the favoured emission direction by using the active grating model. With increasing α, a small phase modulation along the x direction progressively transforms into a saw tooth pattern. At very low perturbation levels ($\alpha \ll 1$)), both the wave vector amplitude ($\vec{k}_s$) and angle (θ_s) vary sinusoidally against x as

$$\vec{k}_s(\vec{r},t) = \vec{k}_1 + \alpha\cos(\Delta\vec{k}\cdot\vec{r} - \Delta\omega t)\Delta\vec{k}. \tag{6.27}$$

The excursion is perfectly up-down symmetric with respect to $\vec{k}_1$. Identical generating volumes thus have wave vectors pointing upward and downward, making no difference between the SFG and DFG

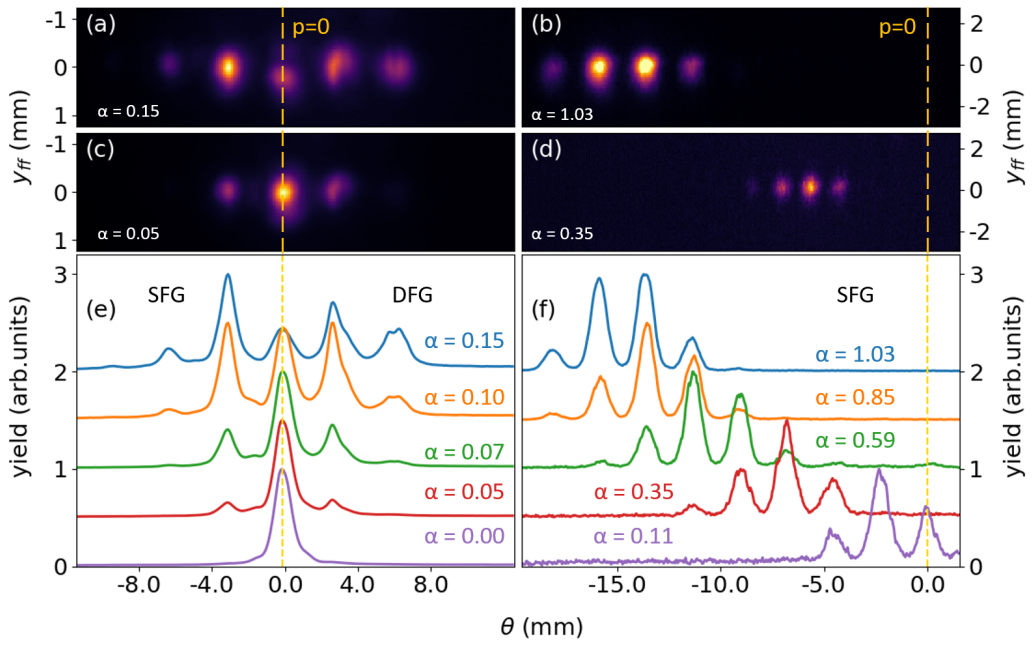

Figure 6.10: Direct images of the diffraction orders observed on the camera (a-d) for harmonic 11 for a given perturbation level. The dashed, yellow lines mark the position of the zeroth order of diffraction.(e-f): The normalized yield of the diffraction orders for a given value of α. The left column is for low and the right for higher perturbation levels. The line-outs for each value of α is given a vertical offset for better visibility.

.

amplitudes. We can thus anticipate equally strong positive and negative diffraction orders in the far-field and only phase matching effects, such as those identified by Heyl et al.[83] could explain any favouring towards DFG.

From the phase map of the composite electric field in Fig. 6.9, we can see that the phase becomes highly blazed with high perturbations ($\alpha = 0.8$ here) and there is a clear accumulation of the wave vectors on the SFG side. This is the case in our experimental data as well. As α progressively increases, the SFG orders dominate while the DFG are slowly extinguished. Fig. 6.10 shows this trend in the experimental data. The left hand side of the figure, panels (a,c,e) show the experimental results for low levels of perturbation ($\alpha < 0.15$). From the line outs of the diffraction orders, we see that SFG and DFG are symmetric in amplitude up to $\alpha = 0.1$ while above this value, there is a marked favouring of SFG. For higher perturbations (images Fig. 6.10.(b) and Fig. 6.10.(d)), we can see that more and more diffraction orders show up with increasing α, while the lower orders get extinguished. This is clear in the line out (Fig. 6.10.(f)) as well. Thus the active grating model answers this much disputed question

of the preferential emission direction for high perturbation levels.

Since the focus of this study is the intensity distribution of each of these diffraction orders in the far field, we will now proceed to derive the expression for the amplitude of the electric field (E_q^p) for each order of diffraction p for a given harmonic q of the fundamental frequency ω_1. Following earlier publications dedicated to the perturbative regime, we will analyse the yields of diffraction orders to test a comprehensive interpretation of NCHHG. However, we will now differentiate the process into two regimes, perturbative and non perturbative depending on the strength of the second field and treat them separately in the following chapters.

CHAPTER 7

Application of the wave model to the perturbative to intermediate regime and comparison to experiments

Since the existing work on emission yields in NCHHG is built around a perturbative power scaling law [42, 82], we start by considering a *perturbative* second field, setting very low α. In Bertrand et al.[42], the experimental yields were shown to vary like α^{2p}, while in Li et al.[82], it was generalized to $\alpha^{2p}\cdot(1-\alpha)^{q-p}$, based on a quantum model (see section 4.3.4). Specifically, we here use the prediction of the dipole model that the field amplitude of a given harmonic, $E_q \propto E_{\mathrm{IR}}^{q_{\mathrm{eff}}}$, to include such kind of inhomogeneous fields formed by the two interfering beams. We will thus derive the expression for the amplitude of the electric field (E_q^p) for each order of diffraction p for a given harmonic q of the fundamental frequency ω_1. Then, we will present experimental results that are in excellent agreement with our theoretical model, and further match with a direct full 3D numerical model based on the resolution of the Schrödinger Equation within the strong field approximation. The results could also be interpreted in terms of photon channels associated to each beamlet, bridging the gap with previous interpretations, providing a field-based analytical framework for explaining NCHHG and its possible spectroscopic applications.

7.1 Modelling the intensity of diffraction orders

In the previous chapter, we already obtained the equation of the electric field for the harmonics at the exit of the medium. Assuming *low perturbation*, we start by expanding each term of this equation (6.13) separately as a Taylor series against α.

7.1.1 Taylor expansion of the yields

To recall, the electric field of the harmonic at the exit of the medium is modelled as,

$$E_q^{nf} \propto G\left[E_1 \cdot f_s(\alpha, \vec{r}, t)\right] \cdot e^{iq_s\varphi_s(\vec{r},t)} \cdot e^{i\alpha_{at}E_1^2 \cdot f_s^2(\alpha,\vec{r},t)}. \tag{7.1}$$

Amplitude

Assuming that the harmonic yield scales as an effective non linear order (q_{eff}) of the driving field, the first term in equation 7.1 reads,

$$\begin{aligned} G(E_1.f_s(\alpha,\vec{r},t)) &= E_1^{q_{\text{eff}}} f_s^{q_{\text{eff}}} \\ &= E_1^{q_{\text{eff}}}(1+\alpha^2+2\alpha cos(\Delta\vec{k}\cdot\vec{r}-\Delta\omega t))^{q_{\text{eff}}/2} \\ &= E_1^{q_{\text{eff}}}(1+\alpha^2+\alpha(e^{i(\Delta\vec{k}\cdot\vec{r}-\Delta\omega t)}+e^{-i(\Delta\vec{k}\cdot\vec{r}-\Delta\omega t)}))^{q_{\text{eff}}/2} \\ &= E_1^{q_{\text{eff}}}(1+\alpha e^{i(\Delta\vec{k}\cdot\vec{r}-\Delta\omega t)})^{q_{\text{eff}}/2}(1+\alpha e^{-i(\Delta\vec{k}\cdot\vec{r}-\Delta\omega t)})^{q_{\text{eff}}/2}. \end{aligned} \tag{7.2}$$

Using the binomial expansion $(1+x)^b = C_0^b x^0 + C_1^b x^1 + C_2^b x^2 + ...$, we re-write

$$(1+\alpha e^{i(\Delta\vec{k}\cdot\vec{r}-\Delta\omega t)})^{q_{\text{eff}}/2} = \sum_{n\geq 0} a_n \alpha^n e^{in(\Delta\vec{k}\cdot\vec{r}-\Delta\omega t)} \tag{7.3}$$

and equation 7.2 becomes

$$G(E_1.f_s(\alpha,\vec{r},t)) = E_1^{q_{\text{eff}}} \sum_{n\geq 0}\sum_{m\geq 0} a_{nm}\alpha^{(n+m)} e^{i(n-m)(\Delta\vec{k}\cdot\vec{r}-\Delta\omega t)} \tag{7.4}$$

Let us define,

$$\begin{aligned} k' &= n+m \ ; \ k' \geq 0 \\ k &= n-m \end{aligned}$$

which gives

$$k + k' = 2n \tag{7.5}$$

$$k' - k = 2m \geq 0. \tag{7.6}$$

Equation 7.5 implies that k and k' should be of the same parity as their sum is an even number. Equation 7.6 sets $k' \geq k$ as $m \geq 0$. Figure 7.1 is a graphical representation of these constraints on k and k'. Let us define unit vectors $\vec{e}_n$ (resp. $\vec{e_m}$) along the n (resp. m) axis, and vectors $\vec{r}_{nm} = n\vec{e}_n + m\vec{e_m}$, with n and m two positive integers. The allowed values of (n,m) correspond to $\vec{r}_{nm}$ vectors pointing

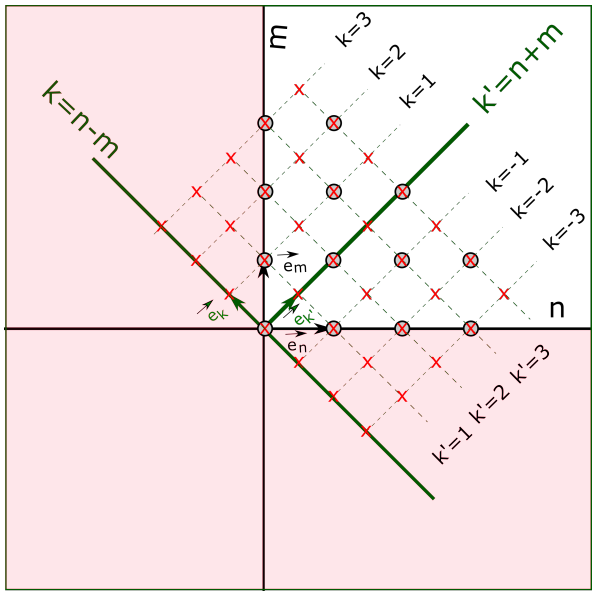

Figure 7.1: Graphical representation of the change of index of equation 7.4. The unit vectors for the (n,m) (resp. (k,k')) coordinates are in black (resp. green). The corresponding grids are respectively in black circles and red crosses which is twice as dense as the original one.

in the upper right quadrant, represented as black circles in the non shaded area. The second (k,k') coordinates system is likewise defined through $\vec{e}_k = \frac{1}{2}(\vec{e}_n - \vec{e_m})$ (resp. $\vec{e_{k'}} = \frac{1}{2}(\vec{e}_n + \vec{e_m})$). With (k,k') being two integers, the vectors $\vec{r}_{kk'} = k\vec{e}_k + k'\vec{e_{k'}}$ form the grid with red crosses. In this new coordinate system, every other cross not matching a black circle should thus be excluded, which is given by the condition k and k' of identical parities. Two conditions arise from the restriction to stay within the non shaded area: $k' \geq |k|$ and $k' \geq 0$. Therefore, the Taylor expansion of $G\left[E_1 \cdot f_s(\alpha, \vec{r}, t)\right]$ (equation 7.4) against α reads

$$G(E_1, f_s(\alpha, \vec{r}, t)) = E_1^{q_{\text{eff}}} \sum_{k=-\infty}^{+\infty} \sum_{\substack{k' \geq |k| \\ \text{same parity}}} a_{kk'} \cdot \alpha^{k'} \cdot e^{ik\left(\Delta\vec{k}\cdot\vec{r} - \Delta\omega t\right)}. \tag{7.7}$$

With this change of indexing, we retrieve the usual form of a Taylor expansion against α.

Geometrical phase

The geometrical phase, φ_s, is approximated as

$$\varphi_s(\vec{r}, t) \simeq \alpha \sin(\Delta\vec{k}\cdot\vec{r} - \Delta\omega t) \tag{7.8}$$

The second term of equation 7.1 may be expanded using the Jacobi-Anger identity as

$$e^{iq_s\varphi_s(\vec{r},t)} = \sum_{k''=-\infty}^{+\infty} J_{k''}(q_s\alpha) e^{ik''\left(\Delta\vec{k}\cdot\vec{r} - \Delta\omega t\right)} \tag{7.9}$$

where $J_{k''}(q\alpha)$ are the Bessel function of the first kind. For $q\alpha \ll |k"|$, $J_{k''}(q\alpha) \simeq \frac{1}{|k''|!}\left(\frac{q_s\alpha}{2}\right)^{|k''|}$, giving

$$e^{iq_s\varphi_s(\vec{r},t)} = \sum_{k''=-\infty}^{+\infty} \frac{1}{|k''|!}\left(\frac{q_s\alpha}{2}\right)^{|k''|} e^{ik''\left(\Delta\vec{k}\cdot\vec{r}-\Delta\omega t\right)} \tag{7.10}$$

Again, it is the standard form of a Taylor expansion.

Atomic phase

The atomic phase is

$$\begin{aligned}\varphi_{at}(\vec{r},t) &= \alpha_{at}E_1^2 f_s^2 \\ &= \alpha_{at}E_1^2(1+\alpha^2+2\alpha cos(\Delta\vec{k}\cdot\vec{r}-\Delta\omega t)) \\ &= 2\alpha_{at}\alpha E_1^2\cos(\Delta\vec{k}\cdot\vec{r}-\Delta\omega t)\end{aligned} \tag{7.11}$$

after having dropped the constant terms. Typical values for HHG in Argon with a $\lambda = 800$ nm driving laser is $\alpha_{at}\cdot E_s^2 \simeq 1$ rad [92], while q can be dozens of orders, making $q\varphi_s(\vec{r},t)$ the dominant phase term that is modulated. We thus neglect this term in the following calculations as it would not change the conclusion as it shares the symmetry as φ_s, the cosine being replaced by sine.

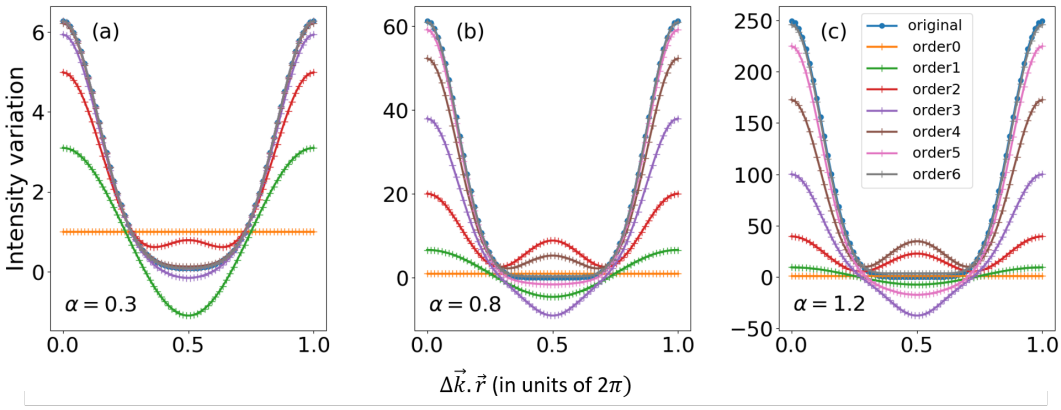

Figure 7.2: Comparison of the amplitude function obtained by symbolic computation for three different values of α and their Taylor expansions. Each colour is for the limit on the number of terms in the expansion. The blue curve is obtained from numerical computation of equation 7.2 considering $q_{\text{eff}} = 3.5$.

Global Taylor expansion

Putting all the terms of the amplitude and the geometrical phase together, we get the Taylor expansion of equation 7.1 as

	p=-6	p=-5	p=-4	p=-3	p=-2	p=-1	p=0	p=1	p=2	p=3	p=4	p=5	p=6
a_0							2						
a_1						14		14					
a_2					17.5		24.5		17.5				
a_3				8.75		61.25		61.25		8.75			
a_4			1.1		30.62		38.3		30.62		1.1		
a_5		0.1		3.83		3.83		38.3		3.83		0.1	
a_6	0.03		0.38		4.78		9.6		4.78		0.38		0.03

Table 7.1: Coefficients of expansion of equation 7.13 computed for the amplitude term in the far field amplitude of H15.

$$E_q^{\mathrm{nf}}(E_1,\alpha,\vec{r},t) \quad \propto \quad \sum_{k=-\infty}^{+\infty} \sum_{\substack{k'\geq|k| \\ k'\geq 0 \\ \text{same parity}}} \sum_{k''=-\infty}^{+\infty} a_{kk'k''} \cdot \alpha^{k'+|k''|} \cdot e^{i(k+k'')\left(\Delta\vec{k}\cdot\vec{r}-\Delta\omega t\right)} \tag{7.12}$$

Each $e^{i(k+k'')\left(\Delta\vec{k}\cdot\vec{r}-\Delta\omega t\right)}$ term corresponds to a p^{th} order of diffraction in the far field where p= k+k", with a scaling that goes as $\alpha^{p'}$ where $p' = k' + |k''|$. Equation 7.12 demonstrates that only odd(resp even) powers survive for an odd(resp even) diffraction order as k'+|k"| has the same parity as k+k", k' having the same parity as k. Hence for a given diffraction order p, the electric field at the exit of the medium reads as

$$E_q^p \propto \left(\sum_{\substack{p'\geq|p| \\ \text{same parity}}} a_{p'}\, \alpha^{p'} \right) e^{ip\left(\Delta\vec{k}.\vec{r}-\Delta\omega t\right)}. \tag{7.13}$$

This is in agreement with the quantum model of Li et al. [82] which predicts the yield of a given photon channel to give the power scaling of equation 4.9.

7.2 Computation

To check these derivations and get values of the relevant coefficients, we performed with symbolic computation a Taylor expansion of these functions, first individually and then globally. We need to specify the harmonic order q, which we set as 15, and the value of q_{eff}, which we arbitrarily set to 3.5. The conclusions remain unchanged for other reasonable values of q and q_{eff} that we tested.

7.2.1 Amplitude

The electric field reads, up to the sixth order of expansion for harmonic q as:

$$|E_q^p| \propto a_p\alpha^p + a_{p+2}\alpha^{p+2} + a_{p+4}\alpha^{p+4} + a_{p+6}\alpha^{p+6} \tag{7.14}$$

	p=-6	p=-5	p=-4	p=-3	p=-2	p=-1	p=0	p=1	p=2	p=3	p=4	p=5	p=6
a_0							1						
a_1						7.5		7.5					
a_2					-31.8		-56.25		24.37				
a_3				-101		-239		-182.3		44.68			
a_4			265		30.62		777		-335.15		50.27		
a_5		609.4		1987.2		2460		2460		-377		35.2	
a_6	1269.6		-4570.5		6458.4		-4510.6		1602.5		-264		14.7

Table 7.2: Coefficients of expansion of equation 7.13 computed for the phase term in the far field amplitude of H15.

The values of the coefficients obtained for H15, considering $q_{\text{eff}} = 7/2$ and $\alpha_{at} = 0$ are shown in table 7.1. The even (resp. odd) diffraction orders only take even (resp. odd) powers of α. We observe that the contributions of positive and negative orders receive equal contributions. This is as expected as the amplitude grating is not blazed. The approximation is excellent for α up to 1.2 (Fig. 7.2).

7.2.2 Phase

As for the phase of the composite beam, expanded for harmonic 15 in table 7.2, the approximation is valid over a narrower range of α values (Fig. 7.3) for the entire space. However, for large α it stays close

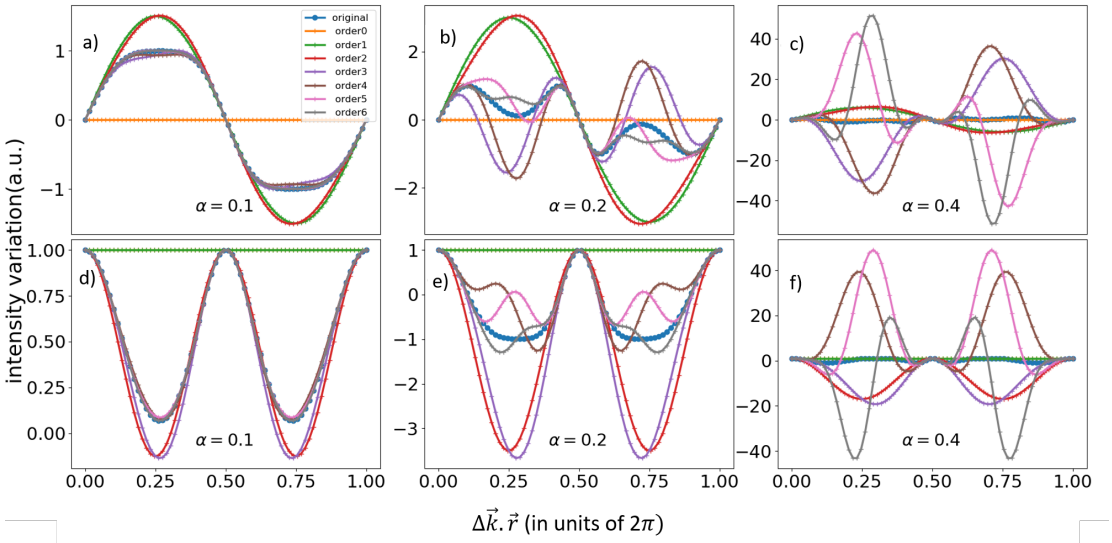

Figure 7.3: Same as Fig. 7.2, but for the geometrical phase. Each column is for a given value of α with the top row (a-c) showing the imaginary part and the bottom row (d-f) showing the real part. Each colour is for the limit on the number of terms in the expansion.

	p=-6	p=-5	p=-4	p=-3	p=-2	p=-1	p=0	p=1	p=2	p=3	p=4	p=5	p=6
a_0							1						
a_1						4		11					
a_2					10		-44		55				
a_3				20		-8		-220		165			
a_4			35		-220		550		-660		330		
a_5		56		-385		1100		1650		-1320		462	
a_6	84		-616		1925		-3300		3300		-1848		462

Table 7.3: Coefficients of expansion of equation 7.13 computed for the total field, including the amplitude and phase terms, for H15. The alternating signs of the coefficients is evident from the cell colours, where blue represents positive values and red, negative.

to the function in the areas close to the peak intensity ($2\pi r = 0[\pi]$) where harmonic emission is possible, justifying its use. We notice the asymmetry in the magnitude of coefficients for positive/negative orders (see table 7.2). This is true for any harmonic considered. This is the main origin of the preferential emission direction. Also, the same parity rules are observed: odd (resp. even) diffraction orders only take odd (resp. even) powers of α, starting at the diffraction order number.

7.2.3 Total Field

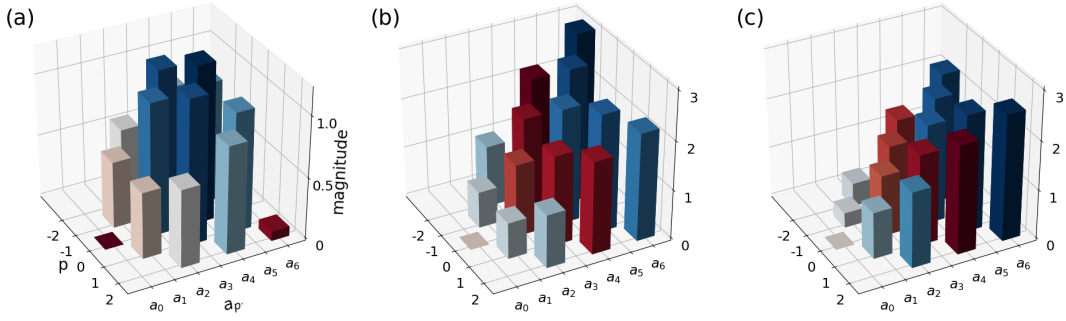

Figure 7.4: Coefficients for different diffraction orders obtained from symbolic computation of Taylor expansion for harmonic order 11 for the terms corresponding to amplitude (a), phase (b) and the total field (c) of $E^{nf}_{q,p}$. Colour blue is for positive and red for negative values.

Finally, the product of the two gives the total field. The symbolic computation validates our analytical expansion. Each diffraction order, p, has a yield which expands as a series of $\alpha^{p+2p''}$, with $p'' > 0$. Also, we note the opposite signs of successive terms, e.g. for the first diffraction order $11\alpha - 220\alpha^3 + 1650\alpha^5$. The α^p scaling is counterbalanced by the α^{p+2}, leading to the experimen-

tally observed saturation. To give an order of magnitude, the second term becomes dominant over the first for $\alpha = 0.22$, and the third over the second for $\alpha = 0.36$, which is within our experimental range. They should certainly not be neglected. It was also the case in Bertrand et al [42], where α was incremented up to 0.7. Fig. 7.4 shows the coefficients of the terms of the Taylor expansion obtained from computation. For the expansion of the amplitude function, we see symmetric amplitudes for the coefficients for SFG and DFG (a) and asymmetric values for the phase term (b) which propagates on to the total field (c). The alternating signs of the coefficients is also retrieved, as can be seen from the colour code in the image.

7.3 Experimental results

Having developed the analytical model to predict the HHG emission yield in the perturbative regime, we proceeded to carry out experiments to test and validate our model. During the experiment, the intensity I_1 was fixed while I_2 was varied such that α spanned from 0 to 0.15. Figure 7.5 is the far-field image of the diffraction orders obtained under these conditions. The geometry of the optical set-up is such that the main beam is in the horizontal plane and the second beam points downwards at an angle of approximately 40 mrad. It is clear that the positive and negative orders are symmetric in amplitude. Also only low orders up to ±2 are observed as predicted by the active grating model. Fig 7.6 shows the high harmonic yields of these different diffraction orders as a function of α. The

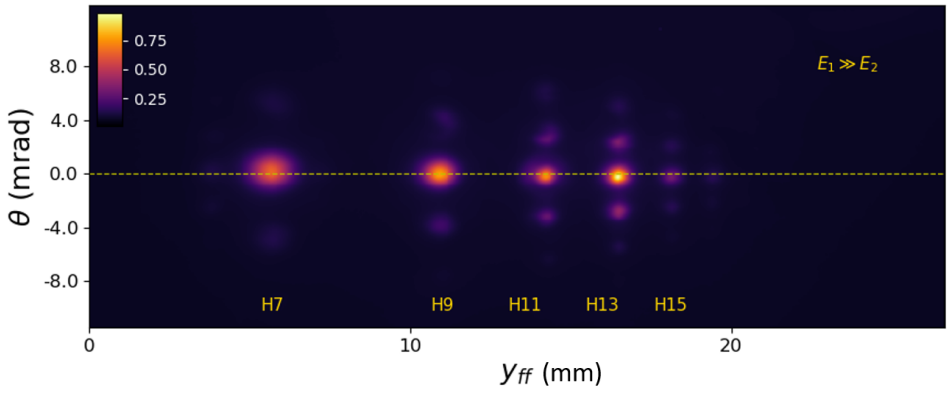

Figure 7.5: Far field image observed on the MCP (X-Y plane) for the perturbative regime. The dashed-yellow line marks the position of the zeroth order of diffraction, i.e, the spectrum generated by the fundamental alone along the $\theta = 0$ axis where θ is the emission angle with respect to the z-axis.

experimental data has been treated as described in Appendix B.

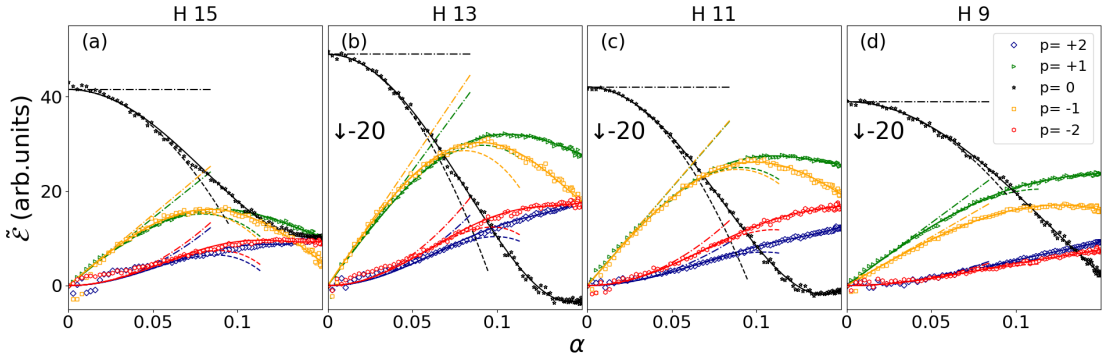

Figure 7.6: The magnitude of the electric fields of the diffraction orders $p = 0, \pm 1$ and ± 2 for harmonics 15,13,11 and 9 as obtained from the experiment. The solid lines are the fitting of the data with the first 3 terms in the expansion of equation 7.13. The dashed lines are fits with two terms and the dot-dashed lines with just one term.

Equation 7.12 tells us that in the far field there will be individual orders of diffraction p = k+k", each with an electric field which reads as

$$E_q^p \propto \left(\sum_{\substack{p' \geq |p| \\ \text{same parity}}} a_{p'} \, \alpha^{|p'|} \right) e^{ip\left(\Delta\vec{k}.\vec{r} - \Delta\omega t\right)} \tag{7.15}$$

Simply put, the amplitude of the electric field for each order p for a given harmonic order q should vary as

$$|E_q^p| \propto a_p \alpha^p + a_{p+2}\alpha^{p+2} + a_{p+4}\alpha^{p+4} + ... \tag{7.16}$$

Now, if we consider the first term alone,

$$\begin{aligned} |E_q^p| &\propto a_p \alpha^p \\ I_q^p = |E_q^p|^2 &\propto a_p^2 \alpha^{2p} \\ &\propto a_p^2 I_2^p \quad (\alpha = \sqrt{I_2/I_1}). \end{aligned}$$

We thus retrieve the power scaling law of [42, 82] for very low perturbations. However, our model goes beyond this to the intermediate regime with the higher order terms.

The fit of the power scaling laws are indicated as dot-dashed lines in Fig 7.6. The trends are the same for all harmonics. We observe that the fit $I_{q,p} \propto \alpha^{2p}$ is acceptable up to 5-10% of perturbation. However the experimental intensities progressively depart from this law and we note a saturation followed by a strong decrease down to zero. The case of $p = 0$ is specific as it seems to depart from a constant value even quicker. The dot-dashed lines in Fig.7.6 are obtained with a single term (as already mentioned above), the dashed line with two, and the solid with three, of the expected parity.

For instance, the order of diffraction 1 is fitted with the test function $a_1\alpha + a_3\alpha^3 + a_5\alpha^5$. The fit function with three terms is excellent for all sets of data over this α range, while reproducing correctly the data up to only $\alpha \simeq 0.08$ with only two terms.

We now examine the coefficients of expansion obtained by fitting our experimental data with our analytical model. The coefficients a_p of the fitting functions for H11 are reported in Fig. 7.7. We observe a progressive increase of their value with p and, strikingly, systematic alternating signs as expected from the computation.

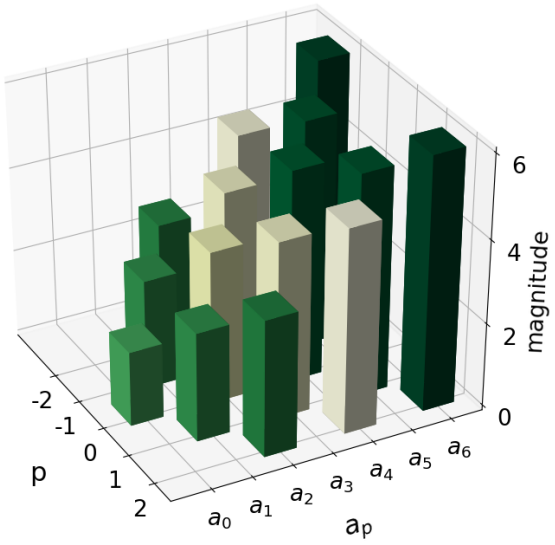

Figure 7.7: Coefficients of the Taylor expansion for different diffraction orders obtained from the experimental data for harmonic order 11. The colour green is for positive values and white is for negative values. The alternating signs of the successive terms of the expansion is clear.

Figure 7.8 is a detailed analysis of the coefficients of expansion obtained from the experiment. Panels a, b, c and d are the plots of the logarithmic value of the coefficients of the first six terms in the expansion for the diffraction orders 0, ± 1 and ± 2 for harmonics 9, 11 ,13 and 15. The different colours represent the different diffraction orders. For each diffraction order, the successive coefficients alternate in sign and their magnitudes are increasing. The positive and negative orders stay symmetric in amplitude over this α range.

7.4 Selection of photon-channel

In the photon picture, the combination of two laser fields with a central frequency ω leads to radiation with frequency $\omega_q = (n_1 \pm n_2)\omega$ where $n_1 = q - p$ and $n_2 = p$ are integers and the diffraction order $p = n_2$ is obtained. The same diffraction order could be generated by different pathways, for example, by the absorption of n_1 photons from the first field and n_2 + n photons from the second field and the

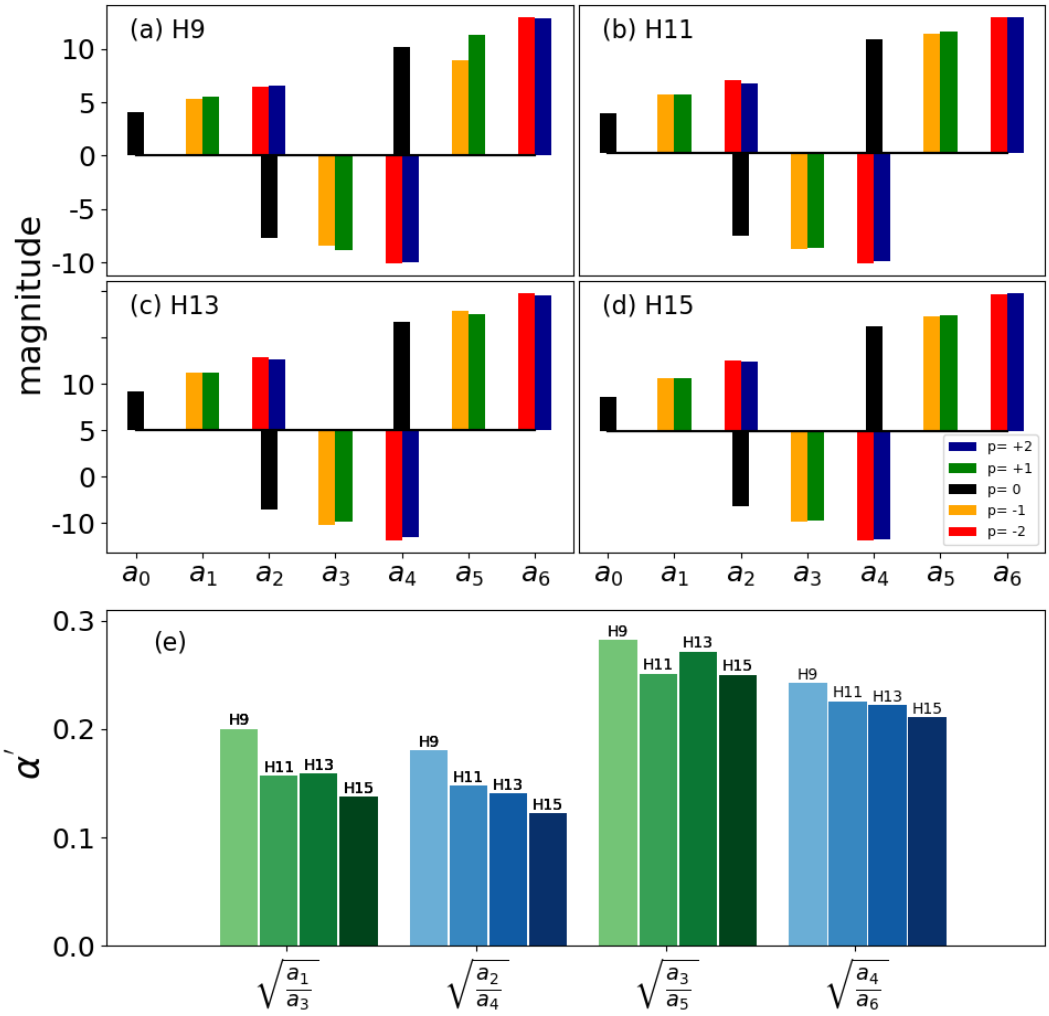

Figure 7.8: The top four panels are the plots of the coefficients of the first six terms in the expansion for the diffraction orders 0, ±1 and ±2 for harmonics 9, 11, 13 and 15. The bottom panel is a bar plot of the different ratios of the coefficients for each of these harmonics for p=+1(green) and p=+2(blue).

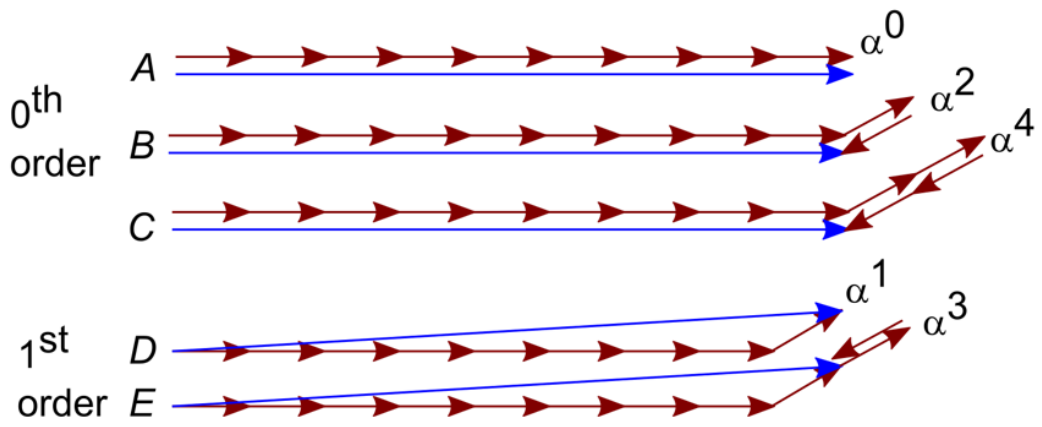

Figure 7.9: Illustration of a few photon paths contributing to the $p = 0^{\text{th}}$ order of diffraction (A to C) and the $p = 1^{\text{st}}$ order (D-E) for harmonic 9.

stimulated emission of n photons from the second field (see Fig 7.9). We still get the same diffraction order p for harmonic q, but the process is now perturbative to the $(p+2n)^{th}$ order. This explains the need for the higher order terms in the expansion 7.13. It is also why only α^{p+2n} terms are observed.

For example, if we consider the order p=3 for harmonic 11, according to our model,

$$|E_{11}^{3}| \propto a_3\alpha^3 + a_5\alpha^5 + a_7\alpha^7 + ... \tag{7.17}$$

The α^3 contribution comes from the absorption of $n_1 = 8, n_2 = 3$, α^5 contribution from the absorption of $n_1 = 8, n_2 = 4$ and the stimulated emission of 1 photon from the second field $(8\omega_1 + 4\omega_2 - 1\omega_2)$ involving a total of 5 photons from the second field, α^7 contribution from $(8\omega_1 + 5\omega_2 - 2\omega_2)$, involving a total of 7 photons from the second field etc.

7.5 Range of the perturbative regime

As α increases, these additional photon pathways are more probable, giving rise to the need for the additional terms to fit the data. The square root of the ratio of the coefficients gives an estimate of the cut-off of each regime. Consider diffraction order $p = 1$ for any harmonic q. The perturbative model states that the electric field would vary as

$$E_q^p = a_1\alpha^1 + a_3\alpha^3 + a_5\alpha^5 + ... \tag{7.18}$$

The value of $\alpha = \alpha'$ at which the contributions from the first two terms are comparable is given by

$$a_1\alpha' = a_3\alpha'^3 \tag{7.19}$$

$$\alpha' = \sqrt{\frac{a_1}{a_3}} \tag{7.20}$$

In this case, at a value of $\alpha'/2$, we are definitely in the perturbative regime where the yields follow the power scaling law. Similarly by looking at $\sqrt{\frac{a_3}{a_5}}$ we can predict when the third term becomes important or at what value of α the next photon pathway is preferred over the previous one. In Figure 7.8, if we look at $p = 1$ (green bars) for H 15 , we can see that the ratios $\sqrt{\frac{a_1}{a_3}}$ and $\sqrt{\frac{a_3}{a_5}}$ show values around 0.15 and 0.25 denoting that this is when the terms α^3 and α^5 in the expansion become dominant. Thus the ratio of the coefficients will give us an estimate of the cut-off of the perturbative regime. We find, for the experimental data (resp. symbolic computation) on diffraction order 1 of harmonic 15, that the first order term dominates for $\alpha < 0.15$ (resp. $\alpha < 0.22$), the third order for $0.15 < \alpha < 0.25$ (resp. $0.22 < \alpha < 0.36$) and the fifth order for $\alpha > 0.25$ (resp. $\alpha > 0.36$). The agreement is good, and observed for all other diffraction orders and harmonics.

According to the photon model, for each harmonic q there can be q number of diffraction orders going from the absorption of $(n_1 = q, n_2 = 0)$ photons to $(n_1 = 1, n_2 = q-1)$. At some value of α, spanning the range 0 to $+\infty$, each of these orders become dominant i.e. q diffraction orders need to be divided over the same α range. Intuitively we can say that the range of these regimes shrinks with increasing harmonic order. Our experimental data in Figure 7.8(e) shows this trend. Another way to say this would be that the channel conversion is faster for larger n_1, as mentioned in [82].

7.6 Conclusion and discussion

The most interesting discovery in this extension to the perturbative model may be the role of the additional terms in equation 7.16. As noted above, several photon pathways may reach the same order of diffraction with a wave vector,

$$\vec{k}_{q,p} = (q-p)\,\vec{k}_1 + (p+n)\,\vec{k}_2 - n\,\vec{k}_2, \tag{7.21}$$

where n is a number of simultaneous absorption and stimulated emission of a perturbing photon. These processes for $n \neq 0$ end up on the same energy level and with the same $k_{q,p}$ wave vectors as the $n = 0$ one, all adding up coherently. However, they have a perturbation order $p+2n$. Interestingly, we observe that compared to the fundamental channel, any pair of extra photons involved in an absorption/stimulated emission channel creates a field π out of phase with respect to their preceding and following terms. A parallel may be drawn with theory of multiple-photon XUV+IR cross-correlation techniques used to access the photoionization time delays [93, 94]. In the so-called Reconstruction of Attosecond Beating by Interference of Two-photons Transition (RABBITT) scheme, the atom is photoionized by a combination of XUV and IR fields through different channels involving absorption or stimulated emission of IR photons. The electron goes through intermediate states, according to the selection rules of orbital angular momentum. When an electron undergoes an extra stimulated emission/absorption process, a generic π phase is added to its wave function, in addition to specific atom-dependent phases of generally small magnitude [94, 95]. Through this alternance of sign of the coefficients, we here observe that this π phase shift gets transferred to the emitted photons in the HHG process; which was also theoretically predicted by the field based model presented. Although we could not measure it with our current experimental setup, we anticipate that, like electronic wave

packets in the RABBITT scheme, the electric field emitted by NCHHG with large angles should be sensitive to the phase of continuum-continuum transitions and coulomb phases, offering a new highly nonlinear spectroscopic method. As a final side remark for this chapter, we also note that this observation may be of importance in the current discussion about the phase of stimulated emission [96], or the phase in Above-Threshold Ionization (ATI) processes [97, 98, 95]. In the next chapter, we will progress to the non perturbative regime where the amplitudes of the two fields are comparable and the power scaling law breaks down. But once again, we will identify a signature of these higher order processes.

CHAPTER 8

Application of the wave model to non collinear high harmonic generation in the non perturbative regime and comparison to experiments

So far, we focused on retrieving and explaining the existing power scaling law of NCHHG with a field based analytical model, complementing it with experimental results. In doing so, we extended it to higher powers and found a photon channel interpretation to explain the same. But, what happens when the field strengths of the two interfering beams are comparable? A simple Taylor expansion of the electric field of the harmonic against α would require many more terms and be poorly informative. In this chapter, we develop an alternative treatment of the same model to obtain the harmonic emission yields for *high perturbation* levels.

8.1 Equivalent field and emission *"pockets"*

Equation 7.1 for the electric field of the harmonic in the near field may be treated differently for high perturbation levels, noting that the intensity interference pattern creates well-defined zones of high electric field amplitude, where HHG will predominantly occur (Fig. 6.2). At these locations, $\Delta\vec{k}\cdot\vec{r} - \Delta\omega t = 0[2\pi]$ and remains close to zero. These regions get narrower with increasing α, leading to very thin zones of emission, which we will refer to as "emission pockets". Around these values, the space-

dependent terms that enter in the definition of the local angular frequency and wave-vector of the composite beam are stationary, and we can thus write the composite field (equation 6.2) in these pockets as

$$\tilde{E}_s(\vec{r},t) = (E_1 + E_2)\cdot e^{i\omega_s t - i\vec{k}_s\cdot\vec{r}}, \tag{8.1}$$

with

$$\begin{cases} \vec{k}_s = \vec{k}_1 + \frac{\alpha}{1+\alpha}\vec{\Delta k} = \frac{1}{1+\alpha}\vec{k}_1 + \frac{\alpha}{1+\alpha}\vec{k}_2 \\ \omega_s = \frac{1}{1+\alpha}\omega_1 + \frac{\alpha}{1+\alpha}\omega_2 = \frac{1+\eta\alpha}{1+\alpha}\omega_1. \end{cases} \tag{8.2}$$

The composite field is thus equivalent, at the locations of high intensities, to a monochromatic field of angular frequency and wave vector $(\omega_s, \vec{k}_s)$, with an amplitude equal to the sum of the two amplitudes. HHG radiation, which will be preferentially emitted perpendicular to this composite wavefront, is progressively shifted from $\vec{k}_1$ to $\vec{k}_2$ as α goes from 0 to ∞ (equation 8.2), and is favored towards the SFG side. We will proceed to derive the intensity distribution of the diffraction orders in the far field, in this regime. As already seen, the electric field of harmonic q in the near field reads as

$$E_q^{nf} \propto G\left[E_1 \cdot f_s(\alpha,\vec{r},t)\right]\cdot e^{iq_s\varphi_s(\vec{r},t)}\cdot e^{i\alpha_{at}E_1^2\cdot f_s^2(\vec{r})}. \tag{8.3}$$

The far field intensity distribution will be a spatial Fourier transform of this equation. We will now develop an analytical model to predict this intensity distribution.

8.1.1 Amplitude

The amplitude term of equation 8.3 is modelled as

$$\begin{aligned} G(E_1.f_s(\alpha,\vec{r},t)) &= E_1^{q_{\text{eff}}} f_s^{q_{\text{eff}}} \\ &\propto (1+\alpha^2+2\alpha\cos(\Delta\vec{k}\cdot\vec{r}-\Delta\omega t))^{q_{\text{eff}}/2}. \end{aligned} \tag{8.4}$$

Unfortunately this function does not have an easy Fourier transform. But it may be approximated by a Gaussian, at least for high enough α, as shown in Fig. 8.1. To identify the parameters of the corresponding Gaussian, we write equation 8.4 as

$$\begin{aligned} G(E_1.f_s(\alpha,\vec{r},t)) &\propto E_1^{q_{\mathbf{eff}}}(1+\alpha^2+2\alpha cos\varphi)^{q_{\text{eff}}/2} \\ &\simeq E_1^{q_{\mathbf{eff}}}(1+\alpha^2+2\alpha(1-\frac{\varphi^2}{2}))^{q_{\text{eff}}/2} \\ &\simeq E_1^{q_{\mathbf{eff}}}(1+\alpha)^{q_{\text{eff}}}(1-\frac{\alpha\varphi^2}{(1+\alpha)^2}\frac{q_{\text{eff}}}{2}) \end{aligned}$$

A Gaussian distribution along φ with a width $\delta\varphi$ is of the form

$$G(\varphi) = Ae^{-\frac{\varphi^2}{(\delta\varphi)^2}} \tag{8.5}$$

$$\simeq A(1-\frac{\varphi^2}{(\delta\varphi)^2}) \tag{8.6}$$

We thus replace $G(E_1.f_s(\alpha,\vec{r},t))$ with a Gaussian of the form

$$G(x) = (E_1+E_2)^{q_{\text{eff}}}\cdot e^{-\left(\frac{x}{\delta x}\right)^2} \tag{8.7}$$

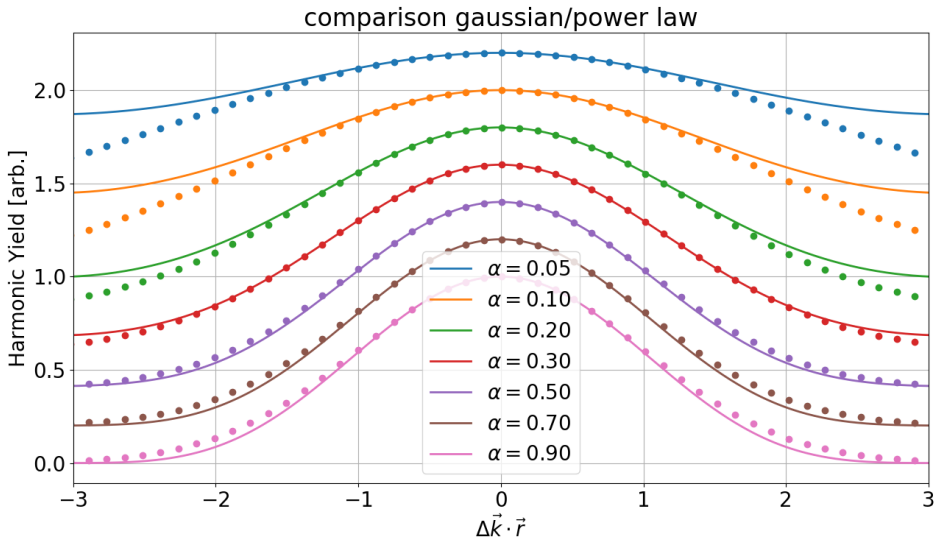

Figure 8.1: Comparison of a power law and a gaussian law for the harmonic yield, for different α's. Solid lines: $f_s^{q_{\text{eff}}} = (1+\alpha^2+2\alpha\cos(\Delta\vec{k}.\vec{r}))^{\frac{q_{\text{eff}}}{2}}$. Dots: $(1+\alpha)^{q_{\text{eff}}}\cdot e^{-(\Delta\vec{k}.\vec{r}/\delta x)^2}$; with $1/\delta x = q_{\text{eff}}\alpha/2(1+\alpha)^2$. The two are plotted over one period. We set $q_{\text{eff}} = 4$. The curves are offset and normalized for sake of visibility.

with

$$\frac{1}{(\delta x)^2} = \frac{q_{\text{eff}}}{2}\cdot\frac{\alpha}{(1+\alpha)^2}\Delta k^{\perp 2}. \tag{8.8}$$

The approximation is excellent for values of $\Delta\vec{k}\cdot\vec{r}$ between -1 and +1, and gets progressively better over the entire range with increasing α.

8.1.2 Atomic phase:

The atomic phase dependence goes as

$$e^{i\alpha_{at}E_1^2\cdot(1+\alpha^2+2\alpha cos(\varphi))} = e^{i\alpha_{at}E_1^2(1+\alpha)^2}\,e^{-i\alpha_{\text{at}}E_1^2\alpha\varphi^2} \tag{8.9}$$

$$\propto e^{-i\alpha I_1\alpha_{at}\Delta k^{\perp 2}x^2}. \tag{8.10}$$

It is once again a Gaussian function for which we will find an easy Fourier transform.

8.1.3 Spatial phase

The spatial phase term in the (xOy) plane of emitters, reads

$$e^{iq_s\varphi_s} = e^{iq_s\vec{k}_s\cdot\vec{r}} = e^{iq_sk_{s_\perp}\cdot x} = e^{iq_sk_{s_\perp}\cdot x} = e^{iq_s\frac{\alpha}{1+\alpha}\cdot\Delta k^{\perp}\cdot x}, \tag{8.11}$$

for which analytical Fourier transform also exists.

8.1.4 Total field:

Finally equation 8.3 reads,

$$E_q^{nf} \propto (E_1+E_2)^{q_{\text{eff}}} e^{(\frac{1}{\delta x^2}+i\alpha I_1 \alpha_{at}\Delta k^{\perp 2})x^2}\ e^{iq_s\varphi_s(\vec{r},t)}. \tag{8.12}$$

where we consider $\Delta\vec{k}\cdot\vec{r} \simeq \Delta k^{\perp}\cdot x$. It can be written as

$$E_q^{\text{nf}}(x) \propto \left[G\left(\frac{x}{\widetilde{\delta x}}\right)\cdot e^{iq_s\frac{\alpha}{1+\alpha}\cdot\Delta k^{\perp}\cdot x}\right] \otimes \text{Ш}(\frac{x}{a}). \tag{8.13}$$

The final convolution is a Dirac comb $\sum_n \delta(x-na)$ to account for the repetition of the emission "pockets" along the x-direction; $a = \lambda_1/\eta\sin\theta_0$. The far-field, at abscissa z, is a Fourier transform giving

$$E_q^{\text{ff}}(\theta) \propto \tilde{G}\left(\frac{\widetilde{\delta x}\pi}{\lambda_q}\left(\theta - \frac{q_s\alpha}{1+\alpha}\cdot\frac{\Delta k^{\perp}\lambda_q}{2\pi}\right)\right)\cdot \text{Ш}(\frac{a\theta}{\lambda_q}). \tag{8.14}$$

where θ is the angle of emission and $\lambda_q = \lambda_1/q$, the XUV wavelength of harmonic q. The overall Gaussian envelope now has a width $1/\widetilde{\delta x}$ with

$$\frac{1}{\widetilde{\delta x}^2} = \left(\Delta k^{\perp}\right)^2\cdot\left(q_{\text{eff}}\frac{\alpha}{(1+\alpha)^2} + i\alpha\cdot\alpha_{\text{at}}\cdot I_1\right). \tag{8.15}$$

The intensity profile in the far field is a series of gaussian peaks with each peak having an amplitude A(q, p, α), with an overall Gaussian envelope ($\tilde{G}$) peaking at an angle θ_{max}. The amplitude of each diffraction order for a given harmonic reads

$$A(q,p,\alpha) \propto \tilde{G}\left[\frac{\pi\widetilde{\delta x}\cdot q}{\lambda_1}\left(\theta_{q,p} - \frac{\eta\alpha}{1+\eta\alpha}\cdot\theta_0\right)\right] \tag{8.16}$$

$$\propto \tilde{G}\left[\frac{\pi\widetilde{\delta x}\cdot\eta\cdot\theta_0}{\lambda_1}\left(p - \frac{\alpha}{1+\alpha}q_s\right)\right]. \tag{8.17}$$

Dominant diffraction order

The dominant order of diffraction is determined by the peak position of the overall Gaussian envelope (see equation 8.14) given by,

$$\begin{aligned}\theta_{max} &= \frac{\alpha}{1+\alpha}\cdot q_s\cdot\frac{\Delta k^{\perp}}{k_q}\\ &= \frac{\alpha}{1+\alpha}\cdot\frac{q_1k_1}{k_s}\cdot\frac{\eta k_1\theta_0}{q_1k_1}\\ &= \frac{\alpha}{1+\alpha}\cdot\frac{k_1}{k_s}\cdot\eta\theta_0\\ &= \frac{\alpha}{1+\eta\alpha}\eta\theta_0\end{aligned} \tag{8.18}$$

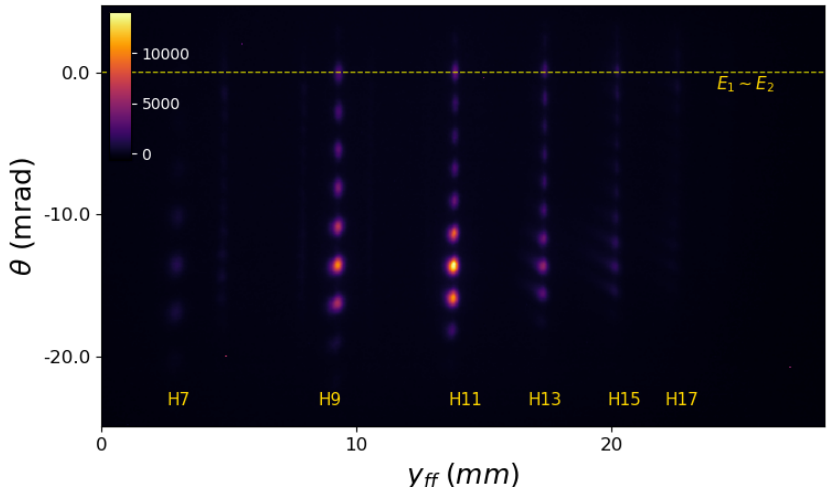

Figure 8.2: Far field image observed on the MCP (X-Y plane) for the non perturbative regime. The dashed-yellow line marks the position of the zeroth order of diffraction, i.e, the spectrum generated by the fundamental alone along the $\theta = 0$ axis where θ is the emission angle with respect to the z-axis.

We observe that it is independent of the harmonic order, while the spacing between the diffraction orders is inversely proportional to q (see Appendix A). In other words, if it is the diffraction order p that dominates for harmonic q, it will be the order $2p$ for harmonic $2q$, if it exists.

In vectorial form, this equation tells us that the dominant order shows at $\vec{k}_q$, whose component vectors read,

$$k_q^{\perp} = qk_1\theta_{max} = \frac{q\alpha}{1+\eta\alpha}\cdot\eta\theta_0 k_1 = \frac{q\alpha}{1+\eta\alpha}\cdot k_2^{\perp} \tag{8.19}$$

and

$$\begin{aligned} k_q^{\parallel} &\simeq qk_1 \\ &= \frac{q\alpha}{1+\eta\alpha}\cdot k_2^{\parallel} - \frac{q\alpha}{1+\eta\alpha}\cdot k_2^{\parallel} + qk_1 \\ &= \frac{q\alpha}{1+\eta\alpha}\cdot k_2^{\parallel} + qk_1 - \frac{q\alpha}{1+\eta\alpha}\cdot\eta k_1 \\ &= q\frac{1}{1+\eta\alpha}\cdot k_1 + \frac{q\alpha}{1+\eta\alpha}\cdot k_2^{\parallel}. \end{aligned} \tag{8.20}$$

i.e.

$$\vec{k}_q = \frac{1}{1+\eta\alpha}\cdot q\vec{k}_1 + \frac{\alpha}{1+\eta\alpha}\cdot q\vec{k}_2 \tag{8.21}$$

We note that it corresponds to

$$\vec{k}_q = n_1\vec{k}_1 + n_2\vec{k}_2 \tag{8.22}$$

with $n_1 = \frac{q}{1+\eta\alpha}$ and $n_2 = \frac{q\eta\alpha}{1+\eta\alpha}$, the number of photons absorbed from each beam. For identical frequencies, it reduces to the probabilistic prediction that $q\cdot 1/(1+\alpha)$ photons should be absorbed from

the first beam, $q \cdot \alpha/(1+\alpha)$ from the second. Also, for $\alpha = 1$ (resp. 0 and ∞), we get the dominant order as the central one as observed in [43] (resp. the first one, the last one, as predicted by the perturbative approach).

In conclusion, the analytical model anticipates each harmonic to show a series of diffraction orders below a global envelope. The dominant order of diffraction and the amplitude distribution of each diffraction order depends on α. All the diffraction orders are shifted even further towards the SFG side as α gets stronger.

8.2 Experimental results and analysis

8.2.1 Experimental results

To access this non perturbative regime by experiment, we performed the same experimental scans as in section 7.3, but spanning a broader range of α values. The far-field image is shown in Fig. 8.2. Here, the optical set-up was aligned such that the main beam pointing upwards and the second beam pointing downwards meet at the focus of the gas jet, making an angle of approximately 28 mrad with each other. We see the 0^{th} order of diffraction at $\theta = 0$ (where the harmonic would fall if the main beam alone was used to generate) and many more positive orders of diffraction coming up along the vertical axis. In this case, SFG is obviously favoured over DFG as predicted by the active grating model. The experimental yields of each order of diffraction for harmonics 9, 11, 13 and 15 are reported in Fig. 8.3. The spacing between the diffraction orders decrease with the harmonic number, as expected (see Appendix A). We could observe almost the full set of diffraction orders (9 diffraction orders for H 11). In the contour maps of the top panel, we note that increasing the value of α, different orders of diffraction light up and each order reaches a maximum at a given value of α (α_{max}) and eventually fade out. The bottom panels show the intensity distribution of each diffraction order against α. The experimental data (marker-points) for each diffraction order p is fitted with the numerical model (equation 8.17).

8.2.2 Treatment of experimental data in the non-perturbative regime

The yield of each diffraction order is predicted to follow the formula in equation 8.17. It can be simplified as

$$I(q_1, p, \alpha) \propto \tilde{G}^2 \left[\left(p - \frac{\alpha}{1+\alpha} q_s \right) / \sigma^2 \right] \text{ where,} \tag{8.23}$$

$$\frac{1}{\sigma^2} = \frac{q_{\text{eff}}}{8\alpha} \frac{1}{\frac{q_{\text{eff}}^2}{4(1+\alpha)^2} + \alpha_{at}^2 I_1^2 (1+\alpha)^2}. \tag{8.24}$$

Using equation 8.23, we can fit our experimental data to retrieve the constants q_{eff} and α_{at}. But first, we will try to get these values from theory. The basis of our model is the theoretical response which reads

$$d_q(x,t) \propto E^{q_{\text{eff}}} e^{i \alpha_{at}^{q,j} I(x,t)}, \tag{8.25}$$

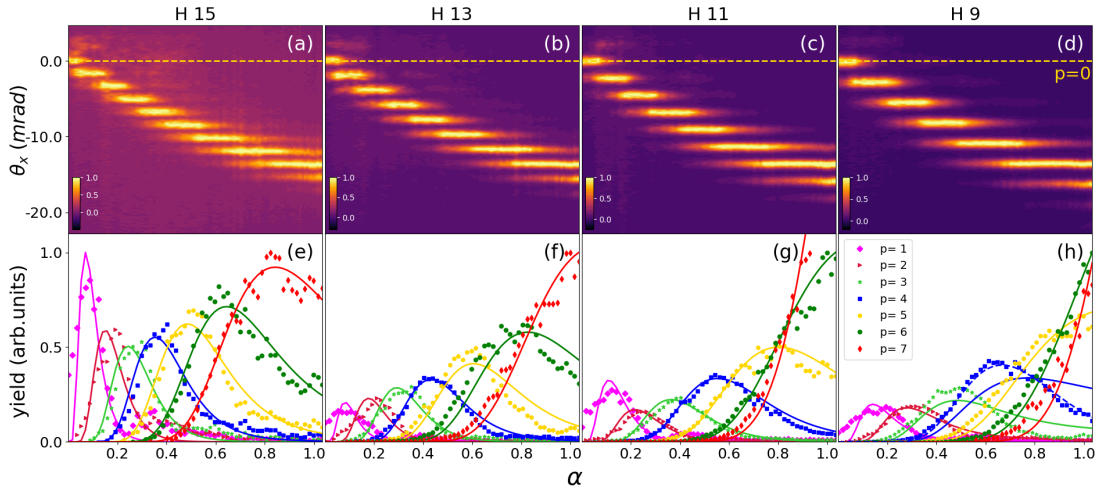

Figure 8.3: The experimental data for harmonics 15,13,11 and 9 for high perturbation levels are presented. The top panels(a-d) show the position and presence/absence of each order of diffraction as α increases. The bottom panels(e-h) show emission yields of different diffraction orders of the corresponding harmonic order. The dark lines are the fits of equation 8.17 on the experimental data. For H9, the blue dashed line is the same equation fitted with p=3.6.

where q_{eff} and α_{at} are constants for a given harmonic and trajectory and E is the amplitude of the driving field. We can also extract the q_{eff} values theoretically from the numerical solution of time-dependent Schrödinger equation (TDSE) [99] for argon atom in the Single Active Electron Approximation (SAE) [100] . Figure 8.4 reports the calculated values of the dipole for the driving laser intensity range 0.1 to $2.5{\cdot}10^{14} W/cm^2$ for four different harmonics in log-log scale, computed by Thierry Auguste using TDSE. q_{eff} is determined by the slope coefficient of a linear fit to this data. We calculate the slope for different ranges of intensity of the driving laser. The value of q_{eff} depends on whether the harmonic falls in the plateau or the cut-off region. We get q_{eff} values that fall between 1.0 and 10.3 The oscillations in the data that arise from the interference of long and short trajectories causes the observed irregularity. However the theoretical values for qeff that we get are within the range reported in the literature [101]. Fig. 8.5.(a) is the plot of the atomic phase for harmonic 19 generated in Argon at different driving intensities adapted from [92]. According to this work, for the driving intensity used in our experiment, $\alpha_{at} \cdot I_1$ should fall between 0 and -1.5. It is also confirmed by TDSE theoretical calculations done by our group, as shown in Fig. 8.5.(b).

We now proceed to retrieve q_{eff} and α_{at} from the experimental data. For a given diffraction order p, $I_{q,p}$ is governed by a leading amplitude term and σ which itself depends on q_{eff} and $\alpha_{at} \cdot I_1$. The two latter parameters being a constant for all diffraction orders, we initially tried to fit the data for all diffraction orders with the same values of q_{eff} and α_{at}, but individual amplitudes. This sets a constraint of nine fitting parameters for a set of seven nonlinear curves of 60 points each. Despite

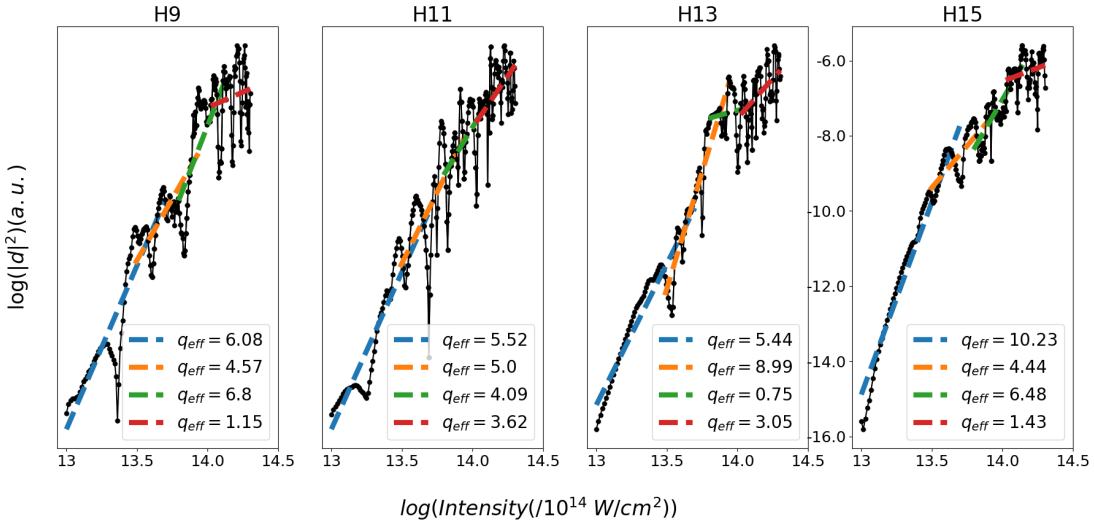

Figure 8.4: Markers are theoretical data from TDSE calculations in Argon gas. The dashed lines are a linear fits of the data in log-log scale for various intensity ranges 0.1 to $2.5{\cdot}10^{14} W/cm^2$. Its slope is the effective nonlinear order q_{eff} displayed in the insets.

our efforts to constraint the fits, we could not get them to converge with a reasonably small residual error for all diffraction orders of a given harmonic at once.

The bell shaped curves are firstly ruled by the standard deviation of the Gaussian, σ, which is made of two terms (see equation 8.24). Given the numerical values given above, we note that for low enough α, $\frac{q_{\text{eff}}^2}{4(1+\alpha)^2} \gg \alpha_{at}^2 I_1^2 (1+\alpha)^2$. For instance, for $\alpha = 0.7$, the first term is about 2.16 and the second 0.1 considering reasonable values of 3.5 and 0.2 for q_{eff} and $\alpha_{at} I_1$ respectively. Since this second term does not play a role for the lowest orders of diffraction, it is not constraining the fit well enough, explaining the poor convergence of the overall procedure.

However, this observation offers a mitigation step. We can harness it to split the procedure in two steps. A first set of curves for which the second term does not play a role is isolated, and we fit these curves with the first term only. In practice, we selected a few orders of p whose α_{max} falls between 0.2 and 0.7 (see Fig. 8.6). While we have just seen that for $\alpha = 0.7$ this approximation is surely valid, the lower bound $\alpha = 0.2$ is an estimation of the domain of validity of the model. We thus did a global fitting of these selected orders by forcing α at to 0, and retained the outcome on q_{eff}. In the second step, using q_{eff} obtained from the above fit, we fit the data once again, but now with the full equation 8.23. The amplitude, diffraction order, p, and α_{at} are the free parameters of this second fit. This "handmade" procedure would be equivalent to using a fitting model which would put more weight on the first few diffraction orders to find q_{eff}.

Fig. 8.7 shows the result of these fits. Thus, for each harmonic, we fit the data for all diffraction

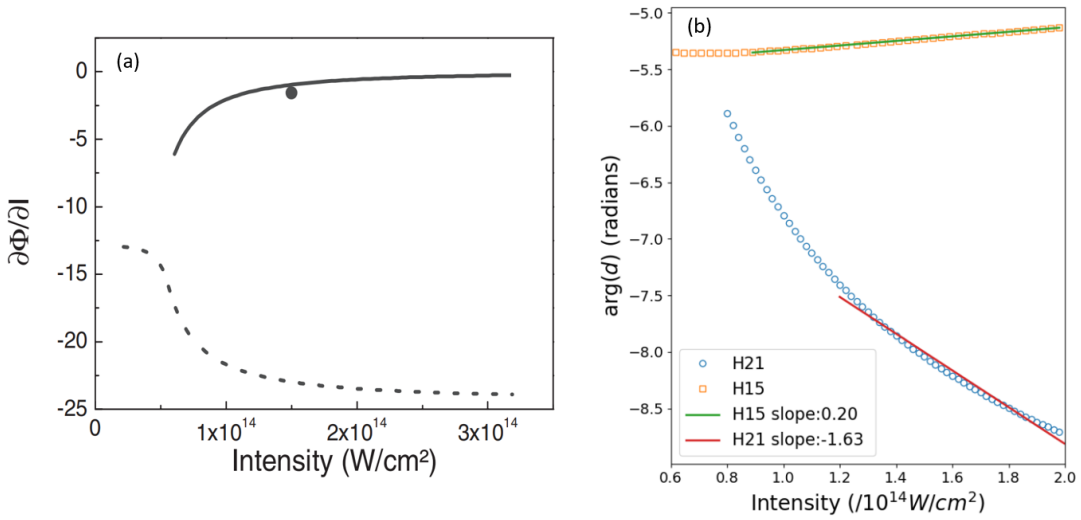

Figure 8.5: Atomic Phase: (a) Variation of the derivative of $\varphi_{at}^{q,j}$ with the laser intensity I for the harmonic 19 in argon (adapted from [92]).The solid and dashed lines refer to the first (shortest) and second (next shortest) trajectories calculated using the strong field approximation. The solid circle is experimental data extracted from XFROG measurements. (b) TDSE calculations showing the variation of $\alpha_{at}^{q,j}$ with the laser intensity I for harmonics 15 and 21 in argon.

orders with the same values of q_{eff} and $\alpha_{at} \cdot I_1$, but individual amplitudes. Using the above procedure, for the atomic phase, we found $\alpha_{at} \cdot I = 0.55$, 0.30, 0.42 and 0.68 respectively for H9 to H15. While SFA computations, for $I = 1 \cdot 10^{14}$ W/cm^2, predict 0.2 for H15 (see Fig. 8.5.(b)). As for q_{eff}, the results of the global fitting are displayed in Fig 8.8.(e), together with the determination from TDSE computations. The shaded area denotes the range within which the q_{eff} values obtained from theoretical calculations falls and the markers are the q_{eff} values extracted from the experimental data. We find a good agreement for all the harmonics, strengthening our understanding of NCHHG in this regime. The experimental confirmation of these values is a first application of this new spectroscopy.

In conclusion, despite a strong constraint on the number of free parameters available for fitting, we find a remarkable agreement between the model and the experimental values for the whole perturbation range, thus validating our model. The agreement between our model and experiment is excellent for all diffraction orders and harmonics except for p=3 and p=4 of harmonic 9.

8.3 Full quantum model of HHG in an active grating

To provide a quantitative model as a support to our analytical model and experimental results, full numerical simulations based on the solution of the non adiabatic, three-dimensional (3D) paraxial wave equation (PWE) was performed in Cartesian geometry by Thierry Auguste. The source term in the PWE is given by the solution of the Schrödinger equation in the strong field approximation

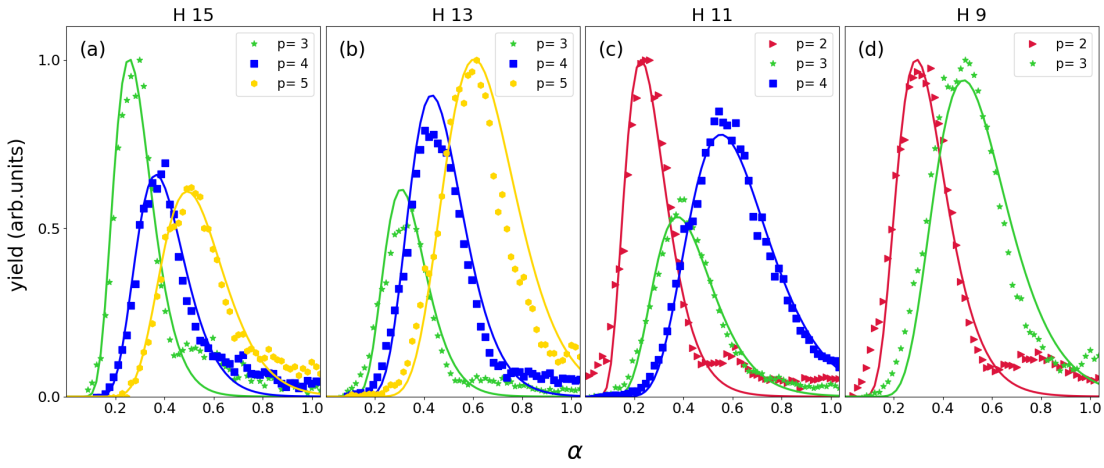

Figure 8.6: Fitting the experimental data with the analytical model to find out q_{eff} values.

(SFA)[7]. We consider two Gaussian beams of 100 μm waist at focus, i.e., 39 mm Rayleigh range. The temporal intensity profiles have sin^4 shapes of 50 fs full-width at half-maximum. Both beams are focused in the middle of a 100μm thin slab of argon gas, where they overlap spatially and temporally. The two beams cross each other with a 20 mrad angle. The total peak intensity at focus is $1.5 \cdot 10^{14}$ W/cm^2, whatever α, and the density of atoms is $3.0 \cdot 10^{17}$atoms/cm^3. The results of the simulation are presented in Fig. 8.8. Fig. 8.8.(a) is the far field image on the detector. Fig. 8.8.(b) is the contour map of the yields of the diffraction orders of harmonic 15 against α, which falls in the plateau region. Fig. 8.8.(d) is the corresponding intensity distribution of these orders. We retrieve the typical bell-shaped curves for each diffraction order yield against α (Fig 8.8.(d)). The abscissa of their peak (α_{max}) also agrees remarkably well with the experimental data and the analytical model (Fig. 8.8.(c)). The most obvious discrepancy between Fig. 8.8.(b) and Fig. 8.3 is the overall decrease of the peak amplitude as p increases. This is mostly due to an overall increase of the total intensity, as the scan is carried out by increasing I_2, without concomitantly decreasing I_1. The corresponding experimental graphs for constant intensity is estimated in Fig. 8.8.(f), where a normalization factor $\propto (1+\alpha)^{-q_{\text{eff}}}$ is applied to the data set as detailed in appendix C, with the value of q_{eff} determined above. This effect receives a simple interpretation: as α increases, the generating pockets get narrower, reducing the overall generation volume and decreasing the yield, which is not compensated by an intensity increase, as in the raw experimental data.

8.4 Conclusion and discussion

In the non-perturbative regime, there is an excellent agreement between the analytical model, experiment and theoretical calculation. In addition to predicting the far field pattern and the intensity distribution of each diffraction order of a given harmonic, we are able to extract the values of the q_{eff}

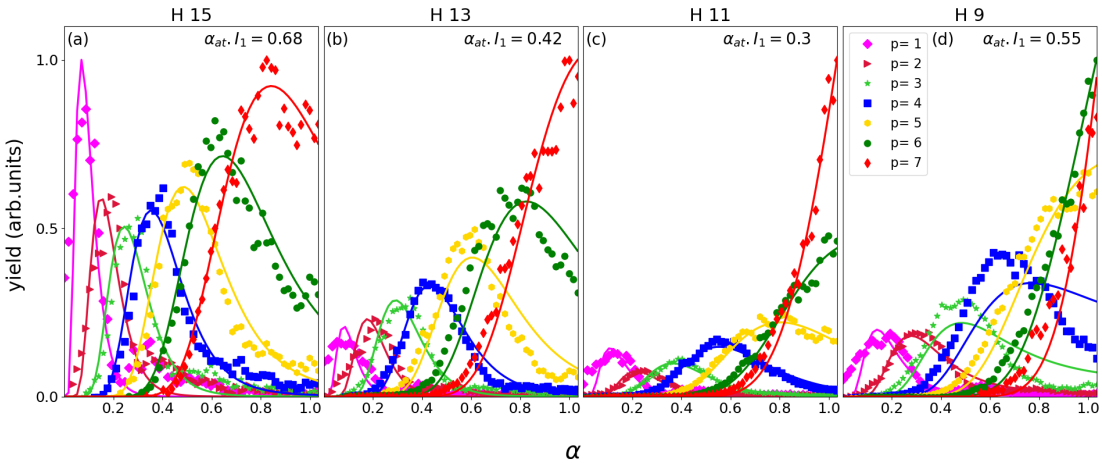

Figure 8.7: Fitting the experimental data with the analytical model to find out α_{at} values.

constant and atomic phase from our experimental data. Such good results may seem surprising given the rough approximations made. So, to conclude this part, we first discuss the validity range of this approximation before elaborating on possible spectroscopic applications.

8.4.1 Domain of the validity of the active grating model

The model relies on a strong spatial modulation of the laser intensity, sufficient to form "pockets" where HHG occurs and complementary zones where it is killed. To estimate the range of αs over which the model is valid, let us arbitrarily consider a threshold intensity, I_{thld} at which HHG turns from off to on. The high nonlinearity of the process makes this model not as crude as it may first seem: even if not strictly zero, the zones of lower intensity are a lot less intense than the zones of high intensity.

The intensity reads

$$I_s(\alpha, \vec{r}, t) = \left[1 + \alpha^2 + 2\alpha \cos\left(\Delta\vec{k}\cdot\vec{r} - \Delta\omega t\right)\right] I_1 \tag{8.26}$$

whose minimum is $(1-\alpha)^2 I_1$, maximum is $(1+\alpha)^2 I_1$ and mean value is I_1. To be within the range of validity of the model, we thus require that

$$\begin{cases} (1-\alpha)^2 I_1 < I_{thld} \\ (1+\alpha)^2 I_1 > I_{thld} \end{cases} \tag{8.27}$$

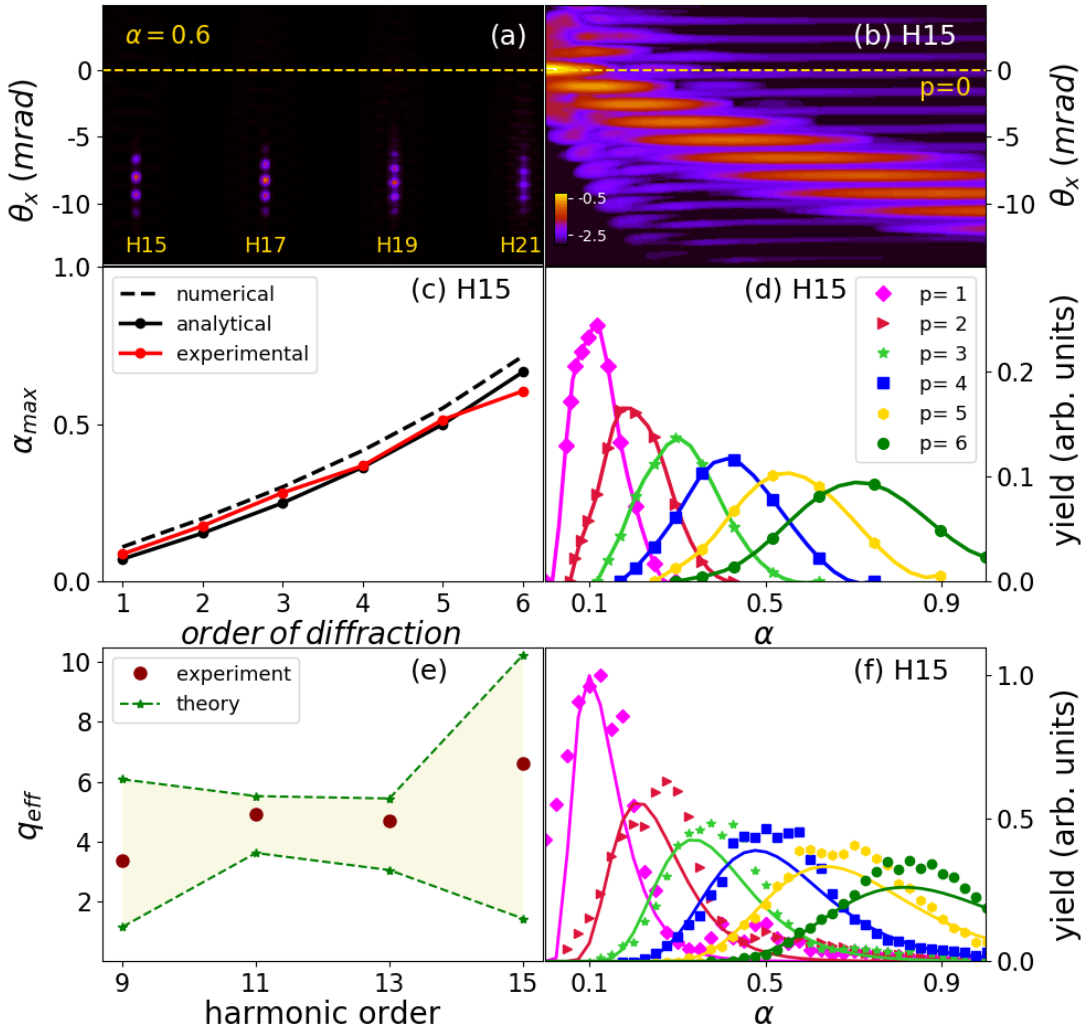

Figure 8.8: TDSE calculations for H15 showing (a) the far field image as expected on the detector for α =0.6, (b) the contour map of the yields of the diffraction orders as a function of α, (c) their α_{max} values and (d) the yield distribution. (e) is the comparison of q_{eff} values obtained from theory and experiment while (f) is the experimentally obtained yields of the diffraction orders for H15; after correcting the data in Fig. 8.3.(e) by $(1+\alpha)^{-q_{\text{eff}}}$, to account for the varying intensity at focus during the experiment.

i.e.

$$\begin{cases} (1-\alpha) < \sqrt{\dfrac{I_{thld}}{I_1}} & \text{if } \alpha < 1 \\ (\alpha-1) < \sqrt{\dfrac{I_{thld}}{I_1}} & \text{if } \alpha > 1 \\ (1+\alpha) > \sqrt{\dfrac{I_{thld}}{I_1}} \end{cases} \tag{8.28}$$

$$\begin{cases} \alpha > 1 - \sqrt{\dfrac{I_{thld}}{I_1}} & \text{if } \alpha < 1 \\ \alpha < 1 + \sqrt{\dfrac{I_{thld}}{I_1}} & \text{if } \alpha > 1 \\ \alpha > \sqrt{\dfrac{I_{thld}}{I_1}} - 1 \end{cases} \tag{8.29}$$

In general, HHG already occurs with a single beam, which corresponds to $I_1 > I_{thld}$ and the last condition is always enforced for $\alpha > 0$. We are thus left with the condition

$$1 - \sqrt{\frac{I_{thld}}{I_1}} < \alpha < 1 + \sqrt{\frac{I_{thld}}{I_1}} \tag{8.30}$$

To give an (arbitrary) figure, if the experiment is started at $I_1 = 1.25\, I_{thld}$, the range of validity is $0.1 < \alpha < 1.9$. This crude estimate indicates that the model is at least valid over the majority of diffraction peaks if the starting intensity is not too high. This is a strong support of the large validity range of our model and of its predictive performances.

8.4.2 Spectroscopic applications

Another interesting observation from the experimental data was the specific case of orders of diffraction p=3 and p=4 of H9. We could not get the fitting procedure to converge simultaneously for these two diffraction orders and the other ones. However, leaving the diffraction order p as a free fitting parameter, we may recover an excellent agreement (see for instance, for the fourth diffraction order, the dashed line in Fig. 8.3 for H9, which converged to p=3.6 instead of p=4). In other words, this diffraction order peaks earlier than the expected value of equation 8.18. This observation can be interpreted with the input of section 7.4. By fitting the experimental data with the numerical model (see Fig. 7.6), we showed that the initial rise of diffraction order p was ruled by the absorption of p photons from the second beam, while at the peak, the dominant process involved p+2 photons, with an extra absorption and stimulated emission. Indeed, for H9 in Argon and a 800 nm driving laser, the first process explores a spectrocopically flat region about 13.9 eV from the ground state, while the second process goes through levels about 15.5 eV from the ground state, right below the ionization potential of this gas, and exactly where very structured absorption spectra are present [102]. We can thus anticipate that for this harmonic, the peaks of the yield curves will be highly dependent on the precise resonances hit by the process. The fact that not all peaks are displaced is probably a signature

of the ponderomotive shifts of the levels as α is increased. Indeed, in our experimental arrangement, α increases concomitantly with the overall intensity: to give an order of magnitude, a change $\delta\alpha = 0.2$ about $\alpha = 0.5$, with an intensity of the first beam of $1 \cdot 10^{14}\mathrm{W/cm}^2$ corresponds to a ponderomotive shift of about 1 eV, enough to scan the whole Rydberg series of Argon. More precise TDSE computations by our collaborators at Laboratoire de Chimie Physique-Matière et Rayonnement (LCPMR) are under progress to support this interpretation. If successful, this finding would provide a new strong field spectroscopic approach, able to probe usually inaccessible levels thanks to the ability of the technique to use a very large span of perturbing intensities able to shift the levels by several eVs. It is also an approach which avoids the strong alteration of phase matching in the absorbing regions, since the final XUV photon is still emitted at its original energy.

Part IV

Phase Matching Effects in Non Collinear High Harmonic Generation

CHAPTER 9

State-of-the-art

As already detailed in Part II of this thesis, phase matching is crucial in high harmonic generation. Typically, the understanding of this process is simplified by considering phase-matching effects along the field propagation axis, defining a longitudinal coherence length. The role of phase matching in the transverse direction in the case of conventional single beam HHG has also been studied in this paper by Garcia et al. [103].

The investigations on phase matching rely on full computations, which are either numerically expensive, or use very coarse approximations. In brief, the individual response of atoms in the gas target is highly dependent on the local electric field, which varies in time as the pulse propagates, and in space, as the beam is focused. Also, as the pulse propagates, the medium is evolving. The densities of electrons and ions increase at each half cycle and the density of neutrals decrease accordingly. This builds an inhomogeneous complex index profile of the medium. In addition, even before the pulse ionizes it, the medium is not homogeneous and shows a density profile. All these aspects should be taken into account for a quantitative description of HHG. However, in doing so, the physics get buried in the numerical results. This justifies the development of simplified models such as the "Constant model"[10]. In this chapter, we will introduce this model in two ways: (i) the "standard" approach using a continuous variable, and (ii) a discretized version that we developed and will be more suited to NCHHG. Finally, we will conclude this part by recalling the origin of a specific geometrical phase matching factor that was identified by Heyl et al.[83] in the case of NCHHG.

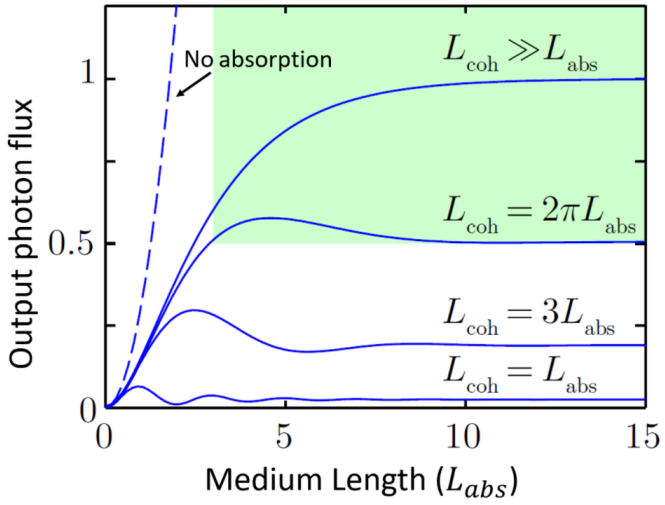

Figure 9.1: Absorption limited generation: harmonic signal as a function of the length of the non-linear medium, normalized to the maximum absorption limited signal obtained for phase-matched generation. The solid lines represent the harmonic signal for four different values of L_{coh} including the optimum case of absorption-limited generation with $\Delta k \simeq 0$ ($L_{\text{coh}} >> L_{\text{abs}}$). The dashed line displays a quadratic signal growth with medium length, corresponding to absorption-free generation and $\Delta k \simeq 0$. The green area indicates the conditions $L_{\text{med}} > 3L_{\text{abs}}$ and $L_{\text{coh}} > 5L_{\text{abs}}$. Adapted from [61].

9.1 Phase matching in collinear geometry

9.1.1 One dimensional model of phase matching with continuous variables

Generally speaking, phase matching involves dealing with the build up of a macroscopic signal, out of individual emitters spread in the generation medium. It particularly emphasizes the role of the optical index. Unlike the case of standard non linear optical phenomena like second and third harmonic generation (SHG and THG), where the imaginary part of these indices which rules absorption generally remains low, it is not the case for XUV light. This absorption is characterised by the absorption coefficient (k^{im}), leading to an exponential decay of the field amplitude during propagation along the z-axis. We detail the existing 1D model to calculate the harmonic flux, following the approach of [10, 104, 105, 61], which includes this absorption on an equal footing with the optical index.

Proceeding as in [106], let us consider a static medium of length L_{med} and coherently sum the response over all single atom emitters. The resulting electric field of a given harmonic q can be written as

$$E_q = \int_0^{L_{\text{med}}} A\rho_0 \exp\left(\mathrm{i}\left[\Delta k + \mathrm{i}k^{\text{im}}\right]\left[L_{\text{med}} - z\right]\right) \mathrm{d}z, \tag{9.1}$$

where A is the amplitude of the generated field (amplitude of single-atom response), ρ_0 is the number density of atoms, and L_{med} is the length of the generation medium. Δk is the phase mismatch and k^{im} is the absorption coefficient of the medium. As mentioned in the introduction above, all

these parameters should be time and space dependent. A coarse simplification is to consider them constant, and the integration then leads to

$$E_q = A\rho_0 \left[\frac{\exp\left(\mathrm{i}\left[\Delta k + \mathrm{i}k^{\mathrm{im}}\right][L_{\mathrm{med}} - z]\right)}{-i\left[\Delta k + i\,k^{\mathrm{im}}\right]} \right]_0^{L_{\mathrm{med}}}. \tag{9.2}$$

After some algebra, the modulus square $I_q = \left|E_q\right|^2$ can be obtained as

$$I_q = 2A_q^2\rho_0^2 \exp\left(-k^{\mathrm{im}}L_{\mathrm{med}}\right) \frac{\cosh\left(k^{\mathrm{im}}L_{\mathrm{med}}\right) - \cos\left(\Delta k L_{\mathrm{med}}\right)}{\Delta k^2 + k^{\mathrm{im}^2}} \tag{9.3}$$

Before proceeding to derive the final formula for the intensity, let us deviate a bit to understand the definition of the wave vector in terms of the coherence length and absorption length. The wave vector of a radiation with wavelength λ, is written as

$$k(\lambda) = n(\lambda)\frac{\omega}{c}, \tag{9.4}$$

where c is the speed of light in vacuum and n, the refractive index of the medium. Since n is complex valued,

$$k(\lambda) = \underbrace{n(\lambda)\frac{\omega}{c}}_{k^{\mathrm{real}}} + i\underbrace{n^{\mathrm{im}}(\lambda)\frac{\omega}{c}}_{k^{\mathrm{im}}}. \tag{9.5}$$

Consequently, the phase mismatch that arises due to dependence on the refractive index of the wavelength of the radiation, will be

$$\Delta k_q = \Delta {k_q}^{\mathrm{real}} + i\Delta {k_q}^{\mathrm{im}}. \tag{9.6}$$

The real part of the refractive index is responsible for phase mismatch between the fundamental and the XUV. The propagation length over which the fundamental and the harmonic get dephased by π, i.e, the propagation distance between two locations of harmonic emission that are exactly out of phase is defined as the coherence length, L_{coh}. Thus we can write

$$\Delta k_q^{\mathrm{real}} = \pi / L_{\mathrm{coh}} \tag{9.7}$$

And from the definition of absorption length (L_{abs}) (see section 3.1.5),

$$k^{\mathrm{im}} = \frac{1}{2L_{\mathrm{abs}}} \tag{9.8}$$

giving,

$$\Delta k_q^{\mathrm{im}} = \frac{1}{2}\left[\frac{q}{L_{\mathrm{abs}}(\lambda_1)} - \frac{1}{L_{\mathrm{abs}}(\lambda_q)}\right] \tag{9.9}$$

Due to very high absorption length of the infrared in gases, the first term in equation (9.9) is neglected. Using equations (9.7) and (9.9), the phase mismatch is often expressed in terms of L_{coh} and L_{abs} as

$$\Delta k_q = \frac{\pi}{L_{coh}(\lambda_q)} + i\frac{1}{2L_{abs}(\lambda_q)}. \tag{9.10}$$

Using these definitions, and that $\cosh(x) = [1+\exp(-2x)]/[2\exp(-x)]$, one can modify equation 9.3 to obtain the equivalent expression of Constant et al. [10].

$$I_q = \rho_0^2 A_q^2 \frac{4L_{\text{abs}}^2}{1+4\pi^2 L_{\text{abs}}^2/L_{\text{coh}}^2}\left[1+\exp\left(-\frac{L_{\text{med}}}{L_{\text{abs}}}\right)-2\cos\left(\frac{\pi L_{\text{med}}}{L_{\text{coh}}}\right)\exp\left(-\frac{L_{\text{med}}}{2L_{\text{abs}}}\right)\right] \tag{9.11}$$

where $\rho_0 = 2k^{\text{im}}/\sigma = 1/(\sigma L_{\text{abs}})$ (σ being the photoionization cross section). Fig. 9.1 shows the evolution of the output photon flux as a function of medium length given by the above equation. It clearly illustrates the well known criteria for optimization conditions (assuming an unlimited medium length is realizable) of:

$$L_{\text{med}} > 3L_{\text{abs}} \text{ and,} \tag{9.12}$$

$$L_{\text{coh}} > 5L_{\text{abs}}. \tag{9.13}$$

Although the approximations are very crude, this 1D model works remarkably well to drive the design of efficient HHG sources [11, 107]. It was extended to three dimensional medium with cylindrical symmetry as well. Again, this predictive model assumes constant values of all parameters for the integration in equation 9.1 to be performed. In particular, the intensity is considered to be constant in the transverse plane. This model has been extended to 3D with cylindrical symmetry as well. However, in the case of NCHHG, the inhomogenities along the transverse axis of the driving field are precisely what rules the diffraction orders, and this model would become rapidly inoperative. However, it inspired us to develop a novel version of it, taking into account the transverse inhomogeneities. It relies on a change of perspective that we will first introduce through the case of a single beam (section 9.1.2). This new approach will later form the building block of our analysis of phasematching effects in NCHHG in 2D.

9.1.2 Simplified one dimensional discretized model of phase matching

This section is adapted, with permission, from this lecture [56] on HHG and attosecond light pulses by Thierry Ruchon. We make two simplifications in the following model,

- First, we consider a spatially large driving pulse, infinitely long in time, and having all of its half cycles of equal intensity in time and space in the generating medium, i.e. a plane monochromatic wave.
- Second, we consider that the ionization of the medium does not change with time. [1]

These two assumptions are the same as in the previous section. These hypotheses allow us to define indices of refraction for both the XUV and IR field that have neither spatial nor time dependence. It makes the model analytically tractable, while still giving insights into the relevant parameters.

[1] This is a very coarse approximation: once ionized, the medium will not be refreshed by any gas flow during the time a regular femtosecond light pulse passes in the medium. And consequently, every half cycle, the ionization of the medium is increasing.

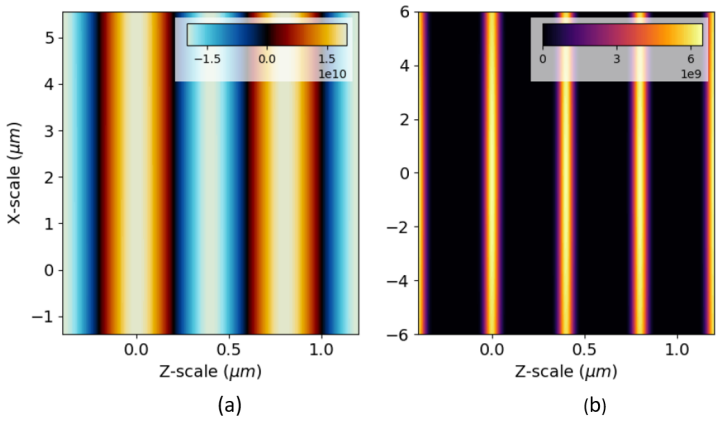

Figure 9.2: (a) Electric field of the driving laser for the phase matching model. The beam is propagating along z. The peak electric field is $4 \cdot 10^{10} V/m$, corresponding to half the saturation field for argon. (b) Corresponding values of the ADK ionization rates in argon. Figure adapted from here [56].

The analytical formula for a plane monochromatic laser electric field, propagating along z direction reads as

$$E(\vec{r}) = E_0 e^{i\omega_1 t - \vec{k}_1 \cdot \vec{r}}, \tag{9.14}$$

at location $\vec{r}$ and time t, ω_1 and $\vec{k}_1$ being its angular frequency and wave vector respectively. Fig. 9.2.(a) is the colour map of the electric field. It forms a series of large, positive and negative stripes. Applying the ADK formula to these stripes yields (Fig. 9.2.(b)) a series of very narrow stripes centered about the extrema of the field. The center of stripe n, corresponding to

$$\omega_1 t - \vec{k}_1 \cdot \vec{r} = n\pi,$$

is located at

$$\vec{r}_n = \left(n\frac{\lambda_1}{2} + ct \right) \cdot \hat{z}. \tag{9.15}$$

Note that though we present the regions of ionizations as stripes, the analysis is restricted to 1D. Every even (resp. odd) n corresponds to a positive (resp. negative) extremum of the field. HHG will occur around these regions. From the quantum mechanical model introduced in chapter 2, we write the electric field of the XUV radiation (near field) emitted with an angular frequency $\omega_q (= q\omega_1)$ from a given location ($\vec{r}$) within stripe n as

$$e^{nf}_{\text{xuv}}(\vec{r}, t) \propto A_q(\vec{r})\, e^{iq(\omega_1 t - \vec{k}_1 \cdot \vec{r})}, \tag{9.16}$$

with $A_q(\vec{r})$ containing the non linear response of the medium. For instance, the SFA approach using the dipole model predicts the amplitude of the electric field of harmonic q to simply vary as $A_q(\vec{r}) \propto E(\vec{r})^{q_{\text{eff}}}$, which can be approximated as a Gaussian function ($G(\vec{r})$) for high enough q_{eff} (see section 8.1.1). We consider all the stripes to be equivalent, thus writing the $\vec{r}$ dependent response of stripe n as $[G(\vec{r}) \otimes \delta(\vec{r} - \vec{r}_n)]$. After propagating a distance $\vec{r}_s$ to the screen and accumulating a corresponding

phase, the elementary electric field from stripe n reads,

$$e_{\text{xuv}}^{nf}(\vec{r},t) = [G(\vec{r}) \otimes \delta(\vec{r}-\vec{r}_n)] \cdot e^{iq\left(\omega_1 t - \vec{k}_1\cdot\vec{r}\right)} \cdot e^{-i\vec{k}_q\cdot(\vec{r}_s-\vec{r})} \tag{9.17}$$

The first exponential just states that the phase of the outgoing radiation is q times the phase of the incoming driving radiation, like in any non linear optical phenomenon. The second exponential is simply the phase accumulated by the XUV radiation from $\vec{r}$ towards the observation point at $\vec{r}_s$. With a convolution, the G function is translated to the right position, $\vec{r}_n$, within a stripe, concentrated around the extrema of the field. Thus, equation 9.17 can be rewritten as

$$\begin{aligned} e_{\text{xuv}}^{nf}(\vec{r},t) &= e^{i\left(\omega_q t - \vec{k}_q\cdot\vec{r}_s\right)} \cdot e^{i\left(\vec{k}_q - q\vec{k}_1\right)\cdot\vec{r}} \cdot G(\vec{r}-\vec{r}_n) \\ &= e^{i\left(\omega_q t - \vec{k}_q\cdot\vec{r}_s\right)} \cdot e^{-i\Delta\vec{k}_q\cdot\vec{r}} \cdot G(\vec{r}-\vec{r}_n), \end{aligned} \tag{9.18}$$

to introduce the phase mismatch,

$$\Delta\vec{k}_q = q\vec{k}_1 - \vec{k}_q. \tag{9.19}$$

Now, to get the contribution from all atoms within a given stripe n to the far-field, we introduce the atomic density ρ, supposed to be homogeneous and sum over space:

$$E_n\left(\Delta\vec{k}_q\right) = e^{i\left(\omega_q t - \vec{k}_q\cdot\vec{r}_s\right)} \cdot \iiint \rho\, d^3\vec{r}\, e^{-i\Delta\vec{k}_q\cdot\vec{r}} \cdot G(\vec{r}-\vec{r}_n) \tag{9.20}$$

Making a change of variable $\vec{r'} = \vec{r} - \vec{r}_n$ we get

$$\begin{aligned} E_n\left(\Delta\vec{k}_q\right) &= \rho e^{i\left(\omega_q t - \vec{k}_q\cdot\vec{r}_s\right)} \cdot e^{-i\Delta\vec{k}_q\cdot\vec{r}_n} \cdot \iiint d^3\vec{r'} \cdot G\left(\vec{r'}\right) \cdot e^{-i\Delta\vec{k}_q\cdot\vec{r'}} \\ &= \rho e^{i\left(\omega_q t - \vec{k}_q\cdot\vec{r}_s\right)} \cdot e^{-i\Delta\vec{k}_q\cdot\vec{r}_n} \cdot \tilde{G}\left(\Delta\vec{k}_q\right) \end{aligned}$$

where $\tilde{G}(\Delta k_q)$ is the 3D Fourier transform of $G(\vec{r})$. Note that only the second term depends on the stripe number. The total field is the sum of all the contributions from the different stripes throughout the extent of the medium. It reads,

$$E_q\left(\Delta\vec{k}_q\right) = \sum_{\text{medium}} E_n\left(\Delta\vec{k}_q\right) \tag{9.21}$$

$$= \rho e^{i\left(\omega_q t - \vec{k}_q\cdot\vec{r}_s\right)} \cdot \tilde{G}\left(\Delta\vec{k}_q\right) \cdot \sum_{\text{medium}} e^{-i\Delta\vec{k}_q\cdot\vec{r}_n} \tag{9.22}$$

$$= \rho e^{i\left(\omega_q t - \vec{k}_q\cdot\vec{r}_s\right)} \cdot \tilde{G}\left(\Delta\vec{k}_q\right) \cdot e^{-i\Delta\vec{k}_q\cdot\hat{z}ct} \cdot \sum_{\text{medium}} e^{-in\cdot\Delta\vec{k}_q\cdot\hat{z}\frac{\lambda_1}{2}} \tag{9.23}$$

where we used equation (9.15) to replace $\vec{r}_n$. The last summation extends for n stripes spanning the generating gas cell/jet. Since the periodicity of the stripes is $\lambda_1/2$, over a length, L_{med}, there will be $2L_{\text{med}}/\lambda_1$ stripes. Therefore, we can choose to label n from 0 to N = $2L_{\text{med}}/\lambda_1$. And we write

$\Delta k_q \cdot \hat{z} = \Delta k_q^z$. We thus have,

$$E_q\left(\Delta\vec{k}_q\right) = \rho e^{i\left(\omega_q t - \vec{k}_q\cdot\vec{r}_s\right)} \cdot \tilde{G}\left(\Delta\vec{k}_q\right) \cdot e^{-i\Delta k_q^z ct} \cdot \sum_{n=0}^{N} e^{-in\cdot\left(\Delta k_q^z \cdot \frac{\lambda_1}{2}\right)} \tag{9.24}$$

$$= \rho e^{i\left(\omega_q t - \vec{k}_q\cdot\vec{r}_s\right)} \cdot \tilde{G}\left(\Delta\vec{k}_q\right) \cdot e^{-i\Delta k_q^z ct} \cdot \frac{1 - e^{i(N+1)\cdot\left(\Delta k_q^z \cdot \frac{\lambda_1}{2}\right)}}{1 - e^{i\cdot\left(\Delta k_q^z \cdot \frac{\lambda_1}{2}\right)}} \tag{9.25}$$

$$= \rho e^{i\left(\omega_q t - \vec{k}_q\cdot\vec{r}_s\right)} \cdot \tilde{G}\left(\Delta\vec{k}_q\right) \cdot e^{-i\Delta k_q^z ct} \cdot \frac{1 - e^{i\Delta k_q^z \cdot L_{med}} e^{i\Delta k_q^z \cdot \frac{\lambda_1}{2}}}{1 - e^{\frac{\Delta k_q^z \cdot \lambda_1}{2}}}. \tag{9.26}$$

Substituting equation(9.10) in equation(9.26), the intensity of the harmonic radiation reads,

$$I_q\left(\Delta\vec{k}_q\right) = \rho^2 \left|\tilde{G}\left(\Delta\vec{k}_q\right)\right|^2 \cdot \left| \frac{1 - e^{-\frac{L_{med}}{2L_{abs}}} \cdot e^{i\frac{\pi L_{med}}{L_{coh}}}}{1 - e^{-\frac{\lambda_1}{4L_{abs}}} \cdot e^{i\frac{\pi\lambda_1}{2L_{coh}}}} \right|^2 \tag{9.27}$$

For optimal phase matching, these lengths are usually of the order of the medium length, $L_{med} \gg \lambda_1$. The denominator can thus be Taylor expanded, giving,

$$I_q\left(\Delta\vec{k}_q\right) \simeq \rho^2 \left|\tilde{G}\left(\Delta\vec{k}_q\right)\right|^2 \cdot \left| \frac{1 - e^{-\frac{L_{med}}{2L_{abs}}} \cdot e^{i\frac{\pi L_{med}}{L_{coh}}}}{-\frac{\lambda_1}{4L_{abs}} + i\frac{\pi\lambda_1}{2L_{coh}}} \right|^2 \tag{9.28}$$

$$= \frac{4\rho^2}{\lambda_1^2} \left|\tilde{G}\left(\Delta\vec{k}_q\right)\right|^2 \cdot \frac{1}{\frac{\pi^2}{L_{coh}^2} + \frac{1}{4L_{abs}^2}} \cdot \left[1 + e^{-\frac{L_{med}}{L_{abs}}} - 2e^{-\frac{L_{med}}{2L_{abs}}} \cdot \cos\left(\frac{\pi L_{\text{med}}}{L_{\text{coh}}}\right)\right] \tag{9.29}$$

$$= \frac{4\left(\rho \cdot L_{\text{med}}\right)^2}{\lambda_1^2} \left|\tilde{G}\left(\Delta\vec{k}_q\right)\right|^2 \cdot \frac{1}{\frac{\pi^2 L_{med}^2}{L_{coh}^2} + \frac{L_{\text{med}}^2}{4L_{\text{abs}}^2}} \cdot \left[1 + e^{-\frac{L_{med}}{L_{abs}}} - 2e^{-\frac{L_{med}}{2L_{abs}}} \cdot \cos\left(\frac{\pi L_{\text{med}}}{L_{\text{coh}}}\right)\right]. \tag{9.30}$$

Thus we retrieve the formula of Constant et. al [10] for the output intensity of a given harmonic, but through a discretization of its integral into a sum, which will be beneficial for the case of NCHHG.

Short medium limit

If the ratios $\frac{L_{\text{med}}}{L_{abs}} \ll 1$ and $\frac{L_{med}}{L_{coh}} \ll 1$, we are in the limit of a short medium. In this case equation 9.30 reduces to

$$\begin{aligned} I_q\left(\Delta\vec{k}_q\right) &= \frac{4\left(\rho \cdot L_{med}\right)^2}{\lambda_1^2} \left|\tilde{G}\left(\Delta\vec{k}_q\right)\right|^2 \cdot \frac{1}{\frac{\pi^2 L_{\text{med}}^2}{L_{coh}^2} + \frac{L_{\text{med}}^2}{4L_{abs}^2}} \cdot 2\left[1 - \cos\left(\frac{\pi L_{med}}{L_{coh}}\right)\right] \\ &= 4\frac{\left(\rho \cdot L_{med}\right)^2}{4\lambda_1^2} \left|\tilde{G}\left(\Delta\vec{k}_q\right)\right|^2 \cdot \frac{4\sin^2\left(\frac{\pi L_{\text{med}}}{2L_{coh}}\right)}{\frac{\pi^2 L_{med}^2}{L_{coh}^2} + \frac{L_{\text{med}}^2}{4L_{abs}^2}} \\ &= \frac{4\left(\rho \cdot L_{med}\right)^2}{\lambda_1^2} \left|\tilde{G}\left(\Delta\vec{k}_q\right)\right|^2 \cdot \frac{1}{1 + \frac{L_{coh}^2}{4\pi^2 L_{abs}^2}}. \end{aligned} \tag{9.31}$$

The intensity of the harmonics is ruled by the product of three terms:

- The single atom response $\left|\tilde{G}\left(\Delta\vec{k}_q\right)\right|^2$,
- $\frac{1}{1+\frac{L_{coh}^2}{4\pi^2 L_{coh}^2}}$ which vary little with the parameters of the experiment in a reasonable range and,
- $\left(\rho\cdot L_{med}\right)^2$. If it is multiplied by the square of the transverse surface of the beam, which was supposed to be infinite (but is in the "transverse" Fourier transforms of $G(\vec{r})$), we get the "number of atoms generating" squared. In other words, the signal scales quadratically with the gas pressure or the volume of the target cell, as already well documented [10, 84]. Also, it can be equivalent to having a very dense and short target, or, a long and very dilute target. In most of the experiments described here after, we are in this limit. For example, see Fig. 11.16.

Perfect phase matching

We consider a limit $L_{coh} \gg L_{med}, L_{abs}$ and $L_{med} \simeq L_{abs}$. The formula becomes

$$I_q\left(\Delta\vec{k}_q\right) = \frac{\left(\rho\cdot L_{abs}\right)^2}{\lambda_1^2}\left|\tilde{G}\left(\Delta\vec{k}_q\right)\right|^2\left[1-e^{-\frac{L_{med}}{L_{abs}}}\right]^2 \tag{9.32}$$

For short media, we retrieve the quadratic variation with the medium length. For media getting longer than L_{abs}, the leading term remains $\left(\rho\cdot L_{abs}\right)^2$: it does not help to increase indefinitely the length of the medium beyond the absorption length. The harmonics generated at the entrance of the medium will be in any case absorbed on their way out and will not increase the overall signal. For long enough medium, any situation is like a medium limited by the absorption length.

To conclude, this model gives the same interpretations of phase matching as the existing ones from literature detailed in the previous section. However, we should still keep in mind that it is by far oversimplified: the ionization rates are not homogeneous in space, and vary in time with the laser pulse. The medium might not be uniformly dense, and the laser may get reshaped as it propagates.

9.2 Phase matching effects due to non collinear geometry

Phase matching in the case of HHG driven by two non collinear beams has been addressed in two seminal publications: Heyl et al. [83] and Ellis et al.[43]. Heyl et al. identified a specific contribution to phase mismatch. A geometrical offset due to the different propagation directions of the driving and generating fields has to be included in the phase mismatch. Thus

$$\Delta k = \Delta k_{\text{collinear}} + \Delta k_{\text{noncollinear}}. \tag{9.33}$$

where,

$$\Delta k_{\text{collinear}} = \underbrace{\Delta k_{\text{Gouy}}}_{<0} + \underbrace{\Delta k_{\text{neutral}}}_{>0} + \underbrace{\Delta k_{\text{plasma}}}_{<0} + \underbrace{\Delta k_{\text{dipole.}}}_{\substack{<0 \text{ for } z<0 \\ >0 \text{ for } z>0}} \tag{9.34}$$

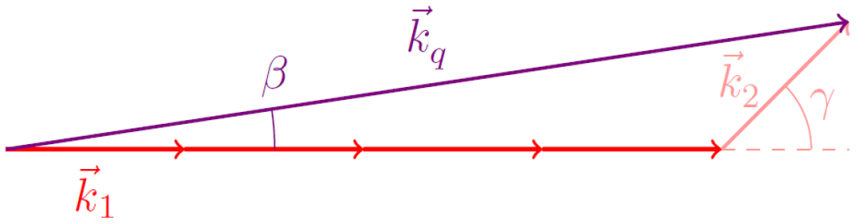

Figure 9.3: Angles and wave vectors involved in the conservation of momentum. Taken from [108].

Now, to find $\Delta k_{\text{noncollinear}}$, following the derivation of Heyl et. al, let us consider the process involving n_1 photons from the first beam and n_2 photons from the second beam (Fig. 9.3). The harmonic emission takes place in the direction defined by conservation of momentum,

$$\vec{k}_q = k_q \vec{u}_q \quad \text{with} \quad \vec{u}_q = \frac{n_1\vec{k}_1 + n_2\vec{k}_2}{\left\| n_1\vec{k}_1 + n_2\vec{k}_2 \right\|}. \tag{9.35}$$

with,

$$k_q = n_1 k_1 + n_2 k_2. \tag{9.36}$$

Geometric considerations (see Fig. 9.3) give the angle of harmonic emission to be

$$\tan\beta = \frac{n_2 k_2 \sin\gamma}{n_1 k_1 + n_2 k_2 \cos\gamma}. \tag{9.37}$$

In the case of two fields having the same angular frequency, $k_2 = k_1, k_q = n_1 k_1 + n_2 k_2 = (n_1 + n_2)k_1$ and $\beta, \gamma \ll 1$, we find :

$$\beta = \frac{n_2}{q}\gamma.$$

The non collinear phase mismatch will be

$$\overrightarrow{\Delta k}_{\angle} = \vec{k}_q - n_1\vec{k}_1 - n_2\vec{k}_2. \tag{9.38}$$

Its projection on $\vec{u}_q$, the propagation direction reads,

$$\begin{aligned}
\Delta k_{\angle} &= k_q - n_1 k_1 \cos\beta - n_2 k_2 \cos(\gamma-\beta) \\
&= n_1 k_1 + n_2 k_2 - n_1 k_1 \cos\beta - n_2 k_2 \cos(\gamma-\beta) \\
&= n_1 k_1 (1-\cos\beta) + n_2 k_2 (1-\cos(\gamma-\beta)) \\
&= (q-n_2)\, k_1 \left(1-\cos\frac{n_2}{q}\gamma\right) + n_2 k_1 \left(1-\cos\left(\gamma-\frac{n_2}{q}\gamma\right)\right) \\
&= (q-n_2)\, k_1 \frac{1}{2}\left(\frac{n_2}{q}\gamma\right)^2 + n_2 k_1 \frac{1}{2}\left(\gamma-\frac{n_2}{q}\gamma\right)^2 \\
&= n_2\gamma^2 k_1 \left(\frac{1}{2}(q-n_2)\frac{n_2}{q^2} + \frac{1}{2}\left(1-\frac{n_2}{q}\right)^2\right) \\
&= \frac{1}{2} n_2\gamma^2 k_1 \left(\frac{n_2}{q} - \frac{n_2^2}{q^2} + 1 - \frac{2n_2}{q} + \frac{n_2^2}{q^2}\right) \\
&= \frac{1}{2} n_2\gamma^2 k_1 \left(1-\frac{n_2}{q}\right).
\end{aligned} \tag{9.39}$$

And $\vec{\Delta k}_{\angle} = \frac{1}{2} n_2\gamma^2 k_1 \left(1-\frac{n_2}{q}\right)\vec{u}_q$. If we now take into account that the phase mismatch terms due to dispersion, Gouy phase and the dipole phase do not change when we add a small angle between the two beams, the total phase mismatch becomes

$$\begin{aligned}
\overrightarrow{\Delta k} &= \vec{k}_q - n_1\vec{k}_1 - n_2\vec{k}_2 \\
&= \Delta k_{\parallel}\vec{u}_q + \overrightarrow{\Delta k}_{\angle} \text{ with } \Delta k_{\angle} = \frac{1}{2} n_2\gamma^2 \left(1-\frac{n_2}{q}\right)\frac{\omega}{c}.
\end{aligned} \tag{9.40}$$

In the case of two-colour field ($k_2 = 2k_1$), we get

$$\beta = \frac{2n_2}{q}\gamma \quad \text{and} \quad \Delta k_{\angle} = n_2\gamma^2 \left(1-\frac{2n_2}{q}\right)\frac{\omega}{c}. \tag{9.41}$$

Due to the additional $\Delta k_{\text{noncollinear}}$ component, phase matching can be made possible in some cases where it is not possible in collinear geometry. For a given n_2, i.e, a given diffraction order, phase matching can be achieved by choosing the right angle, γ. And, $\Delta k_<$ is positive or negative depending on the sign of n_2, i.e., on whether we consider DFG or SFG. In the case of Fig. 9.4.(a), phase matching is possible in collinear geometry, but a phase mismatch occurs for the corresponding non collinear case (Fig. 9.4.(c)), with $\Delta k_<$ being positive (DFG) or negative (SFG). It should be noted that the lengths of the k-vectors do not change with the non collinear angle since neither dispersion, nor focusing effects depend on it. The wavevector mismatch added by the non collinear geometry is thus a purely geometrical mismatch. In Fig. 9.4.(b), showing a non-zero phase mismatch in collinear generation, a corresponding non collinear scheme can typically be found, allowing for phase-matched generation (Fig. 9.4.(d)). In this case, the two terms in equation (9.33) compensate each other.

The difference in signs of $\Delta k_<$ in the case of SFG and DFG once again raises the discussion on the competition between these two channels. Just with this geometrical effect on phase matching, it is obvious that in cases where $\Delta k_{\text{collinear}}$ is negative due to plasma dispersion and Gouy phase effects, as in the case of tight focusing or higher harmonic orders, DFG will dominate due to its positive

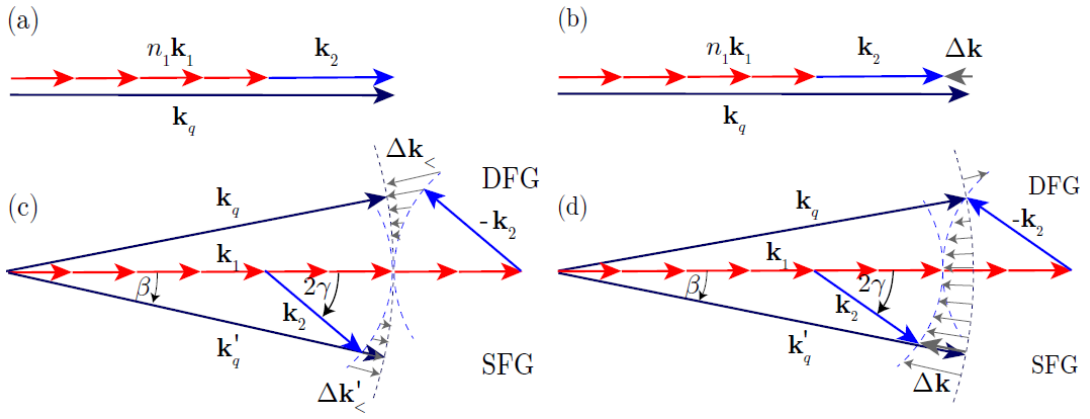

Figure 9.4: Schematic phase matching illustration for NCHHG driven by a $\omega - 2\omega$ laser field. In (a) and (b), collinear generation schemes are shown, considering phase-matched (a) and non phase-matched (b) generation. (c) and (d) depict the corresponding non collinear schemes for both SFG and DFG processes. Taken from [61].

$\Delta k_<$ contribution [83]. However, since DFG involves the absorption of more photons at the same strength of the field, it is less probable and the effect washes out. Also, as we saw in Part III, the transverse macroscopic effects of amplitude and phase modulation favours SFG and dominates over phase matching considerations.

Ellis et al. [43] experimentally and theoretically investigate the macroscopic physics of phase-matched non collinear HHG at high pressures. Due to the fact that the geometry-dependent phase mismatch has different consequences for SFG and DFG, the optimal phase matching pressure and ionization fraction will also vary for the two cases. Specifically, they showed that by tuning the pressure, SFG is phase matched below the critical ionization fraction (see section 11.1.1) and DFG, above it. We will focus only on the case of phase matching below critical ionization in the upcoming chapters.

CHAPTER 10

A two dimensional discretized theoretical model for a homogeneous medium

In part III, we studied in detail the far field properties of the diffraction orders of non collinear high harmonic generation, with emphasis on the amplitude distribution, neglecting the contribution from phase matching effects. In the previous chapter, we presented the simplest model of phase matching, which is a one dimensional model, and a specific contribution to phase mismatch for NCHHG, called the non collinear phase matching term. It is the ambition of this chapter to adapt the 1D model to a structured 2D field and compare its outcome to the empirical addition of a "non collinear" phase matching term in the 1D model.

Our approach is based on defining the interference pattern of the two interfering beams as a two dimensional grid having localised zones of high intensity where HHG emission can occur. The zones have already been introduced as "emission pockets", and form a periodic structure that translates in time. The situation is very similar to X-Ray Diffraction (XRD) in crystals. The atomic planes of a crystal cause an incident beam of x-rays to interfere with one another as they leave the crystal, lighting up specific diffraction spots in the far field. The distribution of x-rays scattered by a rigid, periodic array of atoms/ions can in turn be used to reveal the locations of these atoms/ions within that crystal structure [109]. Like in this situation, here, the emission pockets are individual sources of x-rays and the emission from these coherent sources interfere with one another as they leave the macroscopic generating medium.

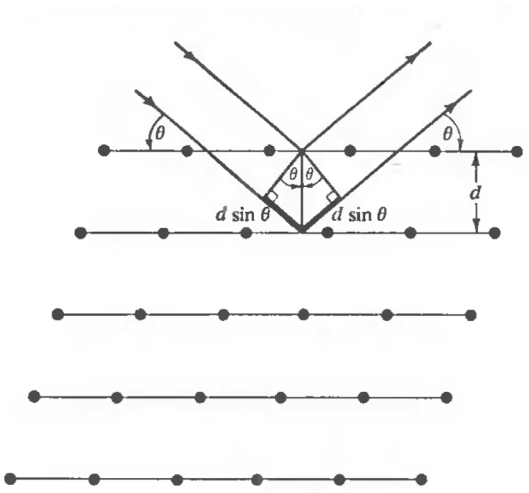

Figure 10.1: A Bragg reflection from a particular family of lattice planes, separated by a distance, d. Incident and reflected rays are shown for the two neighbouring planes. The path difference is $2d\sin\theta$. Figure taken from [109].

10.1 A quick introduction to x-ray scattering in crystals

This section is mainly taken from the book, Solid State Physics, by Neil W.Ashcroft and N.David Mermin [109].

Diffraction peaks: Bragg and Laue formulation

Before developing our theoretical model, let us first revisit a few concepts of crystallography. Crystals consist of planes of atoms that are spaced a distance d apart, but can be resolved into many atomic planes, each with a different d-spacing. English physicists Sir W. H. Bragg and his son Sir W. L. Bragg developed a relationship in 1913 to explain why the cleavage faces of crystals appear to reflect x-ray beams at certain angles of incidence (ζ). The conditions for a sharp peak in the intensity of the scattered radiation are: 1) the x-rays should be specularly reflected by the ions in any one plane, and 2) the reflected rays from successive planes should interfere constructively. The path difference between the two rays is $2d\sin\zeta$ (see Fig. 10.1). For the rays to interfere constructively, this path difference must be an integral number of wavelengths, giving the famous Bragg condition:

$$p\lambda = 2d\sin\zeta \tag{10.1}$$

where p is the order of the corresponding reflection.

Another approach at looking at XRD was the one proposed by Max von Laue. The Laue view is that the intensity maxima of scattered x-rays are the result of the diffraction of waves by crystals. In this case, no particular sectioning of the lattice planes is singled out. Instead, one regards the crystal as composed of identical sets of ions or atoms placed at the sites of a lattice, each of which

can diffract the incident radiation in all directions. Sharp peaks will be observed only in directions and at wavelengths for which the rays scattered from all lattice points interfere constructively. It can be shown that the diffraction maxima will appear only in some specific directions which obey certain conditions known as the Laue's equations. Let us consider two identical scattering centres A and B placed at a distance $\vec{d}$ from each other. The rays emerging from these two points interfere constructively when the change in wave vector is an integral multiple of 2π.

$$\Delta\vec{k}\cdot\vec{d} = 2\pi m \tag{10.2}$$

Due to the periodicity of the crystal, the other atoms placed in the same direction would also scatter the radiations exactly in phase with those scattered from A and B. In a three-dimensional crystal, d may coincide with any of the three crystallographic axes a, b and c. Thus for the occurrence of a diffraction maximum, the following three conditions must be satisfied simultaneously :

$$\Delta\vec{k}\cdot\vec{a} = 2\pi h \tag{10.3}$$

$$\Delta\vec{k}\cdot\vec{b} = 2\pi j \tag{10.4}$$

$$\Delta\vec{k}\cdot\vec{c} = 2\pi k \tag{10.5}$$

where h, j, k are the Miller indices of the reflecting plane.

Structure factor and form factor

The total scattering amplitude from an (h,k,l) plane from all the waves scattered by n atoms in the unit cell is given by

$$F(h,k,l) = \sum_{j=1}^{n} f_j e^{i\phi_j},$$

Each of these waves shows an amplitude proportional to f_j, the atomic scattering factor. It measures the x-ray scattering power of each atom. If we consider the lattice to have identical atoms, then all atoms have $f_j = f$ and

$$F(h,k,l) = fS \text{ where,} \tag{10.6}$$

$$S = \sum_{j=1}^{n} e^{i\phi_j}. \tag{10.7}$$

S is called the geometrical structure factor as it depends upon the geometrical arrangement of atoms within the unit cell. Now, the intensity of a radiation being the square of the amplitude, the intensity of the diffracted beam may be written as

$$I = FF^*. \tag{10.8}$$

10.2 Crystal-like structure of the HHG emission zones

In the active grating model, we already introduced the idea of emission pockets at high perturbations (see section 8.1). The HHG spectrum will mainly result from the emission from these zones of high

intensity. To recall, the composite field formed by the two beams is of the form

$$E_s = \mathscr{R}\left[E_1 e^{i\omega_1 t - i\vec{k}_1\cdot\vec{r}} + \alpha E_1 e^{i\omega_2 t - i\vec{k}_2\cdot\vec{r}}\right] \tag{10.9}$$

Inspecting equation 10.9, these pockets correspond to the two fields being extremum, both positive or negative. We get the double condition,

$$\begin{cases} \omega_1 t - \vec{k}_1\cdot\vec{r} = m_1\pi \\ \omega_2 t - \vec{k}_2\cdot\vec{r} = m_2\pi \\ m_1 \text{ and } m_2 \text{ of same parity} \end{cases} \tag{10.10}$$

$\vec{r}_{m_1,m_2} = (x_{m_1,m_2}, z_{m_1,m_2})$, the coordinates of such a high intensity point. $\hat{z}$ is along the propagation axis and $\hat{x}$ is along the traverse axis. We denote θ_0 as the crossing angle between the two beams. Taking into account that $\vec{k}_1 = (0, k_1)$ and $\vec{k}_2 = (k_2^{\perp}, k_2^{\parallel}) = \eta k_1(\sin\theta_0, \cos\theta_0)$, we have (flipping the signs of m_1 and m_2)),

$$\begin{cases} z_{m_1,m_2} = m_1\dfrac{\pi}{k_1} + \dfrac{\omega_1 t}{k_1} = m_1\cdot\dfrac{\lambda_1}{2} + c\cdot t \\ \vec{k}_2^{\perp}\cdot x_{m_1,m_2} + \vec{k}_2^{\parallel}\cdot z_{m_1,m_2} = m_2\pi + \omega_2 t. \end{cases} \tag{10.11}$$

which is inverted as

$$\begin{aligned} z_{m_1,m_2} &= \frac{\lambda_1}{2}\cdot m_1 + c\cdot t \\ x_{m_1,m_2} &= \frac{\pi}{k_2^{\perp}}\left(m_2 + \frac{\omega_2 t}{\pi} - \frac{k_2^{\parallel}}{k_1}\cdot m_1 - \frac{k_2^{\parallel}}{k_1}\frac{\omega_1 t}{\pi}\right) \\ &= \frac{\lambda_1}{2\eta\sin\theta_0}\left(m_2 - \eta\cos\theta_0\cdot m_1\right) + \frac{\eta\omega_1 t}{\pi}\cdot(1-\cos\theta_0) \\ &= \frac{\lambda_1}{2\eta\sin\theta_0}\left(m_2 - \eta m_1\right) + \frac{\lambda_1}{2\sin\theta_0}(1-\cos\theta_0)\, m_1 + c\cdot t\cdot\tan\left(\frac{\theta_0}{2}\right) \\ &= \frac{\lambda_1}{2}\tan\left(\frac{\theta_0}{2}\right)\cdot m_1 + \frac{\lambda_1}{2\eta\sin\theta_0}\cdot\left(m_2 - \eta m_1\right) + c\cdot t\cdot\tan\left(\frac{\theta_0}{2}\right). \end{aligned} \tag{10.12}$$

The manipulations on the indices is done to get periodicities along the $\hat{x}$ and almost along the $\hat{z}$. Again, m_1 and m_2 can take any value of identical parities.

Now, we know the positions of these pockets in terms of x and z directions. The pockets form a grid that are not purely along the x-z plane. So, we introduce a new coordinate system with unit vectors $\vec{a}$ and $\vec{b}$ (equivalent to the crystallographic axes), to define the location of these pockets. We define the vectors

$$\vec{a} = \begin{pmatrix} a_x \\ a_z \end{pmatrix} = \frac{\lambda_1}{2}\begin{pmatrix} \tan\left(\frac{\theta_0}{2}\right) \\ 1 \end{pmatrix} \quad , \quad \vec{b} = \begin{pmatrix} b_x \\ b_z \end{pmatrix} = \frac{\lambda_1}{2}\begin{pmatrix} \frac{1}{\eta\sin\theta_0} \\ 0 \end{pmatrix} \tag{10.13}$$

and

$$\vec{T}(t) = c\cdot t\cdot\begin{pmatrix} \tan\left(\frac{\theta_0}{2}\right) \\ 1 \end{pmatrix} = \frac{\omega_1 t}{\pi}\vec{a} \tag{10.14}$$

With these notations, we can rewrite equation (10.12) as

$$\vec{r}_{m_1,m_2}(t) = m\vec{a} + m'\vec{b} + \vec{T}(t). \tag{10.15}$$

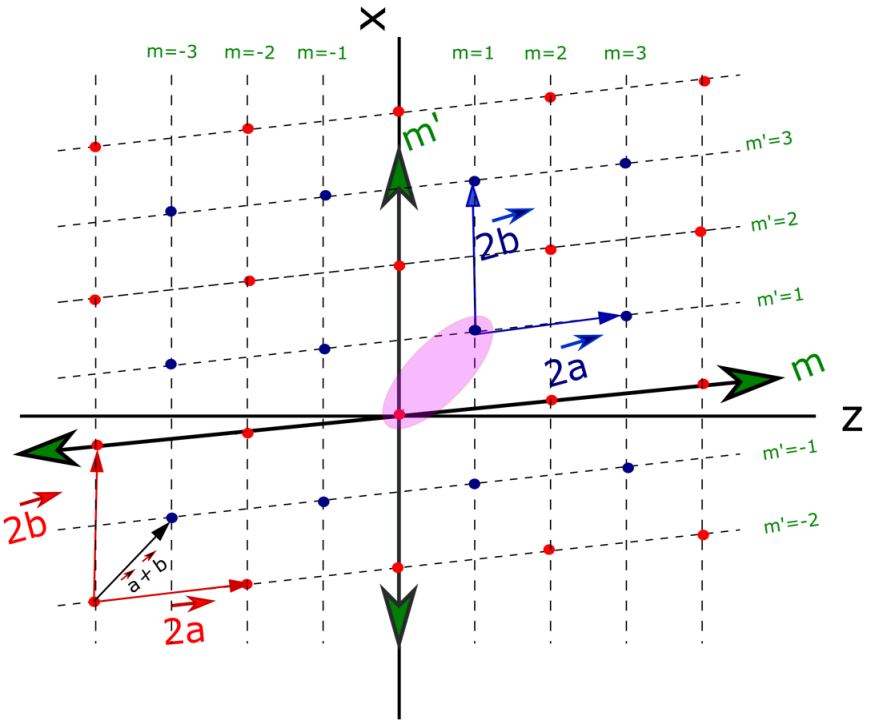

Figure 10.2: Lattice pattern for the case of η = even. We have two sub-lattices made of red and blue dots respectively. The two sub-lattices are offset by $\vec{a}+\vec{b}$. The pink shaded region shows a unit cell formed by one of each pocket from the two sub-lattices.

with $m = m_1$, $m' = m_2 - \eta m_1$, and m_1 and m_2 of identical parities. $\vec{b}$ is purely transverse, while $\vec{a}$ is almost along $\hat{z}$. We can now write the location of the emission pockets in a new a-b plane with indices m and m'. In general, not all values of m' are allowed, and it depends on η. This leads to the possibility of two types of grids as described below.

- **if η is even**, ηm_1 is even, so m' has the parity of m_2. m_1 and m_2 having the same parity is equivalent to **m and m' having the same parity**. Fig. 10.2 shows such a case. It makes two sub lattices, one with even (m, m') indices (depicted as red dots), the other with odd (m, m') indices (blue dots). They are generated with vectors $2\vec{a}$ and $2\vec{b}$ respectively and the sub-lattices themselves are offset by $\vec{a}+\vec{b}$.

- **if η is odd**, ηm_1 has the parity of m_1, and m' is even since m_1 and m_2 should have identical parities. So the condition becomes that **m can take any value and m' should be even**. Fig. 10.3 shows this case. Once again, it makes two sub lattices: one with odd, even (m, m') indices (depicted as blue dots), the other with even, even (m, m') indices (red dots), generated with vectors $2\vec{a}$ and $2\vec{b}$ and offset from each other by $\vec{a}$.

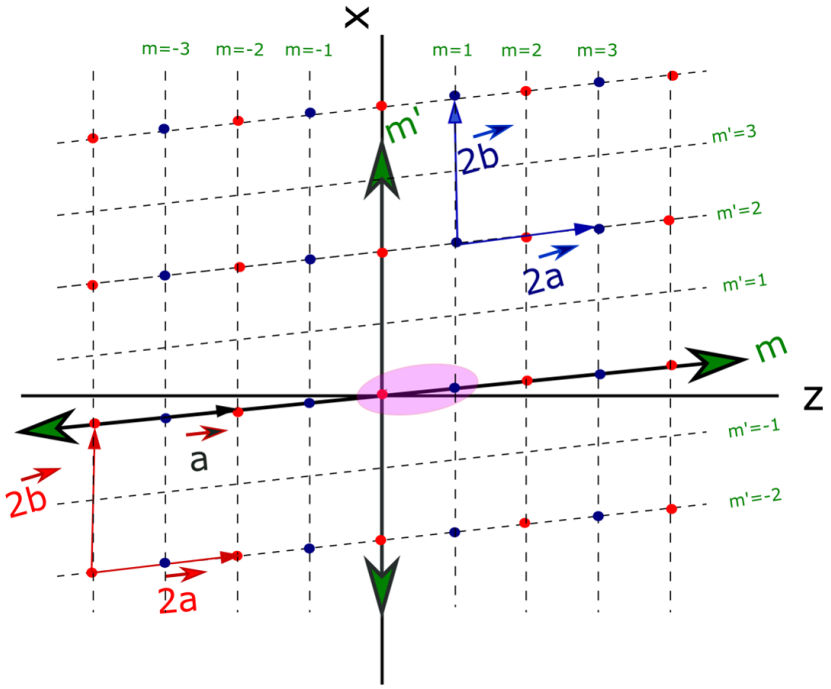

Figure 10.3: Lattice pattern for the case of η = odd. We have two sub-lattices made of red and blue dots respectively. The two sub-lattices are offset by $\vec{a}$. The pink shaded region shows a unit cell formed by one of each pocket from the two sub-lattices.

Following the approach of XRD in crystals mentioned in section 10.1, we will introduce a form factor, linked to the unit cell of the lattice and a structure factor, linked to the macroscopic lattice obtained by the repetition of this unit cell. The unit cell in our case is formed by two lattice points, each from a different sub lattice. (The pink shaded regions in figures 10.2 and 10.3 correspond to a unit cell of the lattice.) For example, starting at the origin, a unit cell can be defined by two points located at $\vec{r}_{0,0}$, and another $\vec{r'}$, at a distance $\vec{a}+\epsilon(\eta)\vec{b}$. As evident from figures 10.2 and 10.3, $\epsilon(\eta)=0$ if η is odd and 1 if η is even.

For the calculations below, each unit cell is considered as a single source of x-ray radiation, already incorporating the phase difference between the emissions from the two generating pockets that constitute them.

10.3 Scattering amplitude from the emission pockets

Following the discretized 1D model introduced in section 9.1.2, we can design the areas of peak intensity with a bell-shaped function G, for instance a Gaussian, defined by typical widths $\delta x \ll a_x, b_x$ along x and $\delta z \ll a_z, b_z$ along z. Since it is common to all pockets, we just convolute it with a Dirac function centered around $\vec{r}_{m,m'}$ to get the contribution from the (m,m') pocket. The elementary electric field detected on a screen at $\vec{r}_s$, generated with a wave-vector $\vec{k}_{q_s}$, angular frequency $\omega_{q_s} = q_s\omega_s$

(see section 6.1), from the location $\vec{r}$ close to the $(m,\ m')$ point reads

$$e^{iq_s\left[\omega_s t-\vec{k}_s\cdot\vec{r}\right]}\cdot e^{-i\vec{k}_{q_s}\cdot(\vec{r}_s-\vec{r})}\cdot\left[G(\vec{r})\circledast\delta\left(\vec{r}-\vec{r}_{m,m'}\right)\right](\vec{r}) \tag{10.16}$$

where $\omega_{q_s}=q_1\omega_1$, giving $q_s=\frac{1+\alpha}{1+\eta\alpha}q_1$. The argument of the first exponential is q_s times the phase of the incoming field, as in any nonlinear process. The second is the phase accumulated by the harmonic during propagation towards the observation point. We write

$$\begin{aligned}\Delta\vec{k}_{q_s}&=q_s\vec{k}_s-\vec{k}_{q_s}\\&=q_s\left(\vec{k}_1+\frac{\alpha}{1+\alpha}\Delta\vec{k}\right)-\vec{k}_{q_s}\\&=q_s\left(\frac{\vec{k}_1+\vec{k}_2}{2}+\frac{\alpha-1}{\alpha+1}\frac{\vec{k}_2-\vec{k}_1}{2}\right)-\vec{k}_{q_s},\end{aligned} \tag{10.17}$$

the phase mismatch for wave-vector $\vec{k}_{q_s}$. The last expression shows its symmetry in $\vec{k}_1$ and $\vec{k}_2$. Again, it takes all optical indices, real and imaginary that may arise in the medium. The elementary electric field of equation 10.16 can then be re-written as

$$e_{m,m'}\left(\vec{k}_{q_s},\vec{r}\right)=e^{i\omega_{q_s}t-i\vec{k}_{q_s}\cdot\vec{r}_s}\cdot e^{-i\Delta\vec{k}_{q_s}\cdot\vec{r}}\cdot G\left(\vec{r}-\vec{r}_{m,m'}\right), \tag{10.18}$$

with $G\left(\vec{r}-\vec{r}_{m,m'}\right)$ ensuring that it contributes only from regions close to $\vec{r}_{m,m'}$. Integrating over all space, the electric field in the far-field will be

$$E_{out}=\int\int e_{m,m'}\,d^2\vec{r}=e^{i\omega_{q_s}t-i\vec{k}_{q_s}\cdot\vec{r}_s}\int\int e^{-i\Delta\vec{k}_{q_s}\cdot\vec{r}}\cdot G\left(\vec{r}-\vec{r}_{m,m'}\right)d^2\vec{r}. \tag{10.19}$$

Up to now we proceeded exactly as in section 9.1.2 where we consider the case of HHG with a single beam. Now let us bring in the contribution from the "lattice structure" resulting from the non collinear mixing of two fields.

10.3.1 Form factor and structure factor

If we consider only the contribution from each unit cell, we just have to sum the contributions of the two lattice points that make up the unit cell. If we consider the two lattice points as $\vec{r}_{0,0}=0+\vec{T}(t)$ and $\vec{r}_{0,i}=\vec{r}_{0,0}+\vec{a}+\epsilon(\eta)\vec{b}+\vec{T}(t)$, the electric field detected on the screen at $\vec{r}_s$ from this unit cell would read as

$$E_{out}=e^{i\omega_{q_s}t-i\vec{k}_{q_s}\cdot\vec{r}_s}\sum_{i\in\{0,1\}}\int\int e^{-i\Delta\vec{k}_{q_s}\cdot\vec{r}}\cdot G\left(\vec{r}-\vec{r}_{0,i}\right)d^2\vec{r}. \tag{10.20}$$

We can now define a function $F(\Delta\vec{k}_{q_s})$ equivalent to the form factor in x-ray diffraction in crystals as

$$\begin{aligned}F(\Delta\vec{k}_{q_s})&=\sum_{i\in\{0,1\}}\int\int d^2\vec{r}\;e^{-i\Delta\vec{k}_{q_s}\cdot\vec{r}}\cdot G\left(\vec{r}-\vec{r}_{0,i}\right)\\&=\sum_{i\in\{0,1\}}e^{i\Delta\vec{k}_{q_s}\cdot\vec{r}_{0,i}}\int\int d^2\vec{r}\;e^{-i\Delta\vec{k}_{q_s}\cdot\vec{r}}\cdot G(\vec{r})\\&=\left[\int\int d^2\vec{r}\;e^{-i\Delta\vec{k}_{q_s}\cdot\vec{r}}\cdot G(\vec{r})\right]\cdot\sum_{i\in\{0,1\}}e^{i\Delta\vec{k}_{q_s}\cdot\vec{r}_{0,i}}\\&=\widetilde{G}\left(\Delta\vec{k}_{q_s}\right)\cdot\sum_{i\in\{0,1\}}e^{i\Delta\vec{k}_{q_s}\cdot\vec{r}_{0,i}}.\end{aligned} \tag{10.21}$$

where $\widetilde{G}$ is the Fourier transform of G. The sum can be calculated as

$$e^{i\Delta\vec{k}_{q_s}\cdot\vec{T}(t)}\cdot\sum_{i\in\{0...1\}}e^{i\Delta\vec{k}_{q_s}\cdot\vec{r}_{0,i}}=e^{i\Delta\vec{k}_{q_s}\cdot\vec{T}(t)}\left(1+e^{i\Delta\vec{k}_{q_s}\cdot\left(\vec{a}+\varepsilon(\eta)\vec{b}\right)}\right) \tag{10.22}$$

$$=2e^{i\Delta\vec{k}_{q_s}\cdot\vec{T}(t)+i\Delta\vec{k}_{q_s}\cdot\frac{\vec{a}+\varepsilon(\eta)\vec{b}}{2}}\cdot\cos\left(\frac{\Delta\vec{k}_{q_s}\cdot\left(\vec{a}+\varepsilon(\eta)\cdot\vec{b}\right)}{2}\right). \tag{10.23}$$

We thus have

$$F(\Delta\vec{k}_{q_s})=2e^{i\Delta\vec{k}_{q_s}\cdot\vec{T}(t)+i\Delta\vec{k}_{q_S}\cdot\frac{\vec{a}+\varepsilon(\eta)\cdot\vec{b}}{2}}\cdot\widetilde{G}\left(\Delta\vec{k}_{q_s}\right)\cdot\cos\left(\frac{\Delta\vec{k}_{q_s}\cdot\left(\vec{a}+\varepsilon(\eta)\cdot\vec{b}\right)}{2}\right). \tag{10.24}$$

This is the diffraction amplitude from a given unit cell, i.e., from two lattice points. It is equivalent to twice the contribution from the conventional form factor in XRD. If we consider the two pockets as a single source of emission corresponding to each pulse, we can equate it to the form factor f. This form factor now gathers all the physics about HHG around a peak of the field: intensity profile, atomic phase, ionization rates etc. With our hypothesis of a homogeneous medium, it is exactly the same for any region of the medium at a given time.

Finally, the total electric field will be the sum over all the unit cells. This means the repetition of the unit cell containing two lattice points (hence the constraint on m and m' to be even) over all space. Thus,

$$\vec{E}_{out}(\vec{r}_s,t)=e^{i\omega_{q_s}t-i\vec{k}_{q_s}\cdot\vec{r}_s}F\left(\Delta\vec{k}_{q_s}\right)\sum_{\substack{m,m'\,even\\ \vec{r}_m,m'\in V}}e^{i\Delta\vec{k}_{q_s}\cdot\vec{r}_{m,m'}}. \tag{10.25}$$

where V denotes the volume of the generating medium. And S, the structure factor can be defined as

$$S(\Delta\vec{k}_{q_s})=\sum_{\substack{m,m'\,even\\ \vec{r}_m,m'\in V}}e^{i\Delta\vec{k}_{q_s}\cdot\vec{r}_{m,m'}}. \tag{10.26}$$

10.3.2 Total amplitude

To calculate the electric field of the diffraction peaks, we have to calculate the two factors, $F\left(\Delta\vec{k}_{q_s}\right)$ and $S\left(\Delta\vec{k}_{q_s}\right)$. The important terms in these factors are defined as

$$\begin{aligned}\phi_m&=\Delta\vec{k}_{q_s}\cdot\vec{a}\text{ and,}\\ \phi_{m'}&=\Delta\vec{k}_{q_s}\cdot\vec{b}.\end{aligned} \tag{10.27}$$

The emission from all the unit cells of the main lattice will be in phase at the maxima. Knowing that the unit cells are separated by a distance $2\vec{a}$ and $2\vec{b}$, we can write the Laue conditions as follows:

$$\begin{aligned}\Delta\vec{k}_{q_s}\cdot2\vec{a}&=2\pi h,\\ \Delta\vec{k}_{q_s}\cdot2\vec{b}&=2\pi j.\end{aligned} \tag{10.28}$$

We can now write the form factor as

$$F(\Delta\vec{k}_{q_s})=2e^{i\Delta\vec{k}_{q_s}\cdot\vec{T}(t)+i\Delta\vec{k}_{q_S}\cdot\frac{\vec{a}+\varepsilon(\eta)\cdot\vec{b}}{2}}\cdot\widetilde{G}\left(\Delta\vec{k}_{q_s}\right)\cdot\cos\left(\frac{\pi(h+\varepsilon(\eta)j}{2}\right). \tag{10.29}$$

Let us introduce the transverse and longitudinal sizes of the medium, as measured along $\vec{a}$ and $\vec{b}$: L^a_{med} and L^b_{med} . We discretize it in unit cells of steps |a| and |b|, with $m \in [\![0, m_0]\!]$ along $\vec{a}$ and $m' \in [\![0, m'_0]\!]$ along $\vec{b}$. From the definition of m_0 and m'_0 we define

$$\begin{cases} \vec{L}^a_{\text{med}} = L^a_{\text{med}} \frac{\vec{a}}{|\vec{a}|} = m_0 \vec{a} \\ \vec{L}^b_{\text{med}} = L^b_{\text{med}} \frac{\vec{b}}{|\vec{b}|} = m'_0 \vec{b}. \end{cases} \tag{10.30}$$

As for the structure factor, since the unit cell was taking two nodes in each dimension, it should be the sum over even integers in both dimensions. It reads

$$\begin{aligned} S\left(\Delta\vec{k}_q\right) &= \sum_{\substack{m\in[\![0,m_0/2]\!] \\ m'\in[\![0,m'_0/2]\!]}} e^{i2m\phi_m + i2m'\phi_{m'}} \\ &= e^{i((\frac{m_0}{2}-1)\phi_m + (\frac{m'_0}{2}-1)\phi'_m)} \cdot \frac{\sin\left(\frac{m_0\phi_m}{2}\right)}{\sin\phi_m} \cdot \frac{\sin\left(\frac{m'_0\phi_{m'}}{2}\right)}{\sin\phi_{m'}}. \end{aligned} \tag{10.31}$$

Putting the structure factor and the form factor together, equation 10.25 now reads as

$$\begin{aligned} \vec{E}_{out}\left(\vec{r}_s, \widetilde{k_{q_s}}^{\parallel}, \widetilde{k_{q_s}}^{\perp}, \widetilde{\Delta k}^{\parallel}, \alpha, t\right) = 2e^{i\omega_{q_s}t - i\vec{k}_{q_s}\cdot\vec{r}_s} \cdot \\ e^{i\Delta\vec{k}_{qs}\cdot\vec{T}(t) + i\frac{m_0}{2}\phi_m + \frac{m'_0 - 1 + \varepsilon(\eta)}{2}\phi'_m} \cdot \\ \widetilde{G}\left(\Delta\vec{k}_{q_s}\right) \cdot \cos\left(\frac{\phi_m + \varepsilon(\eta)\phi_{m'}}{2}\right) \cdot \frac{\sin\left(\frac{m_0\phi_m}{2}\right)}{\sin\left(\phi_m\right)} \cdot \frac{\sin\left(\frac{m'_0\phi_{m'}}{2}\right)}{\sin\left(\phi_{m'}\right)}. \end{aligned} \tag{10.32}$$

10.4 Longitudinal and transverse phase matching effects

Rewriting $m_0\phi_m = m_0\Delta\vec{k}_{q_s}\cdot\vec{a} = \Delta\vec{k}_{q_s}\cdot\vec{L}^a_{\text{med}}$ and $m'_0\phi_{m'} = m'_0\Delta\vec{k}_{q_s}\cdot\vec{b} = \Delta\vec{k}_{q_s}\cdot\vec{L}^b_{\text{med}}$, equation 10.32 becomes:

$$\begin{aligned} \vec{E}_{out}\left(\vec{r}_s, \widetilde{k_{q_s}}^{\parallel}, \widetilde{k_{q_s}}^{\perp}, \widetilde{\Delta k}^{\parallel}, \alpha, t\right) = \\ -\frac{1}{2} e^{i\omega_{q_s}t - i\vec{k}_{q_s}\cdot\vec{r}_s} \cdot \widetilde{G}\left(\Delta\vec{k}_{q_s}\right) \cdot e^{i\Delta\vec{k}_{q_s}\cdot\frac{\vec{L}^a_{med} + \vec{L}^b_{med} + 2\vec{T}(t)}{2}} \cdot e^{i\frac{\varepsilon(\eta)-1}{2}\Delta\vec{k}_{q_s}\cdot\vec{b}} \cdot \\ \frac{e^{i\frac{\Delta\vec{k}_{q_s}\cdot\vec{L}^a_{med}}{2}} - e^{-i\frac{\Delta\vec{k}_{q_s}\cdot\vec{L}^a_{med}}{2}}}{\sin(\Delta\vec{k}_{q_s}\cdot\vec{a})} \cdot \frac{e^{i\frac{\Delta\vec{k}_{q_s}\cdot\vec{L}^b_{med}}{2}} - e^{-i\frac{\Delta\vec{k}_{q_s}\cdot\vec{L}^b_{med}}{2}}}{\sin\left(\Delta\vec{k}_{q_s}\cdot\vec{b}\right)}. \end{aligned} \tag{10.33}$$

It is the product of the local response $\widetilde{G}\left(\Delta\vec{k}_{q_s}\right)$, a transverse ($\simeq \vec{b}$) and longitudinal ($\simeq \vec{a}$) phase matching terms. Note that with the exponential expression, the role of absorption can be readily seen. We write

$$G_a\left(\Delta\vec{k}_{q_s}, \vec{L}^a_{med}\right) = e^{i\frac{\Delta\vec{k}_{q_s}\cdot\vec{L}^a_{med}}{2}} \cdot \frac{e^{i\frac{\Delta\vec{k}_{q_s}\cdot\vec{L}^a_{med}}{2}} - e^{-i\frac{\Delta\vec{k}_{q_s}\cdot\vec{L}^a_{med}}{2}}}{\Delta\vec{k}_{q_s}\cdot\vec{a}} \tag{10.34}$$

$$G_b\left(\Delta\vec{k}_{q_s}, \vec{L}^a_{med}\right) = e^{i\frac{\Delta\vec{k}_{q_s}\cdot\vec{L}^b_{med}}{2}} \cdot \frac{e^{i\frac{\Delta\vec{k}_{q_s}\cdot\vec{L}^b_{med}}{2}} - e^{-i\frac{\Delta\vec{k}_{q_s}\cdot\vec{L}^b_{med}}{2}}}{\sin\left(\Delta\vec{k}_{q_s}\cdot\vec{b}\right)} \tag{10.35}$$

Here $\sin(\Delta\vec{k}_{q_s}\cdot\vec{a})$ is approximated as $(\Delta\vec{k}_{q_s}\cdot\vec{a})$ since it takes very small values as can be seen from equation D.6. The far field electric field thus reads

$$\vec{E}_{out}\left(\vec{r}_s,\vec{k}^{\parallel}_{q_s},\vec{k}^{\perp}_{q_s},\Delta\vec{k}^{\parallel},\alpha,t\right) = -\frac{1}{2}e^{i\omega_{q_s}t-i\vec{k}_{q_s}\cdot\vec{r}_s}\cdot e^{i\Delta\vec{k}_{q_s}\cdot\left(\vec{T}(t)+\frac{\varepsilon(\eta)-1}{2}\vec{b}\right)}\cdot \widetilde{G}\left(\Delta\vec{k}_{q_s}\right)\cdot G_a\left(\Delta\vec{k}_{q_s}\right)\cdot G_b\left(\Delta\vec{k}_{q_s}\right). \quad (10.36)$$

Here $\widetilde{G}\left(\Delta\vec{k}_{q_s}\right)$ is the amplitude term giving the contribution from the microscopic response and $G_a\left(\Delta\vec{k}_{q_s}\right)$, the contribution from the longitudinal phase matching effects and $G_b\left(\Delta\vec{k}_{q_s}\right)$ from the transverse phase matching effects. We will now analyse the effects of G_a and G_b separately. This last equation, showing the factorization into a microscopic, longitudinal and transverse terms is one of the main results of this model.

10.4.1 Longitudinal phase matching

To look at the effects arising from the coherence and absorption lengths, we introduce the projections of $\Delta\vec{k}_{q_s}$ on $\vec{a}$ and $\vec{b}$ as:

$$\begin{cases} \Delta\vec{k}_{q_s}\cdot\dfrac{\vec{a}}{|\vec{a}|} = \dfrac{\phi_m}{|\vec{a}|} = \dfrac{\pi}{L^a_{coh}} + i\dfrac{1}{2L^a_{abs}} \\ \Delta\vec{k}_{q_s}\cdot\dfrac{\vec{b}}{|\vec{b}|} = \dfrac{\phi_{m'}}{|\vec{b}|} = \dfrac{\pi}{L^b_{coh}} + i\dfrac{1}{2L^b_{abs}} \end{cases} \quad (10.37)$$

with L^a_{coh} and L^a_{abs} the coherence and absorption lengths along $\vec{a}$ and L^a_{coh} and L^a_{abs} along $\vec{b}$. It will depend on both the harmonic as well as the diffraction order. It gives

$$\begin{aligned} \left|G_a\left(\Delta\vec{k}_{q_s},\vec{L}^a_{med}\right)\right|^2 &= e^{-\frac{L^a_{med}}{L^a_{abs}}}\cdot\left|\frac{e^{i\frac{\pi L^a_{med}}{2L^a_{coh}}-\frac{L^a_{med}}{4L^a_{abs}}}-e^{-i\frac{\pi L^a_{med}}{2L^a_{coh}}+\frac{L^a_{med}}{4L^a_{abs}}}}{\frac{\pi a}{L^a_{coh}}+i\frac{a}{2L^a_{abs}}}\right|^2 \\ &= \frac{\left(\frac{2L^a_{abs}}{a}\right)^2}{1+\left(\frac{\pi 2L^a_{abs}}{L^a_{coh}}\right)^2}\cdot\left[1+e^{\frac{-L^a_{med}}{L^a_{abs}}}-2e^{\frac{-L^a_{med}}{2L^a_{abs}}}\cos\left(\frac{\pi L^a_{med}}{L^a_{coh}}\right)\right]. \end{aligned} \quad (10.38)$$

This is exactly the formula of Constant et al.[10] that we retrieved in section 9.1.1 for the case of collinear HHG in 1D along the propagation axis.

Geometric effects in longitudinal phase matching

We can write the reduced phases as (see appendix D)

$$\begin{cases} \widetilde{\phi_m} = \dfrac{\phi_m}{\pi} = -\dfrac{k^{\perp}_{q_s}}{k_1}\cdot\tan\left(\dfrac{\theta}{2}\right) - \dfrac{k^{/\!/}_{q_s}}{k_1} + \dfrac{1+\eta\alpha}{1+\alpha}q_s \\ \widetilde{\phi_{m'}} = \dfrac{\phi_m}{\pi} = -\dfrac{k^{\perp}_{q_s}}{\eta k_1\sin\theta} + \dfrac{\alpha}{1+\alpha}\cdot q_s \end{cases} \quad (10.39)$$

We thus have

$$\begin{cases} \dfrac{\widetilde{\phi_m}}{|\vec{a}|} = \dfrac{\Delta\vec{k}_{q_s}\cdot\vec{a}}{\pi|\vec{a}|} \simeq \dfrac{1+\eta\alpha}{1+\alpha}\dfrac{q_s}{|\vec{a}|} - \dfrac{1}{|\vec{a}|}\cdot\dfrac{k_{q_s}}{k_1}\left[\tan\left(\dfrac{\theta}{2}\right)\sin\theta_{q_s}+\cos\theta_{q_s}\right] \\ \dfrac{\widetilde{\phi_{m'}}}{|\vec{b}|} = \dfrac{\Delta\vec{k}_{q_s}\cdot\vec{b}}{\pi|\vec{b}|} \simeq \dfrac{\alpha}{1+\alpha}\cdot\dfrac{q_s}{|\vec{b}|} - \dfrac{1}{|\vec{b}|}\cdot\dfrac{k_{q_s}}{\eta k_1\sin\theta}\sin\theta_{q_s}. \end{cases} \tag{10.40}$$

with

$$\begin{cases} k_1|\vec{a}| \simeq \dfrac{\pi}{\cos\frac{\theta}{2}} \\ k_1|\vec{b}| \simeq \dfrac{\pi}{\eta\sin\theta}. \end{cases} \tag{10.41}$$

It yields

$$\begin{cases} \dfrac{\widetilde{\phi_m}}{|\vec{a}|} \simeq \dfrac{1+\eta\alpha}{1+\alpha}\dfrac{q_s k_1}{\pi}\cos\dfrac{\theta}{2} - \dfrac{k_{q_s}}{\pi}\left[\sin\dfrac{\theta}{2}\sin\theta_{q_s}+\cos\dfrac{\theta}{2}\cos\theta_{q_s}\right] \\ \qquad \simeq \dfrac{q_1 k_1}{\pi}\cos\dfrac{\theta}{2} - \dfrac{k_q}{\pi}\cos\left(\theta_{q_s}-\dfrac{\theta}{2}\right) \\ \dfrac{\widetilde{\phi_{m'}}}{|\vec{b}|} \simeq \dfrac{\alpha}{1+\alpha}\cdot\dfrac{\eta q_1 k_1}{\pi}\sin\theta - \dfrac{k_{q_s}}{\pi}\sin\theta_{q_s} \\ \qquad \simeq \dfrac{\eta\alpha}{1+\eta\alpha}\cdot\dfrac{q_1 k_1}{\pi}\sin\theta - \dfrac{k_{q_s}}{\pi}\sin\theta_{q_s} \\ \widetilde{\phi_{m'}} \simeq \dfrac{\alpha}{1+\alpha}q_s - \dfrac{k_{q_s}}{\eta k_1}\dfrac{\sin\theta_{q_s}}{\sin\theta} \end{cases} \tag{10.42}$$

Where we have used $q_s = \frac{1+\alpha}{1+\eta\alpha}q_1$, and $k_{q_s} = q_s k_s \simeq q_s\frac{1+\eta\alpha}{1+\alpha}k_1$. $\widetilde{\phi_{m'}}$ can take any value $p\in\mathbb{Z}$ to satisfy the Laue conditions. We consider the experimental situation in which we adjust α so that $\frac{\alpha}{1+\alpha}q_s = p_0\in\mathbb{Z}$. The second Laue equation reads $\widetilde{\phi_{m'}} = p = p_0 - \frac{k_q\sin\theta_{q,p}}{\eta k_1\sin\theta}$, i.e. $\sin\theta_{q,p} = (p_0-p)\cdot\frac{\eta k_1\sin\theta}{k_q}$. The first equation of (10.42) then reads

$$\begin{aligned} \frac{\widetilde{\phi_m}}{|\vec{a}|} &\simeq \frac{q_1k_1-k_q}{\pi}\cdot\left[1-\frac{1}{2}\left(\frac{\theta}{2}\right)^2\right] - \\ &\qquad \frac{k_q}{\pi}\left[\frac{\theta}{2}\cdot(p_0-p)\cdot\frac{\eta k_1\theta}{k_q} - \frac{1}{2}\cdot\left((p_0-p)\cdot\frac{\eta k_1\theta}{k_q}\right)^2\right] \\ &= \frac{1}{\pi}\cdot[q_1k_1-k_q]\cdot\left[1-\frac{\theta^2}{8}\right] - \\ &\qquad (p_0-p)\cdot\frac{\eta k_1\theta^2}{2\pi}\left[1-(p_0-p)\cdot\frac{\eta k_1}{k_q}\right] \end{aligned} \tag{10.43}$$

as expected. The first term is the regular phase matching factor, but for a second order correction due to the crossing angle. This is what is reduced to zero when we adjust the experiment to have a well phase matched, dominant p_0 order.

The second term is the geometrical phase mismatch term of Heyl et al.(equation 9.41). It implies that, if the phase matching is optimized for one diffraction order, the other orders ($p\neq p_0$) will not be phase matched at the same. There is a correction that increases with $p-p_0$ [1].

[1] In Heyl et al., this geometrical phase mismatch term was derived considering that the zeroth order of diffraction was best phase matched. Here, we have generalized the derivation to situations where any order p_0 is best phase matched.

10.4.2 Transverse phase matching

The contribution to transverse phase matching comes from the term G_b in equation 10.36.

$$\begin{aligned}&\left|G_b\left(\Delta\vec{k}_{q_s},\vec{L}^b_{med}\right)\right|^2\\&=\sin\left(\frac{\left(\frac{2L^b_{abs}}{b}\right)^2}{1+\left(\frac{\pi 2L^b_{abs}}{L^b_{coh}}\right)^2}\right)\cdot\left[1+e^{\frac{-L^b_{med}}{L^b_{abs}}}-2e^{\frac{-L^b_{med}}{2L^b_{abs}}}\cos\left(\frac{\pi L^b_{med}}{L^b_{coh}}\right)\right].\end{aligned}\tag{10.44}$$

It takes the same form as G_a, but along the transverse axis. This would mean that G_b plays the same role as G_a in collinear, absorption limited HHG, but along the transverse length of the medium. However, in this case, L^b_{med}, the medium length along the transverse direction has the dimensions of the beam waist ω_0 (of a few tens of microns), while the absorption length, L^b_{abs}, is of the order of a few millimeters. Therefore, $L^b_{abs} \gg L^b_{med}$ always. There is no problem of the harmonic efficiency being limited by absorption along $\vec{b}$. Equation 10.44 reduces to

$$\left|G_b\left(\Delta\vec{k}_{q_s},\vec{L}^b_{med}\right)\right|^2=\sin\left(\frac{\left(\frac{2L^b_{abs}}{b}\right)^2}{1+\left(\frac{\pi 2L^b_{abs}}{L^b_{coh}}\right)^2}\right)\cdot 2\sin^2\left(\frac{\pi L^b_{med}}{2L^b_{coh}}\right).\tag{10.45}$$

As a result, G_b peaks when $L^b_{\text{med}} = L^b_{\text{coh}}$, but with different amplitudes for the different diffraction orders. And for a given harmonic, the best phase matched diffraction order will depend on α due to the dependence of L^b_{abs} on α. Hence G_b contributes a purely geometrical effect on the HHG efficiency that manifests itself in the harmonic yield.

10.5 Discussion

With this new 2D theoretical model, we can successfully identify the microscopic and macroscopic effects in HHG emission yields independently. The term $\widetilde{G}\left(\Delta\vec{k}_{q_s}\right)$ give the single atom response, i.e., the response of an individual atom to the intense laser field. The contribution from the term $\left[\widetilde{G}\left(\Delta\vec{k}_{q_s}=0\right)\cdot G_b\left(\Delta\vec{k}_{q_s}=0\right)\right]$ was considered in detail in the previous part of this thesis where we developed the "three intertwined gratings" model to predict the intensity distribution of the emission yield of each diffraction order. Now, when considering the macroscopic response of the medium, we discover two additional terms $G_a\left(\Delta\vec{k}_{q_s}\right)$ and $G_b\left(\Delta\vec{k}_{q_s}\right)$, giving insight into phase matching effects along the longitudinal and transverse directions respectively. $G_a\left(\Delta\vec{k}_{q_s}\right)$ is the well known formula of Constant et al. introduced in section 9.1.1 obtained from the 1D model that has been used as the standard approach in describing phase matching effects in HHG in absorbing gases up to now [10, 104, 110]. We could also retrieve the geometrical non collinear phase mismatch term identified by Heyl et.al [83], that is implicit in $G_a\left(\Delta\vec{k}_{q_s}\right)$.

$G_b\left(\Delta\vec{k}_{q_s}\right)$ on the other hand is a term that arises from the non collinear geometry that has been overlooked up to now. This additional term arising from the transverse extent of the medium is quite

interesting due to its effect on the harmonic emission yields. In the next chapter, we will present results of numerical simulations and experiment which shows the importance of the identification of this new geometrical phase matching factor.

CHAPTER 11

Numerical simulations, experimental results and discussion

In the previous chapter, we developed a 2D theoretical model to explain the harmonic emission in NCHHG. In particular, we could identify three separate contributions to the intensity distribution arising from the microscopic effects and the longitudinal and transverse phase matching effects respectively. Phase matching factors along the longitudinal direction was shown to play the same role in NCHHG as in conventional collinear high harmonic generation. However, the macroscopic extent of the medium in the transverse direction plays an additional role in phase matching in NCHHG, which has not been identified so far. Naturally, we expect this to have an effect on the far field properties of the harmonics. In Part III, we developed the active grating model focusing on the microscopic response of the medium and the transverse grating structure, to arrive at a bell shaped amplitude distribution for the harmonic yield of the various diffraction orders as a function of the amplitude ratio of the two driving beams. But a closer look at the experimental data reveals that the amplitude distribution is not strictly bell-shaped (see Fig. 11.1). There is a revival of intensity, a detail that did not show up in theoretical prediction of part III. In addition, there are some wiggles in the curve (for example, around $\alpha = 0.4$ and 0.6 in Fig. 11.1.(a) and $\alpha = 0.7$ in Fig. 11.1.(c)). In this chapter, we will see if we can explain the appearance of these revivals and wiggles by introducing phase matching effects into the model. More precisely, we will study in detail the individual terms that play a role in determining the shape of the intensity distribution curves of the diffraction orders, complementing them with the results of numerical simulations.

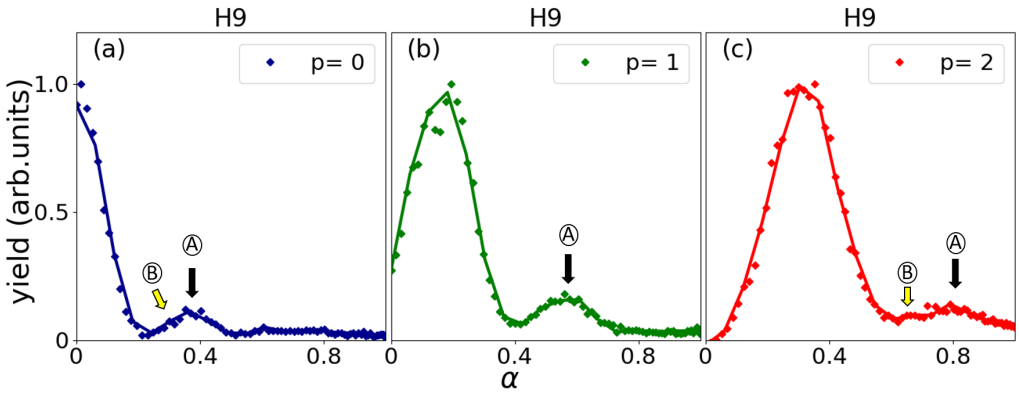

Figure 11.1: The evolution of the harmonic yield with increasing perturbation for the 0^{th}, 1^{st} and 2^{nd} diffraction orders of H9. The markers are experimental data points fitted with a cubic spline (solid curve). Ⓐ point out the revivals and Ⓑ, the wiggles.

11.1 Numerical results

The simulations presented in this section are implemented by a Python code that was adapted from the Github repository (https://github.com/c-benko/HHG_Phasematching) of Craig Benko. The code was developed during the course of his PhD thesis [111] in the Atomic, Molecular and Optics Physics and precision measurements group of Prof. Jun Ye at JILA, University of Colarado. It is written for a general HHG phase matching simulation, implementing the absorption-limited formula of Constant et al.[10]. It can provide the harmonic yield and parameters like the coherence length as a function of time across a pulse or an integrated yield over the pulse for a variety of experimental conditions. The HHG yield is obtained by the numerical calculation of the amplitude of harmonic q, with an atomic response modelled as $E^{q_{\text{eff}}}$ and the ratio of electron density to neutrals density in the medium computed from the integration of ADK formula and plugged into the optical indices. For the results presented below, this code was adapted to include transverse phase matching effects, introduced in the previous chapter. The simulations have been done for $\lambda = 800$ nm, 25 fs Gaussian beam with the peak intensity varying from 0.5 to 2*10^{14} W/cm^2 with α ranging from 0 to 1. The medium length is set as 1 mm along the longitudinal direction (L^a_{med}), and as 100μm along the transverse (L^b_{med}). These figures are chosen to approximately match the experimental conditions where we had a beam waist of 30 μm, and a hole for gas inlet of 500 μm. The target gas is Argon, unless otherwise specified.

11.1.1 Ionization

The generating medium plays a large role in phase matching through its effect on $\Delta k_{\text{neutral}}$ and Δk_{plasma}. These terms have opposite signs and their relative contributions are determined by the ionization

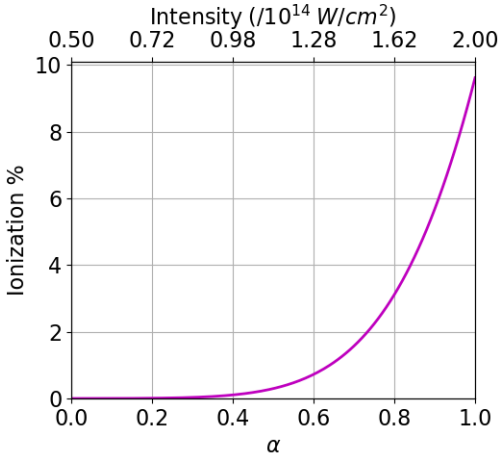

Figure 11.2: The percentage of ionized argon gas as a function of α. The first beam is maintained at an intensity of $0.5 * 10^{14}$ W/cm^2. The intensity at focus corresponding to the α values are indicated on top.

fraction. If the ionization fraction is large enough so that the plasma term is greater than the neutral term, then Δk_q can never be zero. Therefore, at high enough ionization fractions, phase matching cannot occur [43]. The ionization fraction at which this happens is known as critical ionization (η_c), which sets an upper limit on the intensity that can be used for HHG with a given wavelength. $\eta_c \simeq 2\%$ for argon when generating with 800 nm. By varying the pressure, good phase matching can be achieved as long as $\eta < 5\%$ [112].

In the simulation results shown in this chapter, the gas density is set at $\rho_0 = 0.4 * 10^{17}$atoms/cm^3 which will vary with time as $\rho(t) = \rho_0(1-\eta(t))$ over the laser pulse. The ionization fraction, η is calculated by,

$$\eta = 1 - \exp\left[-\int_{-\infty}^{\infty} \omega_{ADK}(t), \mathrm{dt}\right] \tag{11.1}$$

where $\omega_{ADK}(t)$ is the ionization rate calculated using ADK theory modified by Tong and Lin [113]. Fig. 11.2 shows the time integrated ionization fraction of argon when scanning α from 0 to 1 for I_1 = 0.5 to $2 * 10^{14}$ W/cm^2. Less than 10% of argon is ionized within the selected α range and the ionization fraction crosses 5% around $\alpha = 0.9$ corresponding to an intensity of around $1.8 * 10^{14}$ W/cm^2 at the focus of the two beams.

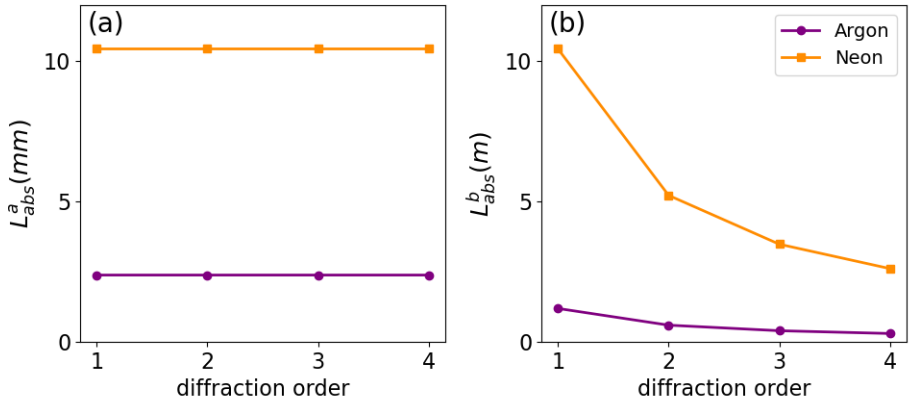

Figure 11.3: Absorption lengths along the longitudinal axis (a) and the transverse axis (b) calculated for different diffraction orders of H15, with two different target gases, argon (purple) and neon (orange). The two beams cross at an angle of 15 mrad. The total intensity at focus is $0.5 * 10^{14}$W/cm^2 once the pulse has left the medium. The gas density is $\rho_0 = 0.4 * 10^{17}$atoms/cm^3 in both cases.

.

11.1.2 Absorption length and coherence length

As already seen, the conditions for good phase matching are determined by coherence and absorption lengths. In section 10.4.1, they were defined as

$$\begin{aligned} \frac{\phi_m}{|\vec{a}|} &= \Delta\vec{k}_{q_s} \cdot \frac{\vec{a}}{|\vec{a}|} = \frac{\pi}{L^a_{coh}} + i\frac{1}{2L^a_{abs}} \text{ and} \\ \frac{\phi_m}{|\vec{a}|} &= \Delta\vec{k}_{q_s} \cdot \frac{\vec{b}}{|\vec{b}|} = \frac{\pi}{L^b_{coh}} + i\frac{1}{2L^b_{abs}}. \end{aligned} \tag{11.2}$$

For small angles, we may approximate

$$\begin{cases} \dfrac{\widetilde{\phi_m}}{|\vec{a}|} \simeq \dfrac{qk_1}{\pi}\cos\dfrac{\theta}{2} - \dfrac{k_q}{\pi}\cos\left(\theta_q - \dfrac{\theta}{2}\right) \\ \dfrac{\widetilde{\phi_{m'}}}{|\vec{b}|} \simeq \dfrac{\eta\alpha}{1+\eta\alpha} \cdot \dfrac{\eta k_1}{\pi}\sin\theta - \dfrac{k_q}{\pi}\sin\theta_q. \end{cases} \tag{11.3}$$

Thus L^a_{abs} and L^b_{abs} can be obtained from the imaginary part of the above formulae.

$$\begin{aligned} L^a_{\text{abs}} &= \frac{\pi}{2k_q^{\text{im}}\cos\left(\theta_q - \frac{\theta}{2}\right)} \\ &= \frac{\pi}{\sigma\rho\cos\left(\theta_q - \frac{\theta}{2}\right)} \qquad (11.4) \\ &\simeq \frac{\pi}{\sigma\rho}. \qquad (11.5) \end{aligned}$$

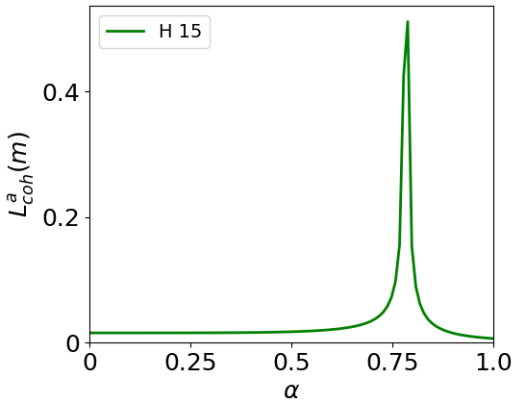

Figure 11.4: The coherence length of H 15 as a function of α in the case of collinear HHG in argon gas. The first beam is maintained at an intensity of $0.5 * 10^{14}\ W/\text{cm}^2$.

where σ is the ionization cross section and ρ, the atomic density of the target atom. Similarly,

$$L^b_{\text{abs}} = \frac{\pi}{\sigma\rho\sin\theta_q} \simeq \frac{\pi}{\sigma\rho\cdot\theta_q(q,p)}. \tag{11.6}$$

The above equations show that L^a_{abs} is almost independent of the order of diffraction up to the second order terms while L^b_{abs} changes considerably with the order of diffraction through $\theta(q,p)$. Also, the absorption lengths are independent of α, but for the (limited) change of atomic density during the laser pulse. In Fig. 11.3 are presented the values of L^a_{abs} and L^b_{abs} obtained from simulation. L_{coh} is given by the real part of equation 11.3. Fig .11.4 is an example of the typical coherence length calculated with the above model in the case of collinear high harmonic generation with two beams. There is a given value of α for which L^a_{coh} peaks. When η remains below the critical ionization value, the coherence length remains fairly constant. With increasing infrared intensity, the ionization crosses the critical value and L^a_{coh} peaks, maximising harmonic emission and drops after. After this point, phase matching is no longer possible for the given gas density.

In the case of non collinear HHG, multiple diffraction orders are possible, each with its own L^a_{coh} value. In Fig. 11.5.(a) are plotted the values of L^a_{coh} for different diffraction orders of H15 as a function of α. The coherence lengths of higher diffraction orders do not vary much with α, unlike the case of $p = 0$. For $p = 0$, there exists a value of α for which $\Delta\vec{k}_{q_s}$ is close to zero and L^a_{coh} peaks. But when $p \neq 0$, even for the case of perfect phase matching, there is an additional geometrical phase mismatch term (the second term in equation 10.43) dictating the value of L^a_{coh}.

L^b_{coh}, on the other hand, has distinct values of α at which it peaks depending on the order of diffraction (Fig. 11.5.(b)). With the active grating model, we have already seen that it is the transverse grating structure of the medium that gives rise to the diffraction orders and the dominant order of diffraction is α dependent. In other words, at a given α, there is one order of diffraction that is best phase matched. The value of α (α_{max}) which satisfies the best phase matching condition for a given

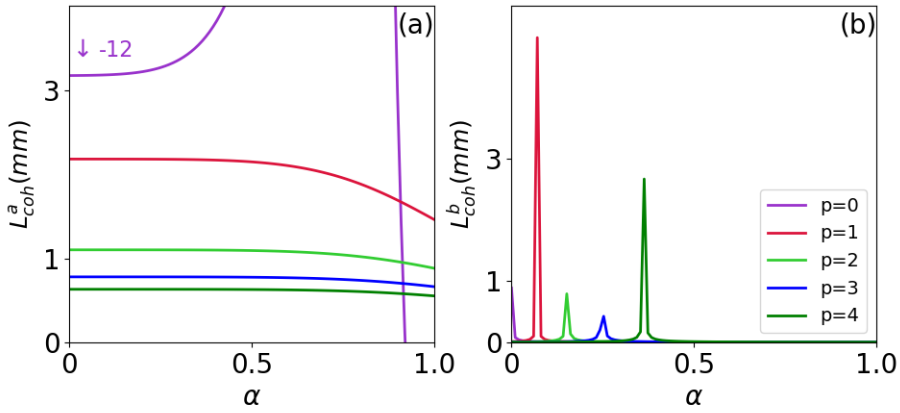

Figure 11.5: Coherence lengths along the longitudinal axis (a) and the transverse axis (b) as a function of α for H15. The first beam is maintained at an intensity of $0.5 * 10^{14}$ W/cm^2. The two beams cross at an angle of 15 mrad.

diffraction order is determined by L^b_{coh}. In the following section we will see this effect of L^b_{coh} in the intensity distribution curve; how it may be articulated with the active grating model and can be validated by experimental data.

11.1.3 Intensity distribution of the diffraction orders

To recall, the electric field amplitude of a given harmonic in the far field is a factorisation of three terms $\widetilde{G}$, G_a and G_b.

$$I_q \propto \left|\widetilde{G}\left(\Delta\vec{k}_{q_s}\right)\right|^2 \left|G_a\left(\Delta\vec{k}_{q_s}\right)\right|^2 \left|G_b\left(\Delta\vec{k}_{q_s}\right)\right|^2. \tag{11.7}$$

We will analyze each of these terms individually to see the role they play in the intensity distribution curves.

Microscopic response

We first focus on the microscopic response, given by $\widetilde{G}\left(\Delta\vec{k}_{q_s}\right)$. In section 10.3, we introduced $G(\vec{r})$ as the function defining the amplitude of the harmonic emission and its intrinsic atomic phase, φ_{at}. From TDSE computation, we showed that the yield of the harmonics should read $|d|^2 \simeq I^{q_{\text{eff}}}$, which for the field reads $|d| \simeq |E|^{q_{\text{eff}}}$ and $\varphi_{at} = \alpha_{at} I$ (see section 8.2.2). It may be approximated by a Gaussian in the HHG emission pockets, at least for high enough α, where the approximation was made along the transverse direction. However, now we consider the contributions along both the transverse x axis and the longitudinal z axis. The approximation holds for the z axis as well. Thus, along the same

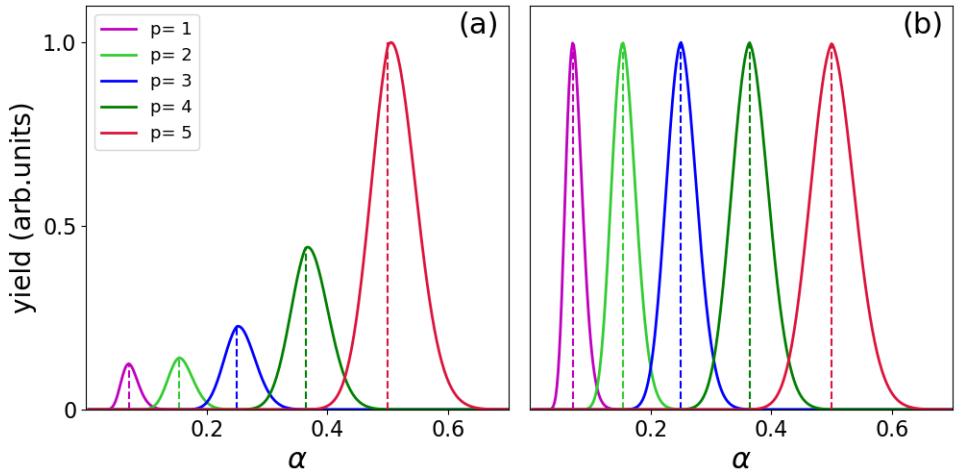

Figure 11.6: The microscopic response $\widetilde{G}\left(\Delta\vec{k}_q\right)$, as a function of α for H15, calculated using equation 11.12, with the leading amplitude term (equation E.13) (a) and without (b). $I_1 = 0.5 * 10^{14}\ W/\mathrm{cm}^2$. The two beams cross at an angle of 15 mrad.

lines as in section 8.1.4, we set

$$G(x,z) = E_1^{q_{\mathrm{eff}}}(1+\alpha)^{q_{\mathrm{eff}}} \cdot e^{-\left(\frac{\Delta\vec{k}.\vec{r}}{\varphi_G}\right)^2} e^{-i\alpha_{at} I(\vec{r})} \tag{11.8}$$

$$= E_1^{q_{\mathrm{eff}}}(1+\alpha)^{q_{\mathrm{eff}}} \cdot e^{-\left(\frac{\Delta\vec{k}.\vec{r}}{\widetilde{\varphi}_G}\right)^2} \tag{11.9}$$

with the α dependent complex parameter:

$$\frac{1}{\widetilde{\varphi}_G^2} = \frac{q_{\mathrm{eff}}}{2} \cdot \frac{\alpha}{(1+\alpha)^2} + i\alpha_{at} \cdot \alpha \cdot I_0. \tag{11.10}$$

The microscopic response is the 2D Fourier transform of this function which reads as (see appendix E)

$$\widetilde{G}\left(\Delta\vec{k}_q\right) = \underbrace{\sqrt{\pi} E_1^{q_{\mathrm{eff}}} \cdot \frac{(1+\alpha)^{q_{\mathrm{eff}}} \widetilde{\varphi}_G}{|\Delta\vec{k}|}}_{amplitude} \cdot e^{-\frac{\widetilde{\varphi}_G^2}{4} \cdot \left(\frac{\Delta k_q^{\perp}}{\Delta k^{\perp}}\right)^2}. \tag{11.11}$$

It may be written in terms of coherence and absorption lengths as (see appendix E)

$$\widetilde{G}(\Delta\vec{k}_q) \quad = \quad A_q(\alpha,\theta_0) \cdot exp\left[-\frac{\mathscr{R}(\varphi_G^2)}{4}\frac{\lambda_1^2}{4\theta_0^2}\left\{\frac{1}{L_{coh}^{b^2}}^2 + \frac{-1}{\pi^2 L_{abs}^{b^2}}\right\}\right] exp\left[\frac{\mathscr{I}(\varphi_G^2)}{4}\frac{\lambda_1^2}{4\theta_0^2}\left(\frac{2}{L_{coh}^b L_{coh}^a}\right)\right].$$

where,

$$A_q(\alpha,\theta_0) = \frac{E_1^{q_{\mathrm{eff}}}}{\sqrt{\alpha}} \cdot \frac{(1+\alpha)^{q_{\mathrm{eff}}}}{\frac{q_{\mathrm{eff}}^2}{4(1+\alpha)^4} + \alpha_{at}^2 \cdot I_0^2}^{\frac{1}{4}} \cdot \frac{1}{\eta\theta_o k_1} \tag{11.12}$$

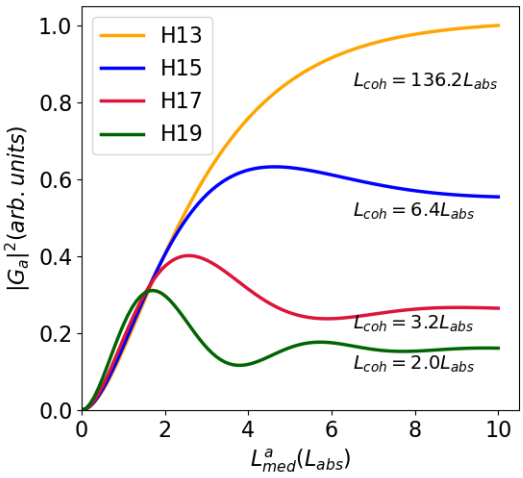

Figure 11.7: Phase matching along the propagation direction in NCHHG. Harmonic yield ($|G_a\left(\Delta\vec{k}_{q_s}\right)|^2$) for p=0 as a function of the medium length, along $\vec{a}$. The solid lines represent the harmonic signal for four different harmonics which give four different values of L_{coh} along $\vec{a}$. The intensity of the main beam is $0.5 * 10^{14}$ W/cm^2, with $\alpha = 0.2$. The two beams cross at an angle of 30 mrad.

Fig.11.6.(a) shows the evolution of $\widetilde{G}\left(\Delta\vec{k}_q\right)$ for H15, having introduced the coherence and absorption lengths. We get a Gaussian amplitude distribution for each curve as expected from the active grating model described in chapter 8, where we considered the medium as a thin sheet with zero longitudinal extent. But in that case, the harmonic field at the output was given by $\widetilde{G}(\vec{r}, \Delta\vec{k}_q = 0) \cdot G_b(\Delta\vec{k}_q = 0)$, ignoring phase matching effects. Fig. 11.6.(b) is the plot of only the Gaussian term of equation 11.12, excluding the leading term $A_q(\alpha, \theta_0)$. Although we introduced a longitudinal dimension to the pockets, we retrieve the Gaussian distribution centered at $\alpha_{\max}$ for each diffraction order.

Longitudinal phase matching effects

The longitudinal phase matching term reads,

$$\left|G_a\left(\Delta\vec{k}_{q_s}, \vec{L}^a_{med}\right)\right|^2 = \frac{\left(\frac{2L^a_{abs}}{a}\right)^2}{1+\left(\frac{\pi 2L^a_{abs}}{L^a_{coh}}\right)^2} \cdot \left[1 + e^{\frac{-L^a_{med}}{L^a_{abs}}} - 2e^{\frac{-L^a_{med}}{2L^a_{abs}}} \cos\left(\frac{\pi L^a_{med}}{L^a_{coh}}\right)\right]. \tag{11.13}$$

$|G_a|^2$ is plotted against L^a_{med} in Fig. 11.7 for the case of different harmonics generated with two beams crossing at an angle of 30 mrad. The value of $\frac{L_{\text{coh}}}{L_{\text{abs}}}$ varies with harmonic order q and the phase matching changes accordingly. We get results similar to those of Constant et.al [10] (see Fig. 9.1) and retrieve

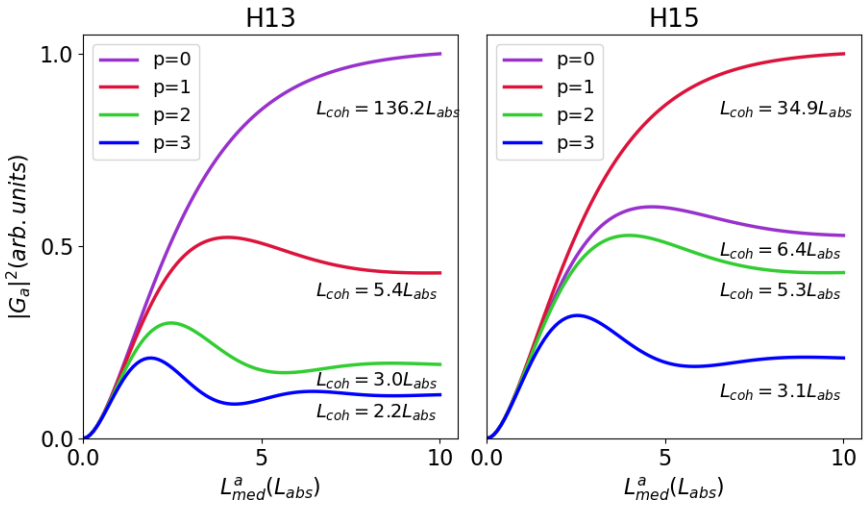

Figure 11.8: Harmonic yield as a function of the medium length, in units of absorption length along $\vec{a}$ for a) H13 and b) H15. The solid lines represent the harmonic signal for four different diffraction orders. The intensity of the main beam is $0.5 * 10^{14}$W/cm^2 and $\alpha = 0.2$. The two beams cross at angle of 10 mrad and the gas density is $1.2 * 10^{17}$atoms/cm^2.

the conditions

$$\begin{cases} L^a_{\text{med}} > 3L^a_{\text{abs}} \\ L^a_{\text{coh}} > 5L^a_{\text{abs}} \end{cases} \tag{11.14}$$

for good phase matching along the propagation direction ($\vec{a}$). This is a check of the numerical code we adapted. Since both L^a_{coh} and L^a_{abs} are dependent on the harmonic order, q, and the emission angle, $\theta_q \left(= \frac{p\theta}{q}\right)$, the phase matching conditions are different for different diffraction orders. Fig. 11.8 shows the harmonic signal calculated with only G_a for two different harmonics, H13 and H15. While diffraction order p=0 satisfies the good phase matching conditions for H13, it is p=1 that is best phase matched for H15. This effect arises due to the non collinear geometry. For a given harmonic order, a given diffraction order satisfies the best phase matching conditions as already seen in section 10.4.1.

Transverse Phase Matching Effects

The term G_b has its origin in $\frac{\sin\left(\frac{m'_0\phi_{m'}}{2}\right)}{\sin(\phi_{m'})}$. This function has a maxima when $\phi_{m'}$ takes values around any multiple of π. We write $\varphi_{m'} = j\pi + \delta$, with j an integer and $\delta \ll \pi$. We thus have $\sin(j\pi + \delta) = (-1)^j\delta$. In terms of coherence and absorption lengths,

$$\phi_{m'} = |\vec{b}|\left(\frac{\pi}{L^b_{coh}} + i\frac{1}{2L^b_{abs}}\right) = \Delta\vec{k}_{q_s} \cdot \vec{b}, \tag{11.15}$$

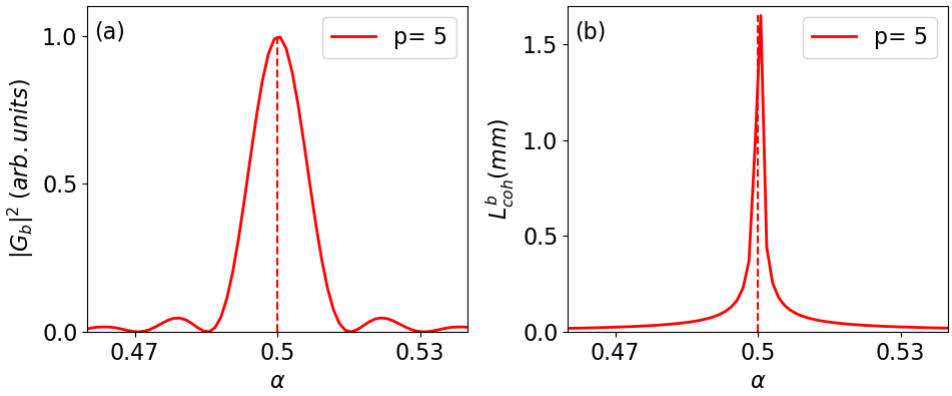

Figure 11.9: (a)Harmonic yield considering only the term $|G_b|^2$, plotted as a function of α for $p = 5$ of H15. The medium length, $L^b_{\text{med}} = 100\,\mu m$, $\text{I}_1 = 0.5 * 10^{14}\text{W/cm}^2$ and the two beams cross at an angle of 40 mrad. (b) L^b_{coh} for the same parameters. The dashed lines denote the position of α_{max}.

which gives

$$\left|G_b\left(\Delta\vec{k}_{q_s}, \vec{L}^b_{med}\right)\right|^2 = \left(\frac{\sin\left(\frac{m'_0\phi_{m'}}{2}\right)}{(-1)^j\delta}\right)^2 = \frac{\sin^2\left(m'_0|\vec{b}|\left(\frac{\pi}{L^b_{coh}} + i\frac{1}{2L^b_{abs}}\right)\right)}{\delta^2}. \tag{11.16}$$

The values of j and δ are numerically obtained from $(\Delta\vec{k}_{q_s}\cdot\vec{b})$. $|G_b|^2$ as a function of increasing perturbation is plotted in Fig. 11.9 for the case of p=5 of H15. It is a $sinc$ function against $\phi_{m'}$. When plotted against α, G_b thus shows a maximum at $\alpha_{\text{max}} = p - q_s\frac{\alpha}{1+\alpha}$. This is as expected from the condition for the case of perfect phase matching (equation D.8) given by

$$\phi_{m'} = (p - \frac{\alpha}{1+\alpha}\cdot q_s)\pi = j\pi.$$

Successive diffraction orders will peak at successive values of α, given by $\alpha_{\text{max}} = p - \frac{\alpha}{1+\alpha}\cdot q_s$. This is where the coherence lengths along $\vec{b}$ for each diffraction order also peaks. (see Fig. 11.9.(b)). Between two such main peaks, the yield shows some wiggles whose periodicity is ruled by $\frac{(m'_0)}{2} = \frac{L^b_{\text{med}}}{2b}$. It is also interesting to note that unlike in the case of G_a, there is no problem of the harmonic efficiency being limited by absorption along $\vec{b}$ as $L^b_{abs} \gg L^b_{med}$ always. In Fig. 11.10 is plotted G^2_b as a function of medium length, L^b_{med}, in units of the focal spot size. The yield increases quadratically with increasing L^b_{med} up to the size of the focal spot. L^b_{med} being always within this range, the generation is not limited by absorption.

11.1.4 Total yield

The total contribution to intensity from both microscopic and the macroscopic responses is plotted in Fig. 11.11.(a) where the amplitude distribution for a given diffraction order of a harmonic

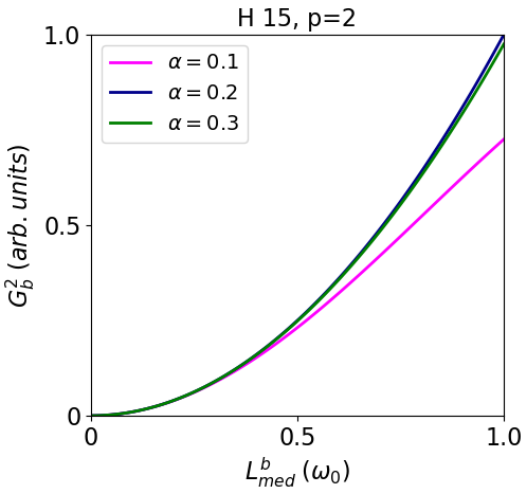

Figure 11.10: (a)Harmonic yield considering only the term $|G_b|^2$, plotted as a function of L^b_{med} in units of focal spot size for $p = 2$ of H15. The medium length, $L^b_{\text{med}} = 100\mu$m, $I_1 = 0.5 * 10^{14}$W/cm^2 and the two beams cross at an angle of 30 mrad. The different colours represent the calculations for three different α values.

against α is not simply a Gaussian distribution, but exhibits a revival of intensity. The maximum of each diffraction order is still centered at α_{max}, determined by L^b_{coh}. Our first hypothesis is that the revival in the amplitude distribution observed in the experiment is reproduced here. Even better, we could attribute it to G_b. The three functions $|\widetilde{G}(\Delta\vec{k}_{q_s})|^2$, $|\widetilde{G}(\Delta\vec{k}_{q_s})|^2 \cdot |G_a(\Delta\vec{k}_{q_s})|^2$ and $|\widetilde{G}(\Delta\vec{k}_{q_s})|^2 \cdot |G_a(\Delta\vec{k}_{q_s})|^2 \cdot |G_b(\Delta\vec{k}_{q_s})|^2$ are plotted in Fig. 11.12.(a), (b) and (c) respectively. The function corresponding to the microscopic response, $\widetilde{G}$ is a Gaussian distribution as expected (Fig. 11.12.(a)). The addition of phase matching effects along the propagation direction does not change the shape of the curve (Fig. 11.12.(b)). However, it is still responsible for the macroscopic growth of the harmonic signal as in the case of conventional HHG with a single beam. The signal strength depends on L^a_{coh}. And L^a_{coh} varies with diffraction order, thus deciding the diffraction order with the highest yield. This is evident when comparing Fig. 11.12.(a), (b) and Fig. 11.5.(a). The consideration of phase matching effects along the transverse direction, on the other hand, changes the intensity distribution curve to produce the revivals or wiggles Fig. 11.12.(c). The intensity distribution curves of diffraction orders 1, 2 and 3 of harmonic 9 to 15 are plotted in Fig.11.13. The position of α_{max} is harmonic dependent. The overall Gaussian envelope of $\widetilde{G}$ determines the number and amplitude of the secondary peaks that are visible. G_b thus appears as a good candidate for these revivals. And importantly, all harmonics show the same trend (see Fig. 11.13).

11.1.5 Effect of G_b on the intensity distribution curves

The physical origin of this intensity revival due to G_b is purely geometrical, with no interplay with the refractive indices of the medium. It arises from the fringe pattern created by the two crossing beams at focus. If the transverse extent of the medium is the same as the fringe width (or the case of single beam HHG), there would not be a revival in the intensity. In Fig.11.14 is plotted the amplitude distribution of diffraction order, p=1 of H15 for three different crossing angles. We see that, with increasing θ_0, the revival occurs earlier, with a possibility for multiple revivals. In Fig. 11.14, we see the rise of a new peak (black dashed line) as well as a shift in position of existing peak (red, dashed line) to a lower value of α with increasing θ_0. Further proof that this revival is a purely geometric effect is that the amplitude distribution does not change for different gas media or pressure. In Fig. 11.15 is shown the intensity curves for two different target gases (a) and at two different gas densities for the same gas (b). In both argon and neon, the intensity distribution is exactly the same, except for the relative signal strength. This is a sure sign that the secondary peaks do not come from the macroscopic response of the medium. Also, on increasing the gas pressure to twice its value, harmonic signal from argon still gives the same intensity distribution curve, but with a higher signal due to the quadratic growth of signal with pressure. Since the peak positions are not altered with gas pressure, this revival effect arising from phase matching is purely geometrical.

With these results and conclusions from the theoretical model and the numerical simulations, we will now try to validate our model with experimental results.

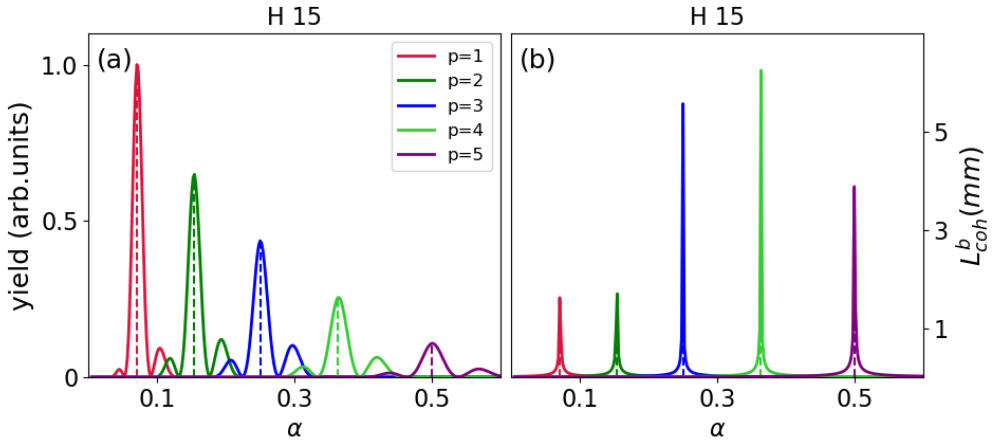

Figure 11.11: The total intensity distribution as a function of α for H15 including the longitudinal and transverse phase matching effects(a) and the corresponding values of L^b_{coh} (b). $I_1 = 0.5 * 10^{14} \text{W/cm}^2$ and the two beams cross at an angle of 15 mrad. The dashed lines denote the position of α_{max}.

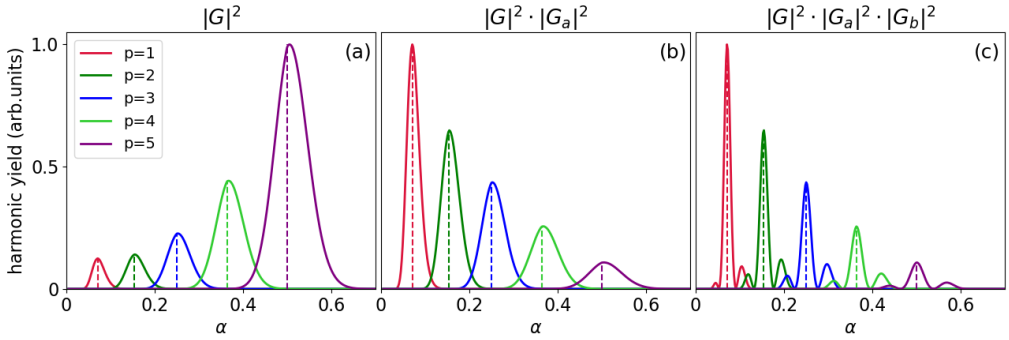

Figure 11.12: The total yield of H15, considering (a) only the microscopic response, (b) the microscopic response and longitudinal phase matching and (c) the microscopic response and longitudinal and transverse phase matching. $I_1 = 0.5 * 10^{14} W/cm^2$ and the two beams cross at an angle of 15 mrad. The dashed lines denote the position of α_{max}.

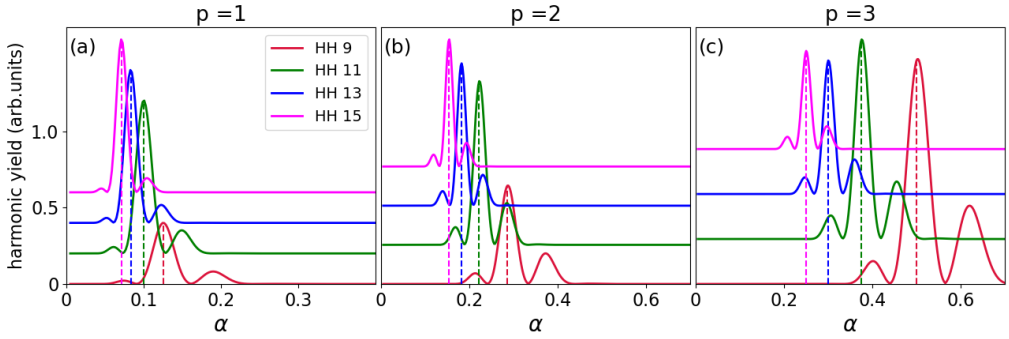

Figure 11.13: The amplitude distribution of p=1, p=2 and p=3 orders of diffraction for harmonics 9,11,13 and 15. $I_1 = 0.5 * 10^{14}$ W/cm^2 and $\theta_0 = 15$mrad. The plots are offset along the vertical axis for the sake of visibility. The dashed lines denote the position of α_{max}.

11.2 Experimental results

To support our hypothesis that the revivals and wiggles are arising from G_b and is a geometrical effect, we will compare the experimental data to our theoretical model. However, phase matching in an HHG experiment is a complicated process that is dynamic and spatially inhomogeneous. The optimisation of the harmonic signal requires the delicate control over many parameters, mainly gas pressure, laser intensity etc. Therefore, we will first try to confirm that the pressure dependent terms in G_a, G_b and $\widetilde{G}$, are well optimised for the selected experimental conditions and is not affecting the amplitude distribution.

11.2.1 Pressure scaling

In the low ionization regime, under a critical ionization rate, phase matching is achieved by tuning the gas density in such way that the positive dispersion phase mismatch compensates the negative geometrical and atomic dipole phase mismatches. Under these conditions, the XUV emission scales as the squared number of emitters, i.e. as the squared density [85]. A quadratic signal growth with pressure is thus a clear indication that the phase matching conditions are not changing significantly with gas pressure. This means that the coherence and absorption lengths are not altered greatly by a change in pressure and the experiment is done under conditions in which the terms in G_a and G_b, dependent on L_{coh} and L_{abs} are optimised for HHG and are not changing. Fig. 11.16 shows the experimental yield of diffraction order 1 of H9 evolving with α for two different backing pressures. The dashed line is the yield obtained after scaling to the quadratic increase of yield with pressure. It is a good indication that any alteration in the shape of the intensity distribution is an effect which does not depend on $\widetilde{G}$, G_a or G_b through their dependence on gas pressure. Note that the peak positions are not altered in the two cases as well.

11.2.2 Dependence on gas

The generating medium also plays a very important role in phase matching. The phase mismatch terms Δk_{dipole} and $\Delta k_{\text{neutral}}$ depends on the generating gas. The degree of ionization (r_{ion}) is different for different gases and we have already seen that it plays an important role in determining the coherence length. The microscopic response also changes with the generating medium through its atomic

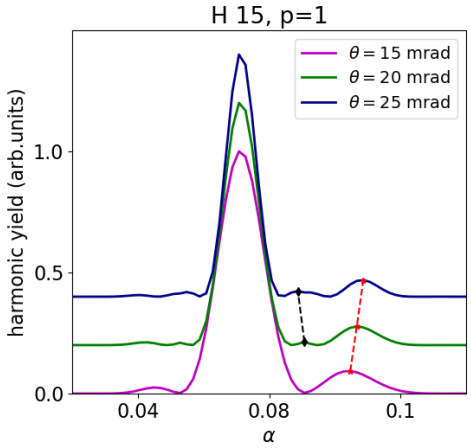

Figure 11.14: The amplitude distribution of p=1 order of diffraction for H15, plotted for different crossing angles θ_0 between the two beams. $I_1 = 0.5 * 10^{14} W/cm^2$. The plots are offset along the vertical axis for the sake of visibility.

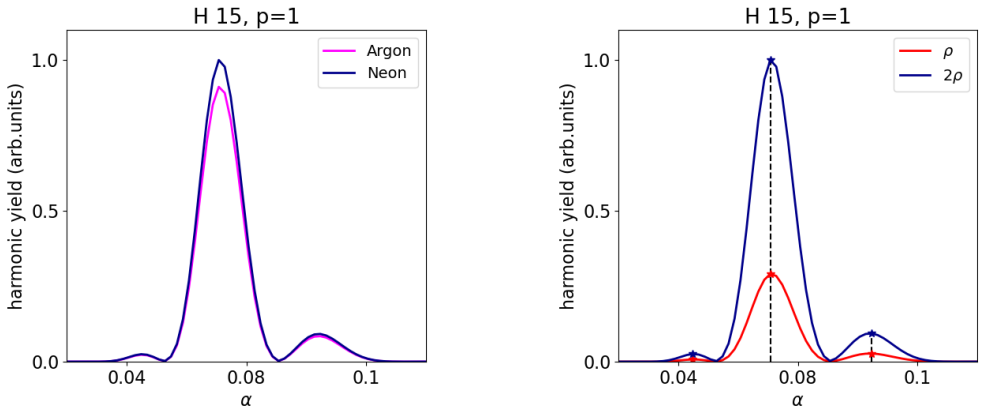

Figure 11.15: The amplitude distribution of p=1 order of diffraction for H15, plotted for different target gases (a) and different gas densities (ρ) in argon gas. $I_1 = 0.5 * 10^{14} W/cm^2$ and the two beams cross at an angle of 15 mrad. $\rho = 0.4 * 10^{17} atoms/cm^3$.

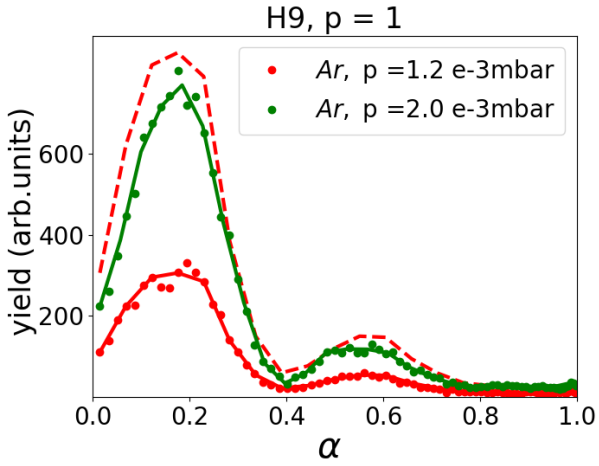

Figure 11.16: Experimentally obtained harmonic yield for diffraction order 1 of H15, generated in argon gas. The red dashed line is the yield of the red curve multiplied by a scaling factor of $(2/1.2)^2$ to show the quadratic scaling of harmonic yield with pressure. The values indicated in the legend are the backing pressures in the generating chamber.

phase dependence. Any change in the shape of intensity distribution curve, when comparing two different gases could indicate an effect on phase matching conditions due to the above parameters.

Fig. 11.17 is a comparison between the harmonic yield of H15 generated in argon and nitrogen under the same experimental conditions. It is observed that a change in gas does not alter the intensity distribution. Once again, the revival persists in nitrogen and occurs at the same value of α as in

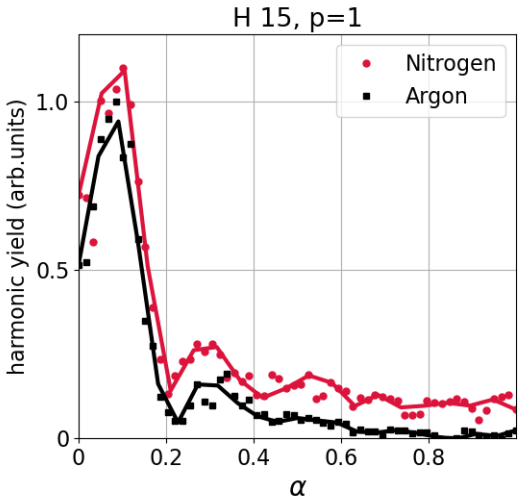

Figure 11.17: Experimentally obtained harmonic yield for p=1 of H15, generated in argon (black) and nitrogen (red). The markers are the experimental data and the dashed lines are the fits of the analytical model. The plots are vertically offset for the sake of visibility.

argon.

The results presented above are a good indication that this revival in intensity is not due to the refractive index dependent terms in phase matching in NCHHG. The question remains if it could be the geometrical part of G_b. To test this, we will fit our experimental data to the theoretical model.

11.2.3 Modelling the intensity distribution

The microscopic response $\widetilde{G}$ is of the form,

$$\left|\widetilde{G}(\Delta\vec{k}_q)\right| \propto A_q(\alpha,\theta_0)\cdot exp\left[-\mathscr{R}\left(\varphi_G^2\right)\left(\frac{\phi_{m'}}{\pi}\right)^2\right]. \tag{11.17}$$

This would give us an overall Gaussian that peaks around the value $\alpha_{\max} = \frac{p}{q-p}$ for a given diffraction order p of harmonic q, in the case of perfect phase matching. This was already seen in Part III of this thesis. The function G_b writes as

$$G_b = \frac{\sin\left(\beta\phi_{m'}\right)}{\sin\phi_{m'}} \tag{11.18}$$

where $\beta = \frac{m_0'}{2} = \frac{L_{\text{med}}^b}{2|b|}$. This $sinc$ function has the first maxima at α_{max} and consecutive maxima which occur with a periodicity $\beta\pi$. The total yield is modelled as a product of $\tilde{G}$ and G_b since G_a does not have a significant effect on the shape of the distribution, but only on the amplitude which is left as a free parameter in the fitting. The $sinc^2$ function, given the right periodicity, will allow the secondary

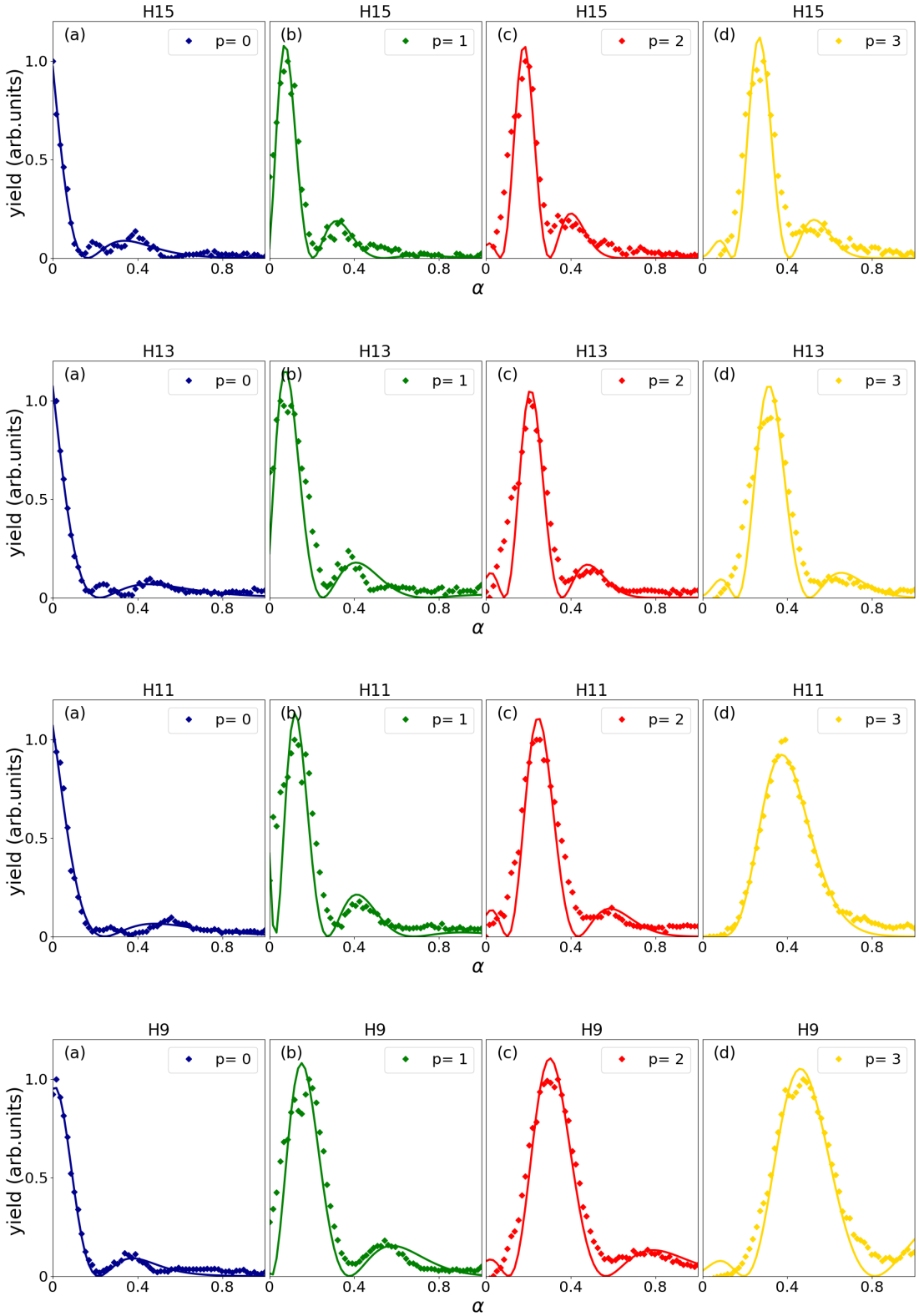

Figure 11.18: The harmonic yield as a function of α for different harmonic orders (individual rows). The markers are the experimental data and the solid lines are the fit of the curves using equation 11.19.

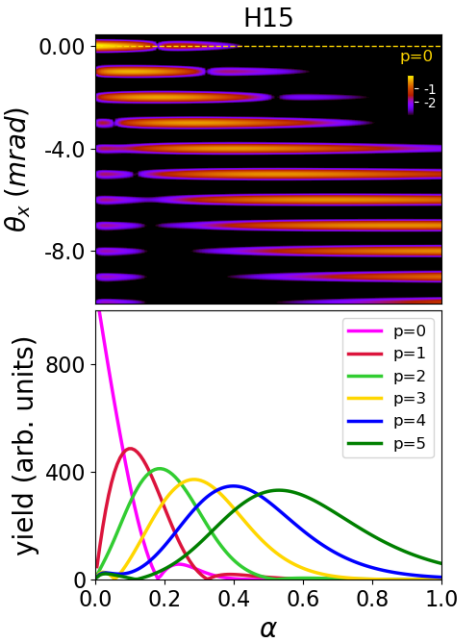

Figure 11.19: The results from the computation of the Fourier transform of equation 11.20 for H15. The top panel show the position and presence/absence of each order of diffraction with increasing α. The bottom panel shows emission yields of different diffraction orders of the corresponding harmonic order.

.

peaks to fall within the overall Gaussian envelope given by $\widetilde{G}$. We fit our experimental data for the total yield to the formula

$$I_q^p \propto \left[exp\left[-\mathscr{R}(\varphi_G^2)(p - q\frac{\alpha}{1+\alpha})^2 \right] \frac{\sin\left(\beta\pi(p - q\frac{\alpha}{1+\alpha} + \delta)\right)}{\sin\pi(p - q\frac{\alpha}{1+\alpha} + \delta)} \right]^2 . \tag{11.19}$$

where I_q^p is the intensity of diffraction order p of harmonic q. Fig. 11.18 shows the experimental data (markers) and the fit of the data (solid lines) using equation 11.19. The amplitude and the width of the Gaussian , $\mathscr{R}(\varphi_G^2)$ are the free parameters of the fit. Within a range of β between 0.1 to 0.4, we are able to fit to a good extent our data to the above model for diffraction orders 1 to 3 of harmonics 9,11,13 and 15. However, 1) such a value of β defined as $\frac{L_{\text{med}}^b}{2|b|}$, would correspond to a medium showing a single fringe and 2) looking at the results from the simulation, the periodicity of the revival obtained in the experiment is much less than the ones expected due to transverse phase matching. These two reasons lead us to believe that the wiggles of higher frequency are very likely to have their origin in G_b^2, but the main "revival peaks" in the experimental data do not arise from phase matching effects in $|G_b|^2$. Also, the fit does not converge for the case of $p = 0$ for all harmonics. We thus turn back to the initial active grating model to introduce refinements.

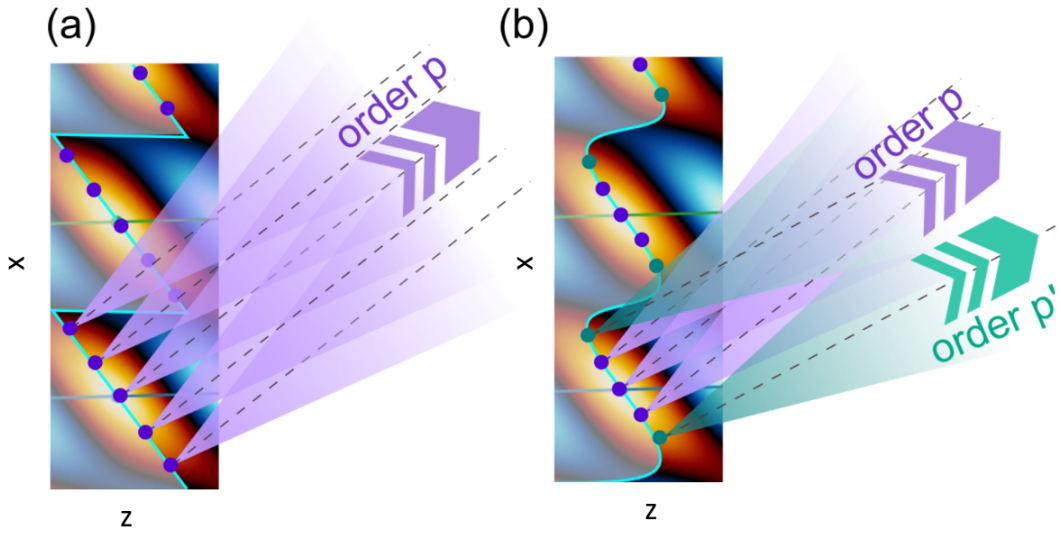

Figure 11.20: Pictorial representation of the amplitude grating and the phase grating at the generation region.(a) At high α, the emission pockets see a phase linearly varying along x at all points. There is a single blazed grating with a dominant blaze angle. (b) At lower α, the phase is more modulated and different parts of the emission zone sees either the linearly varying phase grating (purple), or the secondary grating (green) with another dominant emission direction.

.

11.3 Tracing the origin of the revival: back to the active grating model

The main essence of the active grating model is the simplification of the composite field at focus into three separate gratings: the amplitude grating, the geometric phase grating and the atomic phase grating. To recall, the composite field was written as (see section 6.2)

$$E_q^{nf} \propto e^{iq_s\omega_s t} \cdot \underbrace{E_s^{q_{\text{eff}}}(\alpha,\vec{r},t)} \cdot \underbrace{e^{iq_s\varphi_s(\alpha,\vec{r},t)}} \cdot \underbrace{e^{i\alpha_{at}E_1^2\cdot f_s^2(\alpha,\vec{r},t)}}. \tag{11.20}$$

where the amplitude term,

$$E_s^{q_{\text{eff}}} = E_1^{q_{\text{eff}}}(1+\alpha^2+2\alpha cos(\Delta\vec{k}\cdot\vec{r}-\Delta\omega t))^{q_{\text{eff}}/2} \tag{11.21}$$

is modelled as a Gaussian for high enough values of α and the geometric phase is modelled as that of a blazed grating,

$$\varphi_s = \frac{\alpha}{1+\alpha}\cdot 2\pi \cdot \frac{x}{\Lambda} \tag{11.22}$$

approximately linear with x, the transverse coordinate. This would mean that in the non perturbative regime, each individual pocket of emission will see a linearly varying phase, giving rise to a dominant direction of emission and other lesser ones. The spatial Fourier transform of equation 11.20 gives the

field amplitude in the far field as

$$E_q^{\text{ff}}(\theta) \propto \tilde{G}\left(\frac{\widetilde{\delta x}\pi}{\lambda_q}\left(\theta - \frac{q_s\alpha}{1+\alpha}\cdot\frac{\Delta k^{\perp}\lambda_q}{2\pi}\right)\right)\cdot \text{Ш}(\frac{a\theta}{\lambda_q}). \tag{11.23}$$

There is a dominant order of diffraction for a given α and each diffraction order has a Gaussian like

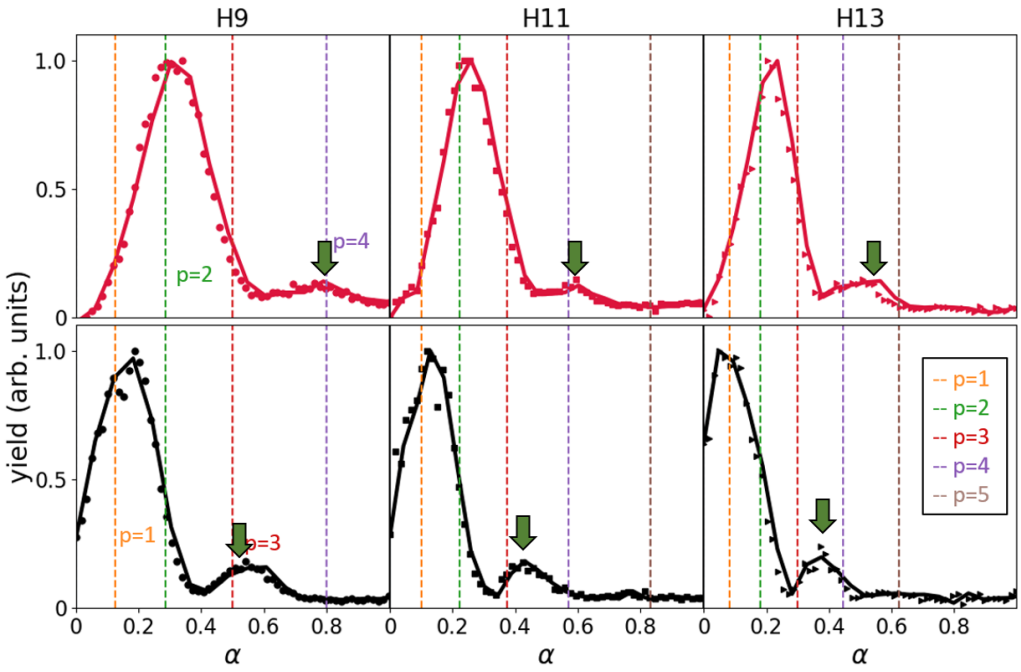

Figure 11.21: Experimental yields of diffraction order p=1 (bottom) and p=2 (top) of H9, H11 and H13. The dashed lines are for the position of α_{max} for the respective diffraction order.

intensity distribution curve coming from the modelling of the pockets as a Gaussian distribution.

The model relies heavily on the two approximations mentioned above. The linear approximation of the geometric phase might not be sufficient to explain the full picture. We will go a step further and try to look at the far field distribution by using the appropriate formula of φ_s and $E_s^{q_{\text{eff}}}$. Recalling that,

$$\varphi_s(\alpha,\vec{r},t) = \arctan\frac{\alpha\sin\left(\Delta\vec{k}\cdot\vec{r}-\Delta\omega t\right)}{1+\alpha\cos\left(\Delta\vec{k}\cdot\vec{r}-\Delta\omega t\right)}. \tag{11.24}$$

and expanding it as a Taylor series up to the second term,

$$\varphi_s(\alpha,\vec{r},t) = \frac{\alpha}{1+\alpha}\left(\Delta\vec{k}\cdot\vec{r}-\Delta\omega t\right) + \frac{\alpha(1-\alpha)}{6(1+\alpha)^3}\left(\Delta\vec{k}\cdot\vec{r}-\Delta\omega t\right)^3. \tag{11.25}$$

We will now substitute the above expansion in equation 11.20 and compute a spatial Fourier transform to obtain the far field properties. Fig.11.19 shows the evolution of the diffraction orders with α.

With the better approximation of φ_s, we retrieve the revival of intensity observed in the experimental results. It should not depend on gas or pressure and is purely geometric. In particular, it shows up at a much higher value of α, as compared to the wiggles of G_b. We thus conclude that the revival is likely to be not an effect due to phase matching, but an effect of the grating structure formed by the composite field, implicit in $\widetilde{G}\left(\Delta\vec{k}_{q_s}=0\right)\cdot G_b\left(\Delta\vec{k}_{q_s}=0\right)$. To understand the physical origin of this revival, we can imagine the geometric phase as two separate gratings superimposed on the field: the primary blazed grating and a secondary grating due to the non linear phase seen by the wings of the Gaussian emission pockets. The diffraction orders made by these regions are weaker because of the weaker intensity. While the central region of the pocket sees the primary grating with the linear "blazed phase" with a dominant blaze angle contributing to order p, the less intense outer wings see the secondary grating contributing to order p' and having twice the periodicity (see Fig. 11.20.(b)). For a given α, if a given diffraction order is dominant (ruled by the blaze angle), at a higher α, the secondary grating could contribute to this diffraction order once again, at another value of α, causing the revival. However, as α gets very high, the phase is fully blazed as shown in Fig. 11.20.(a), and there is lesser possibility of a revival.

In Fig.11.21 is presented the experimental data of the amplitude distribution of p=1 (bottom panel) and p=2 (top panel) of harmonics 9,11 and 13. Looking at the case of H9, for diffraction order p=1 , there is a revival at $\alpha_{\max}$ corresponding to p=3 and for p=2, there is a revival at $\alpha_{\max}$ corresponding to p=4. However, this periodicity appears to evolve slowly with harmonic order. In Fig.11.22 is

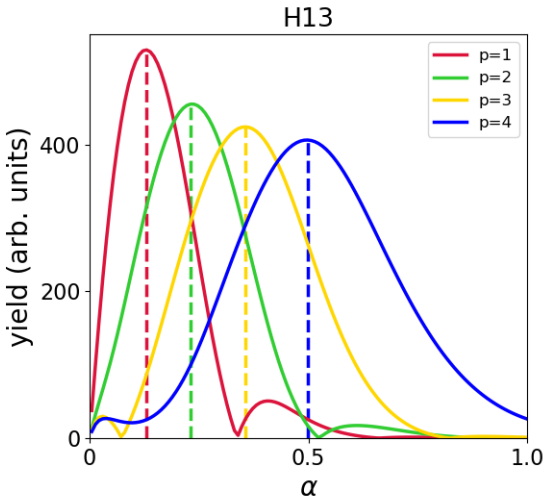

Figure 11.22: Computed yields of diffraction order of H13.

presented the computed intensities of the diffraction orders of H13. We see a similar trend as in the experimental data. For example, the revival of p=1 order occurs when p=3 is dominant and the revival of p=2 occurs when p=4 is dominant. The nice agreement between the secondary peaks positions and

the experiment is a strong indication of the leading role of the third order phase in the appearance of these revivals, while the higher frequency oscillations are mostly coming from transverse phase matching.

11.4 Conclusion and Discussion

A major portion of this thesis is dedicated to understanding the amplitude distribution of the harmonic signal of different diffraction orders generated in non collinear geometry. In the previous part, we could explain the same with a field-based model that complemented the existing photonic model. In this part, we extended our studies on NCHHG to include phase matching effects. It helps us to get a comprehensive understanding of the process and identify factors that play a role in phase matching that has been unknown up to now. Phase matching in HHG, though much studied, is a difficult subject to tackle, especially in experiments. So far, the basic phase matching principles in HHG was nicely explained by the simple 1D model of Constant et al.[10]. And the extension to non-collinear geometry was confined to the identification of a geometric non collinear phase mismatch factor of Heyl et al.[83]. We introduced a new approach to study phase matching, developing a 2D model for a homogeneous medium, inspired from x-ray diffraction in crystals. With this new model we can retrieve the results of the existing 1D model as well as gain insight into additional effects of the non collinear geometry. The main advantage of the model is that we can factorize phase matching effects along the longitudinal and transverse directions and study each of them individually.

With the results of our numerical simulations and experiment, we could identify two new features. Wiggles with a high periodicity which match the transverse phase matching factor effect, and a revival that was modelled by a refinement of the purely linearly blazed grating. The two effects are purely geometrical, not dependent on gas pressure or the generating gas. These two effects, nicely reproduced, validate our model that can now be used in other experimental conditions, for example, at higher ionization fractions, different laser wavelength, to optimize HHG in cavities etc.

Part V

Magnetic Helicoidal Dichroism

CHAPTER 12

Introduction

Building on the discovery of the Faraday effect in 1845, the interplay of light with magnetic materials has ever since been strongly focused on polarization-dependent interactions, especially uneven interactions with left and right circularly polarized beams (LCP and RCP). This is because circular polarization imprints a well defined handedness on the photon beam, associated with a Spin Angular Momentum (SAM), making it a unique tool in magneto-optics studies. However, light can also carry Orbital Angular Momentum (OAM), as in the case of Laguerre-Gaussian modes that are indexed with two integers, $(\ell, p) \in (\mathbb{Z}, \mathbb{N})$, and show ℓ intertwined spiralling wavefronts. More precisely, along the azimuth ϕ, the phase of the beam varies like $\ell\phi$ and the projection of the angular momentum along the z-propagation axis, reads $L_z = \ell\hbar$ per photon. But the interest in OAM beams is relatively new and its potential as an optical tool in studying magnetic materials has been scarcely exploited, if at all. One important difference between SAM and OAM is that the topological charge of the latter is not limited, and absolute values of $\ell > 1$ can be imparted to the photon beam, increasing the potential for applications.

However, this situation is evolving very quickly in view of recent theoretical and experimental work. In analogy with the results obtained for the electric-quadrupole interactions of OAM beams with atoms and molecules, it was predicted that the interaction of OAM beams with plain magnetic samples should depend on the value of ℓ [114]. It relies on electric quadrupolar transitions, which require strong beam focusing to be investigated experimentally. Later, it was experimentally demonstrated that the interaction vanishes in the electric-dipole approximation [115], on the other hand. In a further study, Van Veenendaal and McNulty theoretically identified signatures of the absolute value of the OAM in the incoherent diffraction pattern from a magnetic vortex [116]. Such existing work,

and the availability of OAM beams with ultrashort pulse duration in the XUV regime at HHG and FEL sources prompted us to study the effect of OAM beams on magnetic materials. As already shown in chapter 5, the FAB-1-Bis beamline at ATTOLab is an available source of XUV vortex beams, making it possible for us to envisage future in-house experiments to improve our existing knowledge in the field.

In the next two chapters are presented the work of two recent publications from our group as Paper I and Paper II. The first one is a theoretical work on Magnetic Helicoidal Dichroism (MHD)[117], an effect that appears when light beams with OAM are reflected off non-homogeneous magnetic structures. I participated in the very first and then unsuccessful experimental campaign based on the work of Van Veenendaal and McNulty [116], that triggered our interest in this kind of dichroic effect. We realized that the coherence of the source, which was not considered in their work, must play a decisive role in the effect. Then, I was involved in the development of the theoretical model, led by Mauro Fanciulli and Thierry Ruchon, to its final validation and to the writing of the corresponding publication presented here as Paper I.

In the second chapter is presented the pioneering work of Fanciulli et al. that reports the observation of MHD in Magnetic Vortices (MVs) at the FERMI Free Electron Laser facility. The experimental evidence is in good agreement with theoretical predictions and can identify the specific dependence of MHD on the sign of the optical (l) and magnetic (m) vortices. This experimental validation of our theoretical work makes it possible to extend this approach to other complex magnetic structures and even time-resolved experiments by exploiting a femtosecond pump-probe scheme, with the aim of studying the ultrafast dynamics of magnetic vortices by means of this new tool, MHD. I participated in two experimental campaigns at FERMI in Trieste on this topic, developed an early experimental data analysis numerical tool, and was associated to the analysis and writing of the corresponding manuscript.

In this introductory chapter to MHD, I present a brief summary of these two publications.

12.1 Laguerre Gaussian (LG) beams

We here provide a quick introduction to Laguerre Gaussian beams, which are prototypical beams carrying an Orbital Angular Momentum (OAM). For more insight, the reader is refered to the Ph.D. manuscript of Romain Géneaux [55] and references therein, or the following books [118, 119]. Mathematically, an electromagnetic wave with uniform polarization can be described as a scalar field, $u(x,y,z;t)$, with spatial coordinates (x,y,z) and time t, in vacuum, which follows the hyperbolic partial differential equation [120]:

$$\frac{\partial^2 u}{\partial t^2} = c^2 \nabla^2 u$$

where ∇^2 is the Laplacian and c is the speed of light. Assuming that the field is monochromatic, we may isolate its temporal variation as $u(x,y,z;t) = U(x,y,z)e^{-i\omega t}$ and we get the Helmholtz equation:

$$\nabla^2 U + k^2 U = 0,$$

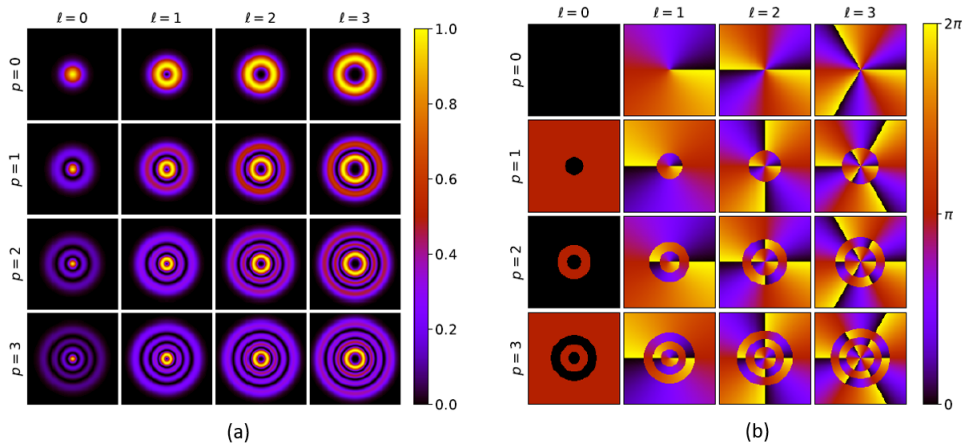

Figure 12.1: Transverse intensity profiles (a) and phase profiles (b) of the first few Laguerre-Gauss modes. Adapted from [108].

where $k = \omega/c = 2\pi/\lambda$ is the wavenumber and λ is the wavelength. It is further simplified with the hypothesis of a slowly varying envelope, allowing to write $U(r,z) = V_z(x,y)e^{-ikz}$, where we isolate the fastly varying phase of the plane wave from the slowly varying envelope $V_z(x,y)$. Neglecting the second order derivative of this envelope, we get the paraxial wave equation:

$$\frac{\partial^2 V_z}{\partial x^2} + \frac{\partial^2 V_z}{\partial y^2} + 2jk\frac{\partial V_z}{\partial z} = 0. \tag{12.1}$$

There exists various sets of eigen solutions to this equation, of mutually orthogonal modes, forming complete bases on which any field may be projected. Among them, LG basis is of particular interest as its modes carry well defined amount of OAM. The set of LG modes is indexed by two integers, ℓ, and p, with $\ell = 0$, $p = 0$ being the regular Gaussian mode.

In cylindrical coordinates (r,ϕ,z), where r is the radial distance from the propagation axis, ϕ is the azimuthal angle formed on the plane perpendicular to the propagation axis, and z is the distance along the propagation axis, the LG beam can be realized as

$$V_z(r,\phi,z) = \sqrt{\frac{2p!}{\pi(p+|\ell|)!}}\frac{1}{w(z)}\left(\frac{r\sqrt{2}}{w(z)}\right)^{|\ell|} \times e^{-\frac{r^2}{w(z)^2}} e^{-\frac{ikr}{2R(z)}} e^{-i\ell\phi} e^{i(2p+|\ell|+1)\gamma(z)} L_p^{|\ell|}\left(\frac{2r^2}{w(z)^2}\right). \tag{12.2}$$

where $p \in \mathbb{N}, \ell \in \mathbb{Z}$, $w(z)$ is the waist of the beam at abscissa z, $R(z)$ its radius of curvature, $\gamma(z)$ the Gouy phase and $L_p^{|l|}$ the generalized Laguerre polynomials. In the case of a collimated beam ($z \approx 0$) with waist, ω_0, the equation simplifies to

$$V_z(r,\phi) = \sqrt{\frac{2p!}{\pi(p+|\ell|)!}}\frac{1}{w_0}\left(\frac{r\sqrt{2}}{w_0}\right)^{|\ell|} \times e^{-\frac{r^2}{w_0^2}} e^{-i\ell\phi} L_p^{|\ell|}\left(\frac{2r^2}{w_0^2}\right).$$

The first few LG profiles are represented in Fig. 12.1. For $\ell \neq 0$, the LG beams have helical phase fronts, and a phase singularity at their center. They also have zero intensity at that point, ensured by

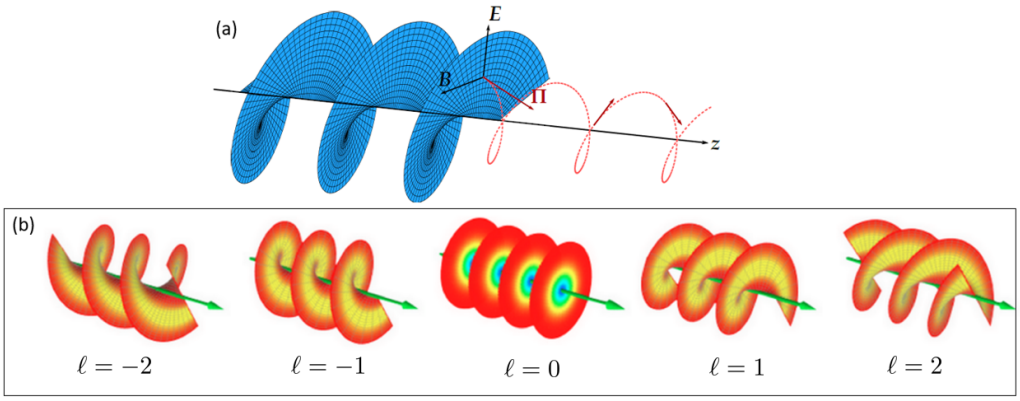

Figure 12.2: (a) Wavefront (blue surface) and Poynting vector (red arrows) of LG mode (ℓ, p) = (1, 0). The evolution of the direction of the Poynting vector during the propagation is represented in red dotted lines for a given distance along the z-axis. Taken from [108]. (b) Spatial phase fronts of the $p = 0$ beams, with the intensity profile added, intensity increases from orange to blue. For $\ell = 0$, we have a plane wave. For other values, the phase front is helical. Taken from here.

the $\left(\frac{r\sqrt{2}}{w_0}\right)^{|\ell|}$ term, which means that their intensity profile is a ring. The radius of the ring depends on ℓ and the number of concentric rings is given by $p+1$. The evolution of the Poynting vector during the propagation of the beam is illustrated in Fig. 12.2.(a) for the case (ℓ, p) = (1, 0). It describes a spiral around the optical axis. Since this vector gives the direction of propagation of energy, we can intuitively infer that a Laguerre-Gauss mode can rotate an object. And the seminal work of Allen et al. [23] did indeed establish that these modes carry a well defined orbital angular momentum of $\ell\hbar$ per photon along the propagation axis. In reference to this structure, the LG modes are sometimes referred to in the literature as "optical vortices" and their azimuthal index as "topological charge".

12.2 Magneto Optical Kerr Effect (MOKE)

Magneto-optical effects are strongly dependent on the polarization of the radiation as well as the interaction geometry of the light with respect to the relative orientation and direction of the magnetization, M [121], i.e, the arrangement of the surface of the sample with respect to the plane of incidence of the light beam and its polarization. At the phenomenological level, they are linked to magnetization dependent optical indices, both real and imaginary, leading to alterations of the amplitude, polarization and phase of a light beam that is reflected off a magnetic sample, or propagating through them. These effects may be separated into a large variety of classes based on their dependence on magnetization, which may be linear, quadratic etc., or their link to real or imaginary parts of the optical index, or, their dependence on reflection or transmission geometry. For instance, in transmission geometry, with a magnetization along the propagation axis of the beam, there exists the

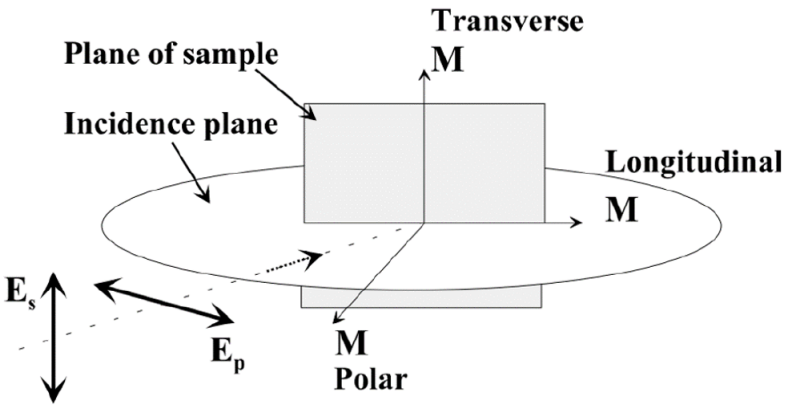

Figure 12.3: Different MOKE configurations. Taken from [122]

Faraday Effect and the Magnetic Circular Dichroism (MCD) effects, respectively linked to the real and imaginary parts of the optical index. Indeed, in this configuration, the eigen solutions of the wave equation in the medium are circularly polarized light of opposite handedness with different optical indices, proportional to the magnetization. If in addition, the medium shows a non cubic symmetry, Magnetic Linear Dichroism may appear. It is an absorption effect, quadratic with the magnetization, which makes it sensitive to antiferromagnetism, unlike MCD. Here, we mostly focused on MOKE configuration, i.e., following an alteration of the optical indices proportional to the magnetization by measuring a reflected beam. There are three possible MOKE configurations (see Fig.12.3), depending on the relative orientation of the magnetization and the incoming linear polarization. If the magnetization is normal to the plane of the sample, it is the "polar" configuration. If it is in the plane of the surface, and in the plane of incidence, this is the "longitudinal" configuration. Finally, if it is in the plane of the surface, and normal to the plane of incidence, it is the "transverse" configuration. In each situation, there are different reflection coefficients for the P and S polarizations.

The reflection of the light beam is modeled by the reflectivity matrix R for which $E_{\text{out}} = RE_{\text{in}}$, where E_{in} and E_{out} are the incoming and outgoing electric fields respectively. For an incoming Jones vector of the incoming field $\left(E_p^{in}, E_s^{in}\right)$, the outgoing field $\left(E_p^{\text{out}}, E_s^{\text{out}}\right)$ reads

$$\begin{pmatrix} E_p^{out} \\ E_s^{out} \end{pmatrix} = \begin{pmatrix} r_{pp}^x & r_{ps}^x \\ r_{sp}^x & r_{ss}^x \end{pmatrix} \begin{pmatrix} E_p^{in} \\ E_s^{in} \end{pmatrix} \tag{12.3}$$

where the superscript x is either l for longitudinal, t for transverse, p for polar, depending on the geometry [123]. Finally,

$$R = m_t^2 T + m_l^2 L + m_p^2 P$$

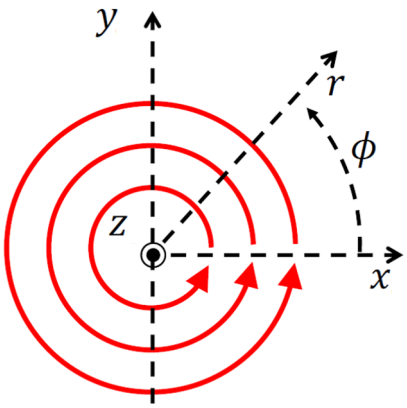

Figure 12.4: Example of a magnetic sample with a counterclockwise magnetic vortex, modelled in cartesian and polar coordinate systems.

with:

$$T = \begin{pmatrix} r_{pp}\left(1 + r_0^t/m_t\right) & 0 \\ 0 & r_{ss} \end{pmatrix}$$
$$L = \begin{pmatrix} r_{pp} & r_{ps}^l/m_l \\ -r_{ps}^l/m_l & r_{ss} \end{pmatrix}$$
$$P = \begin{pmatrix} r_{pp} & r_{ps}^p/m_p \\ r_{ps}^p/m_p & r_{ss} \end{pmatrix}$$

where $m_t = M_t/M_s$, $m_l = M_l/M_s$, $m_p = M_p/M_s$, and $m_t^2 + m_l^2 + m_p^2 = 1$, with M_s the saturation magnetization. In the matrix elements r_{ij}, the subscripts denote the scattering dependence, i.e., r_{ps} couples the incident s-polarized field component upon reflection into a p-polarized component, while r_0 is responsible for a modulation of the signal intensity that is proportional to the magnetization, thus not altering the light polarization.

The magnetization of a homogeneous magnetic sample as well as a non homogeneous magnetic vortex was considered in Paper I. For instance, from Fig.12.4, we can see that it can be modelled as

$$m_l(\phi) = -m_0 \sin\phi$$
$$m_t(\phi) = \ m_0 \cos\phi$$

for a curling, in-plane magnetization.

Once $R(r,\phi)$ is defined, we can calculate the output intensity of the reflected light. To find the dichroic signal we just have to calculate the difference between signals from two different polarizations or magnetizations. The reflectivity coefficients are very much dependent on the angle of incidence of the incoming beam as well as the photon energy. The dichroic signal is usually resonantly enhanced at the edges of the material. In particular, for transition metals which form the basis of common magnetic materials (Fe, Ni, Co), two series of edges are of particular interest: L edges, in the 750-800 eV range, accessible to synchrotrons and new XFELs, and M edges, in the 50-70 eV range,

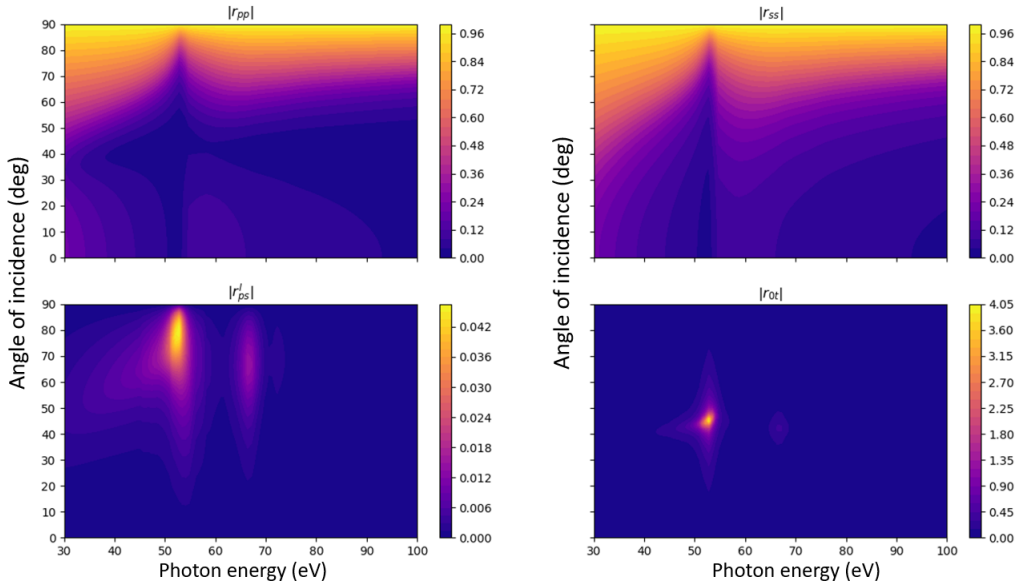

Figure 12.5: Colour map of the amplitude of the optical constants of Fe plotted against photon energy of the incoming beam and the angle of incidence.

accessible to HHG sources in addition to the above sources. We focused on M edges because of the possibility of their potential investigation in our laboratory.

Following [124, 122], the magneto optical coefficients can be expressed as

$$
\begin{aligned}
r^t_{pp} &= \left(\frac{n\beta-\beta'}{n\beta+\beta'}\right)\left(1+\frac{in^2Q\sin 2\theta}{n^2\left(n^2\cos^2\theta-1\right)+\sin^2\theta}\right) = r_{pp}\left(1+r^t_0\right)\\
r^t_{ss} &= \frac{\beta-n\beta'}{\beta+n\beta'} = r_{ss}\\
r^t_{ps} &= r^t_{sp} = 0\\
r^l_{pp} &= \frac{n\beta-\beta'}{n\beta+\beta'} = r_{pp},\\
r^l_{ss} &= \frac{\beta-n\beta'}{\beta+n\beta'} = r_{ss},\\
r^l_{ps} &= -r^l_{sp} = i\frac{\beta Q\sin\theta}{\beta'\left(n\beta+\beta'\right)\left(\beta+n\beta'\right)},
\end{aligned}
\tag{12.4}
$$

where Q is the Voigt magneto optic constant which describes the magneto optical effect. This Voigt term (to the first order) is proportional to the magnetization of the material. θ is the angle of incidence, n is the index of refraction, $\beta = \cos\theta$ and $\beta' = \sqrt{1-\frac{\sin^2\theta}{n^2}}$. The magneto-optical constants thus calculated with the formulae in (12.4), are displayed in Fig. 12.5. The values of optical indices are taken from the Center for X-ray Optics (CXRO) data base and the values of Q are obtained from Valencia et al. [125]. Based on this plot, we chose to work right at the coordinates where r^t_0 peaks, i.e., at the Brewster angle and photon energy corresponding to an edge (52.8 eV).

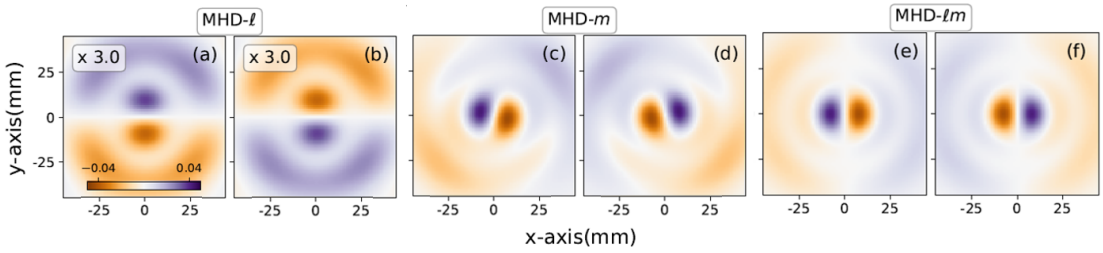

Figure 12.6: Computation of MHD for a magnetic dot of 500 nm with two antiparallel domains. (a) MHD- ℓ for $m = 1$ and (b) for $m = -1$; (c) MHD- m for $\ell = 1$ and (d) for $\ell = -1$; (e) MHD- ℓm as a difference of intensity maps corresponding to $\ell = 1$ and $m = 1$ and $\ell = -1$ and $m = -1$, and (f), MHD- ℓm, difference of intensity maps corresponding to $\ell = 1$ and $m = -1$ and $\ell = -1$ and $m = 1$.

12.3 MOKE with LG beams: Observation of helicoidal dichroism

The interaction of helicoidal wavefront with magnetic materials was not specifically documented when we started this Ph.D. work. Based on the intuition that magnetic structures should be sensitive to the helicoidal twisting sense of an OAM beam, we used the classical formalism described above to study MOKE with LG beams and called the observed dichroic effect as magnetic helicoidal dichroism (MHD).

In our model, we obtain the reflected field using equation 12.3 to see the modification of the OAM by reflection from the magnetic structure. We feed our model with an input LG beam having a single topological charge ℓ. We find that the field after reflection $\vec{E}_{\text{out}}$ is a superposition of topological charges, whose weight and charge depend on the precise shape of the magnetic structure. It can be separated into a magnetic and non magnetic terms ($\vec{E}_{\text{out}} = \vec{E}^{m=0}_{\text{out}} + \vec{E}^{m}_{\text{out}}$) . Indeed the non magnetic term is an OAM beam of the same topological charge as the incoming one. Its polarization will be different from the incoming one due to the different values of the Fresnel coefficients, r_{pp} and r_{ss}, corresponding to the usually observed effects on polarization of light upon reflection from any surface. The magnetic term however shows a population of additional ℓ and p modes, both of which depends on the magnetic structure that is probed and the incidence angle of the incoming beam. Different cases involving different magnetic samples and incidence angles are treated in detail in Paper I.

Next, we look at the far field profile to identify dichroic effects, leading to results that we call differential helicoidal dichroism, i.e., a difference in intensity profiles upon switching the sign of the OAM (MHD-ℓ), of the magnetization (MHD-m), or of both (MHD-ℓm). Here differential is meant as a dichroism that occurs at every single point in the image in the far field. However, the integration over space of the image leads to constant total intensity, independent of the sign of the OAM or of the magnetization, unlike the case of MCD where the difference persists even after spatial integration of the scattered intensity. Light propagation was simulated by computing Fresnel diffraction. This method solves the paraxial wave equation by using 2D Fourier transforms. The theory gives the field

after propagating a distance z as

$$f(x,y,z) = \frac{1}{i\lambda z} e^{\frac{ik}{2z}(x^2+y^2)} \quad \times \iint e^{\frac{ik}{2z}(x'^2+y'^2)} f\left(x',y',0\right) e^{-\frac{i2\pi}{\lambda z}(x'x+y'y)} dx'dy'.$$

The integrals are simply a 2D Fourier transform where $x/\lambda z$ and $y/\lambda z$ are the conjugate variables, x' and y', were computed with the standard fast Fourier Transform routines. The far field intensity computed this way is then used to compute the different dichroic signals. The three different cases of MHD-ℓ, MHD-m and MHD-ℓm are treated in detail in Paper I. We find that as soon as the magnetization is not spatially homogeneous, the reflected beam will populate different OAM modes following some selection rules depending on the magnetic structure. As a result, the intensity pattern in the far field changes when reversing ℓ, the sign of the magnetization or both (see Fig. 12.6). Differently from MCD and MLD, MHD is sensitive to the overall symmetry of magnetic structures. It vanishes for homogeneous structures, and is not self similar if one inverts either the helicity of the beam or the magnetization direction.

The observed dichroic signal being dependent on the particular shape of the magnetic structure as well as on the magneto-optical constants, MHD experiments open a new way to analyze the magnetization, or alternatively to determine the MOKE constants. This provides MHD with the potential of becoming an important new tool to access the properties of magnetic materials, in particular for ultrafast magnetization measurements, which are known to be time-consuming, including time-resolved pump-probe studies of the magnetization dynamics that can be naturally implemented at laser based experimental facilities.

12.4 Experimental observation of magnetic helicoidal dichroism

The experimental technique for observing MHD is very similar to the well established MOKE techniques in reflection geometry. The only additional requirements are an XUV source carrying OAM and experimental capability of focusing the beam to sizes comparable to that of the structure under investigation. Today, OAM beams are readily available in selected laboratories, including ATTOLab, but strong focusing conditions are often missing. However, both these features could be made available at the DiProI beamline in the Free Electron laser Radiation for Multidisciplinary Investigations (FERMI) facility at Trieste, where we performed the first experimental investigation on MHD. Collaborators from Paul Scherrer Institute (Benedikt Rösner et al.) developed the spiral zone plates to impart OAM to the FEL beam and collaborators from Institut des Nanosciences de Paris (INSP, Maurizio Sacchi et al.) and SPINTEC, Grenoble (Bernard Dieny et al.) designed and prepared the samples. From our theoretical model, it appeared that magnetic vortices would be ideal test cases for MHD, as they should populate only two new modes of neighbouring topological charge, compared to the incident beam. And accordingly, the magnetic samples were prepared as magnetic vortices shaped as "Pacman"-like permalloy (Py, Fe20Ni80) dots having a few μm diameter and 80 nm thickness. The Pacman shape was designed to be able to control the curling sense of the magnetic vortex by application of an external moderate magnetic field (20 mT), before the experiment [33]. The details of the experimental set up can be found in Paper II.

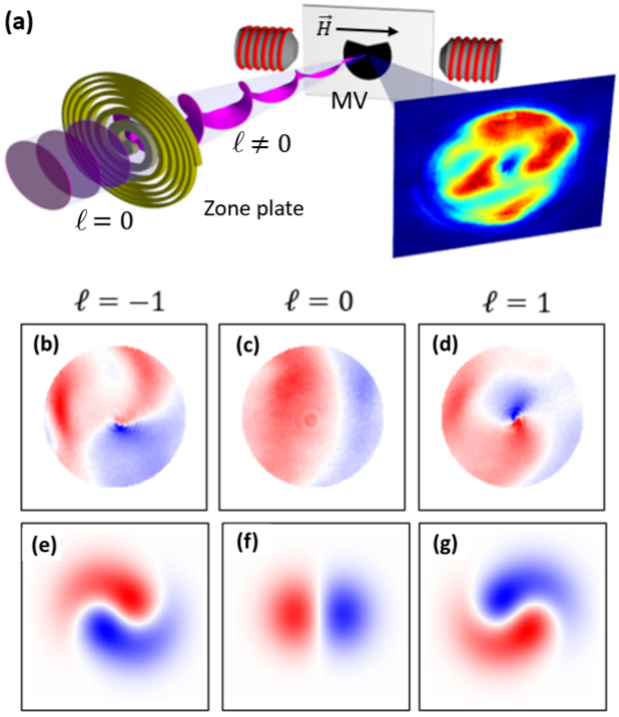

Figure 12.7: Sketch of the experimental set-up (a) showing the incoming FEL beam with planar wavefront, a spiral zone plate that imparts OAM to the FEL beam, the sample placed between the poles of the electromagnet and the image of the scattered beam. Experimentally observed dichroism (corresponding to MHD-m) (b-d) and numerical simulations for the same experimental parameters (e-g).

We could obtain dichroic signals for MHD-m, finding a good agreement with theoretical predictions (see Fig.12.7). The measured dichroic signal is of the order of 20%, giving us first experimental evidence of MHD. The results of this experimental campaign are detailed in Paper II.

With these two papers, we open a new branch of magneto optics, whereby we introduce a new parameter of the incoming beam that plays a role: its topological charge. We have already started to harness it to follow fast dynamics of magnetic vortices. A new experimental campaign, whose results are under analysis, show dynamics of large magnetic vortices in the 20 ps range, way faster than any dynamics identified for magnetic vortices so far. It should be noted that we focused thus far on very specific examples, treating only the case of one incoming polarization (P), no out of plane magnetization, and only in reflective geometry. Other configurations that we have not investigated could be equally interesting and we hope that our work will stimulate their study.

CHAPTER 13

Paper I: Electromagnetic theory of helicoidal dichroism in reflection from magnetic structures

Electromagnetic theory of helicoidal dichroism in reflection from magnetic structures

Mauro Fanciulli,[1,2,*] David Bresteau,[1] Mekha Vimal,[1] Martin Luttmann,[1] Maurizio Sacchi,[3] and Thierry Ruchon[1,†]

[1]*Université Paris-Saclay, CEA, CNRS, LIDYL, 91191 Gif-sur-Yvette, France*

[2]*Laboratoire de Physique des Matériaux et Surfaces, CY Cergy Paris Université, 95031 Cergy-Pontoise, France*

[3]*Sorbonne Université, CNRS, Institut des NanoSciences de Paris, INSP, F-75005 Paris, France*

(Received 21 May 2020; revised 5 November 2020; accepted 16 December 2020; published 4 January 2021)

We present the classical electromagnetic theory framework of reflection of a light beam carrying orbital angular momentum (OAM) by a magnetic structure with generic symmetry. Depending on the magnetization symmetry, we find a change in the OAM content of the reflected beam due to magneto-optic interaction and an asymmetric far-field intensity profile. This leads to three types of magnetic helicoidal dichroism (MHD), observed when switching the OAM of the incoming beam, the magnetization sign, or both. In cases of sufficient symmetries, such as domain walls and magnetic vortices, we establish analytical formulas that link an experimentally accessible MHD signal to the magneto-optical Kerr effect (MOKE) constants.

DOI: 10.1103/PhysRevA.103.013501

I. INTRODUCTION

Laguerre-Gaussian light beams, which are a special case of vortex beams (VB) [1,2], carry orbital angular momentum (OAM) and show a chiral symmetry: their wavefront appears as a spiral surface, the two forms of which, left-handed or right-handed, are mirror images but not superimposable [3,4]. From symmetry principles, one can expect a different response of the two chiralities when interacting with matter presenting no trivial symmetry [5]. For instance, such an effect was observed when a VB was sent on chiral molecules adsorbed on a surface [6], or on structured nanopatterns [7]. These kinds of differential effects, linked to the properties of light, are generally called birefringence or dichroism, whether they appear on the real or imaginary part of the optical index or reflectivity coefficients. They may appear due to microscopic, macroscopic, or induced dissymetries in the medium, providing altogether an extremely rich set of investigation tools.

All these effects have long been identified for light carrying a spin angular momentum (SAM), which is another form of chirality of light beams associated to circular polarization. Discovered by Arago on α-quartz crystals, circular birefringence, also called optical activity, was linked to the symmetry of the macroscopic structure [8]. It is caused by different real optical indices for circularly polarized light beams with opposite helicities (SAM). Biot reported four years later that it also has a microscopic origin, reporting its observation in isotropic liquid media [9]. These seminal discoveries were instrumental towards the discovery by Pasteur of molecular dissymetry [10], today called molecular chirality after Kelvin's work [11]. The counterpart in absorption, circular dichroism (CD), was discovered in 1896 by Cotton [12]. Furthermore, the dissymetry can be induced by external "forces," like a magnetic field. Faraday discovered the magnetic circular birefringence in 1846 [13] and its counterpart in absorption, magnetic circular dichroism (MCD), which later became accessible [14,15], is now a standard investigation method for magnetic samples, especially in the x-ray spectral range [16–18]. All these effects are second-order effects, appearing beyond the first order electric-dipole approximation. However, when the result of the interaction with light is photoionization, first order effects, which appear as an uneven distribution of the photoelectrons on a detector, could be identified, such as, for instance, photoelectron circular dichroism (PECD) [19,20], or circular dichroism in angular distribution (CDAD) on surfaces [21].

As for OAM-dependent light-matter interactions, which we may call Helicoidal Dichroisms (HD) [22], a few of them have already been reported in different contexts, as reviewed in Ref. [23]. To list only a few examples, one could consider the measurements of the OAM of light beams as a kind of HD, may it be used in the framework of classical [24] or quantum light [25,26]. These schemes use either diffraction on nonsymmetrical apertures (e.g., triangular slit), interferences with a beam of different symmetry (e.g., a VB with a plain beam), or modes converters using birefringent prisms. However, none of these schemes is currently of spectroscopic wide interest: matter is here only used to alter the mode content of the beam, without any consideration upon the physics of light-matter interaction.

The question of spectroscopic applications first arises when matter is left in an excited state. A recent specific review dedicated to the interaction of twisted light with atoms is available in Ref. [27]. Briefly, through electric-dipole transitions, twisted light beams do not couple differentially to the internal degrees of freedom of the atomic or molecular system, i.e., the electronic ones, but can act on its external ones [28,29]. This last behavior led to important developments, enriching the scope of techniques available for manipulation and cooling of atoms. The first order of

*mauro.fanciulli@u-cergy.fr

†thierry.ruchon@cea.fr

perturbation sensitive to the OAM linked to internal degrees of freedom is the electric quadrupolar one, as recently demonstrated experimentally in ultra-cold trapped ions [30,31], or theoretically in oriented chiral molecular ensembles [32]. Such a result also holds for bulk magnetic materials [33]. Interestingly, these general conclusions are modified when an atomic system gets ionized through the interaction with a very high intensity beam ($\gtrsim 10^{20}$ W/cm^2): in this context, new selection rules were proposed within the electric dipole approximation [34–37], providing an analog to PECD and CDAD. However, all these spectroscopic HDs remain experimentally extremely challenging nowadays, if possible at all. The difficulty ultimately relies on the necessity for the system to "see" altogether a significant twist of the wave front over its dimensions, and a high enough intensity. When systems are larger than atoms or molecules, these conditions may be less demanding. Important examples are the use of VB to control Bose-Einstein condensates [38] and to generate skyrmions [39,40]. An effect was also predicted for nanodots [41], nanoantennas [42] and chiral dipolar nanostructures [43], and an OAM-dependent plasmonic coupling between SAM and OAM was reported when light is sent through nanoholes [44].

From this brief and selective overview, although many applications emerged using VB and OAM beams [3,23], it appears that the picture of anisotropic effects involving VB remains incomplete as compared to circularly polarized beams. It is even more apparent when considering reflective geometries for which a wealth of magneto-optical Kerr effect (MOKE) [15,45–47] have been identified for different polarization/magnetization combinations which do not find their counterpart for VB. These MOKE effects are particularly enlightening in the extreme ultra violet (XUV) spectral range (50–150 eV), where $3p$ edges of many magnetic material are found [48–50], and in the soft x-ray region (600–900 eV), typical for $2p$ edges [51–53].

In this paper, we contribute to filling the picture by explicitly predicting with classical electromagnetic theory the existence of a phenomenon analogous to MCD, observable with beams carrying OAM instead of SAM: magnetic helicoidal dichroism (MHD). Its value can be very large, comparable to other MOKE effects. Combined with the recent availability of XUV VB both on free-electron laser sources [54–56] and high harmonic sources [57–63], it should make it measurable rapidly. We consider structures with sizes comparable to a standard beam focus (100-nm–few-micrometer width), and materials which exist at ambient temperature. This lifts the above mentioned strong requirements, making MHD a promising spectroscopic tool. For simplicity, only magnetization with constant magnitude and not radially dependent components is considered, but an extension to more general cases can be readily achieved. We will derive the analytical expressions of MHD for reflection of beams carrying OAM in the three different cases of switching the OAM sign, the magnetization sign or both. This approach is similar to what has been derived for dichroism in scattering when switching OAM sign, SAM sign or both [42]. We find that for targets with nonhomogeneous magnetization MHD is always present when the reflected beam profile is spatially resolved, which we indicate as

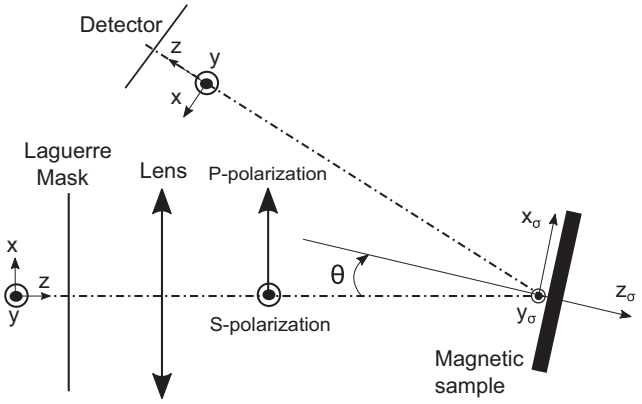

FIG. 1. Sketch of the beam path for the reflection on the magnetic target.

"differential" MHD. This is similar to what has been shown for the case of resonant x-ray scattering of light carrying SAM [64] or OAM [65], or for PECD measurements [19,20]. Furthermore, while MHD also depends on the polarization state of the incident light, its observation does not require any polarimetric analysis, which is convenient especially for the XUV spectral range. We implement our model in numerical calculations, the details of which are reported in Appendix A.

This paper is organized as follows. In Sec. II, we present the analytical model for the input OAM beam and a generic magnetic structure. The two special cases of a magnetic vortex and of two antiparallel magnetic domains are considered explicitly. In Sec. III, we calculate the characteristics of the reflected light beam by the magnetic structure in the near field, finding the rules for the modification of the OAM. In Sec. IV, we propagate the beam to the far field, evaluate the expression for the intensity and find the equations describing the MHD. Finally, discussion and conclusions are presented in Sec. V.

II. MODEL

In this section, we present the analytical framework used in our model to describe the Laguerre-Gaussian (LG) beam and the magnetic structure.

A. Beam propagation and decomposition on the Laguerre-Gaussian basis

We consider sufficiently loose focusing conditions so that the paraxial equation for beam propagation is valid. We start with a collimated Gaussian beam and propagate it in several steps using the Fresnel integral. The beam path is shown in Fig. 1. It first goes through a phase mask, such as a spiral staircase, which imparts OAM to the beam. Then it propagates to a lens, and it is focused on the sample. After reflection, the beam is again propagated to the far field, where the detector is placed. In order to be able to study the results in terms of angular momentum, we use the LG basis to analyze the interaction of an optical vortex with a magnetic structure. The LG basis is a family of solutions of the paraxial equation

forming a complete basis, indexed by the two integers (ℓ, ρ), with ℓ being the azimuthal number, positive or negative, and ρ the radial number, positive. The complex electric field of a given LG mode (focus at $z = 0$) reads [66]

$$\vec{E}_{\text{in}} = C_\rho^{|\ell|} \frac{1}{w(z)} \left(\frac{r\sqrt{2}}{w(z)} \right)^{|\ell|} L_\rho^{|\ell|} \left(\frac{2r^2}{w^2(z)} \right) \times e^{-\frac{r^2}{w^2(z)}} e^{-ik\frac{r^2}{2R(z)}} e^{i\ell\phi} e^{i(\omega t - kz)} e^{i(2\rho+|\ell|+1)\gamma(z)} \begin{pmatrix} \epsilon_P \\ \epsilon_S \end{pmatrix}, \quad (1)$$

where $C_\rho^{|\ell|}$ is a normalization constant specific for the basis (ℓ, ρ), (r, ϕ) are the polar coordinates, $L_\rho^{|\ell|}$ represents the Laguerre polynomial, ω is the angular frequency, and k is the wave vector along the propagation direction z. The vector (ϵ_P, ϵ_S) represents the polarization state of the beam; notably, (1,0), (0,1), and $(1, \pm i)$ correspond to linearly P-polarized, linearly S-polarized, and left and right circularly polarized beams, respectively. The Gouy phase $\gamma(z)$, the beam width $w(z)$ and the radius of curvature $R(z)$ are respectively defined as

$$\gamma(z) = \arctan\left(\frac{z}{z_R}\right), \quad (2a)$$

$$w(z) = w_0 \sqrt{1 + \left(\frac{z}{z_R}\right)^2}, \quad (2b)$$

$$R(z) = z\left[1 + \left(\frac{z_R}{z}\right)^2\right] \quad (2c)$$

with $z_R = \pi w_0^2/\lambda$ being the Rayleigh range and w_0 the waist of the beam. For shortness, we rewrite Eq. (1) as

$$\vec{E}_{\text{in}} = A_\rho^{|\ell|} e^{i\varphi_0} e^{i\ell\phi} \begin{pmatrix} \epsilon_P \\ \epsilon_S \end{pmatrix}, \quad (3)$$

where we introduced $A_\rho^{|\ell|}(r, z) = C_\rho^{|\ell|} \frac{1}{w(z)} \left(\frac{r\sqrt{2}}{w(z)}\right)^{|\ell|} L_\rho^{|\ell|}\left(\frac{2r^2}{w^2(z)}\right) e^{-\frac{r^2}{w^2(z)}} e^{-ik\frac{r^2}{2R(z)}}$ and $\varphi_0(t, z) = \omega t - kz + (2\rho + |\ell| + 1)\gamma(z)$.

B. Model for the optical properties of a magnetic structure

We model our sample as a magnetic dot of typical lateral extension R_0 deposited on a nonmagnetic surface. We will consider only magnetic structures on the surface of the dot, without dependence on its depth. We will use the σ subscript for the sample's frame, with its surface described in cartesian coordinates (x_σ, y_σ) and polar coordinates (r_σ, ϕ_σ). For the sake of simplicity of the analytical derivations, we will consider a structure that is perfectly flat and is larger than the incident beam $(R_0 > w_0)$, so that geometrical and diffraction effects need not be taken into account. Also, we will consider structures with constant magnetization magnitude and no radial dependence, so that the only variation is due to direction change with azimuthal dependence ϕ_σ. For a better description of the structure in numerical calculations see Appendix A.

The reflection of the light beam is modeled by the reflectivity matrix $\mathbf{R}$, for which $\vec{E}_{\text{out}} = \mathbf{R}\vec{E}_{\text{in}}$. When a light beam is reflected off a magnetic surface, the standard Fresnel reflectivity coefficients for the P and S polarizations, denoted r_{PP} and r_{SS}, are complemented by magnetization-dependent terms r_{PS}^l, r_{PS}^p, and r_0^t describing the magneto-optical Kerr effect (MOKE) [45,67,68]. The first two coefficient couples the S and P polarizations in presence of a longitudinal magnetization and polar magnetization respectively, while the third one acts only on the P polarization when there is a transverse component of the magnetization.

For simplicity, we limit ourselves to the MOKE terms linear with the magnetization [69]. We model the reflection matrix as [67,68]

$$\mathbf{R} = \begin{pmatrix} r_{PP} \cdot \left[1 + r_0^t \cdot m_t\right] & r_{PS}^l \cdot m_l + r_{PS}^p \cdot m_p \\ -r_{PS}^l \cdot m_l + r_{PS}^p \cdot m_p & r_{SS} \end{pmatrix}. \quad (4)$$

The matrix $\mathbf{R}$ depends on the azimuthal location on the sample ϕ_σ through the normalized magnetization terms $m_t(\phi_\sigma)$, $m_l(\phi_\sigma)$, and $m_p(\phi_\sigma)$. They are defined as $m_t = M_t/M_{\text{sat.}}$, $m_l = M_l/M_{\text{sat.}}$ and $m_p = M_p/M_{\text{sat.}}$, where $M_{\text{sat.}}$ is the saturation magnetization of the sample and M_t, M_l and M_p are the magnetization components along the transverse (perpendicular to the scattering plane, i.e., along y_σ), longitudinal (parallel to the scattering plane, i.e. along x_σ) and polar (parallel to the sample's normal, i.e., along $-z_\sigma$) directions with respect to the scattering plane in the sample frame (see Fig. 1). All the five reflectivity coefficients are complex quantities, which we consider constant over the structure.

Now we need to model the azimuthal dependence of the magnetization. The formalism of Eq. (4) requires to express the magnetization in its longitudinal, transverse and polar components, $\vec{m}_l = m_l \hat{x_\sigma}$, $\vec{m}_t = m_t \hat{y_\sigma}$ and $\vec{m}_p = m_p \hat{z_\sigma}$ (Fig. 1). To take advantage of the symmetries of the problem, we expand the angular part on the standard basis functions, $\frac{1}{\sqrt{2\pi}} e^{in\phi_\sigma}$. For any function sufficiently regular, the magnetization m_* (with $* = l, p, t$) can thus be written as

$$m_*(\phi_\sigma) = \sum_{n=-\infty}^{+\infty} m_{*,n} e^{in\phi_\sigma} \quad (5)$$

with complex decomposition coefficients

$$m_{*,n} = \frac{1}{2\pi} \int_0^{2\pi} m_*(\phi_\sigma) e^{-in\phi_\sigma} d\phi_\sigma. \quad (6)$$

We notice here that since m_* is a real quantity, we have the property $m_{*,-n} = \overline{m_{*,n}}$. Now we can rewrite the reflection matrix as

$$\mathbf{R}(\phi_\sigma) = \begin{pmatrix} r_{PP} & 0 \\ 0 & r_{SS} \end{pmatrix} + \sum_n \begin{pmatrix} r_{PP} r_0^t m_{t,n} e^{in\phi_\sigma} & r_{PS}^l m_{l,n} e^{in\phi_\sigma} + r_{PS}^p m_{p,n} e^{in\phi_\sigma} \\ -r_{PS}^l m_{l,n} e^{in\phi_\sigma} + r_{PS}^p m_{p,n} e^{in\phi_\sigma} & 0 \end{pmatrix}, \quad (7)$$

where we have separated the magnetization dependent and independent parts.

TABLE I. Properties of the decomposition coefficients for a particular component of the magnetization m_*, depending on its parity with respect to the x_σ and y_σ axes.

		Symmetry w.r.t. y_σ	
		even	odd
Symmetry w.r.t. x_σ	even	n **even** only $m_{*,n}$ **real** $m_{*,n} = m_{*,-n}$	n **odd** only $m_{*,n}$ **real** $m_{*,n} = m_{*,-n}$
	odd	n **odd** only $m_{*,n}$ **imaginary** $m_{*,n} = -m_{*,-n}$	n **even** only $m_{*,n}$ **imaginary** $m_{*,n} = -m_{*,-n}$

1. Magnetic structures with high symmetries

There is *a priori* no restriction on the span of the n values in the decomposition, and different specific geometries will differ by their decomposition coefficients. We analyze in more details some cases of high symmetry that are relevant for magnetization structure, as defined in the following. For each component m_* of the magnetization, we consider even or odd symmetries with respect to (w.r.t.) the x_σ and y_σ axes in the (x_σ, y_σ) plane. Symmetries w.r.t z_σ in other planes are not considered, since we are limited to the case of no magnetization variations in the depth of the dot. Each of these four cases has specific consequences on the properties of the decomposition coefficients, and in particular on their parity. These properties are demonstrated in Appendix B and summarized in Table I. Given the three components of the magnetization, this restriction leads to 64 (i.e., $4 \times 4 \times 4$) different cases of symmetries. In order to further simplify, we consider the cases of magnetic structures having only two magnetization components (16 cases), and with same parities for their decomposition coefficients. This additional restriction leads to eight cases of symmetry, which fall within the same formalism described in Sec. IV C.

2. Two examples of magnetic structures

We provide now two prototypical examples of magnetic configurations, depicted in Fig. 2. In both examples, we consider no polar magnetization component. In the first one [Fig. 2(a)], the sample separates into two magnetically homogeneous domains of equal size, aligned antiparallel to each other. The second case [Fig. 2(b)] consists of a magnetic vortex with counterclockwise circulation of the magnetization.

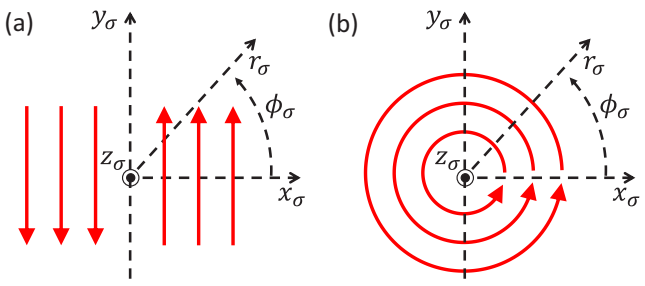

FIG. 2. Examples of magnetic samples with cartesian and polar coordinate systems: (a) two homogeneous and antiparallel magnetic domains and (b) counterclockwise magnetic vortex.

In the case of two antiparallel domains [Fig. 2(a)], the magnetization can be represented as

$$m_l(\phi_\sigma) = 0, \tag{8a}$$

$$m_t(\phi_\sigma) = m_0 \,\mathrm{sgn}(\cos\phi_\sigma), \tag{8b}$$

with m_0 being the constant magnitude of the magnetization normalized by $M_{\mathrm{sat.}}$. In this case, the symmetry of m_t w.r.t. (x_σ, y_σ) is (even, odd). To find the corresponding coefficients, integration of Eq. (6) gives (see Appendix C for the calculation):

$$m_{t,n} = \begin{cases} 0, & \text{for } n \text{ even} \\ \frac{2}{n\pi}\, i^{n-1}\, m_0, & \text{for } n \text{ odd} \end{cases}. \tag{9}$$

In the case of the magnetic vortex [Fig. 2(b)], only two coefficients of the decomposition for both components are nonzero, corresponding to $n = \pm 1$:

$$m_l(\phi_\sigma) = \frac{m_0}{2i} e^{-i\phi_\sigma} - \frac{m_0}{2i} e^{i\phi_\sigma} = -m_0 \sin\phi_\sigma, \tag{10a}$$

$$m_t(\phi_\sigma) = \frac{m_0}{2} e^{-i\phi_\sigma} + \frac{m_0}{2} e^{i\phi_\sigma} = m_0 \cos\phi_\sigma. \tag{10b}$$

In this case, the symmetry of m_l and m_t w.r.t. (x_σ, y_σ) is respectively (odd, even) and (even, odd). The integration in Eq. (6) now gives (Appendix C):

$$m_{*,n} = \begin{cases} 0, & \text{for } n \neq \pm 1 \\ \frac{im_0}{2} n, & \text{for } n = \pm 1, * = l \\ \frac{m_0}{2}, & \text{for } n = \pm 1, * = t \end{cases}. \tag{11}$$

III. MODIFICATION OF THE OAM BY REFLECTION ON A MAGNETIC STRUCTURE

We consider the axis of the OAM beam to pass through the center of the magnetic target. It should be noted that realistic sizes of both magnetic structures and OAM beams can range from hundreds of nanometers to several micrometers. Therefore an experimental implementation can be achieved, with accurate control of the sample holder and beam steering mirrors. In Appendix A, we will show numerically how our results are modified when beam and target are not perfectly aligned. By using Eqs. (3) and (7), we calculate the outgoing electric field $\vec{E}_{\mathrm{out}} = \mathbf{R}\vec{E}_{\mathrm{in}}$, separating the result into two terms corresponding to the nonmagnetic ($\vec{E}^{m=0}_{\mathrm{out}}$) and magnetic ($\vec{E}^{m}_{\mathrm{out}}$) interaction, $\vec{E}_{\mathrm{out}} = \vec{E}^{m=0}_{\mathrm{out}} + \vec{E}^{m}_{\mathrm{out}}$:

$$\vec{E}^{m=0}_{\mathrm{out}} = A^{|\ell|}_\rho(r,0) e^{i\varphi_0} e^{i\ell\phi} \begin{pmatrix} \epsilon_P r_{PP} \\ \epsilon_S r_{SS} \end{pmatrix}, \tag{12a}$$

$$\vec{E}^{m}_{\mathrm{out}} = A^{|\ell|}_\rho(r,0) e^{i\varphi_0} \sum_n e^{i(\ell\phi + n\phi_\sigma)} \times \begin{pmatrix} \epsilon_P r_{PP} r^t_0 m_{t,n} + \epsilon_S \left(r^l_{PS} m_{l,n} + r^p_{PS} m_{p,n} \right) \\ \epsilon_P \left(-r^l_{PS} m_{l,n} + r^p_{PS} m_{p,n} \right) \end{pmatrix}. \tag{12b}$$

We consider that there are no homogeneous magnetization terms: $m_{t,0} = m_{l,0} = m_{p,0} = 0$, since it will considerably simplify the derivation without much loss of generality. In this

way we can express the total field as

$$\vec{E}_{\rm out} = \sum_n \vec{E}_{n,\ell} = A_\rho^{|\ell|}(r,0)e^{i\varphi_0}\sum_n e^{i(\ell\phi+n\phi_\sigma)}\begin{pmatrix}\alpha^x_{n,m}\\ \alpha^y_{n,m}\end{pmatrix}, \quad (13)$$

where we defined the complex quantities $\alpha^x_{n,m}$ and $\alpha^y_{n,m}$ for $n \neq 0$ and $\alpha^x_{0,m}$ and $\alpha^y_{0,m}$ as

$$\begin{aligned}\alpha^x_{0,m} &= \epsilon_P r_{PP},\\ \alpha^x_{n,m} &= m\left[\epsilon_P r_{PP} r^t_0 m_{t,n} + \epsilon_S\left(r^l_{PS} m_{l,n} + r^p_{PS} m_{p,n}\right)\right],\\ \alpha^y_{0,m} &= \epsilon_S r_{SS},\\ \alpha^y_{n,m} &= m\epsilon_P\left(-r^l_{PS} m_{l,n} + r^p_{PS} m_{p,n}\right).\end{aligned} \quad (14)$$

The index $m = \pm 1$ is introduced in order to explicitly describe the reversal of the magnetization direction in Sec. IV, and acts only for $n \neq 0$.

A. Normal incidence

It is important to point out that Eq. (4) is written with respect to a well defined scattering plane, which means off-normal incidence. However, first we consider here an unphysical model system, in which the beam impinges at normal incidence, but the optical constants are still unequal for S and P polarizations. This is a simplification that will allow us to better understand the effect of the magnetic structure on the reflection and to separate it from geometrical effects. Pragmatically, this could be seen as the situation where the incidence angle is very close to normal incidence. Then we will consider the effect of a tilted target in Sec. III B, and we will see in which conditions it is possible to distinguish between the two effects, the trivial geometrical effect and MHD. For normal incidence, the beam and the target share the same polar coordinates, therefore we set $\phi_\sigma = \phi$ and $r_\sigma = r$ in Eq. (12). The field after reflection $\vec{E}_{\rm out}$ is a superposition of different modes. The nonmagnetic term is an OAM beam of the same order as the incoming one. Its polarization will be different from the incoming one due to the different values or r_{PP} and r_{SS} [Eq. (12a)], corresponding to the Kerr effect. The magnetic term is more interesting [Eq. (12b)], and two observations can be made at this point.

(1) The beam is no longer a pure LG mode, since the $|\ell|$ power of r in A and the azimuthal phase no longer match. This leads to the appearance of radial modes ρ different from the incoming one. This effect is already documented in linear processes and was lately rationalized for low-order nonlinear effects [70].

(2) The reflected beam has a different azimuthal mode population with respect to the incoming one. In particular, the incoming OAM of order ℓ will give rise to all the possible orders $\ell + n$ for every n belonging to the decomposition of Eq. (5).

For example, for the case of a magnetic vortex only the coefficients of the decomposition corresponding to $n = \pm 1$ are nonzero, according to Eq. (11). Therefore the interaction of an OAM of order ℓ with a magnetic vortex results in the population of the $\ell \pm 1$ modes. This situation is particularly suitable for the study of MHD, and described in detail in Sec. IV D. As another example, in Fig. 3, we compare the case of a magnetic dot with constant magnetization and a dot

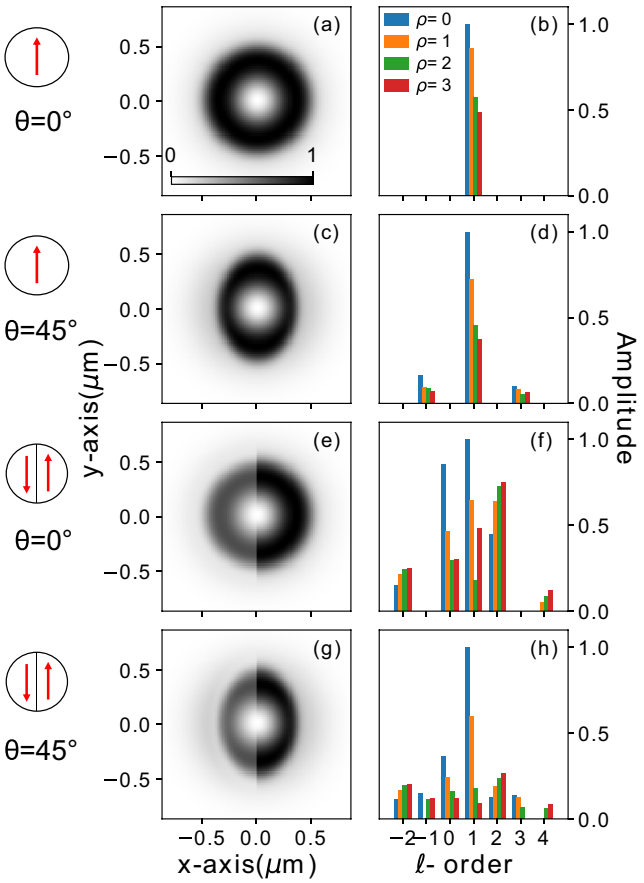

FIG. 3. (Left) Near field intensity profiles and (right) decomposition on the LG-mode basis of a incoming beam with $\ell = 1$ reflected by a magnetic dot of radius 500 nm in four different cases: [(a) and (b)] constant magnetization with incidence angle $\theta = 0°$ and [(c) and (d)] with $\theta = 45°$; [(e) and (f)] two antiparallel magnetic domains as in Fig. 2(a) with incidence angle $\theta = 0°$ and [(g) and (h)] with $\theta = 45°$. The focal spot has a size comparable to that of the magnetic dot. The bar plots values below 4% of the maximum have been forced to 0. Details of the numerical calculations are reported in Appendix A.

with two antiparallel domains as in Fig. 2(a), for an incoming beam with $\ell = 1$. The size of the dot is chosen similar to the beam waist at focus (radius of 500 nm). The details of the numerical calculations are described in Appendix A. The near field intensity profile and the decomposition on the LG basis are shown in Fig. 3, panels (a) and (b) for the case of constant magnetization, while the corresponding ones for the two domains are shown in panels (e) and (f). While there is no modification to the population of ℓ modes in the reflected beam in the case of constant magnetization, in panel (f) we can clearly see the population of $\ell + n$ modes with only n odd terms. In both cases, we find a rich set of radial modes ρ due to the finite size of the target.

It is useful to consider separately the S and P components of the incoming beam. For the S part we set $\epsilon_P = 0$. In this case, $\vec{E}^{m=0}_{\rm out}$ is along the y direction and $\vec{E}^{m}_{\rm out}$ along the x direction. Taking the square of their sum to get the intensity leads to no cross terms. Instead, for the P component of the incoming field, we set $\epsilon_S = 0$, and we find that $\vec{E}^{m=0}_{\rm out}$ is along the x direction while $\vec{E}^{m}_{\rm out}$ has both x and y components. Taking

the square of their sum leads to a cross term, which is at the origin of the dichroism effect that will be discussed in more detail in Sec. IV.

B. Arbitrary incidence angle

We now generalize the model to describe the reflection of an OAM beam at an arbitrary angle of incidence, since in practical situations the sample will be rotated with respect to the incoming beam, in order to be able to collect the reflected beam. This has two effects on the formalism presented before. One is that the reflectivity coefficients will depend on the angle. This can be trivially taken into account and exploited to choose favourable conditions, in which the magneto optical constants will be large compared to the regular Fresnel reflection coefficients. For instance, one may choose the Brewster angle to maximise the magnetic contribution to the reflected intensity, as in transverse MOKE experiments using P-polarized light, with and without polarization analysis [71]. The other effect is a change in the geometry, since the polar coordinates of the beam and the target are no longer the same. For instance, if we consider a magnetic vortex where the magnetization shows a circular pattern, from the point of view of the beam it will appear as an ellipse. This will give rise to a trivial dichroism, which might have different symmetry than the magnetic HD of interest. In order to study this effect, we consider a rotation of the target by an angle θ as depicted in Fig. 1. In this case, the relationship between the cartesian coordinates in the sample frame (x_σ, y_σ) and in the beam frame (x, y) is

$$x_\sigma = \frac{x}{\cos\theta}, \tag{15a}$$

$$y_\sigma = y. \tag{15b}$$

Upon trigonometric inspection and defining the function $g(\phi,\theta) = 1/\sqrt{1-\sin^2\phi\sin^2\theta}$ one finds the following relations (see Appendix D):

$$\sin\phi_\sigma = \sin\phi\, g(\phi,\theta)\cos\theta, \tag{16a}$$

$$\cos\phi_\sigma = \cos\phi\, g(\phi,\theta), \tag{16b}$$

$$e^{i\phi_\sigma} = g(\phi,\theta)\left(\frac{1+\cos\theta}{2}e^{i\phi} + \frac{1-\cos\theta}{2}e^{-i\phi}\right), \tag{16c}$$

$$r_\sigma = \frac{r}{g(\phi,\theta)\cos\theta}. \tag{16d}$$

As expected, for $\theta = 0$ we retrieve the coincidence of the polar coordinates of beam and sample. The azimuthal dependence of the functions of our chosen basis is $e^{in\phi_\sigma}$. With Eq. (16c), we get

$$e^{in\phi_\sigma} = g(\phi,\theta)^n e^{in\phi}\sum_{n_1=0}^{n} C_{n_1}^n \left(\frac{1+\cos\theta}{2}\right)^{n_1} \times \left(\frac{1-\cos\theta}{2}\right)^{n-n_1} e^{i2n_1\phi}, \tag{17}$$

where $C_{n_1}^n$ is the number of combinations of n_1 elements from n. This expression should be inserted in Eq. (12b). Without expressing it fully, we see right away that the phases previously reading $\ell\phi + n\phi$ now become $\ell\phi + (n+2n_1)\phi$. For instance, in the case of the magnetic configurations depicted in Fig. 2 where only odd coefficients are present, the even coefficients remain zero when considering a tilted target. This is clearly shown in Figs. 3(c) and 3(d), where we chose $\theta = 45°$.

Additionally, the radius r_σ and the g function also become function of ϕ, with a $\sin^2\phi$ dependence. Thus they are symmetric with respect to $\phi = \pi$ and $\phi = \pi/2$ and their decomposition yields only even coefficients. We notice that if the incoming beam carries an odd value of the OAM, the phase-dependent term will appear in the odd LG modes, while the radial-dependent terms will populate the even LG modes. Conversely, if the incoming beam carries an even value of OAM, phase-dependent terms will populate the even modes and radial-dependent terms the odd modes. Therefore their influence can always be separated. In particular, we come to the conclusion that the magnetic terms will show up in the LG components of opposite parity compared to the incoming beam, while the nonmagnetic terms populate modes of the same parity, which modifies the observation 2 of the previous section where all the $\ell + n$ modes are populated by the magnetic term and only ℓ by the nonmagnetic one. This case is illustrated in Figs. 3(g) and 3(h) (see Appendix A for further details).

IV. HELICOIDAL DICHROISM IN THE FAR FIELD

So far we focused on the structure and mode content of the field right after reflection by the magnetic object. Here we show how the far field profile of the beam is affected, leading to what we call differential helicoidal dichroism, i.e., a difference in intensity profiles upon switching the sign of the OAM, of the magnetization, or of both. Here "differential" is meant as a MHD that occurs at every single point in the image in the far field. However, the integration over space in the image leads to constant total intensity, independent on the sign of the OAM or of the magnetization. This is qualitatively different from MCD where the difference persists also after spatial integration of the scattered intensity. In this respect, MHD is similar to CDAD of photoemission, which is also a spatially differential effect with no dichroic signal of the spatially integrated intensity.

In the following, we will describe analytically only the case of normal reflection, and in Sec. V we will discuss how a tilted sample can lead in practice to favorable conditions, along the lines of what was discussed in Sec. III B.

A. Propagation of the reflected field from the focus to the far field

In order to propagate $\vec{E}_{\text{out}}$ to the far field, we make use of the Fresnel operator. From now on, we refer to the far field on the screen in Fig. 1 with the coordinate system (r, ϕ, z), and we indicate with the prime the field right after reflection, i.e., the one from Eq. (13). For a function $E(r,\phi,0)$ with separable variables [as it is in our case of Eq. (13)], the Fresnel propagation equation in cylindrical coordinates reads [72]

$$E(t,r,\phi,z) = \frac{e^{i\varphi_0(t,z)}}{i\lambda z} \times e^{\frac{ik}{2z}r^2}\int_0^{2\pi} d\phi' \int_0^{+\infty} r'dr'\, E(r',\phi',0)e^{-\frac{ikrr'}{z}\cos(\phi-\phi')}. \tag{18}$$

The expression in Eq. (18) has the form of a specialized Fourier transform, or a generalized Hankel transform. Therefore we propagate the field of Eq. (13) with Eq. (18). We study what happens to the propagation of any term $E^{x,y}_{n,\ell,m}(r',\phi',0) = A^{|\ell|}_{\rho}(r',0)e^{i(\ell+n)\phi'}\alpha^{x,y}_{n,m}$, and the final result will be given by the sum over n. We have

$$\begin{aligned}
&E^{x,y}_{n,\ell,m}(t,r,\phi,z)\\
&\quad= \frac{e^{i\varphi_0(t,z)}}{i\lambda z}e^{\frac{ik}{2z}r^2}\alpha^{x,y}_{n,m}\int_0^{+\infty} r'dr'A^{|\ell|}_{\rho}(r',0)\\
&\qquad\times\int_0^{2\pi} d\phi'\; e^{i(\ell+n)\phi'}e^{-\frac{ikrr'}{z}\cos(\phi-\phi')}\\
&\quad= \frac{e^{i\varphi_0(t,z)}}{i\lambda z}e^{\frac{ik}{2z}r^2}\alpha^{x,y}_{n,m}e^{i(\ell+n)\phi}\int_0^{+\infty} r'dr'A^{|\ell|}_{\rho}(r',0)\\
&\qquad\times\int_0^{2\pi} d\phi''\; e^{i(l+n)\phi''}e^{-\frac{ikrr'}{z}\cos\phi''} \qquad (19)
\end{aligned}$$

with the substitution $\phi'' = \phi' - \phi$. The last integration is just the definition of the Bessel function $J_{\ell+n}(\frac{krr'}{z})$ multiplied by a factor $2\pi/i^{l+n}$ [72]. We keep implicit the trivial dependence on time in $\varphi_0(z) = \varphi_0(t,z) = \omega t - kz + (2\rho + |\ell| + 1)\gamma(z)$, while we write explicitly the expression of $A^{|\ell|}_{\rho}(r',0) = C^{|\ell|}_{\rho}\frac{1}{w_0}(\frac{r'\sqrt{2}}{w_0})^{|\ell|}L^{|\ell|}_{\rho}(\frac{2r'^2}{w_0^2})e^{-\frac{r'^2}{w_0^2}}$. With $1/i^{\ell+n} = e^{-i\frac{\pi}{2}(\ell+n)}$, we obtain

$$\begin{aligned}
&E^{x,y}_{n,\ell,m}(r,\phi,z)\\
&\quad= 2\pi\frac{e^{i\varphi_0(z)}}{i\lambda z}e^{\frac{ik}{2z}r^2}C^{|\ell|}_{\rho}\frac{1}{w_0}\left(\frac{\sqrt{2}}{w_0}\right)^{|\ell|}\alpha^{x,y}_{n,m}e^{i(\ell+n)(\phi-\frac{\pi}{2})}\\
&\qquad\times\int_0^{+\infty} dr'r'^{|\ell|+1}L^{|\ell|}_{\rho}\left(\frac{2r'^2}{w_0^2}\right)e^{-\frac{r'^2}{w_0^2}}J_{\ell+n}\left(\frac{krr'}{z}\right)\\
&\quad= D^{|\ell|}_{\rho}(r,z)\alpha^{x,y}_{n,m}e^{i(\ell+n)(\phi-\pi/2)}H_{n,\ell}(kr,z), \qquad (20)
\end{aligned}$$

where we introduced the function $D^{|\ell|}_{\rho}(r,z) = 2\pi\frac{e^{i\varphi_0(z)}}{i\lambda z}e^{\frac{ik}{2z}r^2}C^{|\ell|}_{\rho}\frac{1}{w_0}(\frac{\sqrt{2}}{w_0})^{|\ell|}$, and the function $H_{n,\ell}(kr,z)$ as the result of the radial integral. This integral can be evaluated numerically, or for example it is found tabulated for the mode $\rho = 0$ (meaning $L^{|\ell|}_{\rho} = 1$) in Ref. [73]. In particular, we notice the fact that the H functions are real, and that since $J_{-n}(x) = (-1)^n J_n(x)$, we have

$$H_{-n,-\ell}(kr,z) = (-1)^{n+\ell}H_{n,\ell}(kr,z). \qquad (21)$$

From Eq. (20), we confirm that the population of the $\ell + n$ modes is maintained after propagation, as expected.

B. Expressions of the helicoidal dichroism

The intensity detected on the screen placed in the far field, for each of the polarization components x and y, will be the square modulus of the sum over n of the field components $E^{x,y}_{n,\ell,m}$:

$$\begin{aligned}
I^{x,y}_{\ell,m} &= \left|\sum_n E^{x,y}_{n,\ell,m}\right|^2\\
&= \left|D^{|\ell|}_{\rho}\right|^2\left|\sum_n \alpha^{x,y}_{n,m}e^{i(\ell+n)(\phi-\pi/2)}H_{n,\ell}\right|^2\\
&= \left|D^{|\ell|}_{\rho}\right|^2\sum_{n,n'}\alpha^{x,y}_{n,m}\overline{\alpha^{x,y}_{n',m}}e^{i(n-n')(\phi-\pi/2)}H_{n,\ell}H_{n',\ell}\\
&= \left|D^{|\ell|}_{\rho}\right|^2\sum_n\left|\alpha^{x,y}_{n,m}\right|^2H^2_{n,\ell}\\
&\quad+\left|D^{|\ell|}_{\rho}\right|^2\sum_{n\neq n'}\alpha^{x,y}_{n,m}\overline{\alpha^{x,y}_{n',m}}e^{i(n-n')(\phi-\pi/2)}H_{n,\ell}H_{n',\ell}\\
&= \left(I^{x,y}_{\ell,m}\right)_1 + \left(I^{x,y}_{\ell,m}\right)_2, \qquad (22)
\end{aligned}$$

where we introduced the two terms of the sum $(I^{x,y}_{\ell,m})_{1,2}$ for convenience. Also, for the following it is useful to separate the product $\alpha^{x,y}_{n,m}\overline{\alpha^{x,y}_{n',m}}$ in its modulus and phase term:

$$\alpha^{x,y}_{n,m}\overline{\alpha^{x,y}_{n',m}} = \left|\alpha^{x,y}_{n,m}\right|\left|\alpha^{x,y}_{n',m}\right|e^{i\delta\varphi^{x,y}_{n,n'}}. \qquad (23)$$

At this point, we can explicitly write the expressions for MHD, where we need to calculate the difference in far-field intensities between two measurements. We will consider separately three possible dichroism experiments: incoming beams with opposite ℓ (MHD-ℓ), magnetic targets with opposite magnetization direction m (MHD-m), or both (MHD-ℓm). We define the three MHD respectively as

$$\Delta I^{x,y}_{\ell}(r,\phi,z) = I^{x,y}_{\ell,m}(r,\phi,z) - I^{x,y}_{-\ell,m}(r,\phi,z), \qquad (24a)$$

$$\Delta I^{x,y}_{m}(r,\phi,z) = I^{x,y}_{\ell,m}(r,\phi,z) - I^{x,y}_{\ell,-m}(r,\phi,z), \qquad (24b)$$

$$\Delta I^{x,y}_{\ell,m}(r,\phi,z) = I^{x,y}_{\ell,m}(r,\phi,z) - I^{x,y}_{-\ell,-m}(r,\phi,z). \qquad (24c)$$

Now we consider the effect of the two terms $(I^{x,y}_{\ell,m})_{1,2}$ on MHD separately. We show in Appendix E that the first term $(I^{x,y}_{\ell,m})_1$ does not contribute to MHD-m and has negligible contribution to MHD-ℓ and MHD-ℓm in most practical cases. Therefore, in the following we will disregard it. Instead, $(I^{x,y}_{\ell,m})_2$ leads to MHD. As shown in Appendix F, upon manipulation of the indices we can calculate the three MHD expressions:

$$\begin{aligned}
&\Delta I^{x,y}_{\ell}(r,\phi,z)\\
&\quad= 2\left|D^{|\ell|}_{\rho}\right|^2\sum_{\substack{n\neq n'\\ n-n'>0}} H_{n,\ell}(kr,z)H_{n',\ell}(kr,z)\\
&\qquad\times\Big[\left|\alpha^{x,y}_{n,m}\right|\left|\alpha^{x,y}_{n',m}\right|\cos\left((n-n')(\phi-\pi/2)+\delta\varphi^{x,y}_{n,n'}\right)\\
&\qquad-(-1)^{n+n'}\left|\alpha^{x,y}_{-n,m}\right|\left|\alpha^{x,y}_{-n',m}\right|\cos\left((n-n')(\phi-\pi/2)\right.\\
&\qquad\left.-\delta\varphi^{x,y}_{-n,-n'}\right)\Big], \qquad (25)\\
&\Delta I^{x,y}_{m}(r,\phi,z)\\
&\quad= 4\left|D^{|\ell|}_{\rho}\right|^2\sum_{n\neq 0}\left|\alpha^{x,y}_{0,m}\right|\left|\alpha^{x,y}_{n,m}\right|\\
&\qquad\times\cos\left[n(\phi-\pi/2)+\delta\varphi^{x,y}_{n,0}\right]H_{0,\ell}(kr,z)H_{n,\ell}(kr,z), \qquad (26)
\end{aligned}$$

$$\Delta I^{x,y}_{\ell,m}(r,\phi,z) = 2\left|D^{|\ell|}_{\rho}\right|^2 \sum_{\substack{n\neq n'\\ n-n'>0}} H_{n,\ell}(kr,z)H_{n',\ell}(kr,z) \times \left[\left|\alpha^{x,y}_{n,m}\right|\left|\alpha^{x,y}_{n',m}\right|\cos\left((n-n')(\phi-\pi/2)+\delta\varphi^{x,y}_{n,n'}\right) + \chi_{n,n'}(-1)^{n+n'}\left|\alpha^{x,y}_{-n,m}\right|\left|\alpha^{x,y}_{-n',m}\right| \times \cos\left((n-n')(\phi-\pi/2)-\delta\varphi^{x,y}_{-n,-n'}\right)\right]. \quad (27)$$

For the third expression MHD-ℓm of Eq. (27) we defined the function $\chi_{n,n'} = 1$ if $n = 0$ or $n' = 0$ and -1 otherwise.

From Eq. (26), we can draw an important conclusion about the relationship between magnetic structure and observation of MHD. For this, we need to consider that having an OAM with fixed ℓ leads to MHD-m as long as $\Delta I^{x,y}_{m}(r,\phi,z) \neq 0$. Since $\alpha^{x,y}_{0,m}$, the H function and the cosine term cannot be identically zero everywhere in r and ϕ, the only requirement is to have at least one $\alpha^{x,y}_{n,m}$ nonzero. Therefore we find that there will be MHD whenever the magnetization is nonhomogeneous. Here it is important to stress that we considered the nonhomogeneity to be an azimuthal dependence of the magnetization direction with constant magnitude. However, a decomposition of a radial dependent magnetization in a manner similar to Eq. (5) and a amplitude varying magnetization in Eq. (14) would also eventually lead to MHD for similar reasons.

Furthermore, Eq. (26) leads us to another important conclusion. In the particular case of an incoming beam without OAM ($\ell = 0$), there still exists differential MHD when switching the magnetization (MHD-m). As soon as the magnetization has some structure (as in the two cases of Fig. 2, for example) a linearly polarized Gaussian beam will populate different OAM modes after reflection. This requirement of anisotropy for OAM interaction has already been pointed out [74]. As an example, the magnetic vortex [Fig. 2(b)] will populate the modes $\ell = \pm 1$. Measuring the reflected beam profile with spatial resolution will allow to obtain dichroic images when changing the sign of the magnetization. This is an extension to the case of MCD in reflection by a magnetic domain [64], since we find that linearly polarized light even wihtout OAM can still lead to a helicoidal dichroic signal (MHD-m).

Finally, it can be noticed that the information contained in the three MHD of Eqs. (25)–(27) is redundant. Indeed, we have MHD-ℓ = MHD-ℓm + MHD-m [75]. The three equations are the general expressions of MHD for OAM light with generic ℓ and ρ modes and any given symmetry of magnetization, but they are not trivial. For a certain structure with no specific symmetry, any coefficient may exist with any phase and we do not anticipate any further simplification. Instead, they can greatly simplify when considering specific symmetric structures with respect to the center of the beam, or specific incoming polarizations. An example is given in the following section.

C. Example: *P*-polarized beam on a symmetric structure

In order to have a better insight and simplify the expressions of MHD, we consider as an example the case of a *P*-polarized incoming beam reflected by a highly symmetric magnetic structure with only two magnetization components (e.g., m_l and m_t) and with decomposition coefficients n of the same parity, as defined in Sec. II B. In other words, if the component m_l corresponds to a given case of Table I, the component m_t has to be in the same one or in the diagonal one. Therefore we set $\epsilon_S = 0$, and since $m_{*,n} = \overline{m_{*,-n}}$ (Sec. II B), we have $|\alpha^{x,y}_{n,m}| = |\alpha^{x,y}_{-n,m}|$. We also define the two following phases:

$$\varphi_{*,n} = \arg(m_{*,n}) + \arg(m), \quad (28a)$$

$$\varphi^t_0 = \arg\left(r^t_0\right). \quad (28b)$$

We have the following properties: $\varphi_{*,n} = -\varphi_{*,-n}$, and either $\varphi_{*,n} = 0$ or π for real coefficients or $\varphi_{*,n} = \pm\pi/2$ for imaginary coefficients (see Table I). For the α^x values, we calculate

$$\delta\varphi^x_{n,n'} = \begin{cases} \varphi_{t,n} - \varphi_{t,n'} = 0 \text{ or } \pi & \text{if } n, n' \neq 0, \\ -\varphi_{t,n'} - \varphi^t_0 & \text{if } n = 0, \\ \varphi_{t,n} + \varphi^t_0 & \text{if } n' = 0. \end{cases} \quad (29)$$

Instead, for the α^y values, we calculate

$$\alpha^y_{0,m} = 0, \quad (30a)$$

$$\delta\varphi^y_{n,n'} = \varphi_{l,n} - \varphi_{l,n'} = 0 \quad or \quad \pi \text{ if } n, n' \neq 0. \quad (30b)$$

Now we can evaluate the three MHD expressions for this specific case. The full calculations are detailed in Appendix G. It is found that the y component in all cases ΔI^y_ℓ, ΔI^y_m and $\Delta I^y_{\ell,m}$, is identically zero, therefore MHD reduces to the x component. The results are reported in the following, and illustrated in Fig. 4 for the case of a magnetic dot with two antiparallel domains as in Fig. 2(a).

1. Expression of MHD-ℓ

The expression of $\Delta I^x_\ell(r,\phi,z)$ takes a compact form when considering that only either odd or even n terms are present because of the symmetries invoked in this example. For even terms, we obtain

$$\Delta I^x_\ell(r,\phi,z) = -4\left|D^{|\ell|}_{\rho}\right|^2 H_{0,\ell}\left|\alpha^x_{0,m}\right|\sin\varphi^t_0 \times \sum_{\substack{n\neq 0\\ n \text{ even}}} (-1)^{\frac{n}{2}} H_{n,\ell}\left|\alpha^x_{n,m}\right|\sin(n\phi+\varphi_{t,n}), \quad (31)$$

while for odd terms, we obtain

$$\Delta I^x_\ell(r,\phi,z) = 4\left|D^{|\ell|}_{\rho}\right|^2 H_{0,\ell}\left|\alpha^x_{0,m}\right|\cos\varphi^t_0 \times \sum_{\substack{n\neq 0\\ n \text{ odd}}} (-1)^{\frac{n+1}{2}} H_{n,\ell}\left|\alpha^x_{n,m}\right|\sin(n\phi+\varphi_{t,n}). \quad (32)$$

In Figs. 4(a) and 4(b), we can observe this sine azimuthal dependence for the example of two antiparallel domains, calculated for $m = \pm 1$.

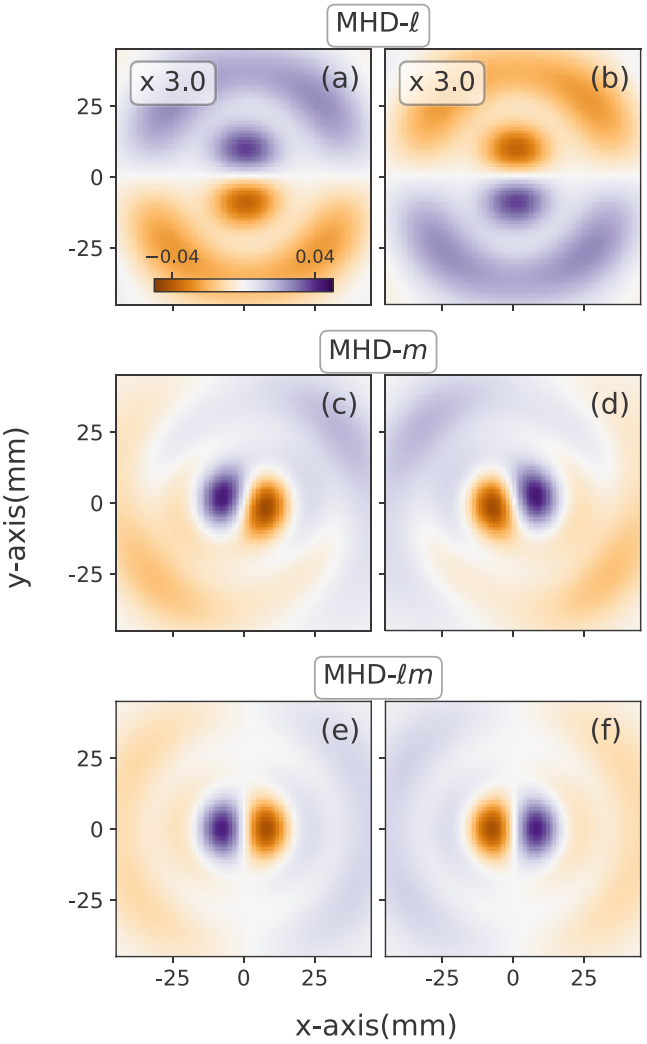

FIG. 4. Computation of MHD for a magnetic dot of 500 nm with two antiparallel domains as in Fig. 2(a). (a) MHD-ℓ for $m = 1$ and (b) for $m = -1$; (c) MHD-m for $\ell = 1$ and (d) for $\ell = -1$; (e) MHD-ℓm as a difference of intensity maps corresponding to $\ell = 1$ and $m = 1$ and $\ell = -1$ and $m = -1$, and (f), MHD-ℓm, difference of intensity maps corresponding to $\ell = 1$ and $m = -1$ and $\ell = -1$ and $m = 1$. The MHD plots are normalized to the global maximum of their corresponding far-field intensity profiles. The incoming polarization is P and the angle of incidence is $\theta = 5^\circ$. The computational details are given in Appendix A.

2. Expression of MHD-m

For the expression of $\Delta I^x_m(r, \phi, z)$, we obtain

$$\Delta I^x_m(r,\phi,z) = 4\left|D^{|\ell|}_\rho\right|^2 H_{0,\ell}\left|\alpha^x_{0,m}\right| \sum_{n\neq 0} H_{n,\ell}\left|\alpha^x_{n,m}\right| \times \cos\left[n(\phi - \pi/2) + \varphi_{t,n} + \varphi^t_0\right]. \quad (33)$$

We can observe this azimuthal dependence for the example of two antiparallel domains in Figs. 4(c) and 4(d), calculated for $\ell = \pm 1$.

3. Expression of MHD-ℓm

In a similar way to the case of MHD-ℓ, the expression of $\Delta I^x_{\ell,m}(r, \phi, z)$ takes a compact form when considering separately the even and odd n terms. For even terms, we obtain

$$\Delta I^x_{\ell,m}(r,\phi,z) = -4\left|D^{|\ell|}_\rho\right|^2 H_{0,\ell}\left|\alpha^x_{0,m}\right| \cos\varphi^t_0 \times \sum_{\substack{n\neq 0\\ n\ \text{even}}} (-1)^{\frac{n}{2}} H_{n,\ell}\left|\alpha^x_{n,m}\right| \cos(n\phi + \varphi_{t,n}) \quad (34)$$

and for odd terms,

$$\Delta I^x_{\ell,m}(r,\phi,z) = 4\left|D^{|\ell|}_\rho\right|^2 H_{0,\ell}\left|\alpha^x_{0,m}\right| \sin\varphi^t_0 \times \sum_{\substack{n\neq 0\\ n\ \text{odd}}} (-1)^{\frac{n+1}{2}} H_{n,\ell}\left|\alpha^x_{n,m}\right| \cos(n\phi + \varphi_{t,n}). \quad (35)$$

The cosine azimuthal dependence is shown in Figs. 4(e) and 4(f) for the example of two antiparallel domains, calculated for $m = \pm 1$ or equivalently for $\ell = \pm 1$.

4. Discussion of MHD expressions

The five formulas Eqs. (31)–(35) summarize the main properties of MHD in structures with high symmetry as defined in Sec. II B, probed with incoming linearly P-polarized light, and detected without any specific polarimetric device. We notice that all contributing terms come from the interference between regular reflectivity, indexed by the subscript 0, and a coefficient of the magnetization, with no cross terms between different magnetization components. We also note that inverting the magnetization corresponds to inverting all $\alpha^{x,y}_{n,m}$ coefficients ($n \neq 0$), i.e., adding a π phase to all $\varphi_{t,n}$. All intensity differences change sign as expected for a dichroism. This is an important point if the process is to be used for determining the chirality of magnetic structures. Importantly, when the structure has only odd (respectively, even) coefficients, $\Delta I^x_\ell(r, \phi, z)$ shows a sine pattern, the amplitude of which is proportional to $\cos\varphi^t_0$ (respectively, $\sin\varphi^t_0$), while $\Delta I^x_{\ell,m}(r, \phi, z)$ shows a cosine pattern, the amplitude of which is proportional to $\sin\varphi^t_0$ (respectively, $\cos\varphi^t_0$). The two patterns can thus be fitted to yield, up to some normalization the cosine and sine of the phase of one of the MOKE constants. In particular, if we consider the common case $|m_{t,n}||r^t_0| \ll 1$, which is typical away from absorption resonance and Brewster's angle [76], then $|\alpha^x_{n\neq 0,m}| \ll |\alpha^x_{0,m}|$ [Eq. (14)], and therefore $I_\ell \propto |\alpha^x_{0,m}|^2 H^2_{0,\ell} = |\epsilon_P r_{PP}|^2 H^2_{0,\ell}$, meaning that the reflected intensity is dominated by $|r_{PP}|^2$. In such a case, one can estimate, e.g., for a sample with odd coefficients, the expression of the normalized dichroism MHD-$\ell = \Delta I_\ell/(I_\ell + I_{-\ell})$:

$$\text{MHD-}\ell \approx 2\sum_{\substack{n\neq 0\\ n\ \text{odd}}} (-1)^{\frac{n+1}{2}} \frac{H_{n,\ell}(kr,z)}{H_{0,\ell}(kr,z)} \times \left|r^t_0\right||m_{t,n}| \sin(n\phi + \varphi_{t,n}) \cos\varphi^t_0, \quad (36)$$

where we have reintroduced the explicit dependence of the $H_{n,\ell}$ functions on space and dropped the x label, since there is

strictly no contribution of the y term to $\Delta I_\ell = (I_\ell - I_{-\ell})$, and only a weak one to $(I_\ell + I_{-\ell})$, of the order of the one discarded for the x term. Similar expressions of the normalized MHD can be obtained in the other cases, replacing the sine and cosine according to Eqs. (31), (34), and (35). Moreover, each component of the $\cos n\phi$ or $\sin n\phi$ images can be separated by a polar Fourier transform or an Abel inversion, and are all proportional to the amplitude of the MOKE constant times the nth coefficient of the decomposition of the magnetization. We expect for this amplitude an order of magnitude corresponding to the ratio of the MOKE constants over the Fresnel constants, which is in the few percent to tens of percents. On the other hand, exploring wavelengths at the absorption edges and geometries near the Brewster angle might give even larger signals.

D. A case study: application to the magnetic vortex state

In this section, we exploit the previous results and explore numerically how to extract the complex magneto-optical constant r_0^t in an example. We consider a P-polarized beam carrying OAM $\ell = \pm 1$ reflected by a magnetic vortex (MV) with sign of its helicity designed by $m = \pm 1$, as the one depicted in Fig. 2. Details of the numerical model we implement to describe the MV as a ferromagnetic dot are given in Appendix A. Using the expressions from the previous sections, we obtain for this case:

$$\text{MHD-}\ell \approx m\left|r_0^t\right| \cos\varphi_0^t(-\mathcal{H}_{-1} - \mathcal{H}_1)\sin\phi, \quad (37a)$$

$$\text{MHD-}m \approx m\left|r_0^t\right| \sum_{n=\pm 1} \mathcal{H}_n \sin(\phi + n\varphi_0^t), \quad (37b)$$

$$\text{MHD-}\ell m \approx m\left|r_0^t\right| \sin\varphi_0^t(\mathcal{H}_{-1} - \mathcal{H}_1)\cos\phi, \quad (37c)$$

where the function $\mathcal{H}_n$ is defined as $\mathcal{H}_n(kr, z) = H_{n,1}(kr, z)/H_{0,1}(kr, z)$. Two of the MHD signals, MHD-ℓ and MHD-ℓm for example, allow to extract r_0^t by fitting the intensity maps to $\sin\phi$ and $\cos\phi$ functions. To test this prediction, we compute MHD-ℓ and MHD-ℓm maps for a MV on an Fe dot at $\theta = 5°$ for several photon energies. They are shown in Figs. 5(a) and 5(b), respectively, for $h\nu = 50.1$ eV. The tilt induces an extra dissymetry, but with a 2ϕ symmetry which does not interfere with the MHD ϕ symmetry, as discussed in Sec. III B. The fit of the lineout taken along the shown circles is excellent for MHD-ℓ, while poor for MHD-ℓm [Fig. 5(c)]. However, since tilt and MHD have different symmetry, the fitted cosine still corresponds to the same line out extracted from the ideal $\theta = 0°$ case. Upon normalization of amplitude and phase, we can retrieve the complex r_0^t, taking care of scaling the circle with $h\nu$. The comparison to their initial values plugged in the model is excellent [Fig. 5(d)], whether the tilt is taken into account or not. Also, the choice of the fitting circle radius has no influence, as long as it gives an intense signal for all wavelengths.

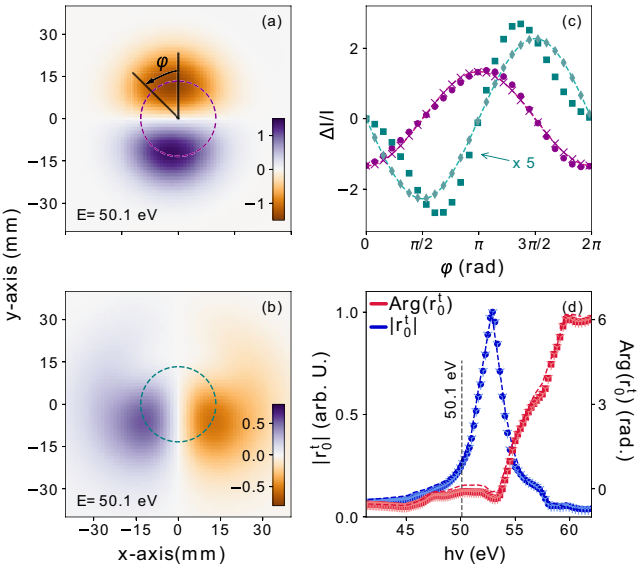

FIG. 5. (a) MHD-ℓ and (b) MHD-ℓm for $\theta = 5°$ and $h\nu = 50.1$ eV. (c) Lineouts along the circles drawn in panel (a) (purple dots) and (b) (green squares), together with the fits from Eq. (37a)–(37c). Purple crosses and green diamonds correspond to the same lineouts obtained from the $\theta = 0°$ case. (d) $h\nu$ dependence of amplitude (blue, left axis) and phase (red, right axis) of the retrieved magneto-optical constant r_0^t for $\theta = 5°$ (full symbols) and $\theta = 0°$ (three-branch crosses). The dashed lines are the corresponding input r_0^t values. Amplitudes are normalized to 1, with same normalization constant for tilted and not tilted cases. Phases are set equal at resonance.

V. CONCLUSION

As allowed by Curie's principle, we identified a dichroism in the intensity pattern of beams carrying orbital angular momentum (ℓ) reflected by a target with a magnetic structure, that we call Magnetic Helicoidal Dichroism. We have restricted our detailed analysis to the case of a magnetization distribution of constant amplitude and no radial dependence, but our model can be readily generalized beyond these constraints. We find that as soon as the magnetization is not spatially homogeneous [74], because of magneto-optic interaction the reflected beam will populate different OAM modes depending on the decomposition of the magnetic structure on the polar basis set. Consequently, because of interference of the different modes the intensity pattern in the far field changes when changing ℓ, the sign of the magnetization or both. The dichroism is differential in the sense that the effect is averaged out when the reflected intensity is integrated in space. For magnetic structures of sufficiently high symmetry, the MHD appears as a simple sinusoidal pattern at any given radius of the reflected image, the parameters of which depend on the particular shape of the magnetic structure and on the magneto-optical constants. In particular, we could directly link the differential image shapes to the coefficients of the polar decomposition of the magnetic structure, providing a new way to analyze the magnetization, or alternatively to determine the MOKE constants without any polarization device in the experiment. For structures with many decomposition coefficients, the MOKE constants are even overdetermined and therefore reliably accessible in an experiment. This provides MHD with the potential of becoming an important new tool to access the properties of magnetic materials, in particular for dynamic studies measurements, which are known to be

time-consuming, including time-resolved pump-probe studies of the magnetization dynamics that can be naturally implemented at laser based experimental facilities.

The common situation of an incoming beam without OAM is a special case in our MHD model. We showed that reflection by a sample with inhomogeneous magnetization redistributes the mode $\ell = 0$ into other modes with $\ell \neq 0$, depending on the sample symmetry. The MHD is still present when switching the sign of the magnetization (MHD-m). This effect, up to now overlooked in magnetic reflection experiments, may provide a new way to either study magnetism or even to produce OAM light. Conversely, special magnetic structures could be engineered in order to obtain light carrying OAM or to analyze the OAM content of a beam.

For practical reasons, an experiment exploiting the MHD requires reflection at an angle out from normal incidence. We found that the symmetry breaking of a tilted sample is an additional way to redistribute the OAM modes population upon reflection, which in general can be mixed to the redistribution due to the interaction with the structure. However, we could identify favorable conditions where the two effects do not mix. A specific case is an incoming P polarized beam, impinging on a structure that shows even or odd magnetization with respect to both the x_σ and y_σ axes. In this case, the magnetic effect only appears on the odd OAM modes, while the geometrical effect appears on the even ones. We examined in more detail the case of a magnetic vortex, which is particularly simple since the decomposition has only two coefficients, and particularly interesting since it allows to study the coupling of a beam carrying topological charge with an object of topological nature itself.

The theory of MHD that we have presented is very general and can be applied to many kinds of magnetic structures, to any polarization state and in different wavelength ranges. We developed it into details and applied it to a few specific cases, showing for instance how it makes it possible to retrieve the MOKE constants in the XUV range without implying any polarization analysis. Among other possible applications, for example, one can envisage to: extend the study to the soft x-ray regime; probe periodic nano- and micro-structures to address the collective response of their magnetization; achieve a rapid readout of the symmetry of the magnetization structure, possibly with micrometer spatial resolution by integrating a beam and/or sample scanning system; explore the coupling with SAM [42,77], since tailoring structured light beams can allow the appearance of new dichroisms [78].

This MHD theory of reflection is developed in the framework of classical electromagnetism, as a result of spatially inhomogeneous reflectivity coefficients coupled to a spatially varying phase term of the beam reflected. Similar arguments could be made for an equivalent of Faraday effect, analyzing the transmission matrix. In order to understand the physical microscopic origin of MHD, however, a quantum description of reflection is needed [79]. Indeed, at this stage it is still unclear whether there is a local transfer of OAM between light and matter, and how the magnetic structure dynamically responds to light with OAM. Experimentally, these questions can be addressed by extending the study to the time domain, which is naturally accessible with HHG and FEL sources. Whether or not there is angular momentum transfer, the redistribution of azimuthal modes in the reflected beam may locally alter the magnetic structure of the sample, which could dynamically respond with an effect similar to spin-orbit torque with large spin density [80], thus leading to a time-dependent MHD. Also, time resolution would provide an access point to the dynamics of magnetic structures such as vortices [81] and skyrmions [82] and potentially to manipulate them, a great interest for topological and spintronics applications.

From this outlook, it appears that the analysis of MHD in the reflection of OAM beams from a magnetic structure can find original applications of both applied and fundamental interest in the field of magneto-optics.

ACKNOWLEDGMENTS

We are very grateful to Giovanni De Ninno for fruitful discussions. This work was supported by the Agence Nationale de la Recherche (under Contracts No. ANR11-EQPX0005-ATTOLAB and No. ANR14-CE320010-Xstase) and by the Schweizerischer Nationalfonds zur Förderung der Wissenschaftlichen Forschung (Project No. P2ELP2_-181877).

APPENDIX A: NUMERICAL CALCULATIONS

1. Optical beam

The theory presented here, was tested with a specifically written python-based propagation code based on Fresnel propagation of light. When propagating from the far-field to the near field or vice versa, a Fourier transform method is used to compute the field in the new plane, while for far-field to far-field propagation we use the convolution method. We set Laguerre mask and lens at the same place (Fig. 1), with focal length of the lens of 1 m. The sample is placed at focus. The waist of the incoming collimated beam is set to $w_0 = 15$ mm. The intensity patterns are computed separately for the *P* and *S* linearly polarized components, before being combined when required. The transverse direction is mapped on a spatial grid of 1024×1024 points.

We consider wavelengths significantly larger than the rugosity of the dot's surface, expected below the nanometer. The beam waist at focus is smaller than the MV diameter, avoiding the treatment of edge diffraction. These hypothesis justify the coherent approach proposed here. With these constraints, a suitable wavelength range for MHD is 10 nm $\lesssim \lambda \lesssim$ 1000 nm, which covers magnetization sensitive electronic excitations at optical and core transitions in most elements of interest for magnetic materials. The wavelength of the beam is set to $\lambda = 23.5$ nm in our simulations when not specified otherwise. However, it is important to stress that the dependence of our results on the wavelength is only due to the variation of the reflectivity coefficients on λ, as illustrated in Fig. 5.

The two orthogonal components of the field calculated on the detector in the far field can be decomposed on a LG basis with a finite number of elements. In order to define the family of LG modes we need to choose the finite amount of ρ and ℓ modes. We noted, on the examples that we treated, that using ρ modes ranging from 0 to 18 and ℓ modes from -9 to 9 (that is 19 ℓ modes in total, and a grand total of 361 modes) was sufficient to accurately describe the intensity

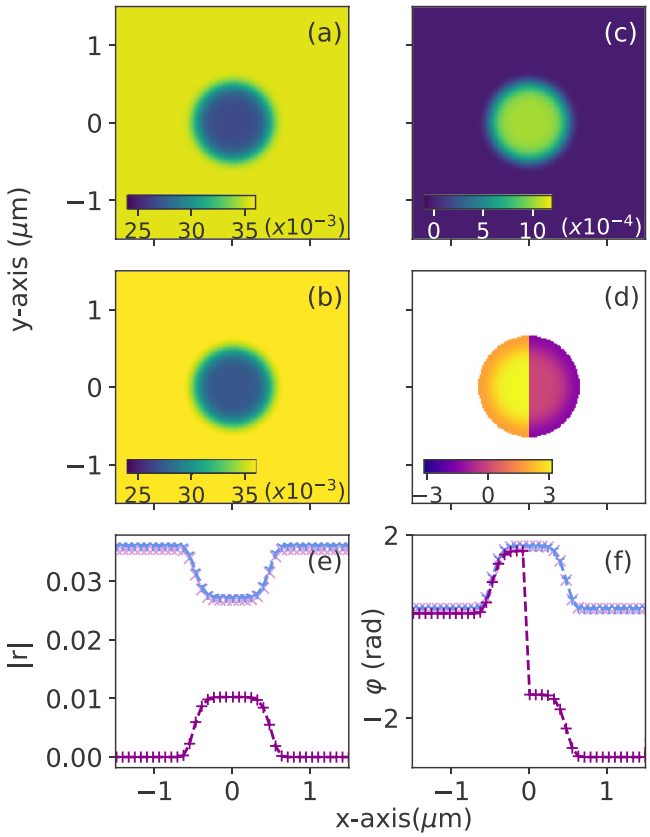

FIG. 6. . Reflectivity coefficients maps used for the computation. $\lambda = 23.5$ nm, angle of incidence $\theta = 5°$. From (a) to (d): $|r_{PP}|$, $|r_{SS}|$, $|r_{PP}\, r_0^t\, m_y|$, and $\arg(r_{PP}\, r_0^t\, m_y)$. For (d), all points with magnitudes of less than 1% of the value at center (maximum), have been set to NaN. (e) Modulus and (f) phase of the following coefficients along the line at $y = 0$. Plum cross: r_{PP}; blue dotted line: r_{SS}; purple plus: r_0^t.

profiles. The decomposition on the LG basis is obtained by computing the integral of the product of any polarization component of the field (S or P) with a given LG mode. If the result is below a given accuracy parameter (set here to 10^{-4}) compared to the dominant mode then it is forced to zero. The trivial radius of curvature of the field wave front in the far field, due to its divergence, is removed before decomposition.

2. Sample

In all numerical examples, we considered a SiN substrate (nonmagnetic material) on which the magnetic material, considered as Fe, was deposited. The optical reflectivity coefficients outside of the sample are thus those of SiN and not of a purely absorbing material, as used for sake of simplification in the analytical derivation in the main text. The corresponding reflectivity coefficients are displayed in Fig. 6. This computational detail has of course no importance when the beam focus is smaller than the magnetic dot.

In order to describe the magnetic dot used as a typical example, we write its height h as

$$h(r_\sigma) = h_0 e^{-\left(\frac{r_\sigma}{R_0}\right)^\beta}, \tag{A1}$$

where R_0 is the radius of the dot, h_0 is the height of the dot in the center and β is an integer. The hyper-Gaussian function takes into account the sharpness of the dot edge. In all numerical applications we set $\beta = 6$.

We develop a numerical example using the magneto-optical constants of Fe in the XUV range corresponding to the $3p \to 3d$ electron excitation. We computed the following values for their maxima at $\theta = 5°$ [67,68,76,83]: $r_{pp} = 0.027e^{-1.38j}$, $r_0^t = 0.038e^{-0.11j}$ and $r_{ps}^l = 0.00051e^{-1.49j}$. We note that the two coefficients $(r_{pp}\, r_0^t)$ and r_{ps}^l have similar amplitude, respectively 3.8% and 1.9% of r_{pp}. The values of the reflectivity coefficients are shown in Fig. 6 for the case of a magnetic dot of radius $R_0 = 500$ nm with two antiparallel magnetic domains as in the example of Fig. 2(a). A smooth transition from the dot to the substrate is ensured by multiplying the reflectivity coefficients by $h(r_\sigma)/h_0$ [Eq. (A1)] for the magnetic dot and by $(1 - h(r_\sigma))/h_0$ for the substrate. The reflectivity matrix thus reads

$$\begin{aligned}\mathbf{R}(r_\sigma, \phi_\sigma) = {} & e^{\frac{i4\pi}{\lambda} h(r_\sigma)} \frac{h(r_\sigma)}{h_0} \\ & \times \begin{pmatrix} r_{PP}\,[1 + r_0^t\, m_t(\phi_\sigma)] & r_{PS}^l\, m_l(\phi_\sigma) \\ -r_{PS}^l\, m_l(\phi_\sigma) & r_{SS} \end{pmatrix} \\ & + \left(1 - \frac{h(r_\sigma)}{h_0}\right) \begin{pmatrix} r_{PP}^\sigma & 0 \\ 0 & r_{SS}^\sigma \end{pmatrix}\end{aligned} \tag{A2}$$

where we have explicitly indicated the dependence of the matrix on the azimuthal location on the sample. The leading phase term of the first line describes the dephasing of the light wave depending on whether it hits the dot or the substrate. For $\lambda \approx h_0$, this phase term is simply $\approx 2 \times 2\pi$, where the factor 2 describes back and forth travel. This dephasing is far from being negligible: the thickness of a permalloy dot is typically $h_0 \approx 20$ nm, comparable to the wavelength of the $3p$ resonance of Fe ($\lambda = 23.5$ nm).

3. Centering of beam and magnetic dot

In Sec. III, we required the axis of the OAM beam to pass through the center of the magnetic dot for our theory, and we argued that this can be achieved with accurate control of the sample holder and beam steering mirrors. However it is interesting to study what happens when beam and target are not perfectly aligned. For this, we consider the two coordinate systems of light and target, (r, ϕ) and (r_σ, ϕ_σ) respectively, to have different origins: the target coordinate system is centered in the point indicated by (ϱ, Φ) in the beam frame. It can be shown by trigonometry that the term $e^{i(\ell\phi + n\phi_\sigma)}$ in Eq. (12b) is modified to $e^{i\ell\phi}[(re^{i(\phi_\sigma - \Phi)} - \varrho)/r_\sigma]^n$. It can be seen that it is quite difficult to carry out the study of the symmetries analytically, therefore we proceed numerically.

In Fig. 7(a), present as an example the study of an incident vortex beam on a magnetic vortex at $\theta = 48°$. Five different relative position of VB and MV are shown. The central one corresponds to a perfect alignment, while the other ones correspond to a shift along the diagonal direction. In panel (b), the corresponding reflected beam intensities in the far field are shown. As one could expect, for small shifts the image is only slightly modified, while it gets more deformed for larger shifts. Interestingly, within the limits of our model the two

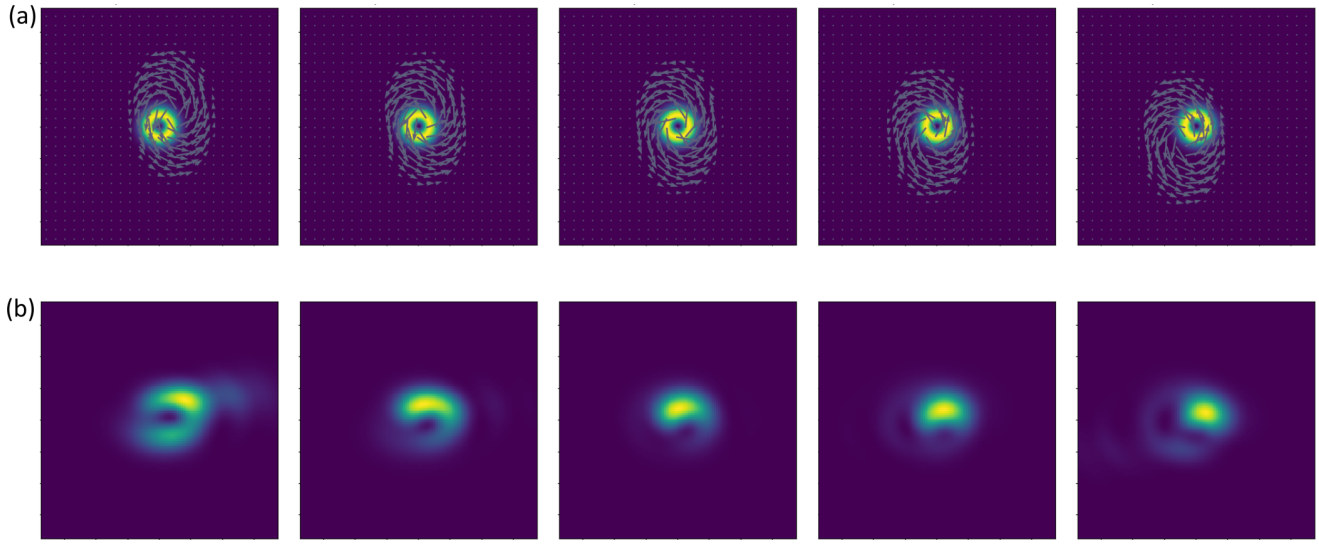

FIG. 7. (a) Numerical simulation of the relative position of an incident beam and a magnetic vortex (diameter of 10 μm and placed at $\theta = 48^\circ$ for this simulation on a square of 17.2 μm) and (b) the resulting reflected intensity in the far field (at 10 cm from the sample here, square of 15 cm).

opposite shifts with respect to the center do not give images that can be converted to one another by any symmetry. For sake of simplicity, here we do not explore further the effect of such shift, and further studies are required to determine if and how it affects the symmetry of the MHD signals. Certainly it should be taken into account in case of experimental studies, and eventually it might be possible to retrieve the actual shift from MHD measurements.

APPENDIX B: PARITY OF THE ANGULAR DECOMPOSITION

We show here how to obtain the symmetry properties of Table I. We express the coefficient $m_{*,n}$ by separating the azimuthal integral in Eq. (6) piecewise as

$$\begin{aligned} m_{*,n} &= \frac{1}{2\pi}\int_0^{\pi} m_*(\phi_\sigma)e^{in\phi_\sigma}d\phi_\sigma + \int_{\pi}^{2\pi} m_*(\phi_\sigma)e^{in\phi_\sigma}d\phi_\sigma \\ &= \frac{1}{2\pi}\int_0^{\pi} [m_*(\phi_\sigma)e^{in\phi_\sigma} + m_*(2\pi-\phi_\sigma)e^{-in\phi_\sigma}]d\phi_\sigma \\ &= \frac{1}{2\pi}\int_0^{\frac{\pi}{2}} [m_*(\phi_\sigma)e^{in\phi_\sigma} + m_*(2\pi-\phi_\sigma)e^{-in\phi_\sigma}]d\phi_\sigma + \int_{\frac{\pi}{2}}^{\pi} [m_*(\phi_\sigma)e^{in\phi_\sigma} + m_*(2\pi-\phi_\sigma)e^{-in\phi_\sigma}]d\phi_\sigma \\ &= \frac{1}{2\pi}\int_0^{\frac{\pi}{2}} [m_*(\phi_\sigma)e^{in\phi_\sigma} + m_*(2\pi-\phi_\sigma)e^{-in\phi_\sigma}] + (-1)^n[m_*(\pi-\phi_\sigma)e^{-in\phi_\sigma} + m_*(\pi+\phi_\sigma)e^{in\phi_\sigma}]d\phi_\sigma \end{aligned} \tag{B1}$$

where we have used the changes of variables $\phi_\sigma \to 2\pi - \phi_\sigma$ and $\phi_\sigma \to \pi - \phi_\sigma$ for the last integrals in lines 2 and 4, respectively. We envision 4 general cases, depending on the symmetry of the azimuthal dependence with respect to x_σ (i.e. $\phi_\sigma = \pi$) and y_σ (i.e. $\phi_\sigma = \pi/2$) being even or odd, as listed in Table I.

For instance, we consider m_* being (even, odd) w.r.t. (x_σ, y_σ), i.e. $m_*(2\pi - \phi_\sigma) = m_*(\phi_\sigma)$ and $m_*(\pi - \phi_\sigma) = -m_*(\phi_\sigma)$. For example, this is the case of m_t of both the antiparallel magnetic domains and the magnetic vortex of Fig. 2. We have

$$m_{*,n} = \frac{1}{2\pi}\int_0^{\frac{\pi}{2}} 2m_*(\phi_\sigma)\cos n\phi_\sigma[1-(-1)^n]d\phi_\sigma\,. \tag{B2}$$

From this integral, we see that all coefficients $m_{*,n}$ with even n will be zero. Instead, they may be nonzero for n odd. In addition, all $m_{*,n}$ are real quantities, and $m_{*,-n} = m_{*,n}$.

An equivalent analysis for the other three symmetry cases leads to all the results presented in Table I.

APPENDIX C: FOURIER DECOMPOSITION OF THE MAGNETIZATION OF EXAMPLES IN FIG. 2

We present the calculation of the Fourier decomposition coefficients for the magnetization in the case of antiparallel magnetic domains [Fig. 2(a)] and magnetic vortex [Fig. 2(b)].

1. Case of the antiparallel domains

$$
\begin{aligned}
m_{t,n} &= \frac{m_0}{2\pi}\int_{-\pi}^{+\pi} d\phi_\sigma \,\mathrm{sign}(\cos(\phi_\sigma))e^{-in\phi_\sigma} \\
&= \frac{m_0}{2\pi}\left(\int_{-\pi/2}^{\pi/2} d\phi_\sigma e^{-in\phi_\sigma} - \int_{\pi/2}^{-\pi/2} d\phi_\sigma e^{-in\phi_\sigma}\right) \\
&= \frac{m_0}{2\pi}\frac{1}{-in}[(-i)^n - i^n - (i^n - (-i)^n)] \\
&= \frac{m_0 i^{n-1}}{n\pi}[1-(-1)^n], \\
m_{t,n} &= \begin{cases} 0, & \text{for n even} \\ \frac{2m_0}{n\pi} i^{n-1}, & \text{for n odd} \end{cases}.
\end{aligned}
$$

2. Case of the vortex

For this case, we use the general result:

$$
\int_{-\pi}^{+\pi} d\phi_\sigma e^{i\kappa\phi_\sigma} = \begin{cases} 0, & \text{for } \kappa \neq 0 \\ 2\pi, & \text{for } \kappa = 0 \end{cases}. \tag{C1}
$$

We thus have for the longitudinal part:

$$
m_{l,n} = \frac{m_0}{4i\pi}\int_{-\pi}^{+\pi} d\phi_\sigma (e^{-i\phi_\sigma} - e^{i\phi_\sigma})e^{-in\phi_\sigma}, \tag{C2}
$$

$$
m_{l,n} = \begin{cases} 0, & \text{for n} \neq \pm 1 \\ \mp\frac{m_0}{2i}, & \text{for } n = \pm 1 \end{cases} \tag{C3}
$$

and for the transverse part,

$$
m_{t,n} = \frac{m_0}{4\pi}\int_{-\pi}^{+\pi} d\phi_\sigma (e^{i\phi_\sigma} + e^{-i\phi_\sigma})e^{-in\phi_\sigma}, \tag{C4}
$$

$$
m_{t,n} = \begin{cases} 0, & \text{for } n \neq \pm 1 \\ \frac{m_0 2}{,} & \text{for } n = \pm 1 \end{cases}. \tag{C5}
$$

APPENDIX D: TRIGONOMETRY

In the following, we present the calculations that allow to obtain Eq. (16). For the $\sin\phi_\sigma$ term,

$$
\begin{aligned}
\sin\phi_\sigma &= \frac{y_\sigma}{\sqrt{y_\sigma^2 + x_\sigma^2}} = \frac{y}{\sqrt{y^2 + \frac{x^2}{\cos^2\theta}}} \\
&= \frac{y}{\sqrt{x^2+y^2}}\frac{1}{\sqrt{\frac{x^2/\cos^2\theta + y^2}{x^2+y^2}}} \\
&= \sin\phi\,\frac{1}{\sqrt{\frac{\cos^2\phi}{\cos^2\theta} + \sin^2\phi}} \\
&= \sin\phi\,\frac{\cos\theta}{\sqrt{\cos^2\phi + \sin^2\phi\cos^2\theta}} \\
&= \sin\phi\,\frac{\cos\theta}{\sqrt{1-\sin^2\phi\sin^2\theta}}.
\end{aligned}
$$

The exact same computations can be carried out for the cosine, replacing the numerator of the first equation by x_σ. We thus get

$$\cos\phi_\sigma = \cos\phi\,\frac{1}{\sqrt{1-\cos^2\phi\sin^2\theta}}$$

and combining them

$$e^{i\phi_\sigma} = \cos\phi_\sigma + i\sin\phi_\sigma = g(\phi,\theta)\,(\cos\phi + i\sin\phi\cos\theta) = g(\phi,\theta)\left(\frac{1+\cos\theta}{2}e^{i\phi} + \frac{1-\cos\theta}{2}e^{-i\phi}\right).$$

For the r_σ term, we calculate

$$r_\sigma = \sqrt{y_\sigma^2 + x_\sigma^2} = \sqrt{y^2 + \frac{x^2}{\cos^2\theta}} = \sqrt{x^2+y^2}\sqrt{\frac{x^2/\cos^2\theta + y^2}{x^2+y^2}} = r\sqrt{\frac{\cos^2\phi}{\cos^2\theta} + \sin^2\phi} = \frac{r}{\cos\theta}\sqrt{1-\sin^2\phi\sin^2\theta}.$$

APPENDIX E: CONTRIBUTION OF $(I^{x,y}_{\ell,m})_1$ TO MHD

In this Appendix, we show that the contribution of the term $(I^{x,y}_{\ell,m})_1$ to MHD is negligible.

1. Case of MHD-ℓ

We calculate $(\Delta I_\ell)_1 = (I^{x,y}_{\ell,m})_1 - (I^{x,y}_{-\ell,m})_1$:

$$\begin{aligned}(\Delta I_l)_1 &\propto \left|\alpha^{x,y}_{0,m}\right|^2\left(H^2_{0,\ell} - H^2_{0,-\ell}\right) + \sum_{n>0}\left|\alpha^{x,y}_{n,m}\right|^2\left(H^2_{n,\ell} - H^2_{n,-\ell}\right) + \sum_{n<0}\left|\alpha^{x,y}_{n,m}\right|^2\left(H^2_{n,\ell} - H^2_{n,-\ell}\right)\\ &\propto \sum_{n>0}\left(\left|\alpha^{x,y}_{n,m}\right|^2 - \left|\alpha^{x,y}_{-n,m}\right|^2\right)\left(H^2_{n,\ell} - H^2_{n,-\ell}\right).\end{aligned}$$

Now, considering Eq. (14), for the y component we see that since $|\alpha^y_{n,m}|^2 = |\alpha^y_{-n,m}|^2$, we have $(\Delta I_\ell)_1 = 0$.

Instead, for the x component we have $\alpha^x_{n,m}$ defined as the sum of two terms. If one of them is zero, for instance the incoming light is P- or S-polarized ($\epsilon_S = 0$ or $\epsilon_P = 0$, respectively) or if the magnetic structure is such that $m_{t,n}$ or $m_{l,n}$ are zero, then also in this case we have simply $|\alpha^x_{n,m}|^2 = |\alpha^x_{-n,m}|^2$, and thus $(\Delta I_\ell)_1 = 0$.

If the experimental conditions are such that both components of $\alpha^x_{n,m}$ are not zero, then $(\Delta I_\ell)_1$ is not necessarily zero. A somewhat lengthy calculation leads to

$$\left(\left|\alpha^x_{n,m}\right|^2 - \left|\alpha^x_{-n,m}\right|^2\right) = -4\left|r^t_0\right|^2|\epsilon_P\epsilon_S r_{PP} r^l_{PS}|\mathrm{Im}\{m_{t,n}\overline{m_{l,n}}\}\sin\left(\varphi_P - \varphi_S + \varphi_{PP} - \varphi^l_{PS}\right),$$

namely, a term proportional to the square of the magnetization and of the MOKE constant r^t_0. This can be an important contribution compared to $(\Delta I_\ell)_2$ in the most general case, and we note that it could be a way to experimentally access the quantity $\varphi_{PP} - \varphi^l_{PS}$ under properly chosen conditions. However, as we will see later (Sec. IV C), for highly symmetric structures and under the reasonable assumption $|m_{*,n}||r^t_0| \ll 1$, $(\Delta I_\ell)_2$ is found to be linear with magnetization and r^t_0, thus $(\Delta I_\ell)_1$ can still be considered negligible. In any case, as pointed out above this issue can be simply avoided by choosing a proper experimental setup.

2. Case of MHD-m

We calculate $(\Delta I_m)_1 = (I^{x,y}_{\ell,m})_1 - (I^{x,y}_{\ell,-m})_1$:

$$(\Delta I_m)_1 \propto \sum_n\left(\left|\alpha^{x,y}_{n,m}\right|^2 - \left|\alpha^{x,y}_{n,-m}\right|^2\right)H^2_{n,\ell}\,. \tag{E1}$$

Since $|\alpha^{x,y}_{n,m}|^2 = |\alpha^{x,y}_{n,-m}|^2$, in this case simply $(\Delta I_m)_1$ is always zero.

3. Case of MHD-ℓm

A similar analysis to that for MHD-ℓ leads to the same conclusion of $(\Delta I_{\ell,m})_1$ giving a negligible contribution to MHD-ℓm.

APPENDIX F: DERIVATION OF GENERAL MHD FORMULAS

In the following, we present the detailed derivation of the general MHD expressions, where we evaluate the three differences of Eq. (24) using the expression of $(I^{x,y}_{\ell,m})_2$ from Eq. (22). In order to simplify the notation we drop the (kr, z) explicit dependence of the $H_{n,l}$ and the m subscript for all $\alpha^{x,y}_n$ terms. We will use the property $H_{-n,-\ell} = (-1)^{n+\ell}H_{n,\ell}$ [Eq. (21)], and the general property of series $\sum_{n-n'>0} s_{n,n'} = \sum_{n'-n>0} s_{n',n} = \sum_{n-n'>0} s_{-n',-n}$.

1. Expression of MHD-ℓ [Eq. (25)]

$$
\begin{aligned}
\Delta I_{\ell}^{x,y}(r,\phi,z) &= \left|D_{\rho}^{|\ell|}\right|^2 \sum_{n\neq n'} \left(\alpha_n^{x,y}\overline{\alpha_{n'}^{x,y}} e^{i(n-n')(\phi-\pi/2)}\right)[H_{n,\ell}H_{n',\ell} - H_{n,-\ell}H_{n',-\ell}] \\
&= 2\left|D_{\rho}^{|\ell|}\right|^2 \sum_{\substack{n\neq n' \\ n-n'>0}} \left|\alpha_n^{x,y}\right|\left|\alpha_{n'}^{x,y}\right| \cos\left[(n-n')(\phi-\pi/2)+\delta\varphi_{n,n'}^{x,y}\right][H_{n,\ell}H_{n',\ell} - H_{n,-\ell}H_{n',-\ell}] \\
&= 2\left|D_{\rho}^{|\ell|}\right|^2 \sum_{\substack{n\neq n' \\ n-n'>0}} \left|\alpha_n^{x,y}\right|\left|\alpha_{n'}^{x,y}\right| \cos\left[(n-n')(\phi-\pi/2)+\delta\varphi_{n,n'}^{x,y}\right][H_{n,\ell}H_{n',\ell} - (-1)^{n+n'}H_{-n,\ell}H_{-n',\ell}] \\
&= 2\left|D_{\rho}^{|\ell|}\right|^2 \sum_{\substack{n\neq n' \\ n-n'>0}} \left|\alpha_n^{x,y}\right|\left|\alpha_{n'}^{x,y}\right| \cos\left[(n-n')(\phi-\pi/2)+\delta\varphi_{n,n'}^{x,y}\right]H_{n,\ell}H_{n',\ell} \\
&\quad - 2\left|D_{\rho}^{|\ell|}\right|^2 \sum_{\substack{n\neq n' \\ n-n'>0}} (-1)^{n+n'}\left|\alpha_n^{x,y}\right|\left|\alpha_{n'}^{x,y}\right| \cos\left[(n-n')(\phi-\pi/2)+\delta\varphi_{n,n'}^{x,y}\right]H_{-n,\ell}H_{-n',\ell} \\
&= 2\left|D_{\rho}^{|\ell|}\right|^2 \sum_{\substack{n\neq n' \\ n-n'>0}} \left|\alpha_n^{x,y}\right|\left|\alpha_{n'}^{x,y}\right| \cos\left[(n-n')(\phi-\pi/2)+\delta\varphi_{n,n'}^{x,y}\right]H_{n,\ell}H_{n',\ell} \\
&\quad - 2\left|D_{\rho}^{|\ell|}\right|^2 \sum_{\substack{n\neq n' \\ -n+n'>0}} (-1)^{n+n'}\left|\alpha_{-n}^{x,y}\right|\left|\alpha_{-n'}^{x,y}\right| \cos\left[-(n-n')(\phi-\pi/2)+\delta\varphi_{-n,-n'}^{x,y}\right]H_{n,\ell}H_{n',\ell} \\
&= 2\left|D_{\rho}^{|\ell|}\right|^2 \sum_{\substack{n\neq n' \\ n-n'>0}} \left|\alpha_n^{x,y}\right|\left|\alpha_{n'}^{x,y}\right| \cos\left[(n-n')(\phi-\pi/2)+\delta\varphi_{n,n'}^{x,y}\right]H_{n,\ell}H_{n',\ell} \\
&\quad - 2\left|D_{\rho}^{|\ell|}\right|^2 \sum_{\substack{n\neq n' \\ n-n'>0}} (-1)^{n+n'}\left|\alpha_{-n'}^{x,y}\right|\left|\alpha_{-n}^{x,y}\right| \cos\left[-(n'-n)(\phi-\pi/2)+\delta\varphi_{-n',-n}^{x,y}\right]H_{n',\ell}H_{n,\ell},\ \Delta I_{\ell}^{x,y}(r,\phi,z) \\
&= 2\left|D_{\rho}^{|\ell|}\right|^2 \sum_{\substack{n\neq n' \\ n-n'>0}} H_{n,\ell}H_{n',\ell}\left[\left|\alpha_n^{x,y}\right|\left|\alpha_{n'}^{x,y}\right| \cos\left((n-n')(\phi-\pi/2)+\delta\varphi_{n,n'}^{x,y}\right)\right. \\
&\quad \left. - (-1)^{n+n'}\left|\alpha_{-n}^{x,y}\right|\left|\alpha_{-n'}^{x,y}\right| \cos\left((n-n')(\phi-\pi/2)-\delta\varphi_{-n,-n'}^{x,y}\right)\right].
\end{aligned}
\tag{F1}
$$

2. Expression of MHD-*m* [Eq. (26)]

$$
\begin{aligned}
\Delta I_{m}^{x,y}(r,\phi,z) &= \left|D_{\rho}^{|\ell|}\right|^2 \sum_{n\neq n'} \left(\alpha_n^{x,y}\overline{\alpha_{n'}^{x,y}} e^{i(n-n')(\phi-\pi/2)}\right)[H_{n,\ell}H_{n',\ell} + \chi_{n,n'}H_{n,\ell}H_{n',\ell}] \\
&= 2\left|D_{\rho}^{|\ell|}\right|^2 \sum_{\substack{n\neq n' \\ n-n'>0}} \left|\alpha_n^{x,y}\right|\left|\alpha_{n'}^{x,y}\right| \cos\left[(n-n')(\phi-\pi/2)+\delta\varphi_{n,n'}^{x,y}\right][H_{n,\ell}H_{n',\ell} + \chi_{n,n'}H_{n,\ell}H_{n',\ell}] \\
&= 4\left|D_{\rho}^{|\ell|}\right|^2 \sum_{\substack{n=0 \text{ or } n'=0 \\ n-n'>0}} \left|\alpha_n^{x,y}\right|\left|\alpha_{n'}^{x,y}\right| \cos\left[(n-n')(\phi-\pi/2)+\delta\varphi_{n,n'}^{x,y}\right]H_{n,\ell}H_{n',\ell} \\
&= 4\left|D_{\rho}^{|\ell|}\right|^2 \sum_{-n'>0} \left|\alpha_0^{x,y}\right|\left|\alpha_{n'}^{x,y}\right| \cos\left[-n'(\phi-\pi/2)+\delta\varphi_{0,n'}^{x,y}\right]H_{0,\ell}H_{n',\ell} \\
&\quad + 4\left|D_{\rho}^{|\ell|}\right|^2 \sum_{n>0} \left|\alpha_n^{x,y}\right|\left|\alpha_0^{x,y}\right| \cos\left[n(\phi-\pi/2)+\delta\varphi_{n,0}^{x,y}\right]H_{n,\ell}H_{0,\ell}
\end{aligned}
$$

$$
\begin{aligned}
&= 4\left|D_\rho^{|\ell|}\right|^2 \sum_{n<0} \left|\alpha_0^{x,y}\right|\left|\alpha_n^{x,y}\right| \cos\left[-n(\phi-\pi/2)-\delta\varphi_{n,0}^{x,y}\right] H_{0,\ell}H_{n,\ell} \\
&\quad + 4\left|D_\rho^{|\ell|}\right|^2 \sum_{n>0} \left|\alpha_n^{x,y}\right|\left|\alpha_0^{x,y}\right| \cos\left[n(\phi-\pi/2)+\delta\varphi_{n,0}^{x,y}\right] H_{n,\ell}H_{0,\ell} \\
&= 4\left|D_\rho^{|\ell|}\right|^2 \sum_{n\neq 0} \left|\alpha_0^{x,y}\right|\left|\alpha_n^{x,y}\right| \cos\left[n(\phi-\pi/2)+\delta\varphi_{n,0}^{x,y}\right] H_{0,\ell}H_{n,\ell}, \\
\Delta I_m^{x,y}(r,\phi,z) &= 4\left|D_\rho^{|\ell|}\right|^2 \left|\alpha_0^{x,y}\right| H_{0,\ell} \sum_{n\neq 0} \left|\alpha_n^{x,y}\right| \cos\left[n(\phi-\pi/2)+\delta\varphi_{n,0}^{x,y}\right] H_{n,\ell}.
\end{aligned} \tag{F2}
$$

3. Expression of MHD-ℓm [Eq. (27)]

The derivation of the expression of $\Delta I_{\ell,m}^{x,y}(r,\phi,z)$ follows the same steps as that of $\Delta I_\ell^{x,y}(r,\phi,z)$ [Eq. (25)].

APPENDIX G: DERIVATION OF MHD FORMULAS FOR THE EXAMPLE OF SEC. IV C

In the following, we drop the explicit dependence of the H functions on the spatial coordinates and the m subscript for all $\alpha_n^{x,y}$ terms. Also, it is useful to express differences and sums of the $\delta\varphi^x$ phase terms as

$$
\frac{\delta\varphi_{n,n'}^x - \delta\varphi_{-n,-n'}^x}{2} = \begin{cases} \varphi_{t,n} - \varphi_{t,n'} = 0 \text{ or } \pi & \text{if } n, n' \neq 0, \\ -\varphi_{t,n'} & \text{if } n = 0, \\ \varphi_{t,n} & \text{if } n' = 0. \end{cases} \tag{G1a}
$$

$$
\frac{\delta\varphi_{n,n'}^x + \delta\varphi_{-n,-n'}^x}{2} = \begin{cases} 0 & \text{if } n, n' \neq 0, \\ -\varphi_0^t & \text{if } n = 0, \\ \varphi_0^t & \text{if } n' = 0. \end{cases} \tag{G1b}
$$

1. Expression of MHD-ℓ [Eqs. (31) and (32)]

Taking into account that $|\alpha_{n,m}^{x,y}| = |\alpha_{-n,m}^{x,y}|$ and using prosthaphaeresis identity, the MHD-ℓ from Eq. (25) reads

$$
\begin{aligned}
&\Delta I_\ell^{x,y}(r,\phi,z) - 4\left|D_\rho^{|\ell|}\right|^2 \sum_{\substack{n\neq n' \\ n-n'>0 \\ n+n' \text{ even}}} (-1)^{\frac{n-n'}{2}} H_{n,\ell}H_{n',\ell}\left|\alpha_n^{x,y}\right|\left|\alpha_{n'}^{x,y}\right| \sin\left((n-n')\phi + \frac{\delta\varphi_{n,n'}^{x,y} - \delta\varphi_{-n,-n'}^{x,y}}{2}\right) \sin\left(\frac{\delta\varphi_{n,n'}^{x,y} + \delta\varphi_{-n,-n'}^{x,y}}{2}\right) \\
&+ 4\left|D_\rho^{|\ell|}\right|^2 \sum_{\substack{n\neq n' \\ n-n'>0 \\ n+n' \text{ odd}}} (-1)^{\frac{n-n'+1}{2}} H_{n,\ell}H_{n',\ell}\left|\alpha_n^{x,y}\right|\left|\alpha_{n'}^{x,y}\right| \sin\left((n-n')\phi + \frac{\delta\varphi_{n,n'}^{x,y} - \delta\varphi_{-n,-n'}^{x,y}}{2}\right) \cos\left(\frac{\delta\varphi_{n,n'}^{x,y} + \delta\varphi_{-n,-n'}^{x,y}}{2}\right).
\end{aligned} \tag{G2}
$$

However, for the y term, we notice that the first line in the expression of $\Delta I_\ell^y(r,\phi,z)$ is zero due to the final sine when $n, n' \neq 0$ and to $\alpha_{0,m}^y = 0$ when $n = 0$ or $n' = 0$. For the second line, if both $n \neq 0$ and $n' \neq 0$, in both cases of symmetries yielding either only odd or only even terms, the sum $n + n'$ is even and is not in the sum. If $n = 0$ or $n' = 0$, $\alpha_{0,m}^y = 0$ and the contribution is null. Therefore, in the framework of our approximations we identically have $\Delta I_\ell^y(r,\phi,z) = 0$.

Instead, the x term $\Delta I_\ell^x(r,\phi,z)$ can be further simplified considering that only either odd or even terms are present because of the symmetries invoked in this example.

a. Even terms

For even terms, only the first line of Eq. (G2) is present since $n + n'$ is necessarily even. If both $n \neq 0$ and $n' \neq 0$, however, the sum is zero because of the last sine term. We are thus left with the sum over either n or $n' = 0$. Since the sum runs over $n - n' > 0$, it amounts to summing, for all even integers, the same expression. We thus split the sum in two subsums:

$$
\begin{aligned}
\Delta I_\ell^x(r,\phi,z) = &-4\left|D_\rho^{|\ell|}\right|^2 \sum_{\substack{n\neq 0 \\ n>0 \\ n \text{ even}}} (-1)^{\frac{n}{2}} H_{n,\ell}H_{0,\ell}\left|\alpha_n^x\right|\left|\alpha_0^x\right| \sin\left(n\phi + \frac{\delta\varphi_{n,0}^x - \delta\varphi_{-n,0}^x}{2}\right) \sin\left(\frac{\delta\varphi_{n,0}^x + \delta\varphi_{-n,0}^x}{2}\right) - 4\left|D_\rho^{|\ell|}\right|^2 \sum_{\substack{0\neq n' \\ -n'>0 \\ n' \text{ even}}} (-1)^{\frac{-n'}{2}} \\
&\times H_{0,\ell}H_{n',\ell}\left|\alpha_0^x\right|\left|\alpha_{n'}^x\right| \sin\left(-n'\phi + \frac{\delta\varphi_{0,n'}^x - \delta\varphi_{0,-n'}^x}{2}\right) \sin\left(\frac{\delta\varphi_{0,n'}^x + \delta\varphi_{0,-n'}^x}{2}\right)
\end{aligned}
$$

$$
\begin{aligned}
&= -4\left|D_\rho^{|\ell|}\right|^2 \sum_{\substack{n\neq 0\\ n>0\\ n\ \text{even}}} (-1)^{\frac{n}{2}} H_{n,\ell} H_{0,\ell} \left|\alpha_n^x\right|\left|\alpha_0^x\right| \sin\left(n\phi+\varphi_{t,n}\right)\sin\left(\varphi_0^t\right) - 4\left|D_\rho^{|\ell|}\right|^2 \sum_{\substack{n\neq 0\\ n<0\\ n\ \text{even}}} (-1)^{\frac{n}{2}} \\
&\quad \times H_{n,\ell} H_{0,\ell} \left|\alpha_n^x\right|\left|\alpha_0^x\right| \sin\left(-n\phi-\varphi_{t,n}\right)\sin\left(-\varphi_0^t\right) \\
&= -4\left|D_\rho^{|\ell|}\right|^2 \sum_{\substack{n\neq 0\\ n\ \text{even}}} (-1)^{\frac{n}{2}} H_{n,\ell} H_{0,\ell} \left|\alpha_n^x\right|\left|\alpha_0^x\right| \sin\left(n\phi+\varphi_{t,n}\right)\sin\left(\varphi_0^t\right)
\end{aligned} \tag{G3}
$$

finding the result of Eq. (31).

b. Odd terms

For odd terms, the first line of Eq. (G2) is present only if both $n \neq 0$ and $n' \neq 0$, however the sum is zero because of the last sine term, and thus only the second line needs to be considered. This also reduces to a sum over either $n = 0$ or $n' = 0$, since it is the only way to have $n + n'$ odd:

$$
\begin{aligned}
\Delta I_\ell^x(r,\phi,z) &= 4\left|D_\rho^{|\ell|}\right|^2 \sum_{\substack{n\neq 0\\ n>0\\ n\ \text{odd}}} (-1)^{\frac{n+1}{2}} H_{n,\ell} H_{0,\ell} \left|\alpha_n^x\right|\left|\alpha_0^x\right| \sin\left(n\phi+\frac{\delta\varphi_{n,0}^x-\delta\varphi_{-n,0}^x}{2}\right)\cos\left(\frac{\delta\varphi_{n,0}^x+\delta\varphi_{-n,0}^x}{2}\right) \\
&\quad + 4\left|D_\rho^{|\ell|}\right|^2 \sum_{\substack{0\neq n'\\ -n'>0\\ n'\ \text{odd}}} (-1)^{\frac{-n'+1}{2}} H_{0,\ell} H_{n',\ell} \left|\alpha_0^x\right|\left|\alpha_{n'}^x\right| \sin\left(-n'\phi+\frac{\delta\varphi_{0,n'}^x-\delta\varphi_{0,-n'}^x}{2}\right)\cos\left(\frac{\delta\varphi_{0,n'}^x+\delta\varphi_{0,-n'}^x}{2}\right) \\
&= 4\left|D_\rho^{|\ell|}\right|^2 \sum_{\substack{n\neq 0\\ n>0\\ n\ \text{odd}}} (-1)^{\frac{n+1}{2}} H_{n,\ell} H_{0,\ell} \left|\alpha_n^x\right|\left|\alpha_0^x\right| \sin\left(n\phi+\varphi_{t,n}\right)\cos\left(\varphi_0^t\right) \\
&\quad + 4\left|D_\rho^{|\ell|}\right|^2 \sum_{\substack{0\neq n'\\ n<0\\ n\ \text{odd}}} (-1)^{\frac{-n+1}{2}} H_{0,\ell} H_{n,\ell} \left|\alpha_0^x\right|\left|\alpha_n^x\right| \sin\left(-n\phi-\varphi_{t,n}\right)\cos\left(-\varphi_0^t\right) \\
&= 4\left|D_\rho^{|\ell|}\right|^2 \sum_{\substack{n\neq 0\\ n\ \text{odd}}} (-1)^{\frac{n+1}{2}} H_{n,\ell} H_{0,\ell} \left|\alpha_n^x\right|\left|\alpha_0^x\right| \sin\left(n\phi+\varphi_{t,n}\right)\cos\left(\varphi_0^t\right),
\end{aligned} \tag{G4}
$$

where we have taken into account for the last step that $(-1)^{\frac{-n+1}{2}} = (-1)^{\frac{n-1}{2}} = -(-1)^{\frac{n+1}{2}}$, and we find the result of Eq. (32).

2. Expression of MHD-*m* [Eq. (33)]

The expression of Eq. (33) is simply obtained by using the definition of $\delta\varphi_{n,0}^x$ from Eq. (29) into Eq. (26).

3. Expression of MHD-ℓm [Eqs. (34) and (35)]

Similarly to the case of MHD-ℓ, we can calculate the full expression of MHD-ℓm. Following a similar derivation as for Eq. (G2), the expression of $\Delta I_{\ell,m}^{x,y}(r,\phi,z)$ is

$$
\begin{aligned}
&\Delta I_{\ell,m}^{x,y}(r,\phi,z) \\
&= 4\left|D_\rho^{|\ell|}\right|^2 \sum_{\substack{n\neq n'\\ n-n'>0\\ n+n'\ \text{even}\\ n=0\,\text{or}\,n'=0}} (-1)^{\frac{n-n'}{2}} H_{n,\ell} H_{n',\ell} \left|\alpha_n^{x,y}\right|\left|\alpha_{n'}^{x,y}\right| \cos\left((n-n')\phi+\frac{\delta\varphi_{n,n'}^{x,y}-\delta\varphi_{-n,-n'}^{x,y}}{2}\right)\cos\left(\frac{\delta\varphi_{n,n'}^{x,y}+\delta\varphi_{-n,-n'}^{x,y}}{2}\right) \\
&\quad - 4\left|D_\rho^{|\ell|}\right|^2 \sum_{\substack{n\neq n'\\ n-n'>0\\ n+n'\ \text{odd}\\ n=0\,\text{or}\,n'=0}} (-1)^{\frac{n-n'+1}{2}} H_{n,\ell} H_{n',\ell} \left|\alpha_n^{x,y}\right|\left|\alpha_{n'}^{x,y}\right| \cos\left((n-n')\phi+\frac{\delta\varphi_{n,n'}^{x,y}-\delta\varphi_{-n,-n'}^{x,y}}{2}\right)\sin\left(\frac{\delta\varphi_{n,n'}^{x,y}+\delta\varphi_{-n,-n'}^{x,y}}{2}\right).
\end{aligned} \tag{G5}
$$

At this point, similarly to the case of MHD-ℓ, we can separate the calculations into the case of even or odd n terms.

a. Even terms

$$\Delta I^x_{\ell,m}(r,\phi,z) = -4\left|D^{|\ell|}_{\rho}\right|^2 \sum_{\substack{n\neq 0\\ n>0\\ n\ \text{even}}} (-1)^{\frac{n}{2}} H^{(n,\ell)} H_{0,\ell} \left|\alpha^x_n\right|\left|\alpha^x_0\right| \cos\left(n\phi + \frac{\delta\varphi^x_{n,0} - \delta\varphi^x_{-n,0}}{2}\right) \cos\left(\frac{\delta\varphi^x_{n,0} + \delta\varphi^x_{-n,0}}{2}\right)$$

$$- 4\left|D^{|\ell|}_{\rho}\right|^2 \sum_{\substack{0\neq n'\\ -n'>0\\ n'\ \text{even}}} (-1)^{\frac{-n'}{2}} H_{0,\ell} H_{n',\ell} \left|\alpha^x_0\right|\left|\alpha^x_{n'}\right| \cos\left(-n'\phi + \frac{\delta\varphi^x_{0,n'} - \delta\varphi^x_{0,-n'}}{2}\right) \cos\left(\frac{\delta\varphi^x_{0,n'} + \delta\varphi^x_{0,-n'}}{2}\right)$$

$$= -4\left|D^{|\ell|}_{\rho}\right|^2 \sum_{\substack{n\neq 0\\ n>0\\ n\ \text{even}}} (-1)^{\frac{n}{2}} H_{n,\ell} H_{0,\ell} \left|\alpha^x_n\right|\left|\alpha^x_0\right| \cos\left(n\phi + \varphi_{t,n}\right) \cos\left(\varphi^t_0\right)$$

$$- 4\left|D^{|\ell|}_{\rho}\right|^2 \sum_{\substack{n\neq 0\\ n<0\\ n\ \text{even}}} (-1)^{\frac{n}{2}} H_{n,\ell} H_{0,\ell} |\alpha^x_n||\alpha^x_0| \cos\left(-n\phi - \varphi_{t,n}\right) \cos\left(-\varphi^t_0\right)$$

$$= -4\left|D^{|\ell|}_{\rho}\right|^2 \sum_{\substack{n\neq 0\\ n\ \text{even}}} (-1)^{\frac{n}{2}} H_{n,\ell} H_{0,\ell} \left|\alpha^x_n\right|\left|\alpha^x_0\right| \cos\left(n\phi + \varphi_{t,n}\right) \cos\left(\varphi^t_0\right) \tag{G6}$$

finding the result of Eq. (34).

b. Odd terms

$$\Delta I^x_{\ell,m}(r,\phi,z) = 4\left|D^{|\ell|}_{\rho}\right|^2 \sum_{\substack{n\neq 0\\ n>0\\ n\ \text{odd}}} (-1)^{\frac{n+1}{2}} H_{n,\ell} H_{0,\ell} \left|\alpha^x_n\right|\left|\alpha^x_0\right| \cos\left(n\phi + \frac{\delta\varphi^x_{n,0} - \delta\varphi^x_{-n,0}}{2}\right) \sin\left(\frac{\delta\varphi^x_{n,0} + \delta\varphi^x_{-n,0}}{2}\right)$$

$$+ 4\left|D^{|\ell|}_{\rho}\right|^2 \sum_{\substack{0\neq n'\\ -n'>0\\ n'\ \text{odd}}} (-1)^{\frac{-n'+1}{2}} H_{0,\ell} H_{n',\ell} \left|\alpha^x_0\right|\left|\alpha^x_{n'}\right| \cos\left(-n'\phi + \frac{\delta\varphi^x_{0,n'} - \delta\varphi^x_{0,-n'}}{2}\right) \sin\left(\frac{\delta\varphi^x_{0,n'} + \delta\varphi^x_{0,-n'}}{2}\right)$$

$$= 4\left|D^{|\ell|}_{\rho}\right|^2 \sum_{\substack{n\neq 0\\ n>0\\ n\ \text{odd}}} (-1)^{\frac{n+1}{2}} H_{n,\ell} H_{0,\ell} \left|\alpha^x_n\right|\left|\alpha^x_0\right| \cos\left(n\phi + \varphi_{t,n}\right) \sin\left(\varphi^t_0\right)$$

$$+ 4\left|D^{|\ell|}_{\rho}\right|^2 \sum_{\substack{0\neq n\\ n<0\\ n\ \text{odd}}} (-1)^{\frac{-n+1}{2}} H_{0,\ell} H_{n,\ell} \left|\alpha^x_0\right|\left|\alpha^x_n\right| \cos\left(-n\phi - \varphi_{t,n}\right) \sin\left(-\varphi^t_0\right)$$

$$= 4\left|D^{|\ell|}_{\rho}\right|^2 \sum_{\substack{n\neq 0\\ n\ \text{odd}}} (-1)^{\frac{n+1}{2}} H_{n,\ell} H_{0,\ell} \left|\alpha^x_n\right|\left|\alpha^x_0\right| \cos\left(n\phi + \varphi_{t,n}\right) \sin\left(\varphi^t_0\right) \tag{G7}$$

finding the result of Eq. (35).

[1] M. Padgett and R. Bowman, Tweezers with a twist, Nat. Phot. **5**, 343 (2011).

[2] D. L. Andrews, *Structured Light and its Applications: An introduction to Phase-Structured Beams and Nanoscale Optical Forces* (Academic Press, Burlington MA, 2008), Vol. XIII.

[3] A. M. Yao and M. J. Padgett, Orbital angular momentum: Origins, behavior and applications, Adv. Opt. Photon. **3**, 161 (2011).

[4] L. D. Barron, *Molecular Light Scattering and Optical Activity* (Cambridge University Press, New York, 2009).

[5] P. Curie, Sur la symétrie dans les phénomènes physiques, symétrie d'un champ électrique et d'un champ magnétique, J. Phys. Theor. Appl. **3**, 393 (1894).

[6] W. Brullot, M. K. Vanbel, T. Swusten, and T. Verbiest, Resolving enantiomers using the optical angular momentum of twisted light, Sci. Adv. **2**, e1501349 (2016).

[7] S. Mei, K. Huang, H. Liu, F. Qin, M. Q. Mehmood, Zhengji Xu, M. Hong, D. Zhang, J. Teng, A. Danner, and C.-W. Qiu, On-chip discrimination of orbital angular momentum of light with plasmonic nanoslits, Nanoscale **8**, 2227 (2016).

[8] F. Arago, Sur une modification remarquable qu'éprouvent les rayons lumineux dans leur passage à travers certains corps diaphanes et sur quelques autres nouveaux phénomènes d'optique, *Mémoires de la classe des Sciences Mathématiques et Physiques de l'Institut Imprial de France* (F. Didot, Paris, 1812), Part 1, 93.

[9] J.-B. Biot, Phénomènes de polarization successive, observés dans les fluides homogènes, Bulletin de la Société Philomatique de Paris **4**, 190 (1815).

[10] L. Pasteur, *La dissymétrie moléculaire*, 1884, https://archive.org/details/91Pasteur/page/n17/mode/2up.

[11] L. Kelvin, *Baltimore Lectures on Molecular Dynamics and the Wave Theory of Light* (Cambridge University Press Warehouse, Cambridge, U. K., 1904), p. 643.

[12] A. Cotton, Recherches sur l'absorption et la dispersion de la lumière par les milieux doués du pouvoir rotatoire, J. Phys. Theor. Appl. **5**, 237 (1896).

[13] M. Faraday, On the magnetization of light, and the illumination of magnetic lines of force, Philos. Trans. R. Soc. Lond. **1**, 104 (1846).

[14] P. J. Stephens, Magnetic circular dichroism, Annu. Rev. Phys. Chem. **25**, 201 (1974).

[15] H. Ebert, Magneto-optical effects in transition metal systems, Rep. Prog. Phys. **59**, 1665 (1996).

[16] M. Sacchi and J. Vogel, *Dichroism in X-ray Absorption*, (Springer, Berlin, Heidelberg, 2001), pp. 87–108.

[17] T. Funk, A. Deb, S. J. George, H. Wang, and S. P. Cramer, X-ray magnetic circular dichroism - A high energy probe of magnetic properties, Coord. Chem. Rev. **249**, 3 (2005).

[18] G. van der Laan and A. I. Figueroa, X-ray magnetic circular dichroism - A versatile tool to study magnetism, Coord. Chem. Rev. **277-278**, 95 (2014).

[19] B. Ritchie, Theory of the angular distribution of photoelectrons ejected from optically active molecules and molecular negative ions, Phys. Rev. A **13**, 1411 (1976).

[20] I. Powis, Photoelectron circular dichroism: Chiral asymmetry in the angular distribution of electrons emitted by (+)-S-carvone, Chirality **20**, 961 (2008).

[21] G. Schönhense, C. Westphal, J. Bansmann, M. Getzlaff, J. Noffke, and L. Fritsche, Circular dichroism in photoemission from surfaces, Surface Science **251-252**, 132 (1991).

[22] Reference [33] calls it "OAM-induced dichroism," while Ref. [6] uses 'helical dichroism."

[23] Y. Shen, X. Wang, Z. Xie, C. Min, Xing Fu, Q. Liu, M. Gong, and X. Yuan, Optical vortices 30 years on: OAM manipulation from topological charge to multiple singularities, Light: Science & Applications **8**, 90 (2019).

[24] M. P. J. Lavery, J. Courtial, and M. J. Padgett, Measurement of light's orbital angular momentum, in *The Angular Momentum of Light*, edited by D. L. Andrews and M. Babiker (Cambridge University Press, New York, 2012), Chap. 13, pp. 330–350.

[25] G. Kulkarni, R. Sahu, O. S. Magaña-Loaiza, R. W. Boyd, and A. K. Jha, Single-shot measurement of the orbital-angular-momentum spectrum of light, Nat. Commun. **8**, 1054 (2017).

[26] G. C. G. Berkhout, M. P. J. Lavery, J. Courtial, M. W. Beijersbergen, and M. J. Padgett, Efficient Sorting of Orbital Angular Momentum States of Light, Phys. Rev. Lett. **105**, 153601 (2010).

[27] M. Babiker, D. L. Andrews, and V. E. Lembessis, Atoms in complex twisted light, J. Opt. **21**, 013001 (2018).

[28] M. Babiker, C. R. Bennett, D. L. Andrews, and L. C. Dávila Romero, Orbital Angular Momentum Exchange in the Interaction of Twisted Light with Molecules, Phys. Rev. Lett. **89**, 143601 (2002).

[29] F. Giammanco, A. Perona, P. Marsili, F. Conti, F. Fidecaro, S. Gozzini, and A. Lucchesini, Influence of the photon orbital angular momentum on electric dipole transitions: Negative experimental evidence, Opt. Lett. **42**, 219 (2017).

[30] C. T. Schmiegelow, J. Schulz, H. Kaufmann, T. Ruster, U. G. Poschinger, and F. Schmidt-Kaler, Transfer of optical orbital angular momentum to a bound electron, Nat. Commun. **7**, 12998 (2016).

[31] M. Solyanik-Gorgone, A. Afanasev, C. E. Carlson, C. T. Schmiegelow, and F. Schmidt-Kaler, Excitation of E1-forbidden atomic transitions with electric, magnetic, or mixed multipolarity in light fields carrying orbital and spin angular momentum, J. Opt. Soc. Am. B **36**, 565 (2019).

[32] K. A. Forbes and D. L. Andrews, Optical orbital angular momentum: Twisted light and chirality, Opt. Lett. **43**, 435 (2018).

[33] M. van Veenendaal and I. McNulty, Prediction of Strong Dichroism Induced by X Rays Carrying Orbital Momentum, Phys. Rev. Lett. **98**, 157401 (2007).

[34] A. Picón, J. Mompart, J. R. Vázquez de Aldana, L. Plaja, G. F. Calvo, and L. Roso, Photoionization with orbital angular momentum beams, Opt. Express **18**, 3660 (2010).

[35] J. Wätzel and J. Berakdar, Discerning on a sub-optical-wavelength the attosecond time delays in electron emission from magnetic sublevels by optical vortices, Phys. Rev. A **94**, 033414 (2016).

[36] S. Franke-Arnold, Optical angular momentum and atoms, Philos. Trans. R. Soc. A: Math., Phys. Engineer. Sci. **375**, 20150435 (2017).

[37] S. Giri, M. Ivanov, and G. Dixit, Signatures of the orbital angular momentum of an infrared light beam in the two-photon transition matrix element: A step toward attosecond chronoscopy of photoionization, Phys. Rev. A **101**, 033412 (2020).

[38] G. Molina-Terriza, J.˜P. Torres, and L. Torner, Twisted photons, Nat. Phys. **3**, 305 (2007).

[39] H. Fujita and M. Sato, Ultrafast generation of skyrmionic defects with vortex beams: Printing laser profiles on magnets, Phys. Rev. B **95**, 054421 (2017).

[40] O. P. Polyakov, I. A. Gonoskov, V. S. Stepanyuk, and E. K. U. Gross, Generation of magnetic skyrmions by focused vortex laser pulses, J. Appl. Phys. **127**, 073904 (2020).

[41] G. F. Quinteiro, A. O. Lucero, and P. I. Tamborenea, Electronic transitions in quantum dots and rings induced by inhomogeneous off-centered light beams, J. Phys.: Condens. Matter **22**, 505802 (2010).

[42] R. M. Kerber, J. M. Fitzgerald, S. S. Oh, D. E. Reiter, and O. Hess, Orbital angular momentum dichroism in nanoantennas, Commun. Phys. **1**, 87 (2018).

[43] PawełWoźniak, I. De Leon, K. Höflich, G. Leuchs, and P. Banzer, Interaction of light carrying orbital angular momentum with a chiral dipolar scatterer, Optica **6**, 961 (2019).

[44] X. Zambrana-Puyalto, X. Vidal, and G. Molina-Terriza, Angular momentum-induced circular dichroism in non-chiral nanostructures, Nat. Commun. **5**, 4922 (2014).

[45] P. M. Oppeneer, *Handbook of Magnetic Materials* (Elsevier, 2001), Chap. 3, pp. 229–422.

[46] J. Ander Arregi, P. Riego, and A. Berger, What is the longitudinal magneto-optical Kerr effect? J. Phys. Ds **50**, 03LT01 (2016).

[47] S. Yamamoto and I. Matsuda, Measurement of the Resonant Magneto-Optical Kerr Effect Using a Free Electron Laser, Appl. Sci. **7**, 662 (2017).

[48] M. Sacchi, G. Panaccione, J. Vogel, A. Mirone, and G. van der Laan, Magnetic dichroism in reflectivity and photoemission using linearly polarized light: 3p core level of Ni(110), Phys. Rev. B **58**, 3750 (1998).

[49] P. Grychtol, R. Adam, S. Valencia, S. Cramm, D. E. Bürgler, and C. M. Schneider, Resonant magnetic reflectivity in the extreme ultraviolet spectral range: Interlayer-coupled Co/Si/Ni/Fe multilayer system, Phys. Rev. B **82**, 054433 (2010).

[50] E. Ferrari, C. Spezzani, F. Fortuna, R. Delaunay, F. Vidal, I. Nikolov, P. Cinquegrana, B. Diviacco, G. Penco, P. Rebernik Ribič, E. Roussel, M. Trovò, J.-B. Moussy, T. Pincelli, L. Lounis, M. Manfredda, E. Pedersoli, F. Capotondi, C. Svetina, N. Mahne, M. Zangrando, L. Raimondi, A. Demidovich, L. Giannessi, G. De Ninno, M. B. Danailov, E. Allaria, and M. Sacchi, Widely tunable two-colour seeded free-electron laser source for resonant-pump resonant-probe magnetic scattering, Nat. Commun. **7**, 10343 (2016).

[51] C. Kao, J. B. Hastings, E. D. Johnson, D. P. Siddons, G. C. Smith, and G. A. Prinz, Magnetic-Resonance Exchange Scattering at the Iron L2 and L3 Edges, Phys. Rev. Lett. **65**, 373 (1990).

[52] M. Sacchi and A. Mirone, Resonant reflectivity from a Ni(110) crystal: Magnetic effects at the Ni 2p edges using linearly and circularly polarized photons, Phys. Rev. B **57**, 8408 (1998).

[53] M. Sacchi, A. Mirone, C. F. Hague, J.-M. Mariot, L. Pasquali, P. Isberg, E. M. Gullikson, and J. H. Underwood, Soft-x-ray resonant scattering from V/Fe (001) magnetic superlattices, Phys. Rev. B **60**, R12569 (1999).

[54] P. Rebernik-Ribič, D. Gauthier, and G. De Ninno, Generation of Coherent Extreme-Ultraviolet Radiation Carrying Orbital Angular Momentum, Phys. Rev. Lett. **112**, 203602 (2014).

[55] P. Rebernik Ribič, B. Rösner, D. Gauthier, E. Allaria, F. Döring, L. Foglia, L. Giannessi, N. Mahne, M. Manfredda, C. Masciovecchio, R. Mincigrucci, N. Mirian, E. Principi, E. Roussel, A. Simoncig, S. Spampinati, C. David, and G. De Ninno, Extreme-Ultraviolet Vortices from a Free-Electron Laser, Phys. Rev. X **7**, 031036 (2017).

[56] J. C. T. Lee, S. J. Alexander, S. D. Kevan, S. Roy, and B. J. McMorran, Laguerre-Gauss and Hermite-Gauss soft X-ray states generated using diffractive optics, Nat. Photonics **13**, 205 (2019).

[57] G. Gariepy, J. Leach, K. T. Kim, T. J. Hammond, E. Frumker, R. W. Boyd, and P. B. Corkum, Creating High-Harmonic Beams with Controlled Orbital Angular Momentum, Phys. Rev. Lett. **113**, 153901 (2014).

[58] R. Géneaux, Le moment angulaire de la lumière en génération d'harmoniques d'ordre élevé, Ph.D. thesis, Université Paris-Saclay, 2016.

[59] D. Gauthier, P. Rebernik Ribič, G. Adhikary, A. Camper, C. Chappuis, R. Cucini, L. F. DiMauro, G. Dovillaire, F. Frassetto, R. Géneaux, P. Miotti, L. Poletto, B. Ressel, C. Spezzani, M. Stupar, T. Ruchon, and G. De Ninno, Tunable orbital angular momentum in high-harmonic generation, Nat. Commun. **8**, 14971 (2017).

[60] F. Kong, C. Zhang, F. Bouchard, Zhengyan Li, G. G. Brown, Dong Hyuk Ko, T. J. Hammond, L. Arissian, R. W. Boyd, E. Karimi, and P. B. Corkum, Controlling the orbital angular momentum of high harmonic vortices, Nat. Commun. **8**, 14970 (2017).

[61] L. Rego, J. S. Román, A. Picón, L. Plaja, and C. Hernández-García, Nonperturbative Twist in the Generation of Extreme-Ultraviolet Vortex Beams, Phys. Rev. Lett. **117**, 163202 (2016).

[62] K. M. Dorney, L. Rego, N. J. Brooks, J. S. Román, C.-T. Liao, J. L. Ellis, D. Zusin, C. Gentry, Q. L. Nguyen, J. M. Shaw, A. Picón, L. Plaja, H. C. Kapteyn, M. M. Murnane, and C. Hernández-García, Controlling the polarization and vortex charge of attosecond high-harmonic beams via simultaneous spin-orbit momentum conservation, Nat. Photonics **13**, 123 (2018).

[63] L. Rego, K. M. Dorney, N. J. Brooks, Q. L. Nguyen, C.-T. Liao, J. S. Román, D. E. Couch, A. Liu, E. Pisanty, M. Lewenstein, L. Plaja, H. C. Kapteyn, M. M. Murnane, and C. Hernández-García, Generation of extreme-ultraviolet beams with time-varying orbital angular momentum, Science **364**, eaaw9486 (2019).

[64] J.-Y. Chauleau, W. Legrand, N. Reyren, D. Maccariello, S. Collin, H. Popescu, K. Bouzehouane, V. Cros, N. Jaouen, and A. Fert, Chirality in Magnetic Multilayers Probed by the Symmetry and the Amplitude of Dichroism in X-Ray Resonant Magnetic Scattering, Phys. Rev. Lett. **120**, 037202 (2018).

[65] M. van Veenendaal, Interaction between x-ray and magnetic vortices, Phys. Rev. B **92**, 245116 (2015).

[66] L. Allen, M. W. Beijersbergen, R. J. C. Spreeuw, and J. P. Woerdman, Orbital angular momentum of light and the transformation of Laguerre-Gaussian laser modes, Phys. Rev. A **45**, 8185 (1992).

[67] C. Piovera, Ultrafast laser induced dynamics in ferromagnets: Towards the control of the spin order from the femtosecond to the sub-nanosecond time scale, Ph.D. Thesis, Politecnico di Milano, 2013.

[68] J. Zak, E. R. Moog, C. Liu, and S. D. Bader, Fundamental magneto-optics, J. Appl. Phys. **68**, 4203 (1990).

[69] However, arguments similar to those of Sec. III B would show that the quadratic terms do not lead to a dependence of the reflected pattern on the sign of the OAM.

[70] W. T. Buono, A. Santos, M. R. Maia, L. J. Pereira, D. S. Tasca, K. Dechoum, T. Ruchon, and A. Z. Khoury, Chiral relations and radial-angular coupling in nonlinear interactions of optical vortices, Phys. Rev. A **101**, 043821 (2020).

[71] E. Oblak, P. Riego, L. Fallarino, A. Martínez-de Guerenu, F. Arizti, and A. Berger, Ultrasensitive transverse magneto-optical Kerr effect measurements by means of effective polarization change detection, J. Phys. D **50**, 23LT01 (2017).

[72] M. Born, E. Wolf, A. B. Bhatia, P. C. Clemmow, D. Gabor, A. R. Stokes, A. M. Taylor, P. A. Wayman, and W. L. Wilcock, *Principles of Optics: Electromagnetic Theory of Propagation, Interference and Diffraction of Light*, 7th ed. (Cambridge University Press, Cambridge, 1999).

[73] W. Rosenheinrich, Tables of Some Indefinite Integrals of Bessel Functions, Ernst-Abbe-Hochschule, Jena, 2019), p. 161, https://www.scribd.com/document/455399762/besint-pdf.

[74] K. A. Forbes and D. L. Andrews, Spin-orbit coupling in vortex light: Can it be revealed in fundamental electronic transitions? in *Spintronics XI*, edited by H.-J. Drouhin, J.-E. Wegrowe, M. Razeghi, and H. Jaffrès (International Society for Optics and Photonics, SPIE, 2018), Vol. 10732, pp. 108–117.

[75] This can be obtained as MHD-ℓ − MHD-$\ell m = -I_{-\ell,m} + I_{-\ell,-m} = -P_x(I_{\ell,m} - I_{\ell,-m}) =$ MHD-m, where the parity inversion P acts on the x coordinate.

[76] S. Valencia, A. Gaupp, W. Gudat, H.-Ch. Mertins, P. M. Oppeneer, D. Abramsohn, and C. M. Schneider, Faraday rotation spectra at shallow core levels: 3p edges of Fe, Co, and Ni, New J. Phys. **8**, 254 (2006).

[77] O. Kfir, S. Zayko, C. Nolte, M. Sivis, M. Möller, B. Hebler, Sri Sai Phani Kanth Arekapudi, D. Steil, S. Schäfer, M. Albrecht, O. Cohen, S. Mathias, and C. Ropers, Nanoscale magnetic imaging using circularly polarized high-harmonic radiation, Sci. Adv. **3**, eaao4641 (2017).

[78] A. A. Sirenko, P. Marsik, C. Bernhard, T. N. Stanislavchuk, V. Kiryukhin, and S.-W. Cheong, Terahertz Vortex Beam as a Spectroscopic Probe of Magnetic Excitations, Phys. Rev. Lett. **122**, 237401 (2019).

[79] K. A. Forbes and A. Salam, Kramers-Heisenberg dispersion formula for scattering of twisted light, Phys. Rev. A **100**, 053413 (2019).

[80] V. E. Demidov, S. Urazhdin, A. Anane, V. Cros, and S. O. Demokritov, Spin-orbit-torque magnonics, J. Appl. Phys. **127**, 170901 (2020).

[81] X. Fu, S. D. Pollard, B. Chen, H. Yang, and Y. Zhu, Optical manipulation of magnetic vortices visualized in situ by Lorentz electron microscopy, Sci. Adv. **4**, eaat3077 (2018).

[82] X. Zhang, J. Xia, Y. Zhou, X. Liu, H. Zhang, and M. Ezawa, Skyrmion dynamics in a frustrated ferromagnetic film and current-induced helicity locking-unlocking transition, Nat. Commun. **8**, 1717 (2017).

[83] M. Ali, Growth and study of magnetostrictive FeSiBC thin films for device applications, Ph.D. Thesis, University of Sheffield, 1999.

CHAPTER 14

Paper II: Observation of magnetic helicoidal dichroism with extreme ultraviolet light vortices

Observation of Magnetic Helicoidal Dichroism with Extreme Ultraviolet Light Vortices

Mauro Fanciulli,[1,2,*,†] Matteo Pancaldi,[3,*] Emanuele Pedersoli,[3] Mekha Vimal,[1] David Bresteau,[1] Martin Luttmann,[1] Dario De Angelis,[3] Primož Rebernik Ribič,[3] Benedikt Rösner,[4] Christian David,[4] Carlo Spezzani,[3] Michele Manfredda,[3] Ricardo Sousa,[5] Ioan-Lucian Prejbeanu,[5] Laurent Vila,[5] Bernard Dieny,[5] Giovanni De Ninno,[3,6] Flavio Capotondi,[3] Maurizio Sacchi,[7,8] and Thierry Ruchon[1,‡]

[1]*Université Paris-Saclay, CEA, CNRS, LIDYL, 91191 Gif-sur-Yvette, France*
[2]*Laboratoire de Physique des Matériaux et Surfaces, CY Cergy Paris Université, 95031 Cergy-Pontoise, France*
[3]*Elettra-Sincrotrone Trieste S.C.p.A., 34149 Basovizza, Trieste, Italy*
[4]*Paul Scherrer Institut, 5232 Villigen-PSI, Switzerland*
[5]*Université Grenoble Alpes, CNRS, CEA, Grenoble INP, IRIG-SPINTEC, 38000 Grenoble, France*
[6]*Laboratory of Quantum Optics, University of Nova Gorica, 5001 Nova Gorica, Slovenia*
[7]*Sorbonne Université, CNRS, Institut des NanoSciences de Paris, INSP, 75005 Paris, France*
[8]*Synchrotron SOLEIL, L'Orme des Merisiers, Saint-Aubin, B. P. 48, 91192 Gif-sur-Yvette, France*

(Received 24 March 2021; accepted 19 January 2022; published 16 February 2022)

We report on the experimental evidence of magnetic helicoidal dichroism, observed in the interaction of an extreme ultraviolet vortex beam carrying orbital angular momentum with a magnetic vortex. Numerical simulations based on classical electromagnetic theory show that this dichroism is based on the interference of light modes with different orbital angular momenta, which are populated after the interaction between light and the magnetic topology. This observation gives insight into the interplay between orbital angular momentum and magnetism and sets the framework for the development of new analytical tools to investigate ultrafast magnetization dynamics.

DOI: 10.1103/PhysRevLett.128.077401

Beyond plane waves, light beams may feature helical wave fronts, with the Poynting vector precessing with time around the beam's propagation axis [1]. The number of intertwined helices spiraling clockwise or anticlockwise defines the topological charge $\ell \in \mathbb{Z}$, which is associated with the orbital angular momentum (OAM) of the light vortices. This is independent from light's polarization state, which instead is associated with a spin angular momentum (SAM) [2]. OAM light beams are nowadays harnessed for an ever increasing scope of applications covering different fields, from microscopy [3–5] and biology [6,7] to telecommunications [8,9] and quantum technologies [10,11]. Vortex beams also play a role in spectroscopy, where the coupling between the OAM and the internal degrees of freedom of atoms, atomic ions, or molecules has been exploited to transfer OAM to these species [12–15] and to enhance enantiomeric sensitivity [16,17]. Also, a rich variety arises for the investigation and manipulation of topologically complex objects, such as chiral magnetic structures [18] and skyrmions [19–21]. In the same way as tuning the wavelength is used to achieve chemical contrast, or tuning the polarization to achieve magnetic contrast, controlling the OAM state of a vortex beam has the potential to provide topological contrast in systems possessing a well-defined handedness. This general statement can eventually find applications in many different extreme ultraviolet (XUV) and x-ray based techniques, like elastic or inelastic scattering and photoelectron emission. The study of magnetic structures is a particularly appealing case, for their practical importance and for the possible control of their topology.

Over the last decade, the development of highly coherent sources and tailored optical schemes has opened new possibilities for generating structured light vortices in the XUV [22–29] and x-ray [30–35] regimes, paving the way to their spectroscopic applications. In this context, magnetic helicoidal dichroism (MHD) has been recently predicted [36], in analogy to the SAM-dependent magnetic circular dichroism (MCD). Upon interaction (reflection or transmission) of a pure Laguerre-Gaussian mode of topological charge ℓ with a magnetic surface, MHD consists in an intensity redistribution into all modes $\ell + n$ in the outgoing beam, where n represents all the azimuthal decomposition coefficients of the magnetic structure symmetry [36]. Different from MCD, MHD is sensitive to the overall topology of the spin texture, it vanishes for homogeneous structures, and is not self-similar if one inverts either the topological charge of the beam or the magnetization direction.

Among a great variety of magnetic structures in two [37] or three dimensions [38], magnetic vortices (MVs) are particularly promising for technological applications [39,40]. They can form in mesoscopic dots that are much larger than their thickness [41], leading to a planar

magnetization with curling direction either clockwise ($m = +1$) or anticlockwise ($m = -1$), which we can associate with a toroidal moment [42,43]. They have been shown to be particularly robust against perturbations [44] and present a rich subnanosecond dynamics [45]. Because of their symmetry, MVs are also a particularly simple test case for MHD, since they only present $n = \pm 1$ [36].

In this Letter, we report on the experimental observation of MHD by measuring the resonant scattering of XUV radiation carrying OAM from a permalloy (Py, $Fe_{20}Ni_{80}$) dot in MV micromagnetic configuration. We compare the experimental results to theoretical predictions [36] and we interpret them in terms of the interference between the different $\ell + n$ modes of the reflected light. Our study illustrates the potential of MHD as a new optical tool for the investigation of magnetic structures and their topology.

The experiment was performed at the DiProI beam line [46] of the FERMI free-electron laser (FEL) [47] using the setup sketched in Fig. 1(a). The spatially coherent close-to-Gaussian FEL beam is focused on the sample by one of three available silicon zone plates [48] mounted on a movable stage. One is a Fresnel zone plate producing a focused beam with $\ell = 0$; the other two are spiraling zone plates (SZPs) that impart OAM to the beam with either $\ell = -1$ or $\ell = +1$. The properties of the zone plates are detailed in [26]. An electron microscope image of the SZP

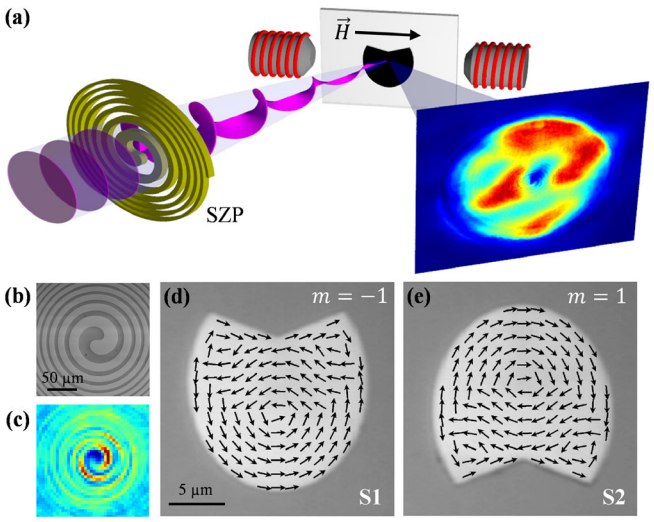

FIG. 1. (a) Schematics of the experimental setup at the DiProI beam line, showing the incoming FEL beam with planar wave front, a SZP that imparts OAM to the FEL beam, the sample placed between the poles of the electromagnet and the image of the scattered beam. (b) Scanning electron microscope image of one SZP ($\ell = +1$). (c) Far field image of the interference pattern of the corresponding OAM beam and the undiffracted, OAM-free beam, featuring a spiraling intensity pattern. (d),(e) Magnetic dots $S1$ and $S2$ with corresponding remanent magnetization after applying a pulse of saturating external field $\vec{H}$ as in (a). An opposite field reverses the curling direction m of the remanent magnetization in both samples.

for $\ell = +1$ is shown in Fig. 1(b), while in Fig. 1(c) the direct image of the beam with OAM collected by a CCD camera shows the expected spiral-shaped far field interference pattern with the undiffracted beam [26,49].

The photon energy was set to 52.8 eV in order to match the Fe $3p \rightarrow 3d$ core resonance [50]. This approach, which is standard in x-ray dichroism, allows one to simultaneously enhance the magneto-optical effects (that would be otherwise negligible at XUV wavelengths, compared to charge scattering) and to introduce element selectivity. The linearly p-polarized XUV beam impinged on the center of the sample at an angle of 48° from the normal, i.e., close to the Brewster extinction condition, in order to maximize the magnetic signal. Using a knife edge scan, we measured a spot size of about 4 μm (full width at half maximum) at the sample plane, in agreement with previous characterizations [51]. The reflected beam is collected by a CCD camera placed 150 mm from the sample.

The samples [$S1$ and $S2$, Figs. 1(d) and 1(e)] are two identical and π-rotated ellipsoidal Py dots with a triangular indent, prepared on the same Si substrate. They are 80 nm thick, their short diameter is 15 μm, and they are protected by a ≈3 nm Al layer (oxidized in air) (see Supplemental Material [48]). Their exact shape was optimized by micromagnetic calculations [52] in order to satisfy two criteria: (i) feature at remanence a single stable MV with a diameter larger than the XUV beam spot size; (ii) enable the switching of the remanent vortex curling direction m by *in situ* application of a moderate external magnetic field pulse. The calculated remanent magnetization after a +20 mT in-plane magnetic pulse [arrow in Fig. 1(a)] shows that MVs with $m = -1$ and $m = +1$ are formed in $S1$ and $S2$ [Figs. 1(d) and 1(e)], respectively, providing a simple way of cross-checking our experimental results. Reversing the magnetic pulse direction switches the sign of m in both MVs. Further experimental details are given in the Supplemental Material [48].

For each sample, we evaluate the dichroic signal by switching the sign of the external magnetic field pulse before measuring at remanence, so that no mechanical or optical adjustment of the setup is required, guaranteeing optimal stability in the measurement conditions. Also, in this way, nonmagnetic contributions to the scattered intensity are largely suppressed from the difference signal. Figures 2(a)–2(f) show the experimental dichroism on the intensity profile of the reflected beam for three incoming ℓ values and for the two samples. Details of the data analysis are given in the Supplemental Material [48]. For sample $S1$, we observe a left-right asymmetry for $\ell = 0$ [Fig. 2(c)] and opposite spiral asymmetries for opposite topological charges of the OAM beam $\ell = \pm 1$ [Figs. 2(a) and 2(e)], showing the differential dependence on the topological charge of the OAM beam. The measured MHD signal is on the order of 20%. The result is reproduced in $S2$ [Figs. 2(b), 2(d), and 2(f)], where the

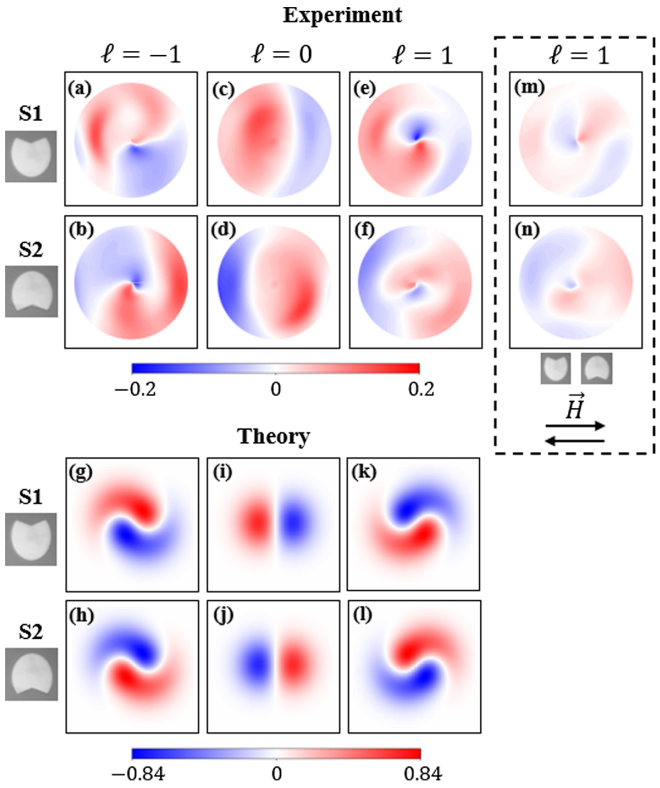

FIG. 2. (a)–(f) Experimental dichroism (corresponding to MHDm) for $\ell = -1, 0, +1$ for MVs in dot $S1$ (top) and $S2$ (bottom). (g)–(l) Numerical simulations for the same experimental parameters. (m),(n) Same as (e),(f), with the same color scale, but with a constant magnetic field applied during the acquisition in order to homogenize sample's magnetization; to be used as a reference. The images corresponding to (a)–(d) can be found in the Supplemental Material [48].

color pattern is reversed since the two samples always have opposite m. This demonstrates the magnetic nature of the observed dichroic signal rather than possible asymmetries induced by the experimental setup. It is worth noting that the symmetry relations observed in Figs. 2(a)–2(f) are almost canceled when the MV topology is perturbed by applying an external magnetic field (Figs. 2(m) and 2(n) and Supplemental Material [48]). The azimuthal Fourier component with period 2π [48], which generates a signal of $\pm 20\%$ in presence of the MV, is strongly reduced (down to ca. $\pm 5\%$ amplitude) when an external magnetic field erases the vortex structure.

In order to interpret the experimental results, we implemented a numerical model for MHD based on Ref. [36], with a perfect Gaussian beam as input, ideal optics, and perfect centering of the beam on the MV. The results of the simulations for the same scattering geometry as in the experiment are shown in Figs. 2(g)–2(l). They can be directly compared with Figs. 2(a)–2(f), showing a good agreement for all configurations. Quantitatively, the experimental dichroism is lower than expected. We believe this is mainly due to the nonmagnetic signal coming from the oxidized Al-capping layer not taken into account in the simulations [48]. The imperfect symmetry of the experimental images [evident, e.g., in Figs. 2(c) and 2(d)] is due to the approximate alignment of the OAM beam on the vortex core, which is impossible to visualize *in situ* (see Supplemental Material [48] for more details). Here it is important to stress that the dependence of the MHD signal on the topological charge is not linked to the particular chosen reflection geometry close to the Brewster angle. From further simulations [48] we predict that, even close to normal incidence, the asymmetry for $\ell = 0$ (left-right) is different from $\ell = \pm 1$ (top-bottom), while the spiral asymmetry of Fig. 2 is due to a combination with geometric effects [36].

In general, in order to evaluate the MHD, three relevant combinations of differences between signals obtained with given values of topological charge of the beam and the curling direction of the MV can be considered [48]. Defining $I_{\ell,m}$ the far field intensity of the reflected beam, we classify these three kinds of dichroisms as [36]

$$\mathrm{MHD}\ell = (I_{\ell,m} - I_{-\ell,m})/(I_{\ell,m} + I_{-\ell,m}) \tag{1a}$$

$$\mathrm{MHD}m = (I_{\ell,m} - I_{\ell,-m})/(I_{\ell,m} + I_{\ell,-m}) \tag{1b}$$

$$\mathrm{MHD}\ell m = (I_{\ell,m} - I_{-\ell,-m})/(I_{\ell,m} + I_{-\ell,-m}). \tag{1c}$$

The dichroism presented in Fig. 2 corresponds to MHDm, since switching the magnetic field direction corresponds to switching the sign of m in the MV for a fixed value of ℓ. In Fig. 3, the other two kinds of MHD from simulations are shown. The dichroic intensity map of MHDm [Figs. 2(g) and 2(k)] differs from MHDℓ [Figs. 3(a) and 3(b)], which ensures a nonzero MHDℓm [Figs. 3(c) and 3(d)]. This is a crucial difference with respect to MCD, where switching the sample magnetization or the light polarization leads to equivalent results. From the experimental point of view, changing m is obtained simply by a magnetic field pulse. On the contrary, changing ℓ implies replacing the SZP, affecting the photon beam trajectory and amplifying the issues in photon–vortex-core alignment already mentioned above. This makes our experimental observation less reliable for MHDℓ and MHDℓm than for MHDm [48].

In order to complement the theoretical analysis proposed in [36], it is interesting to look into the physical mechanism at the origin of MHDm. The local values of the magneto-optical constants are proportional to the curling magnetization, and the reflectivity matrix will thus depend on the azimuth ϕ. This can be used to intuitively retrieve the simple selection rule $\Delta\ell = \pm 1$ for reflection by a MV [36]. In fact, the magnetization terms of the MV, and hence the reflectivity coefficients, vary as $\cos(\phi)$ up to a constant phase term, while the azimuthal dependence of the incoming electric field due to the OAM is $\cos[-(2\pi/\lambda)z - \ell\phi]$, with λ and z being the light wavelength and the propagation

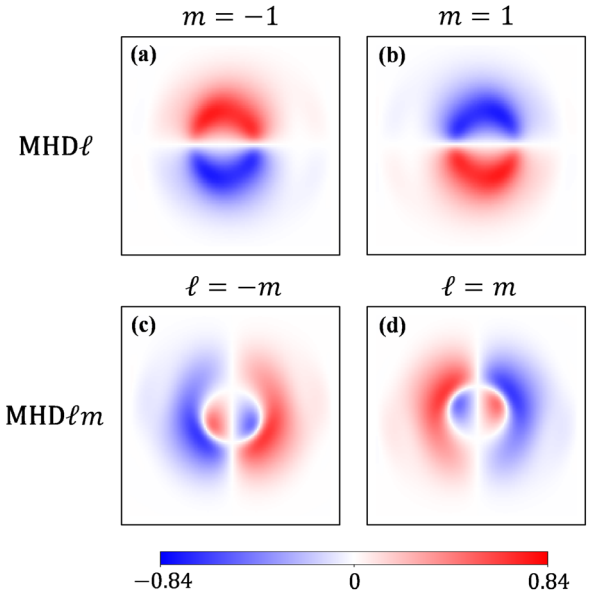

FIG. 3. Numerical simulations with same experimental parameters of (a),(b) MHDℓ for different m and (c),(d) MHDℓm for different combinations of ℓ and m.

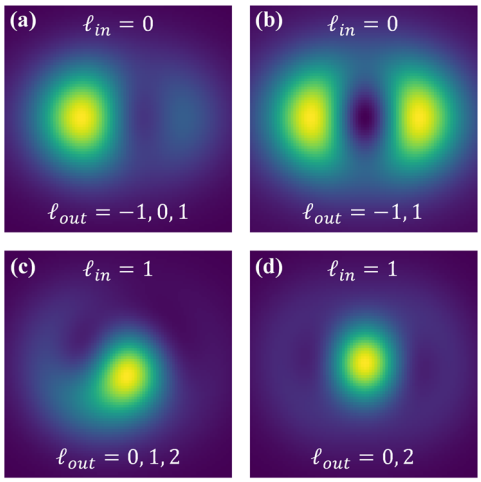

FIG. 4. (a) Far field intensity of a beam with $\ell_{\mathrm{in}} = 0$ reflected by a MV with $m = +1$. (b) Same as (a) when the outgoing mode $\ell_{\mathrm{out}} = \ell_{\mathrm{in}}$ is suppressed. (c),(d) The same results as (a) and (b) when $\ell_{\mathrm{in}} = 1$.

direction, respectively. Without considering geometric effects [36], the magnetic contribution to the outgoing electric field is given by the product of those two terms and will thus show $(\ell \pm 1)\phi$ components, and only these, while the nonmagnetic one is only given by a reflection of the ℓ mode. The propagation of the ℓ and $\ell \pm 1$ modes to the far field will result in interferences in the intensity profile, which is what causes the asymmetries of MHD. Note that this is valid for every incoming ℓ, including $\ell = 0$.

To be more specific, let us consider a p-polarized beam with $\ell_{\mathrm{in}} = 0$, which is a standard Gaussian plane wave without OAM. Figure 4(a) shows the far field simulated intensity after reflection from a $m = +1$ MV, featuring a left-right imbalance that reverses for the case $m = -1$ [48], leading to MHDm [Fig. 2(i)]. If we suppress the propagation of the outgoing mode $\ell_{\mathrm{out}} = 0$ in the simulation and leave only $\ell_{\mathrm{out}} = \pm 1$, we obtain the intensity in Fig. 4(b). This is the typical shape of a Hermite-Gaussian beam of index 1. We can draw two important conclusions. One is that even a standard Gaussian beam with $\ell = 0$ reflected by a magnetic structure such as a MV contains equal weights of modes with opposite nonzero OAM. This is a largely overlooked observation that can be used as a fresh way to look at magneto-optical scattering phenomena. The second conclusion is that the dichroic signal in MHD originates from the interference of the main incoming mode $\ell_{\mathrm{out}} = \ell_{\mathrm{in}}$ with the newly generated ones. This can also be seen, for example, for the case of $\ell_{\mathrm{in}} = 1$. In Fig. 4(d), where $\ell_{\mathrm{out}} = 1$ is suppressed from the reflected beam, one finds signatures of a second-order Hermite-Gaussian beam, while the full beam of Fig. 4(c) is the result of the interference with the central mode, including the $\ell = 1$ mode. In this case, a spiraling shape is obtained. Its mirrored image on the horizontal axis is obtained when one considers $\ell_{\mathrm{in}} = -1$ instead, mirrored on the vertical axis when $\ell_{\mathrm{in}} = -1$ and $m = -1$ and mirrored on both axis when $\ell_{\mathrm{in}} = +1$ and $m = -1$ [48]. The fact that these four cases are not equivalent explains why MHDm and MHDℓ are different, and thus the existence of MHDℓm.

In conclusion, we presented the experimental evidence of magnetic helicoidal dichroism in the resonant reflection of an XUV beam that carries OAM by a magnetic vortex and found a good agreement with theoretical predictions. In particular, we identify the specific dependence of MHD on the sign of the optical (ℓ) and magnetic (m) vortices. Other configurations of OAM and light polarization could be explored [48], providing altogether a new way to look at the magneto-optical scattering process in terms of OAM, as discussed also for the case of an $\ell = 0$ incoming beam.

It is straightforward to extend this approach to other complex magnetic structures. For example, in analogy with the recent observation that infrared vortex beams with opposite ℓ are sensitive to dipolar chiral nanohelix [53,54], one can envision to use MHD for XUV and soft x-ray beams with OAM in order to detect the helical direction of complex 3D spiral spin structures [55] or to study chiral domain walls and skyrmions in magnetic films with strong Dzyaloshinskii-Moriya interaction [56]. Conversely, different structures can be engineered in order to tailor or analyze the OAM content of a light beam [33,35]. A limit of our interpretation is that it is based on classical electromagnetism. A microscopic theory has still to be developed and questions about a possible local exchange of OAM between light and matter remain open. Finally, the feasibility of this experiment with a FEL source naturally opens up the study of MHD in the time domain, as recently performed in nanoplasmonics [57,58]. MHD could then become a

powerful experimental tool for the study of the ultrafast dynamics of magnetic materials and of their topological properties [59,60], but also a way to control and manipulate them, in a similar fashion as in the inverse Faraday effect with SAM [61].

This work was supported by the Agence Nationale pour la Recherche (under Contracts No. ANR11-EQPX0005-ATTOLAB, No. ANR14-CE320010-Xstase and Investissement d'avenir Labex Palm Grant No. ANR-10-LABX-0039-PALM), the Swiss National Science Foundation project No. P2ELP2_181877, the Plateforme Technologique Amont de Grenoble, with the financial support of the CNRS Renatech network, and the EU-H2020 Research and Innovation Programme, No. 654360 NFFA-Europe.

*These authors contributed equally to this work.
†mauro.fanciulli@u-cergy.fr
‡thierry.ruchon@cea.fr

[1] L. Allen, M. W. Beijersbergen, R. J. C. Spreeuw, and J. P. Woerdman, Orbital angular momentum of light and the transformation of Laguerre-Gaussian laser modes, Phys. Rev. A **45**, 8185 (1992).
[2] K. Y. Bliokh and F. Nori, Transverse and longitudinal angular momenta of light, Phys. Rep. **592**, 1 (2015).
[3] T. A. Klar and S. W. Hell, Subdiffraction resolution in far-field fluorescence microscopy, Opt. Lett. **24**, 954 (1999).
[4] S. Wei, T. Lei, L. Du, C. Zhang, H. Chen, Y. Yang, S. W. Zhu, and X.-C. Yuan, Sub-100 nm resolution PSIM by utilizing modified optical vortices with fractional topological charges for precise phase shifting, Opt. Express **23**, 30143 (2015).
[5] F. Tamburini, G. Anzolin, G. Umbriaco, A. Bianchini, and C. Barbieri, Overcoming the Rayleigh Criterion Limit with Optical Vortices, Phys. Rev. Lett. **97**, 163903 (2006).
[6] L. Paterson, M. P. MacDonald, J. Arlt, W. Sibbett, P. E. Bryant, and K. Dholakia, Controlled rotation of optically trapped microscopic particles, Science **292**, 912 (2001).
[7] D. G. Grier, A revolution in optical manipulation, Nature (London) **424**, 810 (2003).
[8] R. Fickler, G. Campbell, B. Buchler, P. K. Lam, and A. Zeilinger, Quantum entanglement of angular momentum states with quantum numbers up to 10,010, Proc. Natl. Acad. Sci. U.S.A. **113**, 13642 (2016).
[9] L. Gong, Q. Zhao, H. Zhang, X.-Y. Hu, K. Huang, J.-M. Yang, and Y.-M. Li, Optical orbital-angular-momentum-multiplexed data transmission under high scattering, Light **8**, 27 (2019).
[10] A. M. Yao and M. J. Padgett, Orbital angular momentum: Origins, behavior and applications, Adv. Opt. Photonics **3**, 161 (2011).
[11] Y. Shen, X. Wang, Z. Xie, C. Min, X. Fu, Q. Liu, M. Gong, and X. Yuan, Optical vortices 30 years on: OAM manipulation from topological charge to multiple singularities, Light **8**, 90 (2019).
[12] K. A. Forbes and D. L. Andrews, Optical orbital angular momentum: Twisted light and chirality, Opt. Lett. **43**, 435 (2018).
[13] C. T. Schmiegelow, J. Schulz, H. Kaufmann, T. Ruster, U. G. Poschinger, and F. Schmidt-Kaler, Transfer of optical orbital angular momentum to a bound electron, Nat. Commun. **7**, 12998 (2016).
[14] A. Afanasev, C. E. Carlson, C. T. Schmiegelow, J. Schulz, F. Schmidt-Kaler, and M. Solyanik, Experimental verification of position-dependent angular-momentum selection rules for absorption of twisted light by a bound electron, New J. Phys. **20**, 023032 (2018).
[15] G. De Ninno *et al.*, Photoelectric effect with a twist, Nat. Photonics **14**, 554 (2020).
[16] W. Brullot, M. K. Vanbel, T. Swusten, and T. Verbiest, Resolving enantiomers using the optical angular momentum of twisted light, Sci. Adv. **2**, e1501349 (2016).
[17] J. Ni, S. Liu, D. Wu, Z. Lao, Z. Wang, K. Huang, S. Ji, J. Li, Z. Huang, Q. Xiong, Y. Hu, J. Chu, and C.-W. Qiu, Gigantic vortical differential scattering as a monochromatic probe for multiscale chiral structures, Proc. Natl. Acad. Sci. U.S.A. **118**, e2020055118 (2021).
[18] A. A. Sirenko, P. Marsik, C. Bernhard, T. N. Stanislavchuk, V. Kiryukhin, and S.-W. Cheong, Terahertz Vortex Beam as a Spectroscopic Probe of Magnetic Excitations, Phys. Rev. Lett. **122**, 237401 (2019).
[19] H. Fujita and M. Sato, Ultrafast generation of skyrmionic defects with vortex beams: Printing laser profiles on magnets, Phys. Rev. B **95**, 054421 (2017).
[20] H. Fujita and M. Sato, Encoding orbital angular momentum of light in magnets, Phys. Rev. B **96**, 060407(R) (2017).
[21] W. Yang, H. Yang, Y. Cao, and P. Yan, Photonic orbital angular momentum transfer and magnetic skyrmion rotation, Opt. Express **26**, 8778 (2018).
[22] G. Gariepy, J. Leach, K. T. Kim, T. J. Hammond, E. Frumker, R. W. Boyd, and P. B. Corkum, Creating High-Harmonic Beams with Controlled Orbital Angular Momentum, Phys. Rev. Lett. **113**, 153901 (2014).
[23] R. Géneaux, A. Camper, T. Auguste, O. Gobert, J. Caillat, R. Taïeb, and T. Ruchon, Synthesis and characterization of attosecond light vortices in the extreme ultraviolet, Nat. Commun. **7**, 12583 (2016).
[24] F. Kong, C. Zhang, F. Bouchard, Z. Li, G. G. Brown, D. H. Ko, T. J. Hammond, L. Arissian, R. W. Boyd, E. Karimi, and P. B. Corkum, Controlling the orbital angular momentum of high harmonic vortices, Nat. Commun. **8**, 14970 (2017).
[25] D. Gauthier, P. R. Ribič, G. Adhikary, A. Camper, C. Chappuis, R. Cucini, L. F. DiMauro, G. Dovillaire, F. Frassetto, R. Géneaux, P. Miotti, L. Poletto, B. Ressel, C. Spezzani, M. Stupar, T. Ruchon, and G. De Ninno, Tunable orbital angular momentum in high-harmonic generation, Nat. Commun. **8**, 14971 (2017).
[26] P. Rebernik Ribič, B. Rösner, D. Gauthier, E. Allaria, F. Döring, L. Foglia, L. Giannessi, N. Mahne, M. Manfredda, C. Masciovecchio, R. Mincigrucci, N. Mirian, E. Principi, E. Roussel, A. Simoncig, S. Spampinati, C. David, and G. De Ninno, Extreme-Ultraviolet Vortices from a Free-Electron Laser, Phys. Rev. X **7**, 031036 (2017).
[27] K. M. Dorney, L. Rego, N. J. Brooks, J. San Román, C.-T. Liao, J. L. Ellis, D. Zusin, C. Gentry, Q. L. Nguyen,

J. M. Shaw, A. Picón, L. Plaja, H. C. Kapteyn, M. M. Murnane, and C. Hernández-García, Controlling the polarization and vortex charge of attosecond high-harmonic beams via simultaneous spin–orbit momentum conservation, Nat. Photonics **13**, 123 (2019).

[28] L. Rego, K. M. Dorney, N. J. Brooks, Q. L. Nguyen, C.-T. Liao, J. S. Román, D. E. Couch, A. Liu, E. Pisanty, M. Lewenstein, L. Plaja, H. C. Kapteyn, M. M. Murnane, and C. Hernández-García, Generation of extreme-ultraviolet beams with time-varying orbital angular momentum, Science **364**, eaaw9486 (2019).

[29] E. Pisanty, L. Rego, J. San Román, A. Picón, K. M. Dorney, H. C. Kapteyn, M. M. Murnane, L. Plaja, M. Lewenstein, and C. Hernández-García, Conservation of Torus-Knot Angular Momentum in High-Order Harmonic Generation, Phys. Rev. Lett. **122**, 203201 (2019).

[30] E. Hemsing, A. Knyazik, M. Dunning, D. Xiang, A. Marinelli, C. Hast, and J. B. Rosenzweig, Coherent optical vortices from relativistic electron beams, Nat. Phys. **9**, 549 (2013).

[31] J. Vila-Comamala, A. Sakdinawat, and M. Guizar-Sicairos, Characterization of x-ray phase vortices by ptychographic coherent diffractive imaging, Opt. Lett. **39**, 5281 (2014).

[32] S. Sasaki, M. Hosaka, M. Katoh, T. Konomi, A. Miyamoto, and N. Yamamoto, Analyses of light's orbital angular momentum from helical undulator harmonics, in *6th International Particle Accelerator Conference (IPAC'15)* (JACoW, Geneva, Switzerland, 2015), p. TUPWA061, 10.18429/JACoW-IPAC2015-TUPWA061

[33] J. C. T. Lee, S. J. Alexander, S. D. Kevan, S. Roy, and B. J. McMorran, Laguerr-Gauss and Hermite-Gauss soft x-ray states generated using diffractive optics, Nat. Photonics **13**, 205 (2019).

[34] L. Loetgering, M. Baluktsian, K. Keskinbora, R. Horstmeyer, T. Wilhein, G. Schütz, K. S. E. Eikema, and S. Witte, Generation and characterization of focused helical x-ray beams, Sci. Adv. **6**, eaax8836 (2020).

[35] J. S. Woods, X. M. Chen, R. V. Chopdekar, B. Farmer, C. Mazzoli, R. Koch, A. S. Tremsin, W. Hu, A. Scholl, S. Kevan, S. Wilkins, W.-K. Kwok, L. E. De Long, S. Roy, and J. T. Hastings, Switchable X-Ray Orbital Angular Momentum from an Artificial Spin Ice, Phys. Rev. Lett. **126**, 117201 (2021).

[36] M. Fanciulli, D. Bresteau, M. Vimal, M. Luttmann, M. Sacchi, and T. Ruchon, Electromagnetic theory of helicoidal dichroism in reflection from magnetic structures, Phys. Rev. A **103**, 013501 (2021).

[37] X. Zhang, Y. Zhou, K. M. Song, T.-E. Park, J. Xia, M. Ezawa, X. Liu, W. Zhao, G. Zhao, and S. Woo, Skyrmion-electronics: Writing, deleting, reading and processing magnetic skyrmions toward spintronic applications, J. Phys. Condens. Matter **32**, 143001 (2020).

[38] A. Fernández-Pacheco, R. Streubel, O. Fruchart, R. Hertel, P. Fischer, and R. P. Cowburn, Three-dimensional nanomagnetism, Nat. Commun. **8**, 15756 (2017).

[39] T. Shinjo, Magnetic vortex core observation in circular dots of permalloy, Science **289**, 930 (2000).

[40] S. D. Bader, Colloquium: Opportunities in nanomagnetism, Rev. Mod. Phys. **78**, 1 (2006).

[41] M. Natali, I. L. Prejbeanu, A. Lebib, L. D. Buda, K. Ounadjela, and Y. Chen, Correlated Magnetic Vortex Chains in Mesoscopic Cobalt Dot Arrays, Phys. Rev. Lett. **88**, 157203 (2002).

[42] A magnetic vortex has the symmetry of a toroidal moment, in the sense defined by J. Hlinka [43]. The pointing direction of this toroidal moment is associated with the clockwise or counterclockwise curling direction (m) of the magnetic vortex. We use this denomination instead of the frequent but strictly speaking improper use of the term "chirality".

[43] J. Hlinka, Eight Types of Symmetrically Distinct Vectorlike Physical Quantities, Phys. Rev. Lett. **113**, 165502 (2014).

[44] H.-B. Braun, Topological effects in nanomagnetism: From superparamagnetism to chiral quantum solitons, Adv. Phys. **61**, 1 (2012).

[45] K. Y. Guslienko, X. F. Han, D. J. Keavney, R. Divan, and S. D. Bader, Magnetic Vortex Core Dynamics in Cylindrical Ferromagnetic Dots, Phys. Rev. Lett. **96**, 067205 (2006).

[46] F. Capotondi *et al.*, Invited article: Coherent imaging using seeded free-electron laser pulses with variable polarization: First results and research opportunities, Rev. Sci. Instrum. **84**, 051301 (2013).

[47] E. Allaria *et al.*, Highly coherent and stable pulses from the FERMI seeded free-electron laser in the extreme ultraviolet, Nat. Photonics, **6**, 699 (2012).

[48] See Supplemental Material at http://link.aps.org/supplemental/10.1103/PhysRevLett.128.077401 for further details on the experimental methods, data analysis procedure and numerical simulations.

[49] S. Fürhapter, A. Jesacher, S. Bernet, and M. Ritsch-Marte, Spiral interferometry, Opt. Lett. **30**, 1953 (2005).

[50] S. Valencia, A. Gaupp, W. Gudat, H.-C. Mertins, P. M. Oppeneer, D. Abramsohn, and C. M. Schneider, Faraday rotation spectra at shallow core levels: $3p$ edges of Fe, Co, and Ni, New J. Phys. **8**, 254 (2006).

[51] B. Rösner, F. Döring, P. R. Ribič, D. Gauthier, E. Principi, C. Masciovecchio, M. Zangrando, J. Vila-Comamala, G. De Ninno, and C. David, High resolution beam profiling of x-ray free electron laser radiation by polymer imprint development, Opt. Express **25**, 30686 (2017).

[52] M. J. Donahue and D. G. Porter, OOMMF User's Guide, Interagency Report NISTIR 6376, National Institute of Standards and Technology, Gaithersburg, 1999, 10.6028/NIST.IR.6376.

[53] P. Woźniak, I. D. Leon, K. Höflich, G. Leuchs, and P. Banzer, Interaction of light carrying orbital angular momentum with a chiral dipolar scatterer, Optica **6**, 961 (2019).

[54] J. Ni, S. Liu, G. Hu, Y. Hu, Z. Lao, J. Li, Q. Zhang, D. Wu, S. Dong, J. Chu, and C.-W. Qiu, Giant helical dichroism of single chiral nanostructures with photonic orbital angular momentum, ACS Nano **15**, 2893 (2021).

[55] M. T. Birch *et al.*, Real-space imaging of confined magnetic skyrmion tubes, Nat. Commun. **11**, 1726 (2020).

[56] W. Legrand, J.-Y. Chauleau, D. Maccariello, N. Reyren, S. Collin, K. Bouzehouane, N. Jaouen, V. Cros, and A. Fert, Hybrid chiral domain walls and skyrmions in magnetic multilayers, Sci. Adv. **4**, eaat0415 (2018).

[57] G. Spektor, D. Kilbane, A. K. Mahro, B. Frank, S. Ristok, L. Gal, P. Kahl, D. Podbiel, S. Mathias, H. Giessen *et al.*, Revealing the subfemtosecond dynamics of orbital angular

momentum in nanoplasmonic vortices, Science **355**, 1187 (2017).

[58] Y. Dai, Z. Zhou, A. Ghosh, R. S. K. Mong, A. Kubo, C.-B. Huang, and H. Petek, Plasmonic topological quasiparticle on the nanometre and femtosecond scales, Nature (London) **588**, 616 (2020).

[59] N. Kerber, D. Ksenzov, F. Freimuth, F. Capotondi, E. Pedersoli, I. Lopez-Quintas, B. Seng, J. Cramer, K. Litzius, D. Lacour, H. Zabel, Y. Mokrousov, M. Kläui, and C. Gutt, Faster chiral versus collinear magnetic order recovery after optical excitation revealed by femtosecond XUV scattering, Nat. Commun. **11**, 6304 (2020).

[60] F. Büttner *et al.*, Observation of fluctuation-mediated picosecond nucleation of a topological phase, Nat. Mater. **20**, 30 (2021).

[61] A. V. Kimel, A. Kirilyuk, P. A. Usachev, R. V. Pisarev, A. M. Balbashov, and T. Rasing, Ultrafast non-thermal control of magnetization by instantaneous photomagnetic pulses, Nature (London) **435**, 655 (2005).

SUPPLEMENTARY MATERIAL
Observation of magnetic helicoidal dichroism with extreme ultraviolet light vortices

Mauro Fanciulli,[1,2] Matteo Pancaldi,[3] Emanuele Pedersoli,[3] Mekha Vimal,[1] David Bresteau,[1] Martin Luttmann,[1] Dario De Angelis,[3] Primož Rebernik Ribič,[3] Benedikt Rösner,[4] Christian David,[4] Carlo Spezzani,[3] Michele Manfredda,[3] Ricardo Sousa,[5] Ioan-Lucian Prejbeanu,[5] Laurent Vila,[5] Bernard Dieny,[5] Giovanni De Ninno,[6,3] Flavio Capotondi,[3] Maurizio Sacchi,[7,8] and Thierry Ruchon[1]

[1] *Université Paris-Saclay, CEA, CNRS, LIDYL, 91191 Gif-sur-Yvette, France*
[2] *Laboratoire de Physique des Matériaux et Surfaces, CY Cergy Paris Université, 95031 Cergy-Pontoise, France*
[3] *Elettra-Sincrotrone Trieste S.C.p.A., 34149 Basovizza, Trieste, Italy*
[4] *Paul Scherrer Institut, 5232 Villigen-PSI, Switzerland*
[5] *Université Grenoble Alpes, CNRS, CEA, Grenoble INP, IRIG-SPINTEC, 38000 Grenoble, France*
[6] *Laboratory of Quantum Optics, University of Nova Gorica, 5001 Nova Gorica, Slovenia*
[7] *Sorbonne Université, CNRS, Institut des NanoSciences de Paris, INSP, 75005 Paris, France*
[8] *Synchrotron SOLEIL, L'Orme des Merisiers, Saint-Aubin, B. P. 48, 91192 Gif-sur-Yvette, France*

Contents

EXPERIMENTAL

Sample preparation

The lithographically designed permalloy ($Fe_{20}Ni_{80}$) samples with thickness of 80 nm were prepared by magnetron sputtering on a Si substrate. They were patterned in the form of ellipses with a triangular indent by e-beam lithography and lift-off. After patterning, the formation of a vortex structure at remanence was checked by magneto-optical Kerr effect (MOKE) microscopy. The MOKE measurements showed a saturating field of the order of 10 mT and ca. 15% remanent magnetization, in agreement with micromagnetic simulations (Fig. 1 of the main text). The samples were capped by a protective layer of Al, $\approx$ 3 nm thick, which transforms into Al_2O_3 once exposed to air. Taking into account the Al_2O_3 capping layer is important when comparing experimental and theoretical data for the magnetic dichroic signal, as in Fig. 2 of the main text.

Fig. S1 compares the reflectivity for the 80 nm permalloy film, bare surface and Al_2O_3-capped, at a photon energy of 52.8 eV and incidence angle of 48° from the normal, as in the experiment. The reflectivity for a capping layer of 3 to 5 nm (as expected in our experiment) increases by a factor of 3 to 6 with respect to the bare Py surface. Since in Fig. 2 of the main text the dichroism is evaluated as the asymmetry ratio, i.e. the difference divided by the sum of the reflected intensities for opposite m, the non-magnetic contribution due to Al_2O_3 cancels in the numerator but sums up in the denominator. This non-magnetic intensity contributed by the reflectivity of the capping layer is the main cause of, and completely accounts for, the large discrepancy in the absolute value of the dichroism between experiment and theory, observed in Fig. 2 of the main text.

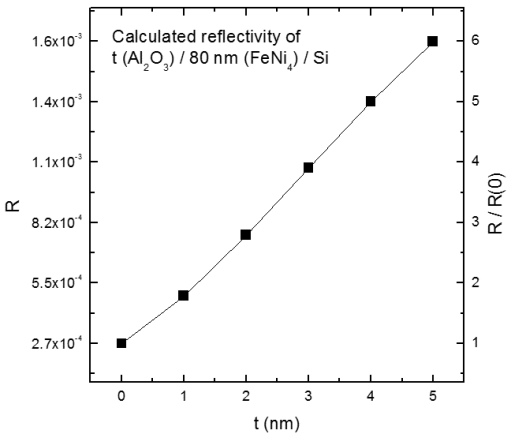

FIG. S1: Calculated reflectivity of 52.8 eV P-polarized radiation at incidence angle of 48° from the normal from an 80 nm thick permalloy film on Si, capped by an Al_2O_3 layer of thickness t. A 1 nm rms roughness is assumed at every interface.

Experimental setup

All the measurements have been carried out at the DiProI beamline [46] of the FERMI free-electron laser (FEL) [47]. The XUV pulses (photon energy of 52.8 eV, 0.1 eV full-width half-maximum bandwidth, linear horizontal polarization, 50 Hz repetition rate) have been transported to the experimental chamber as a collimated beam, in order to properly illuminate the zone plate as the first optical element. Three zone plates (ZPs), etched about 250 nm deep into a 340 nm thick silicon membrane, were mounted on a translation stage for quick exchange. Two of them were spiral ZP (SZPs), whose characteristic pattern imprints the right phase profile to the beam, in order to impart optical angular momentum (OAM) to the transmitted light [26].

The structures shown in Fig. S2(a)-(b) correspond to SZPs producing OAM beams with $\ell = 1$ and $\ell = -1$ (respectively) in the focus of the first diffraction order. The diameter of both these SZPs is 1900 μm, whereas the width of the smallest zone is 1.64 μm, resulting in a focal length of about 133 mm for the considered photon energy. The third ZP corresponds to a Fresnel ZP, as shown in Fig. S2(c). It has been fabricated with the same geometrical parameters as the SZPs in order to have a reference beam with $\ell = 0$ focusing at the same distance. The higher

diffraction orders of the ZPs were spatially filtered by an order sorting aperture of 500 μm diameter placed 100 mm downstream of the ZPs.

The samples have been mounted on a translation stage in the focal plane of the ZPs, allowing for the measurement of the scattered light in reflection, at an angle of 48° from the surface normal in the horizontal plane. Using a knife-edge scan, we measured a spot size of about 4 μm (full width at half maximum) at the sample plane, resulting in a maximum fluence of 15 mJ/cm^2. The scattered light has been collected at a distance of 150 mm from the sample using a charge-coupled device (CCD) camera equipped with a 27.6 mm square sensor, featuring 2048x2048 pixels. Each image was obtained by accumulating at least 2000 FEL shots.

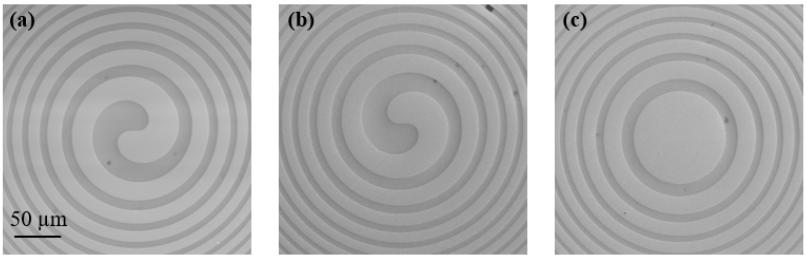

FIG. S2: Scanning electron microscopy images of the zone plates. (a) SZP producing an OAM beam with $\ell = 1$. (b) SZP producing an OAM beam with $\ell = -1$. (c) Fresnel zone plate producing an $\ell = 0$ beam with the same focal length as (a) and (b).

Data acquisition procedure

Experimental data for the two sample $S1$ and $S2$ were acquired with the following procedure:

1. Select the OAM of the beam ($\ell = -1, 0, 1$) by choosing the corresponding ZP.
2. Align the dot in order to center the focused XUV beam at the expected magnetic vortex core position, using encoded translations with 100 nm precision.
3. Acquire CCD image with magnetic field of 20 mT applied in the $-x$ direction [see Fig. S3(a)] during the measurement. The magnetic configuration for the $S1$ dot results in a quasi-uniform, saturated magnetization state.
4. Acquire CCD image at remanence after the previous field has been removed. The magnetic configuration for the $S1$ dot results in a magnetic vortex state, as shown in Fig. 1(d) of the main text.
5. Acquire CCD image with magnetic field of 20 mT applied in the $+x$ direction [see Fig. S3(a)] during the measurement. The magnetic configuration for the $S1$ dot results in a quasi-uniform magnetization state, oriented in the opposite direction with respect to the one described in *step 3* of this list.
6. Acquire CCD image at remanence after the previous field has been removed. The magnetic configuration for the $S1$ dot results in a magnetic vortex curling direction opposite to that of step 4 and of Fig. 1(d) of the main text.
7. Repeat all the previous steps for the other values of OAM.

Since the ZPs were moved only at the end of the procedure, requiring a realignment of the beam on the sample, we consider the experimental MHDm more reliable for comparison with theory than MHDℓ or MHDℓm.

Data analysis

Normalization procedure

We focus on how MHDm images in Fig. 2(a) of the main text and Fig. S7(a) have been obtained (all the other experimental MHD images have been obtained in the same way). The two raw images for Fig. 2(a) corresponding to

step 4 and *step 6* of the data acquisition procedure are shown in Fig. S3(b)-(c), after a dark image has been subtracted in order to remove the CCD background noise. Following the $I_{\ell,m}$ notation, these images are respectively defined as

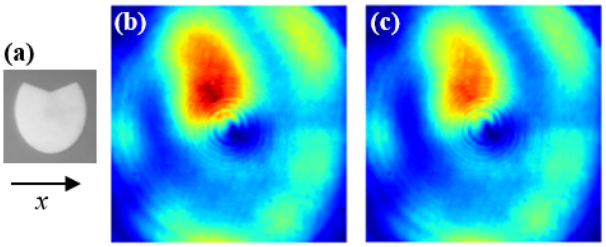

FIG. S3: (a) Scanning electron microscopy image of the $S1$ dot. (b) Raw image corresponding to $I_{-1,1}$. (c) Raw image corresponding to $I_{-1,-1}$. Panels (b) and (c) share the same color scale, and the images have been normalized to the global maximum intensity.

$I_{-1,1}$ and $I_{-1,-1}$, and the MHDm image can be obtained by applying Eq. (1b) of the main text pixel by pixel:

$$\mathrm{MHD}m = \frac{I_{-1,1} - I_{-1,-1}}{I_{-1,1} + I_{-1,-1}}. \tag{S1}$$

We note three remarkable features of these raw images:

1. There is a fairly strong inhomogeneity, which is observed with any incoming OAM and any sample;
2. The peak intensity is different;
3. The overall shape of the pattern is maintained for the two images, acquired within 10 minutes.

Inhomogeneities in the far field image contain contributions from all the elements encountered during the photon transport from source to detector. Fluctuations in the intensity are inherent to the FEL source and an I_0 signal measured upstream of any optical element is recorded shot by shot. Normalizing by this I_0, though, was not sufficient for a precise correction. One reason is that the I_0 is measured for the full delivered beam, which is clipped by the limited acceptance of optical elements (mirrors and SZP) before reaching the sample. Also, we noted that the surface of test samples that had been exposed to the FEL radiation for several hours bear marks of the beam, visible by optical microscopy: a progressive surface contamination may also introduce a decrease of the overall signal in time. To correct for variations in the overall image intensity we define the parameter α that minimizes

$$f(\alpha) = \sum_{\text{pixels}} |I_{-1,1} - \alpha I_{-1,-1}| \tag{S2}$$

In pratice, for all couples of images, we found α to range between 1 and 1.2 approximately. For instance, for the images in Fig. S3, we got $\alpha = 1.11$. We thus modify Eq. (S1) as:

$$\mathrm{MHD}m^* = \frac{I_{-1,1} - \alpha I_{-1,-1}}{I_{-1,1} + \alpha I_{-1,-1}}. \tag{S3}$$

Filtering and signal to noise estimation

With the procedure detailed above, we obtained the images of the first line of Fig. S4 for sample 1. The four panels correspond successively to an incoming beam with $\ell = -1$ (a), $\ell = 0$ (b), $\ell = 1$ (c), $\ell = 1$ with an applied magnetic field (no vortex) (d). Similar images are obtained for S2. While the pixels of the camera form a regular grid, we interpolate the images on a polar basis, yielding the images of the second line. We also integrated the signal between the two blue dashed circles, and computed its angular Fourier transform. The corresponding amplitude of the coefficients are displayed in the last line. The Fourier analysis of the "baseline" image shows coefficients 2 to 3 times smaller than in other panels.

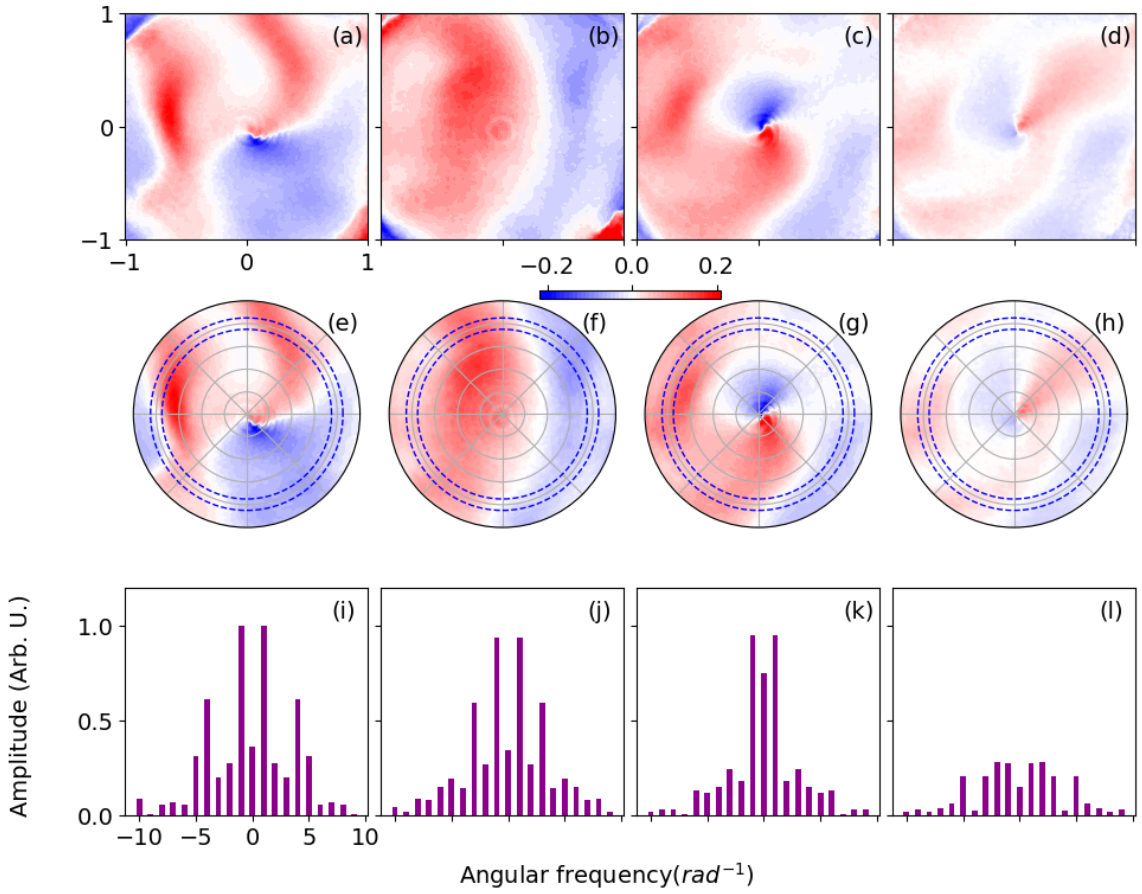

FIG. S4: (a-d) Original MHD images corresponding to $\ell = -1$ (a), $\ell = 0$ (b), $\ell = 1$ (c), $\ell = 1$ with saturated magnetization (d). (e-f) Interpolated images on a polar basis. (i-l) Amplitudes of the Fourier coefficients of the radial sums between the blue circles. The Fourier transform is performed along the azimuth. The images of the two first lines share the same color map.

The same procedure was applied to the theoretical images (Fig. S5). The last column, which is in theory identically zero is not displayed. The x/y scaling is here irrelevant, as the magnification coefficient of the optical system is not considered. We positioned the blue circles for the line-out close to the maximum of the MHDm signal. We observe that only very few angular frequency components are contributing to the signal. All coefficients corresponding to angular frequencies larger than 3 are contributing less than 1% of the main peak.

With this observation, we finally processed the images of Fig. S4 (middle line) in two steps. We first convolved the data radially with a Gaussian filter of width 5 pixels, to remove high radial frequencies. Second, we Fourier transformed the data along the azimuth, applied a Gaussian filter of width σ_G in the Fourier space, and transformed it back to the real domain. The results, for different values of σ_G, are displayed in Fig. S6. The first line correspond to virtually no spectral filtering. It is just the radially convolved version of Fig. S4 (middle line), and share the same patterns. The middle line corresponds to $\sigma_G = 4.5$, a value significantly greater than the last relevant coefficient, allowing to remove many high frequency components.

The bottom line shows that the Ying/Yan pattern is indeed already present with only the three coefficients corresponding to angular frequencies $0, \pm 2\pi$. The data displayed in the main text corresponds to the middle line. A relevant estimate of the signal to noise ratio is thus offered by the ratio of the mean value of the 2π angular frequency components in the vortex and non vortex cases. We find the values displayed in table S1, which are ranging from 1.5 to 8. The highest value is mainly a consequence of a very good baseline for this data set. The mean value, excluding and including the highest one are respectively 2.5 and 3.5, giving an order of magnitude of the signal to noise ratio.

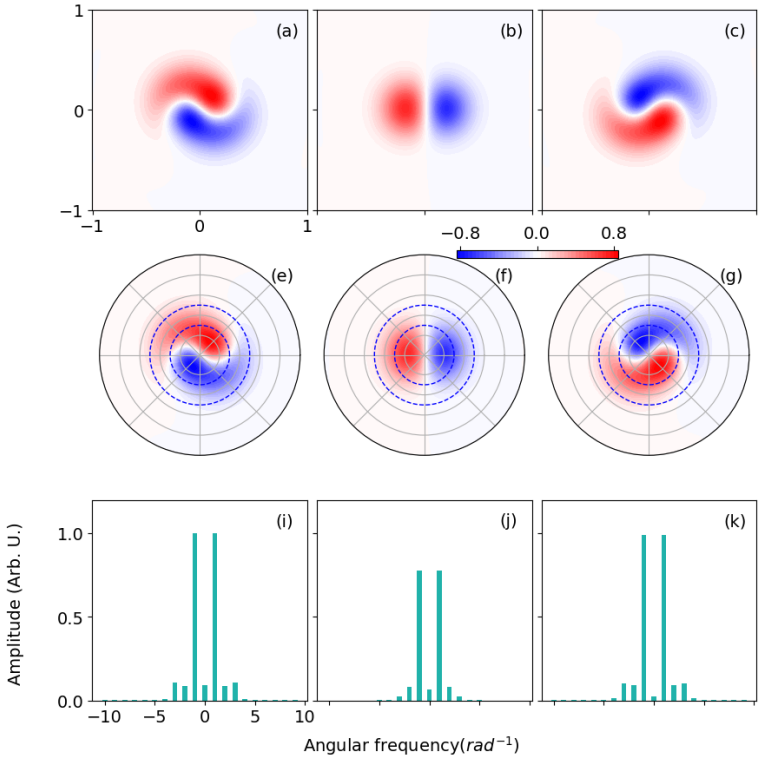

FIG. S5: Same as Fig. S4 for the theoretical data. The fourth column was identically null.

	$\ell = -1$	$\ell = 0$	$\ell = 1$
S1	2.1	1.5	3.1
S2	8.5	4.2	1.8

TABLE S1: Ratio of the 1st angular frequency Fourier coefficient of the signal to baseline image.

Saturated magnetization

Data in Fig. S7 refer to MHDm measurements performed in presence of a nominal field of 20 mT, that should be sufficient to erase the vortex structure. In this case, no MHD is expected, another crucial difference between MHD and MCD. In fact a homogeneous magnetic structure has an azimuthal decomposition coefficient $n = 0$ [36], which does not change the orbital composition of the reflected light, leading to no MHD signal. The measured MHDm does not vanish completely, but is strongly reduced ($\lesssim 5\%$) and most importantly no clear symmetry is observed. The remaining signal can be attributed to incomplete saturation at the applied field and to possible instabilities in the relative position between beam and sample, and also sets the sensitivity limit of our measurements under present experimental conditions.

Estimate of misalignment effects

Ideally, Fig. 2(c-d) of the main text should have a well-defined centered vertical symmetry axis, as it occurs in the simulations [Fig. 2(i-j)]. Here we show that the imperfect symmetry of the experimental images stems mainly from an imperfect centering of the OAM beam on the magnetic vortex core. Indeed, as it is shown in the left panel of Fig. S8, *in vacuum* positioning, as well as possible slight drifts of the beam with respect to the sample during data accumulation, reproduce the observed asymmetry. This is something that is extremely difficult to control in the experiment, since the vortex core position within the sample could not be observed *in situ* and it may even vary slightly after each magnetic pulse.

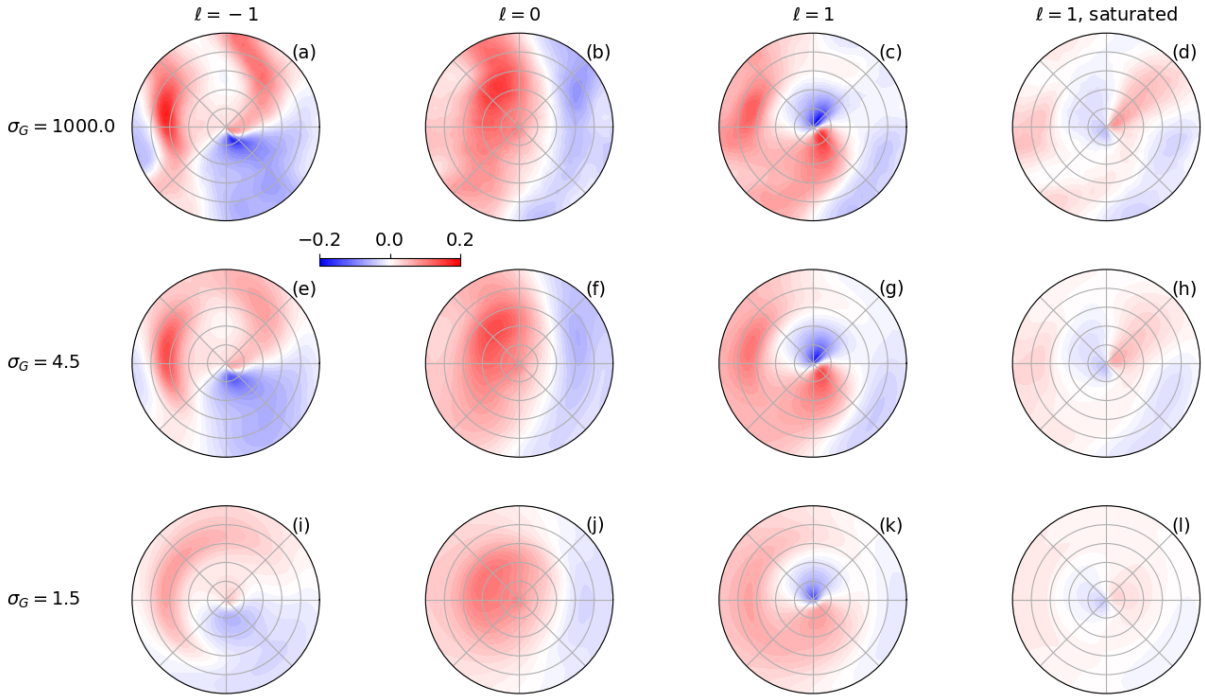

FIG. S6: (a-d) Equivalent of Figs. S4 (e-h) once the Gaussian radial filter is applied, without spectral filtering along the azimuth. (e-h) Same but applying a spectral filter in the Fourier domain, of width $\sigma_G = 4.5$, and (i-l) $\sigma_G = 1.5$. Columns: same as Fig.S4. All images share the same color map.

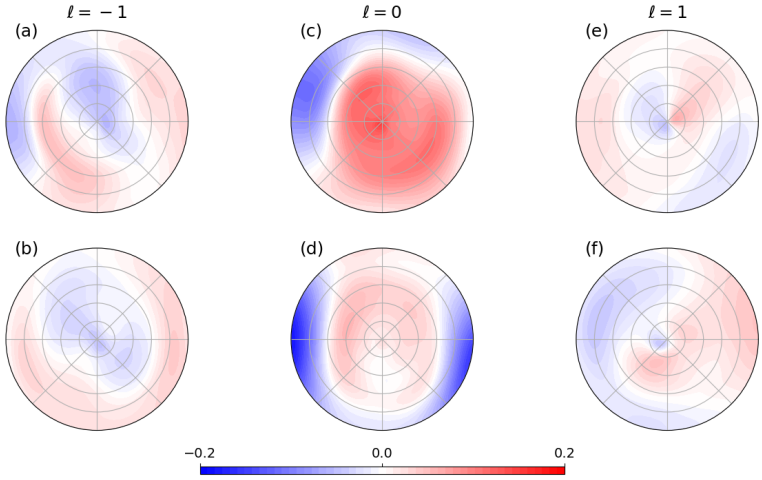

FIG. S7: Experimental MHDm for $\ell = -1, 0, 1$ when a magnetic field of 20 mT is kept applied in the plane of the sample during the measurements. First line: sample #1, second line: sample #2

In the experiment, panels (c) and (d) of Fig. 2 refer to MHDm images obtained for two π-rotated samples that were vertically offset one with respect to the other on the same substrate (see Section *"Data acquisition procedure"*). The right panel of Fig. S8 shows the effect of introducing in the calculations a slight misalignment between the vortex core and the photon beam. We observe that the same displacement has opposite effects on the asymmetry in the MHDm images of the two samples, providing a likely explanation for the experimental observation of Fig. 2(c-d).

Measuring MHDm on a given sample requires only reversing the magnetic field, which does not alter the photon/sample alignment. On the contrary, in the existing setup, measuring MHDℓ and MHDℓm implies taking the

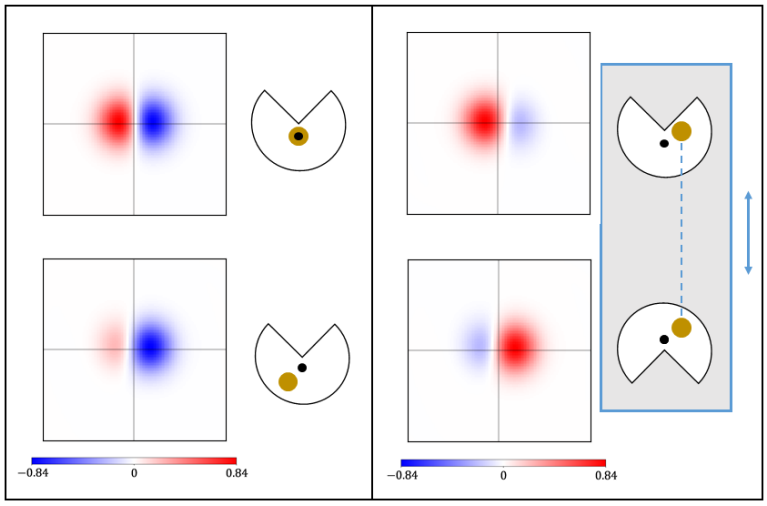

FIG. S8: Effect of photon/sample misalignment on MHDm measurements. (left) Two MHDm images are calculated according to the parameters and procedures described in the main text, assuming either perfect coincidence (top) or slight misalignment (bottom) between the photon beam (yellow dot) and vortex core (black dot) centers. A perfectly symmetric image is obtained in the former case (same as Fig. 2(i-j) of the main text), while a marked asymmetry characterizes the latter. (right) Same calculations, for two π-rotated samples with the same displacement between photon beam and vortex core centers. The introduced misalignment has opposite effects on the asymmetry in the MHDm images of the two π-rotated samples.

difference of two images obtained using different SZPs: this can introduce variations in the angle and position of the photon beam at the sample surface that cannot be perfectly corrected. Therefore, the problematic and delicate photon/sample alignment mentioned above is considerably amplified for MHDℓ and MHDℓm measurements with respect to MHDm. For these reasons, in this work that represents a first experimental approach to helicoidal dichroism we limited ourselves to the investigation of MHDm. We should note that this high sensitivity could turn into an efficient mean to spot the center of a magnetic structure in further experiments and applications.

NUMERICAL SIMULATIONS

MHDm at $\theta = 5^\circ$

Fig. S9 shows MHDm at near normal incidence, to be compared with Fig. 2(g)-(l) of the main text. The difference between the cases $\ell = 0$ and $\ell = \pm 1$ is evident, but the spiral shape of Fig. 2 of the main text is not present, because of the geometrical dependence of MHD [36].

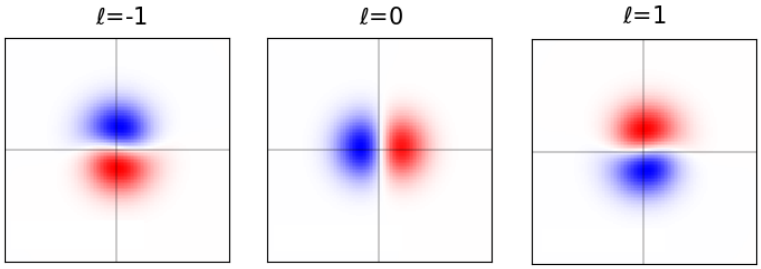

FIG. S9: MHDm calculated for similar conditions as in Fig. 2(g)-(l) of the main text, but for an incidence angle of 5° from the normal. The color scale maximum is 0.65 for $\ell = \pm 1$ and 0.1 for $\ell = 0$.

Far field intensities

The far field intensities of the reflected beam for all four combinations of (ℓ, m) are shown in Fig. S10. Panel (b) corresponds to Fig. 4(c) of the main text.

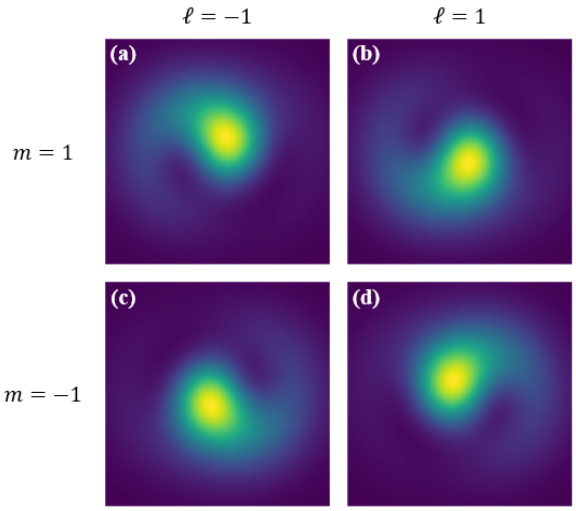

FIG. S10: (a)-(d) Far field intensity of vortex beam (P polarized, photon energy of 52.8 eV, incidence angle of 48° from the normal, as in the main text) reflected by a magnetic vortex for all the four combinations of $\ell = \pm 1$ nd $m = \pm 1$.

Tables of dichroisms

Given all the possible configurations of light polarization [circular right (CR) and left (CL), linear P (LP) and S (LS)], OAM ($\ell = \pm 1$) and the curling direction of the MV ($m = \pm 1$), it is possible to look at magnetic dichroic signals in many different ways. In Figs. S11-S14, all the combinations obtained by simulations are reported for completeness. Calculations are done for a photon energy of 52.8 eV and an incidence angle of 48° from the normal, as in the main text. In order to highlight the symmetries, raw differences without normalization to the sum are shown. Therefore the range of the colorscale, indicated by the parameter a for every panel, is in arbitrary units at the outcome of the simulations. The dichroisms are evaluated as follows:

- MBD is $m = 1$ minus $m = -1$ at fixed ℓ and polarization
- MHD is $\ell = 1$ minus $\ell = -1$ at fixed m and polarization
- MLD is LP minus LS at fixed ℓ and m
- MCD is CR minus CL at fixed ℓ and m

The naming highlights what causes the magnetic dichroism: magnetic B field dichroism (MBD), magnetic helicoidal dichroism (MHD), magnetic linear dichroism (MLD) or magnetic circular dichroism (MCD). Note that MHD and MBD correspond to MHDℓ and MHDm as defined in the main text. It is important to stress once more the difference between MHD and MCD: changing the light polarization (MCD) is equivalent to changing the applied field (MBD), while this is not the case with changing the OAM (MHD).

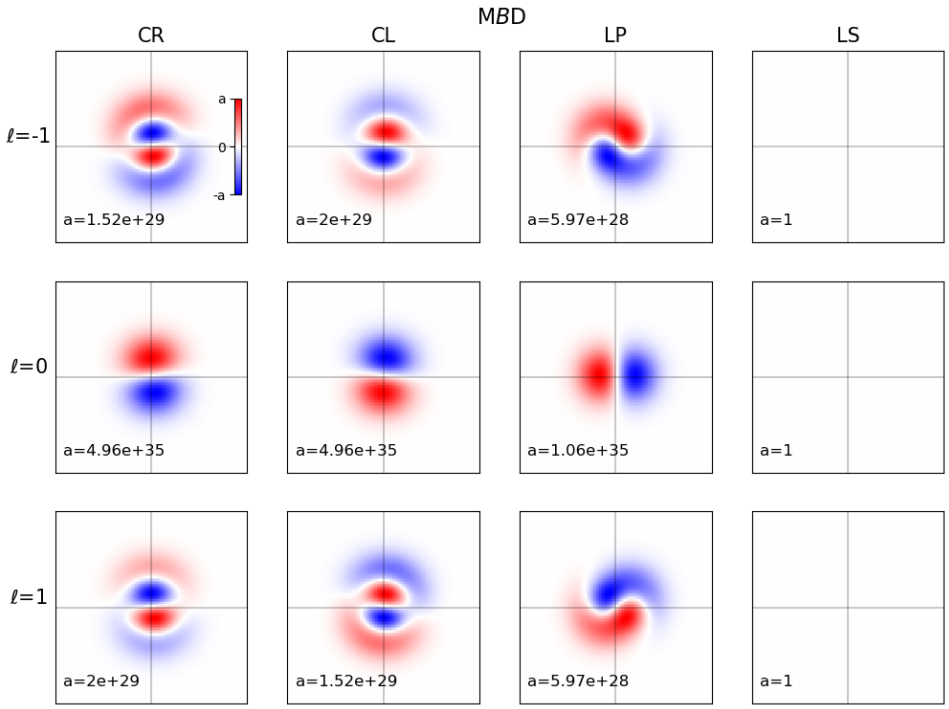

FIG. S11: Magnetic B field dichroism, obtained changing the B field (i.e. the curling direction of the MV m: MHDm) at fixed light polarization and OAM.

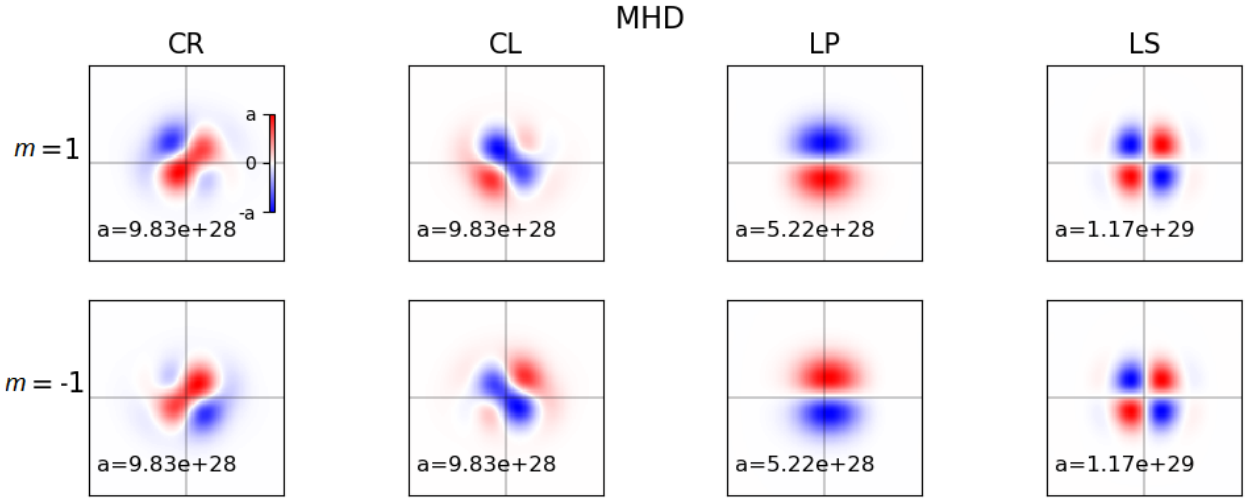

FIG. S12: Magnetic helicoidal dichroism (MHDℓ), obtained changing the OAM of light at fixed polarization and the curling direction of the MV.

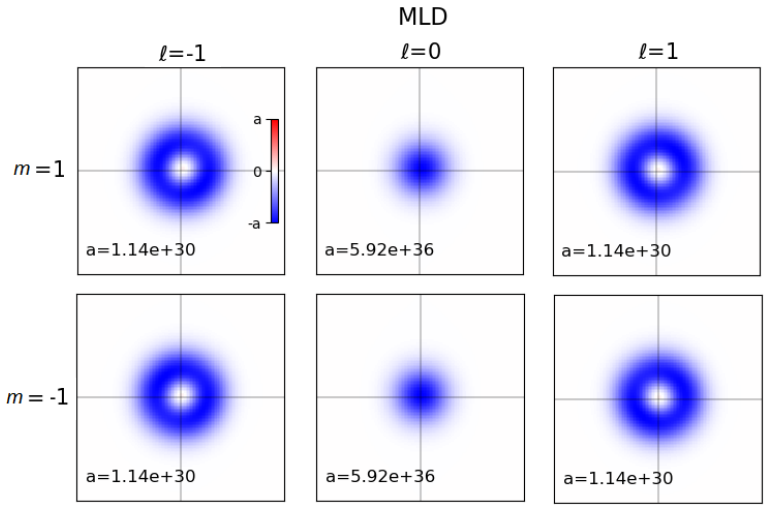

FIG. S13: Magnetic linear dichroism, obtained changing the linear polarization at fixed light OAM and the curling direction of the MV.

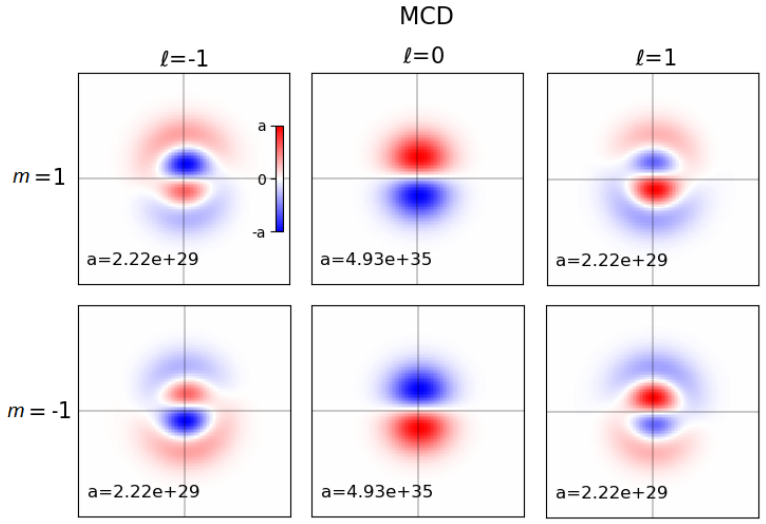

FIG. S14: Magnetic circular dichroism, obtained changing the circular polarization at fixed light OAM and the curling direction of the MV.

[2] K. Y. Bliokh and F. Nori. Transverse and longitudinal angular momenta of light. Physics Reports, 592:1–38, aug 2015.

[26] P. Rebernik Ribič, B. Rösner, D. Gauthier, E. Allaria, F. Döring, L. Foglia, L. Giannessi, N. Mahne, M. Manfredda, C. Masciovecchio, R. Mincigrucci, N. Mirian, E. Principi, E. Roussel, A. Simoncig, S. Spampinati, C. David, and G. De Ninno. Extreme-Ultraviolet Vortices from a Free-Electron Laser. Physical Review X, 7(3):031036, aug 2017.

[36] M. Fanciulli, D. Bresteau, M. Vimal, M. Luttmann, M. Sacchi, and T. Ruchon. Electromagnetic theory of helicoidal dichroism in reflection from magnetic structures. Phys. Rev. A, 103(1):13501, jan 2021.

[46] F. Capotondi, E. Pedersoli, N. Mahne, R. H. Menk, G. Passos, L. Raimondi, C. Svetina, G. Sandrin, M. Zangrando, M. Kiskinova, S. Bajt, M. Barthelmess, H. Fleckenstein, H. N. Chapman, J. Schulz, J. Bach, R. Frömter, S. Schleitzer, L. Müller, C. Gutt, and G. Grübel. Invited Article: Coherent imaging using seeded free-electron laser pulses with variable polarization: First results and research opportunities. Review of Scientific Instruments, 84(5):51301, 2013.

[47] E. Allaria, R. Appio, L. Badano, W. A. Barletta, S. Bassanese, S. G. Biedron, A. Borga, E. Busetto, D. Castronovo, P. Cinquegrana, S. Cleva, D. Cocco, M. Cornacchia, P. Craievich, I. Cudin, G. D'Auria, M. Dal Forno, M. B. Danailov, R. De Monte, G. De Ninno, P. Delgiusto, A. Demidovich, S. Di Mitri, B. Diviacco, A. Fabris, R. Fabris, W. Fawley, M. Ferianis, E. Ferrari, S. Ferry, L. Froehlich, P. Furlan, G. Gaio, F. Gelmetti, L. Giannessi, M. Giannini, R. Gobessi, R. Ivanov, E. Karantzoulis, M. Lonza, A. Lutman, B. Mahieu, M. Milloch, S. V. Milton, M. Musardo, I. Nikolov, S. Noe, F. Parmigiani, G. Penco, M. Petronio, L. Pivetta, M. Predonzani, F. Rossi, L. Rumiz, A. Salom, C. Scafuri, C. Serpico, P. Sigalotti, S. Spampinati, C. Spezzani, M. Svandrlik, C. Svetina, S. Tazzari, M. Trovo, R. Umer, A. Vascotto, M. Veronese, R. Visintini, M. Zaccaria, D. Zangrando, and M. Zangrando. Highly coherent and stable pulses from the FERMI seeded free-electron laser in the extreme ultraviolet. Nature Photonics, 6(10):699–704, 2012.

CHAPTER 15

Conclusion and Perspectives

The field of magneto-optics with OAM is relatively new, with only a few existing theoretical predictions and proof-of-principle experiments. The advent of new radiation facilities has considerably widened the capabilities of magneto-optics studies to study magnetic structures, e.g., Magneto Optical Kerr Effect (MOKE), Faraday and circular dichroism effects into the x-ray range [126]. The work presented in the above chapters broadened these capabilities even further by using x-ray beams carrying OAM to probe magnetic structures with non-uniform in-plane magnetization. A preliminary understanding of the interaction of OAM beams with magnetic vortices has been established with these theoretical and experimental works. The theoretical model predicted that an OAM beam with topological value ℓ is modified into $\ell + n$ upon scattering from a magnetic vortex, with n being the index of the azimuthal Fourier decomposition of the magnetic topology. Three types of MHD were identified as a result of this phenomenon and was experimentally observed for the first time. The future objective is to attain an exhaustive description and a more general understanding of MHD. It is highly promising from both applied and fundamental perspectives. It carries the prospect of designing new magneto-optical devices, sensitive to the OAM of light, as well as easing the creation and/or diagnostics of beams with OAM. Endless applications can be envisioned, from data encoding and processing to spectroscopy and magnetization control. It is also a testing ground for fundamental properties of structured light beams that may now be shaped within an optical cycle. These capabilities requires the introduction of such notions as helicity, transverse angular momenta, spin-orbit coupling of light fields or superchiral fields. The interaction of such structured light beams with magnetic structures, due to their variety, could become a natural and precise test of these new fundamental concepts and advantageously serve the development of structured light spectroscopy.

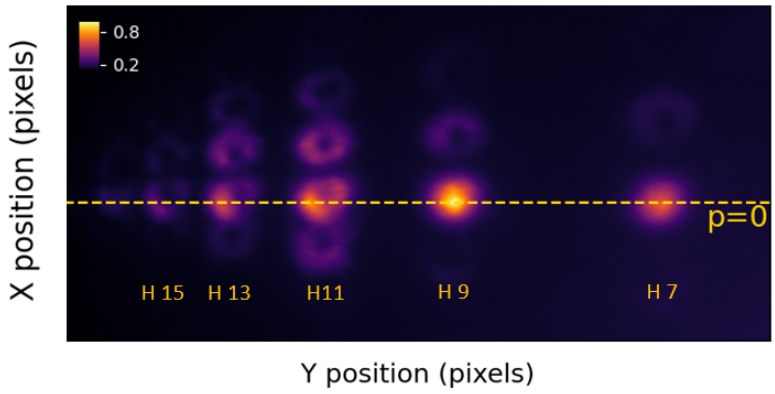

Figure 15.1: Far-field image when harmonics are generated with a Gaussian, perturbed by a Laguerre Gaussian beam with OAM $\ell = 1$.

It is exactly for this reason that the FAB-1-Bis beamline was built to be adapted for generating harmonics with different spatial profiles, in particular the Laguerre Gauss (LG) mode. We can generate harmonics by shaping one or both the beams and study NCHHG with shaped beams. The generation of such beams has already been extensively studied in the two preceding theses from our group [55, 108]. During the course of this thesis, we were able to test the same in the new experimental set-up.

For generating harmonics with orbital angular momentum (OAM), the simplest method is to insert a spiral phase plate (SPP) in the path of the driving laser [55]. Following this method, we could successfully generate the harmonic spectrum with OAM. The OAM of the harmonic order q is then given by the quantum number $\ell_q = q\ell$, where ℓ is the OAM of the driving field [26]. However, this imparts very high values of topological charge to the harmonic beam. A good way to control the OAM that is imparted to the harmonic is the use of two driving fields having topological charges ℓ_1 and ℓ_2. As we have already seen in section 4.3, the OAM of the harmonic order q and diffraction order p is then given by the quantum number $\ell_q = (q-p)\ell_1 + p\ell_2$, following the conservation law. The non collinear geometry is essential for spatially separating the diffraction orders having different OAM values.

It is important to have a comprehensive understanding of the far-field diffraction pattern due to the active grating and the harmonic emission properties in the case of NCHHG with shaped beams first, before proceeding to MHD experiments. Fig. 15.1 shows the far-field image of the harmonics obtained when a Gaussian beam is perturbed by a LG beam in non collinear geometry. The LG spatial profile has been passed on to all the harmonics and their diffraction orders as well, thus effectively transferring the orbital angular momentum of the beam ($\ell_1 = 0, \ell_2 = 1$ in this case). However the characterisation of these harmonics and the discussion of these experimental results are beyond the scope of this thesis and will be discussed elsewhere. In the near future, this beamline will be the source of OAM beams for MHD experiments.

Part VI

Conclusions

CHAPTER 16

Conclusions and Outlook

In this thesis we have presented a detailed investigation of high harmonic generation with two beams in non collinear geometry (NCHHG). The work was divided into three main parts, study of NCHHG and the harmonic emission yields through experiments and analytical modelling, the study of phase matching effects in NCHHG and finally, its application using NCHHG as an XUV source carrying OAM to study magnetic helicoidal dichroism.

Prior to this thesis, NCHHG has been gaining increasing attention, mainly for its applications. It was fast becoming the preferred technique for generating structured XUV light, isolated attosecond pulses etc. However the fundamental properties of the emitted harmonics and the far field properties have been the subject of very few studies. It was explained using an intuitive photon model in the works of Bertrand et al. [42], Heyl et al. [83], Ellis et al.[43] and Li et al. [82]. Ever since we realized the potential of harmonic generation in non collinear geometry as a technique for generating XUV light carrying OAM and SAM, detailed investigations on NCHHG have been going on in ATTOLab [55, 108]. And the work of Chappuis et al. [86] established a field based analytical model to explain the far field properties of NCHHG. More recently, with the idea of having a dedicated beamline delivering OAM pulses to study magnetic materials using techniques like MHD and MOKE, it became ever more important to understood the physics behind NCHHG. Thus it became the objective of this thesis to build a beamline in ATTOLab based on NCHHG and gain insights into the fundamental properties of the emitted harmonics.

NCHHG in the approximation of perfect phase matching

In this part, we discussed in detail High Harmonic Generation with two beams in Non-Collinear geometry (NCHHG), the experimental work, the analytical model developed, and finally the results obtained from experimental and theoretical calculations. The main focus was on predicting the amplitude distribution of the harmonic emission yield, which was described with a simple power scaling law up to now and was constrained to a perturbative regime [42, 82]. Due to the limiting nature of these results, and to go beyond the perturbative regime, we proceeded to develop a theoretical model to obtain a comprehensive understanding of NCHHG. Ignoring phase matching effects, and with a simple analytical "active grating" model developed by us, we were able to predict the emission yield in NCHHG. We obtained a general scaling law to predict the yield distribution from a perturbative to intermediate regime, and to the non perturbative regime.

In doing so, we realized that NCHHG could potentially be a technique to selectively generate certain diffraction orders as per the experimental requirements. The field based model for the perturbative to the intermediate regime perfectly complements the photon picture. In addition, we could also throw light on the competition between different photon-processes that lead to the same diffraction order, which was never commented upon before. More interestingly, we find applications in spectroscopy with this new model. We observed that the photonic processes leading to a diffraction order may be interpreted as a series of absorption and stimulated emission of a couple of photons essentially π out of phase with the preceding process. The interference of these different channels is a promising access point to the phases of multiphoton transition elements in strong field processes.

In the non perturbative regime, we could establish that considering a network of emission pockets driven by an equivalent plane wave, one can capture the essential features of NCHHG . Our model predicts the yield distribution of the diffraction orders and there is excellent agreement between theory and experiments. It even gives access to the important atomic parameters ruling HHG, such as the effective order of non linearity, or the atomic dipole phase.

Phase matching effects in NCHHG

The "active grating" model and the analysis presented in part III, was a simplified model approximating the harmonic generation under conditions of perfect phase matching. However, phase matching effects are very relevant in any study of HHG. Existing studies on phase matching in NCHHG are limited to the identification of a non collinear phase mismatch factor [83] and studies on phase matching effects in harmonic generation above critical ionization [79]. To complete our analytical frame work, we developed a two dimensional theoretical model including phase matching effects, to explain the emission yields in NCHHG. The model was developed by drawing on concepts from xray diffraction in crystals which was surprisingly very efficient.

With this new 2D theoretical model, we could successfully identify the microscopic and macroscopic effects in NCHHG emission yields independently. We came to the conclusion that the microscopic response remains unaltered with the non collinear geometry. When considering the macro-

scopic response of the medium, we discovered two additional terms giving insight into phase matching effects along the longitudinal and transverse directions. The longitudinal phase matching term is almost the well known formula of Constant et al. [10] obtained from the 1D model that has been used as the standard approach in describing phase matching effects in HHG in absorbing gases up to now [10, 104, 110]. The only small difference is that the medium, coherence and absorption lengths considered, should be calculated along the bisector of the two driving beams. The transverse phase matching term helped us to gain new perspective of the process and identify factors that play a role in phase matching that has been hitherto unknown. We could also retrieve the geometrical non collinear phase mismatch term identified by Heyl et.al [83] that is implicit in the longitudinal phase matching term.

With this new 2D model we could explain features in the amplitude distribution of the harmonic emission yield. With the results of our numerical simulations and experiment, we could identify two of these features. *Wiggles* with a high periodicity which match the transverse phase matching factor effect, and a *revival* that could be modelled by a refinement of the purely linearly blazed grating. The two effects are purely geometrical, not dependent on gas pressure or the generating gas. These two effects, nicely reproduced, validate our model that can now be used in any NCHHG experiment.

Magnetic helicoidal dichroism

The main objective of studying NCHHG in detail was to harness its potential as a source of XUV OAM beams to study light-matter interaction. As a first application, we presented the case of magnetic helicoidal dichroism [32]. It is a dichroism in the intensity pattern of beams carrying orbital angular momentum (l), reflected by a target with a magnetic structure. Firstly, we developed the theoretical model, restricting the detailed analysis to the case of a magnetization distribution of constant amplitude and no radial dependence. We find that as soon as the magnetization is not spatially homogeneous, because of magneto-optic interaction, the reflected beam will populate different OAM modes depending on the decomposition of the magnetic structure on the polar basis set. Consequently, because of interference of the different modes the intensity pattern in the far field changes when changing l, or the sign of the magnetization, or both. We also presented the first experimental proof of MHD [33], carried out at the DiProI end-station of the FERMI free-electron laser. There is a good agreement with theoretical predictions and in particular, we identify the specific dependence of MHD on the sign of the optical (l) and magnetic (m) vortices.

Outlook

The results presented in this thesis set a reference framework for the design of new HHG-based attosecond sources in non collinear geometry. It can become the basis for selecting the experimental parameters to obtain the required source conditions. Even though we do not find that the use of two beams in non collinear geometry improves the efficiency of the generation process, great control over the generated diffraction orders can be achieved by controlling the intensity ratio of the two beams.

This in turn gives control over the selection of the fundamental properties of the harmonic source, the OAM content of the beam for example. The revival in intensity is possibly another helpful tool to selectively extract the diffraction orders. In this way, the phase matching effects in non collinear geometry could be advantageous over collinear schemes.

The excellent agreement between the experimental results and the theoretical model in the non perturbative regime is a good indication that the microscopic response of the medium is similar in both NCHHG and conventional HHG with a single beam. This gives us access to the important parameters in HHG like the effective order of non linearity in the process and the atomic phase.

As already mentioned, our analytical model in the perturbative regime validates the existing photon model. The imprint of the π phase shift on the harmonic yield due to the different photon channels could be experimentally observed through a RABBITT experiment. Such an experiment is envisioned in ATTOLab for the near future. The proof of the proposed selection of photon channels through such an experiment will open up several spectroscopic applications in NCHHG. Another indication of the different photon channels involved is the mismatch observed in the case of specific diffraction orders p=3 and p=4 of H9 in the non perturbative regime. If ongoing theoretical computations by our collaborators at Laboratoire de Chimie Physique-Matière et Rayonnement (LCPMR) are successful, it could pave the way for using NCHHG as a new strong field spectroscopic approach, able to probe usually inaccessible atomic levels. In addition, it is also an approach which avoids the strong alteration of phase matching in the absorbing regions, since the emitted XUV photon is not shifted in energy.

While the studies on NCHHG presented in this thesis were under progress, the fundamental studies on MHD were going on in parallel.The experimental work in FERMI validates the theoretical model developed by our group. This enables us to plan future experiments that could harness its potential applications. MHD opens a new way of looking at the magneto-optical scattering process in terms of OAM, highly promising for studying complex spin textures, for example, in topologically protected magnetic structures. It will also help designing new devices that can be used to either impose or probe the OAM of light beams. Moreover, many applications based on angular momentum transfer can be envisaged, from data encoding and processing to magnetization control, that exploit the unlimited orbital momentum $\ell\hbar$ of an OAM beam (where ℓ can take any positive or negative integer value) compared to the spin value σh of circularly polarized photons (where σ can be only ± 1).

Thus, the FAB-1-Bis beamline of ATTOLab has great potential. It is a robust source of XUV attosecond pulses from NCHHG and is constantly developing. In this thesis we showed how we can generate XUV beams carrying a desired OAM value using the beamline. Today, the beamline is one step ahead in that we can deliver few cycle IR pulses of around 5 fs duration carrying OAM. This is achieved using the post-compression technique where an infrared Laguerre-Gaussian beam of 25 fs pulse duration is coupled into a hollow core fiber filled with Neon gas. In the near future these pulses will be used to drive NCHHG experiments to study light- matter interaction in magnetic materials using the technique of MHD. And as the applications of XUV attosecond pulses carrying OAM and SAM are growing, studies on achieving higher efficiency through the use of different laser parameters and

optimising phase matching conditions are evolving fast [127, 128]. The beamline is already equipped for all such experimental studies which are envisioned for the future.

List of Publications

The following articles were published during the course of this thesis.

I **Electromagnetic Theory of Helicoidal Dichroism in Reflection from Magnetic Structures**
Mauro Fanciulli, David Bresteau, Mekha Vimal, Martin Luttmann, Maurizio Sacchi, and Thierry Ruchon.
Physical Review A 103, 013501 (2021).

II **Observation of Magnetic Helicoidal Dichroism with Extreme Ultraviolet Light Vortices**
Mauro Fanciulli, Matteo Pancaldi, Emanuele Pedersoli, Mekha Vimal, David Bresteau, Martin Luttmann, Dario De Angelis, Primož Rebernik Ribič Benedikt Rösner, Christian David, Carlo Spezzani, Michele Manfredda, Ricardo Sousa ,Ioan-Lucian Prejbeanu, Laurent Vila , Bernard Dieny , Giovanni De Ninno, Flavio Capotondi , Maurizio Sacchi and Thierry Ruchon.
Physical Review Letters 128, 077401 (2022).

Part VII

Appendix

APPENDIX A

Emission direction of harmonics

Emission direction

The electric field for the harmonic emitted at the exit of the medium reads (see section 8.1.4),

$$E_q^{\mathrm{nf}}(x) \propto \left[G\left(\frac{x}{\widetilde{\delta x}}\right) \cdot e^{i q_s \frac{\alpha}{1+\alpha} \cdot \Delta k^{\perp} \cdot x} \right] \otimes \mathrm{Ш}(\frac{x}{a}). \tag{A.1}$$

The far-field, at abscissa z, will be a Fourier transform of the above equation, giving a series of diffraction peaks with a spacing $\frac{1}{a}$. Each peak falls at

$$x'(q,p) = \frac{p \cdot u}{a} = p \cdot \frac{\lambda_q z}{a} \tag{A.2}$$

where u is the coordinate in the Fourier plane and x' is the coordinate in the far field. The emission direction of a diffraction order p of harmonic q is

$$\begin{aligned} \theta_{q,p} = \frac{x'(q,p)}{z} &= p \cdot \frac{\lambda_q}{a} \\ &= p \cdot \frac{\lambda_1 / q}{\lambda_1 / \eta \sin\theta_0} \\ &= \frac{p}{q} \cdot \eta\theta_0. \end{aligned} \tag{A.3}$$

APPENDIX B

Treatment of experimental data in the perturbative regime

The experimental data points in Fig. 7.6 have been processed as follows. For each diffraction order, the signal over a constant sized ROI (Region of Interest) box centered on its peak was integrated to get its total intensity ($I_{q,p}$) after background subtraction. The background was taken in a separate box of equal size, where no harmonics were present. For all orders other than p=0, the values of $I_{q,p}$ and α were offset to ensure that the data goes through the origin. To get the magnitude of the electric field, instead of taking a direct square root we used the formula

$$\tilde{\mathcal{E}}_{q,p} = sign(I_{q,p}(\alpha)).\sqrt{|I_{q,p}(\alpha)|},$$

to deal with a few negative $I_{q,p}$ values that resulted from the offset subtraction.

The values of α can be calculated by evaluating E_2/E_1 where the electric field is calibrated using the method detailed in section 5.4.2. However, the use of irises in the interferometer to attenuate the power, along with the non-collinear geometry does not allow a perfect estimate of the real space overlap and the respective focal spot sizes. Therefore, an accurate estimation of intensity (on target) and the relative field strengths is difficult. To check that our calculation was correct, we performed an additional calibration of α using the experimental data of a chosen harmonic, H11 in our case.From the analytical model described in chapter 8, we assume that the yield of the diffraction orders should have an amplitude distribution that follows equation 8.17. Each order of diffraction p for a harmonic q should peak at a value of α,

$$\alpha_{max} = \frac{p}{q-p}. \tag{B.1}$$

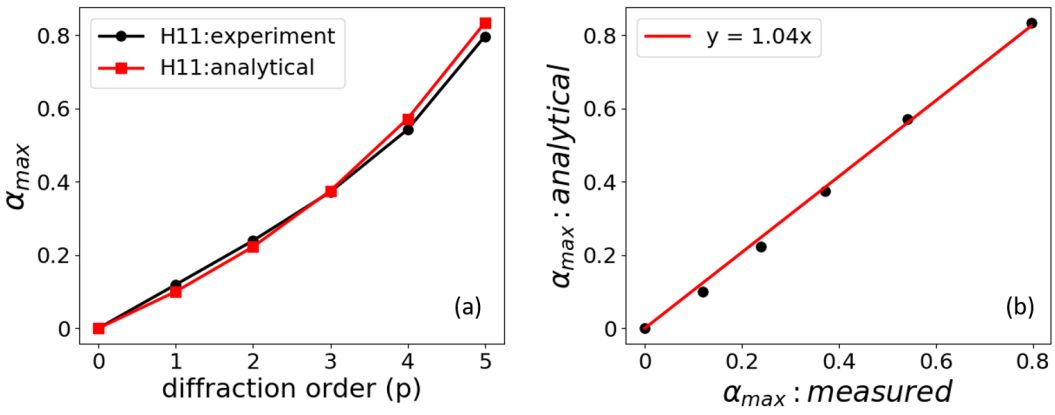

Figure B.1: Calibrating α using the experimental data of H 11.

We plot the analytical predictions of α_{max} against the corresponding experimental values as shown in Fig. B.1.(a). Using a simple linear fit (Fig. B.1.(b)), we calibrate the α values. We find a slope of 1.04, very close to the expected value of 1, thus confirming our first calibration. These calibrated values are used for the data analysis.

APPENDIX C

Scaling the experimental results to theoretical calculation

In theoretical calculations, the total intensity at focus was maintained at $I_0^{th} = 1.5 * 10^{14} W/cm^2$. We define α as:

$$\alpha = \frac{E_2}{E_1} = \sqrt{\frac{I_2}{I_1}} \tag{C.1}$$

The total intensity at any given time is

$$I_0^{th} = I_1 + I_2 = I_1 + \alpha^2 I_1 = (1+\alpha^2) I_1$$

$$\text{therefore, } I_1 = \frac{I_0^{th}}{(1+\alpha^2)} \text{ and}$$

$$I_2 = \alpha^2 \frac{I_0^{th}}{(1+\alpha^2)}$$

The maximum intensity at focus is

$$I_{max}^{th} = I_1 + I_2 + 2\sqrt{I_2 I_1} = \frac{(1+\alpha^2+2\alpha)}{(1+\alpha^2)} I_0^{th} = \frac{(1+\alpha)^2}{1+\alpha^2} I_0^{th}$$

In the case of the experiment, the total intensity is not a constant but I_1 is kept a constant value of I_0^{exp} while I_2 is varied. The maximum intensity at focus is

$$\begin{aligned} I_{max}^{exp} &= I_1 + I_2 + 2\sqrt{I_2 I_1} \\ &= I_0^{exp} + \alpha^2 I_0^{exp} + 2\alpha I_0^{exp} \\ &= (1+\alpha)^2 I_0^{exp} \end{aligned}$$

To compare theoretical and experimental data, we should have the same peak intensities in both situations when scanning α. Here we rather have

$$I_{max}^{th} = N \cdot I_{max}^{exp}$$
$$\text{with } N = \frac{I_0^{th}}{I_0^{exp}(1+\alpha^2)}.$$

Considering an order of non-linearity q_{eff}, we can thus estimate the correction to read $(\frac{I_0^{th}}{I_0^{exp}(1+\alpha^2)})^{q_{\text{eff}}}$. In this case the α values too need a re-calibration. This is because in the fitting, we ignore the α-dependent pre-factor of equation 8.12. Again, we use H11 to calibrate the α.

APPENDIX D

Geometric effects in longitudinal phase matching

The wave vector mismatch components can be written as,

$$\begin{cases} \Delta k^{/\!/} = \eta k_1 \cos\theta - k_1 \simeq (\eta - 1) k_1 - k_1 \theta^2 \\ \Delta k^{\perp} = \eta k_1 \sin\theta \simeq \eta k_1 \theta \end{cases} \tag{D.1}$$

Recall that

$$\vec{a} = \frac{\lambda_1}{2} \begin{pmatrix} \tan\left(\frac{\theta}{2}\right) \\ 1 \end{pmatrix} \quad , \quad \vec{b} = \frac{\lambda_1}{2} \begin{pmatrix} \frac{1}{\eta \sin\theta} \\ 0 \end{pmatrix} \quad , \quad \vec{T}(t) = c \cdot t \cdot \begin{pmatrix} \tan\left(\frac{\theta}{2}\right) \\ 1 \end{pmatrix} \tag{D.2}$$

With the above expressions of the generating vectors, we can write

$$\begin{aligned} \frac{\phi_m}{\pi} &= \left(q_s \frac{\alpha}{1+\alpha} \Delta k^{\perp} - k^{\perp}_{q_s} \right) \cdot \frac{1}{k_1} \frac{\eta k_1 - k_2^{/\!/}}{k_2^{\perp}} + \\ &\quad \left(q_s \left(k_1 + \frac{\alpha}{1+\alpha} \Delta k^{/\!/} \right) - k^{/\!/}_{q_s} \right) \cdot \frac{1}{k_1} \\ &= -\frac{k^{\perp}_{q_s}}{k_1} \cdot \frac{\eta k_1 - k_2^{/\!/}}{k_2^{\perp}} - \frac{k^{/\!/}_{q_s}}{k_1} + q_s + q_s \frac{\alpha}{1+\alpha} \left(\eta - \frac{k_2^{/\!/}}{k_1} + \frac{\Delta k^{/\!/}}{k_1} \right) \\ &= -\frac{k^{\perp}_{q_s}}{k_1} \cdot \frac{\eta k_1 - k_2^{/\!/}}{k_2^{\perp}} - \frac{k^{/\!/}_{q_s}}{k_1} + q_s + q_s \frac{\alpha}{1+\alpha} (\eta - 1) \\ &= -\frac{k^{\perp}_{q_s}}{k_1} \cdot \frac{\eta k_1 - k_2^{/\!/}}{k_2^{\perp}} - \frac{k^{/\!/}_{q_s}}{k_1} + \frac{1 + \alpha\eta}{1+\alpha} \cdot q_s \end{aligned} \tag{D.3}$$

and

$$\begin{aligned}\frac{\phi_{m'}}{\pi} &= \left(q_s \frac{\alpha}{1+\alpha}\Delta k^{\perp} - k^{\perp}_{q_s}\right)\cdot \frac{1}{k_2^{\perp}} \\ &= -\frac{k^{\perp}_{q_s}}{k_2^{\perp}} + \frac{\alpha}{1+\alpha}\cdot q_s\end{aligned} \tag{D.4}$$

Using the two Laue equations, and the definition of q_s, as $|k_{q_s}| = q_s|k_s|$,

$$\begin{cases} \widetilde{\phi_m} = \dfrac{\phi_m}{\pi} = h = -\dfrac{k^{\perp}_{q_s}}{k_1}\cdot\dfrac{\eta k_1 - k_2^{/\!/}}{k_2^{\perp}} - \dfrac{k^{/\!/}_{q_s}}{k_1} + \dfrac{1+\eta\alpha}{1+\alpha}\cdot q_s \\ \widetilde{\phi_{m'}} = \dfrac{\phi_m}{\pi} = j = -\dfrac{k^{\perp}_{q_s}}{k_2^{\perp}} + \dfrac{\alpha}{1+\alpha}\cdot q_s \end{cases} \tag{D.5}$$

For $\eta = 1$, ϕ_m simplifies to

$$\phi_m = (\frac{p\theta_0^2}{2q} + \delta\phi_m)\pi = h\pi. \tag{D.6}$$

where $\delta\phi_m = 0$ for the case of perfect phase matching. And $\phi_{m'}$ simplifies to

$$\phi_{m'} = -(p - \frac{\alpha}{1+\alpha}\cdot q_s + \delta\phi_{m'})\pi = j\pi, \tag{D.7}$$

where $\delta\phi_{m'} \ll \frac{\alpha}{1+\alpha}\cdot q_s$ and to

$$\phi_{m'} = -(p - \frac{\alpha}{1+\alpha}\cdot q_s)\pi = j\pi \tag{D.8}$$

for the case of perfect phase matching. For the reduced phases we get

$$\begin{cases} \widetilde{\phi_m} = \dfrac{\phi_m}{\pi} = -\dfrac{k^{\perp}_{q_s}}{k_1}\cdot\tan\left(\dfrac{\theta}{2}\right) - \dfrac{k^{/\!/}_{q_s}}{k_1} + \dfrac{1+\eta\alpha}{1+\alpha}q_s \\ \widetilde{\phi_{m'}} = \dfrac{\phi_{m'}}{\pi} = -\dfrac{k^{\perp}_{q_s}}{\eta k_1 \sin\theta} + \dfrac{\alpha}{1+\alpha}\cdot q_s \end{cases} \tag{D.9}$$

APPENDIX E

Modelling the microscopic response propagated to the far field, $\widetilde{G}\left(\Delta\vec{k}_q\right)$

The microscopic response has a Gaussian term (see equation 11.9),

$$\begin{aligned} g(x,z) &= e^{-\left(\frac{\Delta\vec{k}\cdot\vec{r}}{\widetilde{\varphi}_G}\right)^2} \\ &= e^{-\left(\frac{\Delta k^{\parallel}\cdot z+\Delta k^{\perp}\cdot x}{\widetilde{\varphi}_G}\right)^2} \\ &= e^{-\left(\frac{\Delta\Delta\vec{k}|}{\widetilde{\varphi}_G}\cdot\left[\frac{\Delta k^{\parallel}}{|\Delta\vec{k}|}\cdot z+\frac{\Delta k^{\perp}}{|\Delta\vec{k}|}\cdot x\right]\right)^2} \\ &= e^{-\left(\frac{\Delta\Delta\vec{k}|}{\widetilde{\varphi}_G}\cdot[\sin\gamma\cdot z+\cos\gamma\cdot x]\right)^2} \end{aligned} \tag{E.1}$$

where we have set γ the angle such that

$$\begin{aligned} \sin\gamma &= \frac{\Delta k^{\parallel}}{|\Delta\vec{k}|} \\ \cos\gamma &= \frac{\Delta k^{\perp}}{|\Delta\vec{k}|} \end{aligned}$$

We can denote R_γ the rotation matrix by an angle γ, and $(x',z') = R_\gamma\cdot(x,z)$ as a coordinate system. We define a rotation matrix by an angle γ as

$$R_\gamma = \begin{pmatrix} \cos\gamma & -\sin\gamma \\ \sin\gamma & \cos\gamma \end{pmatrix}$$

In this rotated co-ordinate system,

$$g_1(x',z') = e^{-\left(\frac{\Delta\vec{k}|}{\widetilde{\varphi}_G}\cdot x'\right)^2} \tag{E.2}$$

is a regular Gaussian function and its Fourier transform,

$$\widetilde{G_1}\left(\Delta\vec{k}_q\right) = \frac{\widetilde{\varphi}_G}{\sqrt{2}|\Delta\vec{k}|} e^{-\left(\frac{\widetilde{\varphi}_G}{2|\Delta\vec{k}|}\cdot\Delta\vec{k}_q^{\perp}\right)^2} \cdot \sqrt{2\pi}\cdot\delta\left(\Delta\vec{k}_q^{\parallel}\right) \tag{E.3}$$

where δ is the Dirac function. The Fourier transform of a rotated function is given by the original Fourier transform in a reciprocal space rotated by the same amount [see ref.]. Fig. E.1 shows a 2D Gaussian function (a) and its Fourier transform, and in the bottom, 2D Gaussian in a rotated coordinate system (c) and its Fourier transform (d). Using this property,

$$\begin{aligned}
\widetilde{G}\left(\Delta\vec{k}_q\right) &= \widetilde{G_1}\left(R_{-\gamma}\cdot\Delta\vec{k}_q\right) \\
&= \frac{\widetilde{\varphi}_G}{\sqrt{2}|\Delta\vec{k}|} e^{-\left(\frac{\widetilde{\varphi}_G}{2|\Delta\vec{k}|}\cdot\left(\cos\gamma\Delta k_q^{\perp}+\sin\gamma\Delta k_q^{\parallel}\right)\right)^2} \cdot \sqrt{2\pi}\cdot\delta\left(-\sin\gamma\Delta k_q^{\perp}+\cos\gamma\Delta k_q^{\parallel}\right) \\
&= \frac{\sqrt{\pi}\widetilde{\varphi}_G}{|\Delta\vec{k}|} e^{-\left(\frac{\widetilde{\varphi}_G}{2||\Delta\vec{k}|}\cdot\left(\cos\gamma\Delta k_q^{\perp}+\sin\gamma\Delta k_q^{\parallel}\right)\right)^2} \cdot\delta\left(-\sin\gamma\Delta k_q^{\perp}+\cos\gamma\Delta k_q^{\parallel}\right)
\end{aligned} \tag{E.4}$$

Using the δ function we can further set,

$$\widetilde{G}\left(\Delta\vec{k}_q\right) = \frac{\sqrt{\pi}\widetilde{\varphi}_G}{|\Delta\vec{k}|} e^{-\left(\frac{\widetilde{\varphi}_G}{2\Delta k^{\perp}}\cdot\Delta k_q^{\perp}\right)^2} \cdot\delta\left(-\Delta k^{\parallel}\cdot\Delta k_q^{\perp}+\Delta k^{\perp}\cdot\Delta k_q^{\parallel}\right) \tag{E.5}$$

In this way, we get the Fourier transform of equation 11.9 to be

$$\begin{aligned}
\widetilde{G}\left(\Delta\vec{k}_q\right) &= E_1^{q_{\text{eff}}}(1+\alpha)^{q_{\text{eff}}}\cdot\frac{\sqrt{\pi}\widetilde{\varphi}_G}{|\Delta\vec{k}|} e^{-\Delta k_q^{\perp 2}\cdot\left(\frac{\widetilde{\varphi}_G}{2\Delta k^{\perp}}\right)^2} \\
&= \underbrace{\sqrt{\pi}E_1^{q_{\text{eff}}}\cdot\frac{(1+\alpha)^{q_{\text{eff}}}\widetilde{\varphi}_G}{|\Delta\vec{k}|}}_{amplitude}\cdot\underbrace{e^{-\frac{\widetilde{\varphi}_G^2}{4}\cdot\left(\frac{\Delta k_q^{\perp}}{\Delta k^{\perp}}\right)^2}}_{exponent}
\end{aligned} \tag{E.6}$$

Let us the try to simplify the leading amplitude term and the exponential term in the above equation to get the formula for the final yield.

Amplitude

The real part of $\widetilde{\varphi}_G^2$ reads

$$\begin{aligned}
\mathscr{R}(\widetilde{\varphi}_G^2) &= \mathscr{R}\left(\frac{1}{\frac{q_{\text{eff}}}{2}\cdot\frac{\alpha}{(1+\alpha)^2}-i\alpha_{at}\cdot\alpha\cdot I_0}\right) \\
&= \mathscr{R}\left(\frac{\frac{q_{\text{eff}}}{2}\cdot\frac{\alpha}{(1+\alpha)^2}+i\alpha_{at}\cdot\alpha\cdot I_0}{q_{\text{eff}}^2\cdot\frac{\alpha^2}{4(1+\alpha)^4}+\alpha_{at}^2\cdot\alpha^2\cdot I_0^2}\right) \\
&= \frac{q_{\text{eff}}}{2\alpha}\cdot\frac{1}{\frac{q_{\text{eff}}^2}{4(1+\alpha)^2}+\alpha_{at}^2\cdot I_0^2\cdot(1+\alpha)^2}.
\end{aligned} \tag{E.7}$$

and the imaginary part

$$\mathscr{I}(\widetilde{\varphi}_G^2) = \frac{\alpha_{at}\cdot I_0}{\alpha}\cdot\frac{1}{\frac{q_{\text{eff}}^2}{4(1+\alpha)^4}+\alpha_{at}^2\cdot I_0^2}. \tag{E.8}$$

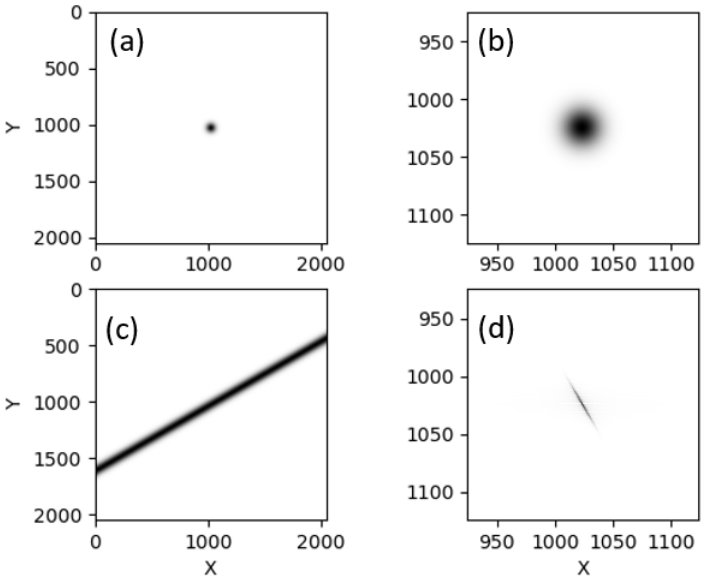

Figure E.1: A 2D Gaussian function (a) and its Fourier transform (b). The Gaussian in a rotated coordinate system (c) and its Fourier transform (d).

giving,

$$[\widetilde{\varphi}_G^2] = \sqrt{\mathscr{R}(\widetilde{\varphi}_G^2)^2 + \mathscr{I}(\widetilde{\varphi}_G^2)^2} \tag{E.9}$$

$$= \frac{1}{\alpha} \cdot \frac{1}{\sqrt{\frac{q_{\text{eff}}^2}{4(1+\alpha)^4} + \alpha_{at}^2 \cdot I_0^2}} \tag{E.10}$$

The α dependent terms in the amplitude can now be written as

$$A_q(\alpha) = (1+\alpha)^{q_{\text{eff}}} \cdot \left|\widetilde{\varphi}_G\right| \tag{E.11}$$

$$= \frac{1}{\sqrt{\alpha}} \cdot \frac{(1+\alpha)^{q_{\text{eff}}}}{\left(\frac{q_{\text{eff}}^2}{4(1+\alpha)^4} + \alpha_{at}^2 \cdot I_0^2\right)^{\frac{1}{4}}}. \tag{E.12}$$

Including the angle dependent terms it becomes

$$A_q(\alpha, \theta_0) = \frac{E_1^{q_{\text{eff}}}}{\sqrt{\alpha}} \cdot \frac{(1+\alpha)^{q_{\text{eff}}}}{\left(\frac{q_{\text{eff}}^2}{4(1+\alpha)^4} + \alpha_{at}^2 \cdot I_0^2\right)^{\frac{1}{4}}} \cdot \frac{1}{\eta \theta_o k_1} \tag{E.13}$$

Exponent

The exponent can be written in terms of coherence and absorption length.

$$\begin{aligned}\Delta k_q^{\perp} &= \frac{2}{\lambda_1}\eta \sin\theta_0 \cdot \Delta\vec{k}_{q_s} \cdot \vec{b} \\ &= \frac{2}{\lambda_1}\eta \sin\theta_0 \cdot \phi_{m'}.\end{aligned} \tag{E.14}$$

We also have

$$\Delta k^{\perp} = \frac{2\pi}{\lambda_1}\eta \sin\theta_0. \tag{E.15}$$

which leads to

$$\frac{\Delta k_q^{\perp}}{\Delta k^{\perp}} = \frac{\phi_{m'}}{\pi}. \tag{E.16}$$

Using equation 11.15 and equation 10.13 we get

$$\frac{\Delta k_q^{\perp}}{\Delta k^{\perp}} = \frac{\lambda_1}{2\theta_0} \cdot \left(\frac{1}{L_{coh}^b} + i\frac{1}{\pi L_{abs}^b} \right). \tag{E.17}$$

The exponential term reads

$$e^{-\frac{\mathscr{R}(\tilde{\varphi}_G^2)}{4} \cdot \left(\frac{\Delta k_q^{\perp}}{\Delta k^{\perp}}\right)^2} \cdot e^{-\frac{i\mathscr{I}(\tilde{\varphi}_G^2)}{4} \cdot \left(\frac{\Delta k_q^{\perp}}{\Delta k^{\perp}}\right)^2} \tag{E.18}$$

The final modulus of the microscopic response is

$$\left|\widetilde{G}(\Delta\vec{k}_q)\right| = A_q(\alpha,\theta_0) \cdot exp\left[-\frac{\mathscr{R}(\varphi_G^2)}{4} \frac{\lambda_1^2}{4\theta_0^2} \left\{ \frac{1}{L_{coh}^{b^2}}^2 + \frac{-1}{\pi^2 L_{abs}^{b^2}} \right\} \right] exp\left[\frac{\mathscr{I}(\varphi_G^2)}{4} \frac{\lambda_1^2}{4\theta_0^2} \left(\frac{2}{L_{coh}^b L_{coh}^a} \right) \right].$$

Bibliography

[1] M. Ferray, A. L'Huillier, X. F. Li, G. Mainfray, and C. Manus. Multiple-harmonic conversion of 1064 nm radiation in rare gases. *J. Phys. B*, **21**:L31, 1988. [Cited on pages 17, 25, and 31.]

[2] A. McPherson, G. Gibson, H. Jara, U. Johann, T. S. Luk, I. A. McIntyre, K. Boyer, and C. K. Rhodes. Studies of multiphoton production of vacuum-ultraviolet radiation in the rare gases. *J. Opt. Soc. Am. B*, **4**:595, 1987. [Cited on pages 17 and 25.]

[3] M. Hentschel, R. Kienberger, Ch. Spielmann, G. A. Reider, N. Milosevic, T. Brabec, P. Corkum, U. Heinzmannß, M. Drescher, and F. Krausz. Attosecond metrology. *Nature*, **414**:509, 2001. [Cited on page 17.]

[4] P. M. Paul, E. S. Toma, P. Breger, G. Mullot, F. Augé, Ph. Balcou, H. G. Muller, and P. Agostini. Observation of a Train of Attosecond Pulses from High Harmonic Generation. *Science*, **292**: 1689, 2001. [Cited on page 17.]

[5] Y. Mairesse, A. de Bohan, L. J. Frasinski, H. Merdji, L. C. Dinu, P. Monchicourt, P. Breger, M. Kovačev, R. Taïeb, B. Carré, H. G. Muller, P. Agostini, and P. Salières. Attosecond Synchronization of High-Harmonic Soft X-rays. *Science*, 302(5650):1540–1543, November 2003. doi: 10.1126/science.1090277. [Cited on page 17.]

[6] K. C. Kulander, K. J. Schafer, and J. L. Krause. Dynamics of short-pulse excitation, ionization and harmonic conversion. In Bernard Piraux, Anne L'Huillier, and Kazimierz Rzazewski, editors, *Super-Intense Laser-Atom Physics*, pages 95–110, Boston, MA, 1993. Springer US. ISBN 978-1-4615-7963-2. doi: 10.1007/978-1-4615-7963-2_10. URL https://doi.org/10.1007/978-1-4615-7963-2_10. [Cited on pages 17, 25, and 74.]

[7] M. Lewenstein, Ph. Balcou, M.Yu. Ivanov, A. L'Huillier, and P. B. Corkum. Theory of high-order harmonic generation by low-frequency laser fields. *Phys. Rev. A*, 49:2117, 1994. [Cited on pages 17, 31, 32, and 108.]

[8] P. Salières, A. L'Huillier, and M. Lewenstein. Coherence control of high-order harmonics. *Phys. Rev. Lett.*, 74:3776, 1995. [Cited on pages 17 and 40.]

[9] P. Balcou, P. Salières, A. L'Huillier, and M. Lewenstein. Generalized phase-matching conditions for high harmonics: The role of field-gradient forces. *Phys. Rev. A*, 55(4):3204–3210, April 1997. [Cited on pages 17 and 41.]

[10] E. Constant, D. Garzella, P. Breger, E. Mével, Ch. Dorrer, C. Le Blanc, F. Salin, and P. Agostini. Optimizing High Harmonic Generation in Absorbing Gases: Model and Experiment. *Phys. Rev. Lett.*, 82:1668, 1999. [Cited on pages 17, 39, 115, 116, 118, 121, 122, 136, 138, 142, 148, 162, and 225.]

[11] J.-F. Hergott, M. Kovacev, H. Merdji, C. Hubert, Y. Mairesse, E. Jean, P. Breger, P. Agostini, B. Carré, and P. Salières. Extreme-ultraviolet high-order harmonic pulses in the microjoule range. *Phys. Rev. A*, 66:021801, Aug 2002. doi: 10.1103/PhysRevA.66.021801. URL https://link.aps.org/doi/10.1103/PhysRevA.66.021801. [Cited on pages 18, 59, and 118.]

[12] Eiji Takahashi, Yasuo Nabekawa, and Katsumi Midorikawa. Generation of 10-μj coherent extreme-ultraviolet light by use of high-order harmonics. *Optics letters*, 27(21):1920–1922, 2002. [Cited on pages 18 and 59.]

[13] Tenio Popmintchev, Ming-Chang Chen, Dimitar Popmintchev, Paul Arpin, Susannah Brown, Skirmantas Ališauskas, Giedrius Andriukaitis, Tadas Balčiunas, Oliver D Mücke, Audrius Pugzlys, et al. Bright coherent ultrahigh harmonics in the kev x-ray regime from mid-infrared femtosecond lasers. *science*, 336(6086):1287–1291, 2012. [Cited on page 18.]

[14] G. Sansone, E. Benedetti, F. Calegari, C. Vozzi, L. Avaldi, R. Flammini, L. Poletto, P. Villoresi, C. Altucci, R. Velotta, S. Stagira, S. De Silvestri, and M. Nisoli. Isolated Single-Cycle Attosecond Pulses. *Science*, 314:443–446, 2006. [Cited on page 18.]

[15] I. J. Sola, E. Mével, L. Elouga, E. Constant, V. Strelkov, L. Poletto, P. Villoresi, E. Benedetti, J.-P. Caumes, S. Stagira, C. Vozzi, G. Sansone, and M. Nisoli. Controlling attosecond electron dynamics by phase-stabilized polarization gating. *Nature Phys.*, 2:319, 2006. [Cited on page 18.]

[16] C. Vozzi, F. Calegari, F. Ferrari, M. Lucchini, S. De Silvestri, O. Svelto, G. Sansone, S. Stagira, and M. Nisoli. Advances in laser technology for isolated attosecond pulse generation. *Laser Physics Letters*, 6(4):259–267, apr 2009. doi: 10.1002/lapl.200810140. URL https://doi.org/10.1002/lapl.200810140. [Cited on page 18.]

[17] Francesca Calegari, Giuseppe Sansone, Salvatore Stagira, Caterina Vozzi, and Mauro Nisoli. Advances in attosecond science. *Journal of Physics B: Atomic, Molecular and Optical Physics*, 49 (6):062001, feb 2016. doi: 10.1088/0953-4075/49/6/062001. [Cited on pages 18 and 25.]

[18] Daniel D. Hickstein, Franklin J. Dollar, Patrik Grychtol, Jennifer L. Ellis, Ronny Knut, Carlos Hernández-García, Dmitriy Zusin, Christian Gentry, Justin M. Shaw, Tingting Fan, Kevin M. Dorney, Andreas Becker, Agnieszka Jaroń-Becker, Henry C. Kapteyn, Margaret M. Murnane, and Charles G. Durfee. Non-collinear generation of angularly isolated circularly polarized high harmonics. 9(11):743–750. doi: 10.1038/nphoton.2015.181. [Cited on pages 18, 20, 47, 49, and 52.]

[19] A. Ferré, C. Handschin, M. Dumergue, F. Burgy, A. Comby, D. Descamps, B. Fabre, G. A. Garcia, R. Géneaux, L. Merceron, E. Mével, L. Nahon, S. Petit, B. Pons, D. Staedter, S. Weber, T. Ruchon, V. Blanchet, and Y. Mairesse. A table-top ultrashort light source in the extreme ultraviolet for circular dichroism experiments. *Nature Photonics*, 9:93–98, feb 2015. doi: 10.1038/nphoton.2014.314. [Cited on pages 18 and 47.]

[20] Kevin M. Dorney, Jennifer L. Ellis, Carlos Hernández-García, Daniel D. Hickstein, Christopher A. Mancuso, Nathan Brooks, Tingting Fan, Guangyu Fan, Dmitriy Zusin, Christian Gentry, Patrik Grychtol, Henry C. Kapteyn, and Margaret M. Murnane. Helicity-selective enhancement and polarization control of attosecond high harmonic waveforms driven by bichromatic circularly polarized laser fields. *Physical Review Letters*, 119(6), aug 2017. doi: 10.1103/physrevlett.119.063201. [Cited on pages 18 and 47.]

[21] Samuel Beaulieu, Antoine Comby, Baptiste Fabre, Dominique Descamps, Amelie Ferre, Gustavo Garcia, Romain Geneaux, Francois Legare, Laurent Nahon, Stephane Petit, Thierry Ruchon, Bernard Pons, Valerie Blanchet, and Yann Mairesse. Probing ultrafast dynamics of chiral molecules using time-resolved photoelectron circular dichroism. *Faraday Discuss.*, 194:325–348, 2016. doi: 10.1039/C6FD00113K. URL http://dx.doi.org/10.1039/C6FD00113K. [Cited on page 18.]

[22] S. Rozen, A. Comby, E. Bloch, S. Beauvarlet, D. Descamps, B. Fabre, S. Petit, V. Blanchet, B. Pons, N. Dudovich, and Y. Mairesse. Controlling subcycle optical chirality in the photoionization of chiral molecules. *Physical Review X*, 9(3), jul 2019. doi: 10.1103/physrevx.9.031004. [Cited on page 18.]

[23] L. Allen, M. W. Beijersbergen, R. J. C. Spreeuw, and J. P. Woerdman. Orbital angular momentum of light and the transformation of laguerre-gaussian laser modes. *Phys. Rev. A*, 45:8185–8189, Jun 1992. doi: 10.1103/PhysRevA.45.8185. URL http://link.aps.org/doi/10.1103/PhysRevA.45.8185. [Cited on pages 18 and 168.]

[24] Halina Rubinsztein-Dunlop, Andrew Forbes, M V Berry, M R Dennis, David L Andrews, Masud Mansuripur, Cornelia Denz, Christina Alpmann, Peter Banzer, Thomas Bauer, Ebrahim Karimi, Lorenzo Marrucci, Miles Padgett, Monika Ritsch-Marte, Natalia M Litchinitser, Nicholas P Bigelow, C Rosales-Guzmán, A Belmonte, J P Torres, Tyler W Neely, Mark Baker, Reuven Gordon, Alexander B Stilgoe, Jacquiline Romero, Andrew G White, Robert Fickler, Alan E Willner, Guodong Xie, Benjamin McMorran, and Andrew M Weiner. Roadmap on structured light. *Journal of Optics*, 19(1):013001, nov 2016. doi: 10.1088/2040-8978/19/1/013001. [Cited on page 19.]

[25] Genevieve Gariepy, Jonathan Leach, Kyung Taec Kim, T. J. Hammond, E. Frumker, Robert W. Boyd, and P. B. Corkum. Creating high-harmonic beams with controlled orbital angular momentum, 2014. 113(15). doi: 10.1103/physrevlett.113.153901. [Cited on pages 19 and 49.]

[26] R. Géneaux, A. Camper, T. Auguste, O. Gobert, J. Caillat, R. Taïeb, and T. Ruchon. Synthesis and characterization of attosecond light vortices in the extreme ultraviolet, 2016. 7:12583. ISSN 2041-1723. doi: 10.1038/ncomms12583. URL http://dx.doi.org/10.1038/ncomms12583. [Cited on pages 19 and 220.]

[27] Kevin M. Dorney, Laura Rego, Nathan J. Brooks, Julio San Román, Chen-Ting Liao, Jennifer L. Ellis, Dmitriy Zusin, Christian Gentry, Quynh L. Nguyen, Justin M. Shaw, Antonio Picón, Luis Plaja, Henry C. Kapteyn, Margaret M. Murnane, and Carlos Hernández-García. Controlling the polarization and vortex charge of attosecond high-harmonic beams via simultaneous spin–orbit momentum conservation. *Nature Photonics*, 13(2):123–130, dec 2018. doi: 10.1038/s41566-018-0304-3. [Cited on page 19.]

[28] F. Sanson, A. K. Pandey, I. Papagiannouli, F. Harms, G. Dovillaire, E. Baynard, J. Demailly, O. Guilbaud, B. Lucas, O. Neveu, M. Pittman, D. Ros, M. Richardson, E. Johnson, W. Li, Ph. Balcou, and S. Kazamias. Highly multimodal structure of high topological charge extreme ultraviolet vortex beams. *Optics Letters*, 45(17):4790, aug 2020. doi: 10.1364/ol.397206. [Cited on page 19.]

[29] A. Picón, J. Mompart, J. R. Vázquez de Aldana, L. Plaja, G. F. Calvo, and L. Roso. Photoionization with orbital angular momentum beams. *Opt. Express*, 18(4):3660–3671, Feb 2010. doi: 10.1364/OE.18.003660. URL http://opg.optica.org/oe/abstract.cfm?URI=oe-18-4-3660. [Cited on page 19.]

[30] A Picón, A Benseny, J Mompart, J R Vázquez de Aldana, L Plaja, G F Calvo, and L Roso. Transferring orbital and spin angular momenta of light to atoms. *New Journal of Physics*, 12(8):083053, aug 2010. doi: 10.1088/1367-2630/12/8/083053. URL https://doi.org/10.1088/1367-2630/12/8/083053. [Cited on page 19.]

[31] Sucharita Giri, Misha Ivanov, and Gopal Dixit. Signatures of the orbital angular momentum of an infrared light beam in the two-photon transition matrix element: A step toward attosecond chronoscopy of photoionization. *Phys. Rev. A*, 101:033412, Mar 2020. doi: 10.1103/PhysRevA.101.033412. URL https://link.aps.org/doi/10.1103/PhysRevA.101.033412. [Cited on page 19.]

[32] Mauro Fanciulli, Matteo Pancaldi, Emanuele Pedersoli, Mekha Vimal, David Bresteau, Martin Luttmann, Dario De Angelis, Primož Rebernik Ribič, Benedikt RÃŕÂ£Â¡sner, Christian David, Carlo Spezzani, Michele Manfredda, Ricardo Sousa, Ioan-Lucian Prejbeanu, Laurent Vila, Bernard Dieny, Giovanni De Ninno, Flavio Capotondi, Maurizio Sacchi, and Thierry Ruchon. Observation of magnetic helicoidal dichroism with extreme ultraviolet light vortices. March 2021. URL https://arxiv.org/abs/2103.13697. [Cited on pages 19, 20, and 225.]

[33] Mauro Fanciulli, Matteo Pancaldi, Emanuele Pedersoli, Mekha Vimal, David Bresteau, Martin Luttmann, Dario De Angelis, Primož Rebernik Ribič, Benedikt Rösner, Christian David, Carlo Spezzani, Michele Manfredda, Ricardo Sousa, Ioan-Lucian Prejbeanu, Laurent Vila, Bernard Dieny, Giovanni De Ninno, Flavio Capotondi, Maurizio Sacchi, and Thierry Ruchon. Observation of magnetic helicoidal dichroism with extreme ultraviolet light vortices. *Phys. Rev. Lett.*, 128:077401, Feb 2022. doi: 10.1103/PhysRevLett.128.077401. URL https://link.aps.org/doi/10.1103/PhysRevLett.128.077401. [Cited on pages 19, 173, and 225.]

[34] Samuel Bengtsson and Johan Mauritsson. Ultrafast control and opto-optical modulation of extreme ultraviolet light. *Journal of Physics B: Atomic, Molecular and Optical Physics*, 52(6): 063002, mar 2019. doi: 10.1088/1361-6455/ab01c2. [Cited on page 20.]

[35] Kuang-Yu Chang, Long-Cheng Huang, Koji Asaga, Ming-Shian Tsai, Laura Rego, Pei-Chi Huang, Hiroki Mashiko, Katsuya Oguri, Carlos Hernández-García, and Ming-Chang Chen. High-order nonlinear dipole response characterized by extreme ultraviolet ellipsometry. *Optica*, 8(4):484, April 2021. doi: 10.1364/OPTICA.413531. [Cited on page 20.]

[36] Kyung Taec Kim, Chunmei Zhang, Thierry Ruchon, Jean-François Hergott, Thierry Auguste, DM Villeneuve, PB Corkum, and F Quéré. Photonic streaking of attosecond pulse trains. *Nature Photonics*, 7(8):651–656, 2013. [Cited on pages 20 and 56.]

[37] Kyung Taec Kim, Kyungseung Kim, and T J Hammond. Phase retrieval approach for an accurate reconstruction of an arbitrary optical waveform in the petahertz optical oscilloscope. *Journal of Physics B: Atomic, Molecular and Optical Physics*, 50(2):024002, jan 2017. doi: 10.1088/1361-6455/50/2/024002. [Cited on page 20.]

[38] M. Louisy, C. L. Arnold, M. Miranda, E. W. Larsen, S. N. Bengtsson, D. Kroon, M. Kotur, D. Guénot, L. Rading, P. Rudawski, F. Brizuela, F. Campi, B. Kim, A. Jarnac, A. Houard, J. Mauritsson, P. Johnsson, A. L'Huillier, and C. M. Heyl. Gating attosecond pulses in a noncollinear geometry. *Optica*, 2(6):563, jun 2015. doi: 10.1364/optica.2.000563. [Cited on page 20.]

[39] AV Birulin, Viktor T Platonenko, and Vasilii Vyacheslavovich Strelkov. High-order harmonic generation in colliding beams. *Quantum Electronics*, 26(5):377, 1996. [Cited on pages 20, 48, and 56.]

[40] S. V FOMICHEV, P BREGER, B CARRE, P AGOSTINI, and D. F. ZARETSKY. Non-collinear high-harmonic generation. In *Proceedings of the Tenth International Laser Physics Workshop (LPHYS'01), Moscow, Russia, July 3-7, 2001*, pages 383–388. [Cited on pages 20 and 48.]

[41] Y. Mairesse, N. Dudovich, J. Levesque, D. Kartashov, D. M. Villeneuve, P. B. Corkum, and T. Auguste. Transient phase masks in high-harmonic generation, 2007. 32(4):436–438. URL http://ol.osa.org/abstract.cfm?URI=ol-32-4-436. [Cited on pages 20 and 56.]

[42] J. B. Bertrand, H. J. Wörner, H.-C. Bandulet, É. Bisson, M. Spanner, J.-C. Kieffer, D. M. Villeneuve, and P. B. Corkum. Ultrahigh-Order Wave Mixing in Noncollinear High Harmonic Gen-

eration, 2011. 106(2):023001. doi: 10.1103/PhysRevLett.106.023001. [Cited on pages 20, 48, 50, 52, 53, 55, 56, 81, 85, 92, 93, 223, and 224.]

[43] Jennifer L. Ellis, Kevin M. Dorney, Charles G. Durfee, Carlos Hernández-García, Franklin Dollar, Christopher A. Mancuso, Tingting Fan, Dmitriy Zusin, Christian Gentry, Patrik Grychtol, Henry C. Kapteyn, Margaret M. Murnane, and Daniel D. Hickstein. Phase matching of noncollinear sum and difference frequency high harmonic generation above and below the critical ionization level, 2017. 25(9):10126. doi: 10.1364/oe.25.010126. [Cited on pages 20, 38, 56, 104, 122, 125, 143, and 223.]

[44] D. Gauthier, P. Rebernik Ribič, G. Adhikary, A. Camper, C. Chappuis, R. Cucini, L. F. DiMauro, G. Dovillaire, F. Frassetto, R. Géneaux, P. Miotti, L. Poletto, B. Ressel, C. Spezzani, M. Stupar, T. Ruchon, and G. De Ninno. Tunable orbital angular momentum in high-harmonic generation, 2017. 8:14971. doi: 10.1038/ncomms14971. [Cited on pages 20, 49, 52, and 56.]

[45] Fanqi Kong, Chunmei Zhang, Frédéric Bouchard, Zhengyan Li, Graham G. Brown, Dong Hyuk Ko, T. J. Hammond, Ladan Arissian, Robert W. Boyd, Ebrahim Karimi, and P. B. Corkum. Controlling the orbital angular momentum of high harmonic vortices, 2017. 8:14970. doi: 10.1038/ncomms14970. [Cited on pages 20, 49, and 52.]

[46] Laura Rego, Kevin M. Dorney, Nathan J. Brooks, Quynh L. Nguyen, Chen-Ting Liao, Julio San Román, David E. Couch, Allison Liu, Emilio Pisanty, Maciej Lewenstein, Luis Plaja, Henry C. Kapteyn, Margaret M. Murnane, and Carlos Hernández-García. Generation of extreme-ultraviolet beams with time-varying orbital angular momentum. *Science*, 364(6447):eaaw9486, jun 2019. doi: 10.1126/science.aaw9486. [Cited on page 20.]

[47] David Ayuso, Ofer Neufeld, Andres F. Ordonez, Piero Decleva, Gavriel Lerner, Oren Cohen, Misha Ivanov, and Olga Smirnova. Synthetic chiral light for efficient control of chiral light–matter interaction. *Nature Photonics*, 13(12):866–871, oct 2019. doi: 10.1038/s41566-019-0531-2. [Cited on page 20.]

[48] X. F. Li, A. L'Huillier, M. Ferray, L. A. Lompre, and G. Mainfray. Multiple-Harmonic Generation In Rare-Gases At High Laser Intensity. *Phys. Rev. A*, 39(11):5751–5761, June 1989. [Cited on page 25.]

[49] C. Vozzi, M. Negro, F. Calegari, G. Sansone, M. Nisoli, S. de Silvestri, and S. Stagira. Generalized molecular orbital tomography. *Nature Physics*, 7:823–827, October 2011. doi: 10.1038/nphys2029. [Cited on page 25.]

[50] Franck Lépine, Misha Y. Ivanov, and Marc J. J. Vrakking. Attosecond molecular dynamics: fact or fiction? *Nature Photonics*, 8(3):195–204, feb 2014. doi: 10.1038/nphoton.2014.25. [Cited on page 25.]

[51] Marcello F Ciappina, José A Pérez-Hernández, Alexandra S Landsman, William A Okell, Sergey Zherebtsov, Benjamin Förg, Johannes Schötz, Lennart Seiffert, Thomas Fennel, Tahir Shaaran,

et al. Attosecond physics at the nanoscale. *Reports on Progress in Physics*, 80(5):054401, 2017. [Cited on page 25.]

[52] P. B. Corkum. Plasma perspective on strong-field multiphoton ionization. *Phys. Rev. Lett.*, **71**, 1993. [Cited on pages 25 and 74.]

[53] M. Y. Kuchiev. Atomic antenna. *Soviet Journal of Experimental and Theoretical Physics Letters*, 45:404, April 1987. [Cited on page 25.]

[54] L .V. Keldysh. Ionization in the Field of a Strong Electromagnetic Wave. *Sov. Phys. JETP*, 20: 1307, 1965. [Cited on page 26.]

[55] Romain Géneaux. *Le moment angulaire de la lumière en génération d'harmoniques d'ordre élevé*. PhD thesis, 2016. URL http://www.theses.fr/2016SACLS474. Thèse de doctorat dirigée par Carré, Bertrand Lasers, molécules, rayonnement atmosphérique Paris Saclay 2016. [Cited on pages 27, 166, 220, and 223.]

[56] Thierry Ruchon. High harmonic generation and attosecond light pulses. URL https://www-llb.cea.fr/Pisp/thierry.ruchon/data/LectureRuchon.pdf. [Cited on pages 28, 36, 42, 118, and 119.]

[57] Christina-Anastasia Alexandridi. *Attosecond spectroscopy : study of the photoionization dynamics of atomic gases close to resonances*. PhD thesis, 2018. URL http://www.theses.fr/2018SACLS571. [Cited on page 29.]

[58] J. L. Krause, K. J. Schafer, and K. C. Kulander. High-order harmonic generation from atoms and ions in the high intensity regime, 1992. *Phys. Rev. Lett.*, **68**:3535, 1992. [Cited on page 29.]

[59] J. Tate, T. Auguste, H. G. Muller, P. Salières, P. Agostini, and L. F. DiMauro. Scaling of wavepacket dynamics in an intense midinfrared field. *Phys. Rev. Lett.*, 98:013901, Jan 2007. doi: 10.1103/PhysRevLett.98.013901. URL https://link.aps.org/doi/10.1103/PhysRevLett.98.013901. [Cited on page 30.]

[60] A. D. Shiner, C. Trallero-Herrero, N. Kajumba, H.-C. Bandulet, D. Comtois, F. Légaré, M. Giguère, J-C. Kieffer, P. B. Corkum, and D. M. Villeneuve. Wavelength scaling of high harmonic generation efficiency. *Phys. Rev. Lett.*, 103:073902, Aug 2009. doi: 10.1103/PhysRevLett.103.073902. URL https://link.aps.org/doi/10.1103/PhysRevLett.103.073902. [Cited on page 30.]

[61] Christophe Heyl. *Scaling and Gating Attosecond Pulse Generation*. PhD thesis, Lund University, 2014. [Cited on pages 30, 116, and 125.]

[62] Aura Inés Gonzalez, Gaëtan Jargot, Philippe Rigaud, Loïc Lavenu, Florent Guichard, Antoine Comby, Thierry Auguste, Olivier Sublemontier, Michel Bougeard, Yoann Zaouter, Patrick Georges, Marc Hanna, and Thierry Ruchon. Spatio-spectral structures in high harmonic generation driven by tightly focused high repetition rate lasers. *Journal of the Optical Society of America B*, 35(4):A6, feb 2018. doi: 10.1364/josab.35.0000a6. [Cited on pages 31, 33, and 43.]

[63] P. Salières, B. Carré, L. Le Déroff, F. Grasbon, G. G. Paulus, H. Walther, R. Kopold, W. Becker, D. B. Milošević, A. Sanpera, and M. Lewenstein. Feynman's Path-Integral Approach for Intense-Laser-Atom Interactions. *Science*, **292**:902, 2001. [Cited on page 32.]

[64] Olga Smirnova and Misha Ivanov. *Multielectron High Harmonic Generation: Simple Man on a Complex Plane*, chapter 7, pages 201–256. John Wiley Sons, Ltd, 2014. ISBN 9783527677689. doi: https://doi.org/10.1002/9783527677689.ch7. URL https://onlinelibrary.wiley.com/doi/abs/10.1002/9783527677689.ch7. [Cited on page 32.]

[65] F Catoire, A Ferré, O Hort, A Dubrouil, L Quintard, D Descamps, S Petit, F Burgy, E Mével, Y Mairesse, et al. Complex structure of spatially resolved high-order-harmonic spectra, 2016. *Physical Review A*, 94(6):063401. [Cited on pages 33, 37, and 75.]

[66] M. Fatih Erden and Haldun M. Ozaktas. Accumulated gouy phase shift in gaussian beam propagation through first-order optical systems. *J. Opt. Soc. Am. A*, 14(9):2190–2194, Sep 1997. doi: 10.1364/JOSAA.14.002190. URL http://www.osapublishing.org/josaa/abstract.cfm?URI=josaa-14-9-2190. [Cited on page 36.]

[67] Hartmut Ruf. *Dynamique moléculaire par imagerie attoseconde*. PhD thesis, Université de Bordeaux I, 2012. URL http://www.theses.fr/2012BOR14651. Thèse de doctorat dirigée par Mevel, Eric et Mairesse, Yann Laser, Matière et Nanoscience Bordeaux 1 2012. [Cited on pages 40, 60, and 64.]

[68] R Weissenbilder, S Carlström, L Rego, C Guo, CM Heyl, P Smorenburg, E Constant, CL Arnold, and A L'Huillier. Efficient generation of high-order harmonics in gases. *arXiv preprint arXiv:2202.08202*, 2022. [Cited on page 44.]

[69] Anna Gabriella Ciriolo, R Martínez Vázquez, Valer Tosa, Aldo Frezzotti, Gabriele Crippa, Michele Devetta, Davide Faccialà, Fabio Frassetto, Luca Poletto, Aditya Pusala, et al. High-order harmonic generation in a microfluidic glass device. *Journal of Physics: Photonics*, 2(2): 024005, 2020. [Cited on page 44.]

[70] M. D. Perry and J. K. Crane. High-order harmonic emission from mixed fields, 1993. [Cited on pages 47, 49, and 50.]

[71] I. J. Kim, C. M. Kim, H. T. Kim, G. H. Lee, Y. S. Lee, J. Y. Park, D. J. Cho, and C. H. Nam. Highly Efficient High-Harmonic Generation in an Orthogonally Polarized Two-Color Laser Field. *Phys. Rev. Lett.*, 94:243901, 2005. [Cited on page 47.]

[72] Leonardo Brugnera, Felix Frank, David J. Hoffmann, Ricardo Torres, Thomas Siegel, Jonathan G. Underwood, Emma Springate, Chris Froud, Edmond I. C. Turcu, John W. G. Tisch, and Jonathan P. Marangos. Enhancement of high harmonics generated by field steering of electrons in a two-color orthogonally polarized laser field, 2010. *Opt. Lett.*, 35(23):3994–3996, . doi: 10.1364/OL.35.003994. URL http://www.osapublishing.org/ol/abstract.cfm?URI=ol-35-23-3994. [Cited on page 47.]

[73] T. Siegel, R. Torres, D. J. Hoffmann, L. Brugnera, I. Procino, A. Zaïr, Jonathan G. Underwood, E. Springate, I. C. E. Turcu, L. E. Chipperfield, and J. P. Marangos. High harmonic emission from a superposition of multiple unrelated frequency fields, 2010. *Opt. Express*, 18(7):6853–6862. doi: 10.1364/OE.18.006853. URL http://www.osapublishing.org/oe/abstract.cfm?URI=oe-18-7-6853. [Cited on page 47.]

[74] Leonardo Brugnera, David J. Hoffmann, Thomas Siegel, Felix Frank, Amelle Zaïr, John W. G. Tisch, and Jonathan P. Marangos. Trajectory selection in high harmonic generation by controlling the phase between orthogonal two-color fields, 2011. *Phys. Rev. Lett.*, 107:153902, . doi: 10.1103/PhysRevLett.107.153902. URL https://link.aps.org/doi/10.1103/PhysRevLett.107.153902. [Cited on page 47.]

[75] Ankur Mandal, Pranawa C Deshmukh, and Kamal P Singh. Controlling high harmonic generation using inhomogeneous two-color driving laser pulse, 2021. *Laser Physics*, 31(7):075302. doi: 10.1088/1555-6611/abfe55. URL https://doi.org/10.1088/1555-6611/abfe55. [Cited on page 47.]

[76] S. L. Voronov, I. Kohl, J. B. Madsen, J. Simmons, N. Terry, J. Titensor, Q. Wang, and J. Peatross. Control of laser high-harmonic generation with counterpropagating light, 2001. *Phys. Rev. Lett.*, 87:133902. doi: 10.1103/PhysRevLett.87.133902. URL https://link.aps.org/doi/10.1103/PhysRevLett.87.133902. [Cited on page 48.]

[77] N.Bloembergenl. *Nonlinear Optics*. New York:Benjamin. [Cited on page 48.]

[78] A. V. Birulin, V. T. Platonenko, and V. V. Strelkov. High-harmonic generation in interfering waves, 1996. *Soviet Journal of Experimental and Theoretical Physics*, 83(1):33–38. [Cited on page 48.]

[79] Jennifer L Ellis. *Development and application of extreme ultraviolet light sources :harnessing novel geometries of high-harmonic generation and using photoelectron spectroscopy to study nanoparticle dynamics, 2018*. PhD thesis. [Cited on pages 49 and 224.]

[80] Avner Fleischer, Ofer Kfir, Tzvi Diskin, Pavel Sidorenko, and Oren Cohen. Spin angular momentum and tunable polarization in high-harmonic generation, 2014,. 8(7):543–549. doi: 10.1038/nphoton.2014.108. [Cited on page 49.]

[81] Avner Fleischer and Nimrod Moiseyev. Attosecond laser pulse synthesis using bichromatic high-order harmonic generation, 2006. *Physical Review A*, 74(5):053806. doi: 10.1103/physreva.74.053806. URL http://link.aps.org/abstract/PRA/v74/e053806. [Cited on page 50.]

[82] Liang Li, Pengfei Lan, Lixin He, Xiaosong Zhu, Jing Chen, and Peixiang Lu. Scaling law of high harmonic generation in the framework of photon channels, 2018. *Physical Review Letters*, 120 (22). doi: 10.1103/physrevlett.120.223203. [Cited on pages 54, 55, 56, 85, 89, 93, 97, 223, and 224.]

[83] C. M. Heyl, P. Rudawski, F. Brizuela, S. N. Bengtsson, J. Mauritsson, and A. L'Huillier. Macroscopic effects in noncollinear high-order harmonic generation, 2014. *Physical Review Letters*, 112(14). doi: 10.1103/physrevlett.112.143902. [Cited on pages 56, 76, 81, 82, 115, 122, 125, 138, 162, 223, 224, and 225.]

[84] Khoa Anh Tran, Khuong Ba Dinh, Peter Hannaford, and Lap Van Dao. Phase-matched four-wave mixing in the extreme ultraviolet region, 2018. *Journal of Applied Physics*, 124(1):015901. doi: 10.1063/1.5028436. [Cited on pages 56 and 122.]

[85] A. Comby, D. Descamps, S. Beauvarlet, A. Gonzalez, F. Guichard, S. Petit, Y. Zaouter, and Y. Mairesse. Cascaded harmonic generation from a fiber laser: a milliwatt xuv source. *Opt. Express*, 27(15):20383–20396, Jul 2019. doi: 10.1364/OE.27.020383. URL http://opg.optica.org/oe/abstract.cfm?URI=oe-27-15-20383. [Cited on pages 62 and 154.]

[86] C Chappuis, D Bresteau, T Auguste, O Gobert, and T Ruchon. High-order harmonic generation in an active grating. *Physical Review A*, 99(3):033806, 2019. [Cited on pages 71, 72, 81, and 223.]

[87] Y Mairesse, D Zeidler, Nirit Dudovich, M Spanner, J Levesque, DM Villeneuve, and PB Corkum. High-order harmonic transient grating spectroscopy in a molecular jet, 2008. *Physical Review Letters*, 100(14):143903, 2008. [Cited on page 71.]

[88] Olga Smirnova and Misha Ivanov. Multielectron high harmonic generation: Simple man on a complex plane, 2014. In *Attosecond and XUV Physics*, pages 201–256. Wiley-VCH Verlag GmbH & Co. KGaA. doi: 10.1002/9783527677689.ch7. [Cited on pages 74 and 75.]

[89] Kasra Amini, Jens Biegert, Francesca Calegari, Alexis Chacón, Marcelo F Ciappina, Alexandre Dauphin, Dmitry K Efimov, Carla Figueira de Morisson Faria, Krzysztof Giergiel, Piotr Gniewek, Alexandra S Landsman, Michał Lesiuk, Michał Mandrysz, Andrew S Maxwell, Robert Moszyński, Lisa Ortmann, Jose Antonio Pérez-Hernández, Antonio Picón, Emilio Pisanty, Jakub Prauzner-Bechcicki, Krzysztof Sacha, Noslen Suárez, Amelle Zaïr, Jakub Zakrzewski, and Maciej Lewenstein. Symphony on strong field approximation. *Reports on Progress in Physics*, 82(11): 116001, oct 2019. doi: 10.1088/1361-6633/ab2bb1. [Cited on page 74.]

[90] Anh-Thu Le, RR Lucchese, S Tonzani, Toru Morishita, and CD Lin. Quantitative rescattering theory for high-order harmonic generation from molecules. *Physical Review A*, 80(1):013401, 2009. [Cited on page 75.]

[91] MB Gaarde, Ph Antoine, Anders Persson, B Carré, Anne L'Huillier, and Claes-Göran Wahlström. High-order tunable sum and difference frequency mixing in the xuv region. *Journal of Physics B: Atomic, Molecular and Optical Physics*, 29(5):L163, 1996. [Cited on page 81.]

[92] Katalin Varju, Yann Mairesse, B Carré, Mette B Gaarde, Per Johnsson, S Kazamias, Rodrigo López-Martens, Johan Mauritsson, KJ Schafer, Ph Balcou, et al. Frequency chirp of harmonic and attosecond pulses. *Journal of Modern Optics*, 52(2-3):379–394, 2005. [Cited on pages 88, 105, and 107.]

[93] J Marcus Dahlström, Diego Guénot, Kathrin Klünder, Matthieu Gisselbrecht, Johan Mauritsson, Anne LâĂŹHuillier, Alfred Maquet, and Richard Taïeb. Theory of attosecond delays in laser-assisted photoionization. *Chemical Physics*, 414:53–64, 2013. [Cited on page 97.]

[94] Divya Bharti, David Atri-Schuller, Gavin Menning, Kathryn R Hamilton, Robert Moshammer, Thomas Pfeifer, Nicolas Douguet, Klaus Bartschat, and Anne Harth. Decomposition of the transition phase in multi-sideband schemes for reconstruction of attosecond beating by interference of two-photon transitions. *Physical Review A*, 103(2):022834, 2021. [Cited on page 97.]

[95] Mattias Bertolino and Jan Marcus Dahlström. Multiphoton interaction phase shifts in attosecond science. *Physical Review Research*, 3(1):013270, 2021. [Cited on pages 97 and 98.]

[96] Markus Pollnau. Phase aspect in photon emission and absorption. *Optica*, 5(4):465–474, 2018. [Cited on page 98.]

[97] Lucas J Zipp, Adi Natan, and Philip H Bucksbaum. Probing electron delays in above-threshold ionization. *Optica*, 1(6):361–364, 2014. [Cited on page 98.]

[98] Samuel Beaulieu, Antoine Comby, Alex Clergerie, Jérémie Caillat, Dominique Descamps, Nirit Dudovich, Baptiste Fabre, Romain Géneaux, François Légaré, Stéphane Petit, et al. Attosecond-resolved photoionization of chiral molecules. *Science*, 358(6368):1288–1294, 2017. [Cited on page 98.]

[99] HG Muller. *An efficient propagation scheme for the time-dependent Schrödinger equation in the velocity gauge, 1999*, volume 9, pages 138–148. Interperiodica. [Cited on page 105.]

[100] HG Muller. Numerical simulation of high-order above-threshold-ionization enhancement in argon. *Physical Review A*, 60(2):1341, 1999. [Cited on page 105.]

[101] S. Kazamias, S. Daboussi, O. Guilbaud, K. Cassou, D. Ros, B. Cros, and G. Maynard. Pressure-induced phase matching in high-order harmonic generation. *Phys. Rev. A*, 83:063405, Jun 2011. doi: 10.1103/PhysRevA.83.063405. URL https://link.aps.org/doi/10.1103/PhysRevA.83.063405. [Cited on page 105.]

[102] Wei Cao, Erika R Warrick, Daniel M Neumark, and Stephen R Leone. Attosecond transient absorption of argon atoms in the vacuum ultraviolet region: line energy shifts versus coherent population transfer, 2016. 18(1):013041. doi: 10.1088/1367-2630/18/1/013041. URL https://doi.org/10.1088/1367-2630/18/1/013041. [Cited on page 111.]

[103] C. Hernández-García, I. J. Sola, and L. Plaja. Signature of the transversal coherence length in high-order harmonic generation. *Phys. Rev. A*, 88:043848, Oct 2013. doi: 10.1103/PhysRevA.88.043848. URL https://link.aps.org/doi/10.1103/PhysRevA.88.043848. [Cited on page 115.]

[104] S. Kazamias, D. Douillet, F. Weihe, C. Valentin, A. Rousse, S. Sebban, G. Grillon, F. Augé, D. Hulin, and Ph. Balcou. Global optimization of high harmonic generation. *Phys. Rev. Lett.*, 90:193901, May 2003. doi: 10.1103/PhysRevLett.90.193901. URL https://link.aps.org/doi/10.1103/PhysRevLett.90.193901. [Cited on pages 116, 138, and 225.]

[105] Thierry Ruchon, CP Hauri, Katalin Varju, Erik Mansten, Marko Swoboda, R López-Martens, and Anne L'Huillier. Macroscopic effects in attosecond pulse generation, 2008. *New Journal of Physics*, 10(2):025027, 2008. [Cited on page 116.]

[106] Balázs Major and Katalin Varju. Extended model for optimizing high-order harmonic generation in absorbing gases. *Journal of Physics B: Atomic, Molecular and Optical Physics*, dec 2021. doi: 10.1088/1361-6455/ac3fbe. URL https://doi.org/10.1088/1361-6455/ac3fbe. [Cited on page 116.]

[107] Christoph M Heyl, Helene Coudert-Alteirac, Miguel Miranda, Maite Louisy, Katalin Kovács, Valer Tosa, Emeric Balogh, Katalin Varjú, Anne LâĂŹHuillier, Arnaud Couairon, et al. Scale-invariant nonlinear optics in gases. *Optica*, 3(1):75–81, 2016. [Cited on page 118.]

[108] Celine Chappuis. *Génération d'harmoniques d'ordre élevé à deux faisceaux portant du moment angulaire*. Theses. URL https://tel.archives-ouvertes.fr/tel-02292788. [Cited on pages 123, 167, 168, 220, and 223.]

[109] Neil W. Ashcroft and N. David Mermin. *Solid State Physics*. Cengage Learning. [Cited on pages 127 and 128.]

[110] C M Heyl, C L Arnold, A Couairon, and A L'Huillier. Introduction to macroscopic power scaling principles for high-order harmonic generation. *Journal of Physics B: Atomic, Molecular and Optical Physics*, 50(1):013001, dec 2016. doi: 10.1088/1361-6455/50/1/013001. URL https://doi.org/10.1088/1361-6455/50/1/013001. [Cited on pages 138 and 225.]

[111] C Benko. *Extreme ultraviolet frequency combs for precision measurement and strong-field physics (Order No. 10150896)*. PhD thesis. [Cited on page 142.]

[112] Andy Rundquist, Charles G Durfee III, Zenghu Chang, Catherine Herne, Sterling Backus, Margaret M Murnane, and Henry C Kapteyn. Phase-matched generation of coherent soft x-rays. *Science*, 280(5368):1412–1415, 1998. [Cited on page 143.]

[113] XM Tong and CD Lin. Empirical formula for static field ionization rates of atoms and molecules by lasers in the barrier-suppression regime. *Journal of Physics B: Atomic, Molecular and Optical Physics*, 38(15):2593, 2005. [Cited on page 143.]

[114] Michel van Veenendaal and Ian McNulty. Prediction of strong dichroism induced by x rays carrying orbital momentum. *Physical review letters*, 98(15):157401, 2007. [Cited on page 165.]

[115] Renaud Mathevet, Bruno Viaris de Lesegno, Laurence Pruvost, and Geert LJA Rikken. Negative experimental evidence for magneto-orbital dichroism. *Optics express*, 21(4):3941–3945, 2013. [Cited on page 165.]

[116] Michel van Veenendaal. Interaction between x-ray and magnetic vortices. *Physical Review B*, 92(24):245116, 2015. [Cited on pages 165 and 166.]

[117] Mauro Fanciulli, David Bresteau, Mekha Vimal, Martin Luttmann, Maurizio Sacchi, and Thierry Ruchon. Electromagnetic theory of helicoidal dichroism in reflection from magnetic structures, 2021. 103:013501. doi: 10.1103/PhysRevA.103.013501. URL https://link.aps.org/doi/10.1103/PhysRevA.103.013501. [Cited on page 166.]

[118] StephenM. Barnett and Roberta Zambrini. Orbital angular momentum of light. In MikhailI. Kolobov, editor, *Quantum Imaging*, pages 277–311. Springer New York, 2007. ISBN 978-0-387-33818-7. doi: 10.1007/0-387-33988-4_12. URL http://dx.doi.org/10.1007/0-387-33988-4_12. [Cited on page 166.]

[119] DL Andrews. *Structured Light and its Applications: An introduction to Phase-Structured Beams and Nanoscale Optical Forces*, volume xiii. Academic, Burlington MA, 2008. URL https://ueaeprints.uea.ac.uk/38325/. [Cited on page 166.]

[120] Timothy Doster and Abbie T Watnik. Laguerre–gauss and bessel–gauss beams propagation through turbulence: analysis of channel efficiency. *Applied Optics*, 55(36):10239–10246, 2016. [Cited on page 166.]

[121] Hartmut Höchst, Dennis Rioux, Dai Zhao, and David L Huber. Magnetic linear dichroism effects in reflection spectroscopy: A case study at the fe m 2, 3 edge. *Journal of applied physics*, 81(11):7584–7588, 1997. [Cited on page 168.]

[122] Mannan Ali. *Growth and study of magnetostrictive FeSiBc thin films for device applications*. PhD thesis, 1999. URL http://www.study-on-line.co.uk/whoami/thesis/thesisro.pdf. [Cited on pages 169 and 171.]

[123] Christian PIOVERA. *Ultrafast laser induced dynamics in ferromagnets: towards the control of the spin order from the femtosecond to the sub nanosecond time scale*. PhD thesis, 2013. URL https://www.politesi.polimi.it/handle/10589/74704. [Cited on page 169.]

[124] J Zak, ER Moog, C Liu, and SD Bader. Fundamental magneto-optics. *Journal of applied physics*, 68(8):4203–4207, 1990. [Cited on page 171.]

[125] S Valencia, A Gaupp, W Gudat, H-Ch Mertins, PM Oppeneer, D Abramsohn, and CM Schneider. Faraday rotation spectra at shallow core levels: 3p edges of fe, co, and ni. *New Journal of Physics*, 8(10):254, 2006. [Cited on page 171.]

[126] Shingo Yamamoto and Iwao Matsuda. Measurement of the resonant magneto-optical kerr effect using a free electron laser. *Applied Sciences*, 7(7):662, 2017. [Cited on page 219.]

[127] Zhiyang Lin, You Chen, Jixiong Pu, and Xuanyang Lai. Enhancing circularly polarized xuv vortices from bicircular laguerre-gaussian fields. *Opt. Express*, 30(2):2636–2645, Jan 2022. doi: 10.1364/OE.450049. URL http://opg.optica.org/oe/abstract.cfm?URI=oe-30-2-2636. [Cited on page 227.]

[128] Zhong Guan, Zhiming Yin, and Cheng Jin. Macroscopic phase-matching mechanism for orbital angular momentum spectra of high-order harmonics by mixing two laguerre-gaussian vortex modes. *Phys. Rev. A*, 105:023107, Feb 2022. doi: 10.1103/PhysRevA.105.023107. URL https://link.aps.org/doi/10.1103/PhysRevA.105.023107. [Cited on page 227.]

Acknowledgements

Firstly, I would like to thank my jury members for agreeing to review this manuscript. Special thanks to Eric Constant and Christoph Heyl for their careful reading and comments.

When I moved to France to do a PhD, I was not expecting it to turn out to be such an enjoyable experience. I was afraid that the next three years of my life was going to be rather dull, cooped up in a lab with no social life. But the love, warmth and hospitality I received here was beyond all my expectations. It was one of the best decisions of my life to move to this beautiful country and experience its culture.

I feel really lucky to have been able to do my PhD in this group. Thank you Thierry for being such an incredible mentor. Thank you for being my advisor and family at the same time, being a rock through all those difficult times. David, thanks a lot for being such a cool post-doc giving a novice lot of confidence and courage and even letting me tag along with you to your parties. Thank you Martin for being the Tortis to my Otis in all my stupidities and making the days brighter. You learnt very quickly and improved the experiment so much. Je suis trés fier de toi! A big hug and thank you to my fun office-mate and best man Mau-Mau. And Alice, I am so glad that I could share this journey with you and Eloise! Even though we could not spend much time together, I am happy to have got the chance to meet you Matthieu, good luck to you to start your PhD.

I would like to thank everyone in Attolab for their warm support and encouragement. Especially, Pascal, for taking care of the administrative parts of the job so that students can focus on science, and Pad'Ol for his kind conversations and ready smile. A big thanks to Dominique for sharing his Python programming skills, it helped me a lot! And merci Constant and Christian who in their own little ways gave me a lot of support while I was writing. Thank you Romain for the ping pong breaks and your thesis, which was a great foundation to start with. I would like to thank the laser team for making sure that we had the beam every morning. I would also like to thank my master's thesis advisor, Vandana

Sharma, who inspired me to follow this path. And all my teachers throughout my life.

Outside of the lab, there are many nice friendships I made in France that made this journey easier for me. I am happy to have had this introduction to French culture through these little adventures. Thank you Jenny and all my colocs along the way. All my life, my friends have been my support system. As bad as COVID-times was, it brought us closer together. Thank you guys for still staying connected from all around the world. Love you Goonja, Leks and Bibin who have been just a phone call away any time of the day and is always there for me.

Thank you Koki for your quiet strength and patience. You made the "D-day" so easy. You really stepped up in a lot of ways. Merci beaucoup.

I am so very grateful to my family who makes me "me" and who are the reason for all my success and happiness in life.